Optical Design of Generalised Gradient-Index Lenses
for the optimisation of size, mass and cost-critical optical systems

Boyd, A.M.

Important note
To cite this publication, please use the final published version (if applicable).
Please check the document version above.

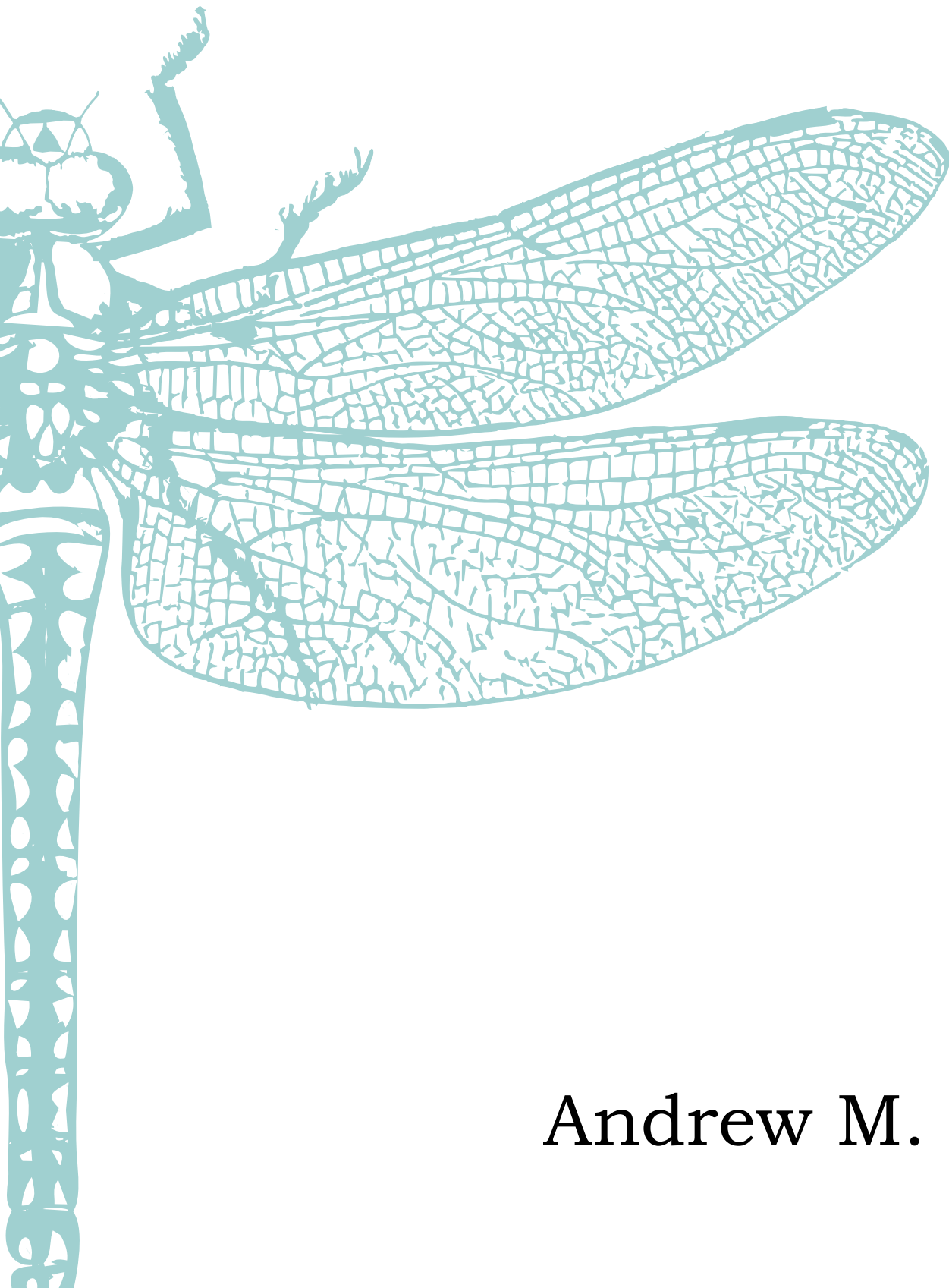# Optical Design of Generalised Gradient-Index Lenses

for the optimisation of size, mass, and cost-critical optical systems

Andrew M. Boyd

Optical Design of Generalised Gradient-Index Lenses

for the optimisation of size, mass, and cost-critical optical systems

Dissertation

for the purpose of obtaining the degree of doctor at Delft University of Technology,
by the authority of the Rector Magnificus: Prof.dr.ir. T.H.J.J. van der Hagen,
chair of the Board for Doctorates,
to be defended publicly at 15:00 on Tuesday 18th of March, 2025.

by

Andrew Martyn BOYD

This dissertation has been approved by the promotors.

Doctoral committee:

Rector Magnificus,	Chairperson
Em.prof.dr. H.P. Urbach,	Delft University of Technology, Promotor
Dr F. Bociort,	Delft University of Technology, Copromotor

Independent members:

Prof.dr. J. Bentley,	U. of Rochester, USA
Prof.dr. W.M.J.M. Coene,	Delft University of Technology
Dr. B. Kruizinga,	TNO, Netherlands
Prof.dr. S. Stallinga,	Delft University of Technology

Reserve member:

Dr. J. Kalkman,	Delft University of Technology

An electronic version of this thesis is available at http://repository.tudelft.nl/.

Preface

Cover image: Emperor dragonfly (*Anax imperator* adapted from a drawing in "British Dragon-flies (Odonata)" by W. J. Lucas, 1900.

These elegant insects inspired the cover of this work in several ways. The dragonfly itself is one of nature's great designs, largely unchanged in hundreds of millions of years. The dragonfly is one of the most successful aerial hunters known, which is in no small part due to its sophisticated visual system comprising not just the striking compound eyes, but also three remarkably complex "simple eyes" or ocelli. Both contain significant refractive index gradients.

The dragonfly's eyes (and those of most animal life on earth) serve as a reminder for the technologist to remain optimistic. A key research question of this work was to determine if gradient-index optics can be advantageously deployed in future optical systems. When we consider the success of this phenomenon in innumerable organisms over millions of years, it is clear that they already have a past and a present. We should be optimistic in our ability to one day replicate this success in human-made optics, with awe for the natural processes can still assemble GRIN distributions that exceed the sophistication of what can be manufactured today.

The inner beauty within the eyes of a dragonfly also reminds us to be humble. For all humankind's ambition and invention, we are perhaps not as smart as we like to think. For unlike the dragonfly, our two simple eyes cannot take in both the detail and the perspective at once. So often, our intense focus blinds us to the bigger picture, and perhaps impending danger. We must remember, that for gradient-index optics to have a future, so must all life on earth.

Finally, the dragonfly reminds me of some happy times amongst the long journey that is a PhD. The image overleaf depicts a pond of waterlilies in St Asaph, not far from the Qioptiq site. Over the years I have spent many a lunchtime sat by this small, secluded pool, thronged by all manner of dragonflies and damselflies nurtured by the lush Denbighshire climate. Indeed it was the site of many of the ideas contained within, a place to contemplate impending fatherhood, and a sanctuary from stress, pandemics, war, bellicose politicians, and every other worry bar getting back to my desk before 1. Dear reader, wherever you are in life's journey, I do hope you find and cherish your own lily pond.

AMB, January 2025.

Contents

List of Figures

List of Tables

List of Abbreviations

AI   Artificial Intelligence

AUT   Automatic Design

CNC   Computer Numerical Control

COS   Continuous Optical System

CTE   Coefficient of Thermal Expansion

CVD   Chemical Vapour Deposition

DLL   Dynamic Link Library

EPD   Entrance Pupil Diameter

F/#   F-Number or Focal Ratio

FOV   Field of View

FPA   Focal Plane Array

GRIN GRadient INdex

HMD   Head/Helmet-Mounted Display

IR   Infrared

LED   Light-Emitting Diode

LGRIN Layered GRadient INdex

LLC   Limited Liability Company

LWIR Long-Wave Infrared

MTF   Modulation Transfer Function

MWIR Mid-Wave Infrared

NA   Numerical Aperture

NIR   Near Infrared

NRE   Non-Recurring Expenditure

OLED Organic Light-Emitting Diode

ONERA Office National d'Etudes et de Recherches Aérospatiales

OTF   Optical Transfer Function

P-V   Peak-to-Valley

PMMA Poly-Methyl-Methacrylate

PSF   Point-Spread Function

PVDF Polyvinylidene Fluoride

RMS   Root-Mean-Squared

RSS   Root-Sum-of-Squares

SAN17 Stryrene-Acrylonitrile

SCRIBE Sub-surface Controllable Refractive Index via Beam Exposure

SPDT Single Point Diamond Turning

SPIE Society of Photo-Instrumentation Engineers

SWAP-C Size, Weight, Power and Cost

SWIR Shortwave Infrared

TOR Wavefront Differential Tolerancing

TRL Technology Readiness Level

UV Ultraviolet

VIRGO Volumetric Index of Refraction Gradient Optics

Summary

Within the optics industry, there is a continuous drive to reduce the size, weight, power consumption and cost of optical systems (known as SWAP-C). A new generation of fabrication technologies for GRadient-INdex (GRIN) materials promise the capability to manufacture GRIN media of arbitrary refractive index distribution (within index variation and spatial resolution limits). This represents an opportunity to further optimise the SWAP-C of lens systems, yet also presents challenges for the optical designer. The necessary optical design tools for arbitary GRINs are not widely implemented, and the potential applications where arbitrary GRINs provide a benefit are not widely explored.

This work addresses these design challenges via two routes. In the first body of work we explore the necessary design tools for generalised GRIN lenses. An efficient mathematical representation is a vital foundation for the design of GRIN lenses. We explore a mathematical representation for GRIN lenses based on the relative composition of the constituent materials, that is amenable to optimisation, and can be easily constrained to materials that are manufacturable. This approach is particularly beneficial for GRINs consisting of more than two base materials.

A critical step in any optical design task is the selection of a starting point from which further optimisation is performed. This presents a challenge for generalised GRIN design as very few such starting solutions exist. We explore a procedure via which the paraxial properties of homogeneous lens systems can be reconstructed as a generalised GRIN medium, to serve as a starting solution for further optimisation. It is shown that complex homogeneous optical designs can be reconstructed in this manner, including the worked example of a fourteen-element lithographic stepper lens. The technique is extended to polychromatic systems, where chromatic dispersion of the parent system is reconstructed in the GRIN starting point. This approach is demonstrated via the reconstruction then optimisation of a GRIN Cooke Triplet equivalent that was composed of the same materials as the parent solution (which were two glass types and air). These starting solution examples are then optimised to high performing optical solutions. We conclude that paraxial reconstruction is a powerful technique in starting point generation, that with further development can greatly improve the time efficiency of GRIN lens design.

A noteworthy capability of GRIN lenses is their capacity to generate focusing power while possessing planar surfaces. We explore the consequences of the use of plano GRIN lenses in imaging lens designs, particularly with respect to the correction of the aberration, coma, through fulfilment of the Abbé sine condition. We demonstrate that generalised GRIN lenses have the ability to correct for coma in a thin, plano-plano geometry, yet the approach increases the refractive index variation and complexity of the GRIN distribution, which presents a trade-off to the lens designer when considering cost-effective fabrication. It is conversely shown that a GRIN medium combined with surface curvature can correct for coma with a simpler GRIN distribution that has smaller index variation, implying that an optimal strategy for the use of GRIN media in optical designs is to apply them in combination with curved surfaces, particularly in areas where GRIN materials have comparative advantage over homogeneous optics such as chromatic aberration correction.

In the second body of work we explore the applications that directly benefit from GRIN optics. We demonstrate that layered polymer GRIN lenses of spherical distribution display the potential to yield colour-corrected lenses with lower mass than glass doublets and without the diffractive ghosts of diamond-turned aspero-diffractive hybrid lenses. The highly dispersive combination of polymers was found to be an effective means of correcting chromatic aberrations within diameter limits defined by the moulded curvature of the lens preform. It was observed that radial GRINs and materials with negative GRIN chromatic dispersion show even greater potential to control chromatic aberrations.

We also explore the application of freeform-GRIN distributions (with no axis of rotational symmetry) to the optical design of a head-mounted display (HMD). We show that freeform-GRIN media act in a comparable manner to tilted and decentred lens elements, as well as toric and freeform surfaces. This is demonstrated through GRIN solutions that have equivalent performance to homogeneous designs with freeform surfaces. It is also shown that a freeform-GRIN medium can be used to restore a common mechanical axis in HMD designs, potentially offering significant simplification of the opto-mechanical design. Polymer GRIN-based HMD designs are shown to have substantially reduced mass compared to their homogeneous counterparts.

Finally, we investigate the application of GRIN materials to the extreme colour correction challenges posed by imaging over several discrete wavebands (known as multispectral optics). We show how GRINs based on infrared materials can greatly simplify an objective lens operating over the short-wave infrared (SWIR) and long-wave infrared (LWIR) wavebands for a common focal plane. The extreme optical dispersion generated by GRIN materials enables a much more benign optical power construction that reduces residual aberrations, allowing significantly fewer optical components and reduced mass and size.

We conclude that the required design infrastructure for arbitrary GRIN lenses is feasible and emerging, and that there are technological challenges in modern optical design that justify ongoing research into GRIN optics. Progress in the optical design of generalised GRINs must be accompanied by refinement in manufacture, metrology, and environmental qualification to enable widespread adoption and deployment.

Samenvatting

In de optische industrie is er een voortdurend streven naar het verkleinen van de afmetingen, het gewicht, het energieverbruik en de kosten van optische systemen (bekend als SWAP-C). Een nieuwe generatie fabricagetechnologieën voor GRadient-INdex (GRIN) materialen belooft de mogelijkheid om GRIN-media te produceren met willekeurige brekingsindexverdeling (binnen grenzen van indexvariatie en ruimtelijke resolutie). Dit biedt een kans om de SWAP-C van lenssystemen verder te optimaliseren, maar brengt ook uitdagingen met zich mee voor de optisch ontwerper. De benodigde optische ontwerptools voor willekeurige GRIN's zijn niet breed geïmplementeerd, en de potentiële toepassingen waar willekeurige GRIN's voordeel bieden zijn niet uitgebreid onderzocht.

Dit werk pakt deze ontwerpuitdagingen via twee routes aan. In het eerste deel verkennen wij de benodigde ontwerptools voor gegeneraliseerde GRIN-lenzen. Een efficiënte wiskundige representatie is een vitale basis voor het ontwerp van GRIN-lenzen. Wij onderzoeken een wiskundige representatie voor GRIN-lenzen gebaseerd op de relatieve samenstelling van de bestanddelen, die geschikt is voor optimalisatie en eenvoudig kan worden beperkt tot materialen die produceerbaar zijn. Deze aanpak is vooral voordelig voor GRIN's die uit meer dan twee basismaterialen bestaan.

Een cruciale stap in elk optisch ontwerp is de selectie van een startpunt van waaruit verdere optimalisatie wordt uitgevoerd. Dit vormt een uitdaging voor gegeneraliseerd GRIN-ontwerp omdat er zeer weinig van dergelijke startoplossingen bestaan. Wij onderzoeken een procedure waarbij de paraxiale eigenschappen van homogene lenssystemen kunnen worden gereconstrueerd in een gegeneraliseerd GRIN-medium, om te dienen als startoplossing voor verdere optimalisatie. Er wordt aangetoond dat complexe homogene optische ontwerpen op deze manier kunnen worden gereconstrueerd, inclusief het uitgewerkte voorbeeld van een veertien-element lithografische stepper-lens. De techniek wordt uitgebreid naar polychromatische systemen, waarbij chromatische dispersie van het oorspronkelijke systeem wordt gereconstrueerd in het GRIN-startpunt. Deze aanpak wordt gedemonstreerd via de reconstructie en optimalisatie van een GRIN Cooke Triplet-equivalent dat was samengesteld uit dezelfde materialen als de oorspronkelijke oplossing (twee glastypes en lucht). Deze startoplossingsvoorbeelden worden vervolgens geoptimaliseerd tot hoogwaardige optische oplossingen. We concluderen dat paraxiale reconstructie een krachtige techniek is bij het genereren van startpunten, die met verdere ontwikkeling de tijdsefficiëntie van GRIN-lensontwerp aanzienlijk kan verbeteren.

Een opmerkelijke eigenschap van GRIN-lenzen is hun vermogen om focusserende sterkte te genereren terwijl ze vlakke oppervlakken hebben. Wij onderzoeken de gevolgen van het gebruik van plano GRIN-lenzen in beeldvormende lensontwerpen, met name met betrekking tot de correctie van de aberratie coma, door het voldoen aan de Abbé sinusvoorwaarde. Wij tonen aan dat gegeneraliseerde GRIN-lenzen het vermogen hebben om coma te corrigeren in een dunne, plano-plano geometrie, maar de aanpak verhoogt de indexvariatie en complexiteit van de GRIN-verdeling, wat een afweging vormt voor de lensontwerper bij het overwegen van kosteneffectieve fabricage. Omgekeerd wordt aangetoond dat een GRIN-medium gecombineerd met oppervlaktekromming coma kan corrigeren met een eenvoudigere GRIN-verdeling die kleinere indexvariatie heeft, wat impliceert dat een optimale strategie voor het gebruik van

GRIN-media in optische ontwerpen is om ze toe te passen in combinatie met gebogen oppervlakken, vooral in gebieden waar GRIN-materialen comparatief voordeel hebben ten opzichte van homogene optica, zoals chromatische aberratiecorrectie.

In het tweede deel onderzoeken wij de toepassingen die direct profiteren van GRIN-optica. Wij tonen aan dat gelaagde polymeer GRIN-lenzen met sferische verdeling het potentieel hebben om kleur-gecorrigeerde lenzen te produceren met een lagere massa dan glazen doubletten en zonder de diffractieve spookbeelden van diamant-gedraaide asferisch -diffractieve hybride lenzen. De zeer dispersieve combinatie van polymeren bleek een effectief middel voor het corrigeren van chromatische aberraties binnen diameterlimieten die worden bepaald door de gevormde kromming van de lens-preform. Er werd waargenomen dat radiale GRIN's en materialen met negatieve GRIN chromatische dispersie nog meer potentieel hebben om chromatische aberraties te beheersen.

Wij onderzoeken ook de toepassing van freeform-GRIN verdelingen (zonder as van rotatiesymmetrie) in het optische ontwerp van een head-mounted display (HMD). We laten zien dat freeform-GRIN media op vergelijkbare wijze werken als gekantelde en gedecentreerde lenselementen, evenals torische en freeform oppervlakken. Dit wordt aangetoond door GRIN-oplossingen die vergelijkbare prestaties hebben als homogene ontwerpen met freeform oppervlakken. Er wordt ook aangetoond dat een freeform-GRIN medium kan worden gebruikt om een gemeenschappelijke mechanische as in HMD-ontwerpen te herstellen, wat mogelijk een aanzienlijke vereenvoudiging van het opto-mechanische ontwerp biedt. HMD-ontwerpen op basis van polymeer GRIN blijken aanzienlijk minder massa te hebben in vergelijking met hun homogene tegenhangers.

Ten slotte onderzoeken wij de toepassing van GRIN-materialen op de extreme kleurcorrectie-uitdagingen die worden gesteld door beeldvorming over verschillende discrete golfbanden (bekend als multispectrale optica). Wij laten zien hoe GRIN's op basis van infrarood materialen een objectieflens die werkt over de kortgolf-infrarood (SWIR) en langgolf-infrarood (LWIR) golfbanden voor een gemeenschappelijk brandvlak aanzienlijk kunnen vereenvoudigen. De extreme optische dispersie gegenereerd door GRIN-materialen maakt een veel mildere optische sterkteconstructie mogelijk die resterende aberraties vermindert, waardoor aanzienlijk minder optische componenten en verminderde massa en omvang mogelijk zijn.

Wij concluderen dat de vereiste ontwerpinfrastructuur voor willekeurige GRIN-lenzen haalbaar en opkomend is, en dat er technologische uitdagingen zijn in modern optisch ontwerp die voortgezet onderzoek naar GRIN-optica rechtvaardigen. Vooruitgang in het optisch ontwerp van gegeneraliseerde GRIN's moet gepaard gaan met verfijning in fabricage, metrologie en milieu-kwalificatie om wijdverspreide adoptie en implementatie mogelijk te maken.

1

Introduction

1.1. Motivation

At the time of writing in 2025, optical imaging and display systems are ubiquitous throughout the modern world. Major advances in digital sensors and displays have enabled a wide range of applications from mass-produced consumer cameras [3], to long range surveillance equipment operating in multiple wavebands [4].

The widespread and mass-produced nature of optical systems within a competitive marketplace has led to a continuous drive to enhance optical performance whilst simultaneously minimising size, mass and cost. This is often referred to by an industry acronym, SWAP-C (size, weight, power and cost).

The drive for SWAP-C minimisation has emerged amidst an ever expanding array of platforms and devices that leverage optical imaging systems. Defence and aerospace end-users are a particularly strong driver of SWAP-C minimisation, with platforms such as dismounted infantry, autonomous airborne systems and piloted aircraft requiring ever smaller, lighter, and more capable optics [5]. Autonomous airborne vehicles are required to perform an ever expanding variety of optical sensing applications, whilst their mass remains a critical design aspect due to the limited ability of current propulsion technologies to carry large payloads for extended periods. The modern dismounted soldier requires ever greater observational and targeting capability from optical systems to retain a tactical advantage over adversaries, yet such increased capability is often accompanied by an increased weight burden that must be minimised. Piloted fast jets require advanced avionic systems to convey information to pilots whilst minimising safety-critical "heads down" time. This need must be fulfilled on a very fast moving platform that may undergo very high g-forces under manoeuvres and cockpit ejection. To this end, low mass optics for helmet-mounted displays (HMDs) are a vital aim. Furthermore, the space envelope of avionic optics may often be challenging, frequently needing to fit within a compact setting such as a helmet or in a narrow region of a cockpit, making size reduction a valuable development.

The SWAP-C of optical instruments is very often limited by the optics themselves. While electronic components of opto-electronic systems have benefited from drastic reductions in scale, famously observed as Moore's law, optical modules are generally limited in scale by the

fundamental first-order properties of the optic, such as focal length and aperture. For a perfectly corrected optic, the angular resolution is directly proportional to the aperture diameter (as observed by Rayleigh)

$$\sin\theta = \frac{1.22\lambda}{D},\qquad(1.1)$$

where θ is the minimum resolvable angle according to the Rayleigh criterion, λ is the wavelength and D is the clear aperture diameter. The approximation $\sin\theta \approx \theta$ can generally be applied as θ is very small at visible and infrared wavelengths. Diffraction caused by the edges of the optical aperture limits resolution, with such a system referred to as *diffraction limited*. Whilst not all optical systems are diffraction limited, broadly, detection of objects at longer range or in finer detail requires longer focal lengths and larger apertures.

Strategies to improve optical SWAP-C are often centred around reducing the number, size, and mass of optical components. Reducing the number of optical surfaces required to provide a specified level of optical performance may simultaneously reduce mass and cost. Examples of such technologies are aspheric surfaces that improve the monochromatic aberration correction potential of optical surfaces, and diffractive-refractive hybrid optics that use the extremely strong chromatic dispersion of an optically powered diffraction grating to correct chromatic aberrations. Reduction in mass of optical components can often be achieved by changing the optical material to one with a lower density, such as changing from a glass to an optical polymer.

Reduction of the length of optical systems also has the potential to reduce SWAP-C. The ratio of physical length to focal length (referred to as telephoto ratio) is a major driver of the level of optical correction, with systems that are forced to a shorter physical length tending to have increased aberrations compared to longer ones, due to a more extreme construction of the lens element optical powers. In this regard, additional degrees of freedom for aberration correction are a powerful tool to achieve shorter, optimised SWAP-C systems whilst maintaining a given level of aberration correction. A good example of this approach is illustrated by camera lenses for mobile phones, which must image a wide field of view within a very compact space envelope. This is achieved using a telephoto construction* and copious use of aspheric surfaces to correct aberrations.

A method of SWAP-C minimisation that has seen substantial recent development is computational imaging. A notable example of this is multi-aperture optics [6, 7]. By this technique, a larger aperture can be approximately synthesised by arranging a number of shorter-focal-length, smaller-aperture lens systems, greatly reducing the optical module length. Recovery of system resolution is then undertaken by post-processing of the sub-images. A further example of the use of computational imaging is *wavefront coding* [8], whereby the point-spread function (PSF) of an optic is deliberately aberrated such that it remains stable over an extended focus range. The image is then restored by deconvolution of the aberrated PSF. The benefit of wavefront coding lies in the simplification of the optical construction, such as through the removal of a focus mechanism (enabled by the extended depth of focus). In general, computational imaging systems experience trade-offs in system noise and image artefacts, as well as demanding increased computational complexity to operate (and therefore increased power consumption and latency). Furthermore, multi-aperture imaging systems remain bound by the diffraction limit. Transforming a system into a set of smaller sub-apertures reduces the diffraction limit of the system to that of the individual sub-apertures.

---

*A telephoto lens is generally recognised as a lens with a shorter physical length than its focal length.

A further method of SWAP-C minimisation that has seen particular recent attention in the literature is multispectral optics [4]. Many imaging platforms require capability in multiple wavebands simultaneously. Wavebands such as visible light and short-wave infrared (SWIR) generally provide information to a user based on *reflected* radiation from a scene of interest. By contrast, longer wavelength infrared wavebands such as the mid-wave MWIR (3-5 μm) and long-waveLWIR (8-12 μm) provide a substantial amount of information from *emitted* thermal blackbody radiation. To date, imaging both thermal and shorter-wavelength infrared typically requires two separate optical systems with separate sensors; however recent developments in focal plane array (FPA) technology are now enabling multiple wavebands to be recorded simultaneously on a common focal plane. If such a sensor is combined with a common optical aperture that images all wavebands simultaneously, the SWAP-C benefits are significant. Adversely, the optical design of multispectral systems is very challenging, particularly with respect to chromatic aberration correction. Chromatic aberration correction must be achieved over a significantly broader waveband with a smaller set of optical materials (as the transmissive spectral waveband of materials used must span the entire waveband of the system). The wide range of commonly used optical glasses offer very little transmission in the infrared wavebands for example, whilst common infrared materials such as germanium and silicon do not transmit in the visible and NIR wavebands due to their respective electronic bandgaps. There is significant SWAP-C enhancement available if such imaging capability can be reduced to a single optical aperture (rather than two separate systems).

GRadient-INdex optics (GRIN) can be regarded as a degree of freedom to minimise the SWAP-C of conventional optical systems. By adding functionality to the bulk of an optical component, we may improve the aberration correction of an optical system without adding mass, and may trade the resulting degrees of freedom for reduction in the size or optical component-count of the optic. A key motivation for this work, is to explore the possibilities provided by recent GRIN fabrication technologies for the SWAP-C enhancement of a range of optical systems, as well as to devise tools and techniques for the optical design of such GRIN systems.

1.2. Historical Context

GRIN has long been a phenomenon of interest in the design and manufacture of optical systems. Some of the earliest observations of this effect in deeper antiquity (Cleomedes and Ptolemy) were of atmospheric refraction effects [9]. It was discovered that refraction by the atmosphere caused a change in the apparent position of astronomical bodies when observed close to the horizon, although it would be many centuries until this phenomenon was correctly interpreted as a GRIN effect. One of the earliest historical examples of a GRIN optical design was the fisheye lens of Maxwell [10] (1854). Maxwell demonstrated a theoretical GRIN medium where all rays travel along circular arcs, resulting in perfect geometric imaging between any two opposing points on the surface of the lens. Maxwell's design however; was not manufacturable at optical wavelengths with any fabrication technology of the time. Luneburg [11] (1944) generalised the design principle of Maxwell's fisheye lens to include imaging from an object at infinite conjugates. In the early 20th century, GRIN lensing was first experimentally demonstrated by a cylindrical index distribution, fabricated by soaking a gelatine cylinder in water, the eponymous Wood lens [12, Chapter 4] (1911, although R. W. Wood himself attributed the discovery to Exner and Matthiesen). This work itself built on observations by Exner and Matthiesen (1891) on the compound eyes of insects, which were observed to be arrays of GRIN rod lenses [13].

1.2.1. Gradient-Index Lenses in Nature

GRIN lenses are widespread in living organisms. A review in 2012 by Pierscionek and Regini observed that all biological eyes examined to date exploit some form of GRIN effect [14]. Index gradients freely form in biological eyes due to the assembly of the eye from a large number of individual cells. These cells spatially vary the amount of refractive index modifying protein to produce a GRIN of general form (although the eyes may generally resemble the basic index distributions described in Section 1.7.2).

Strong index gradients are particularly prevalent in aquatic organisms, where the amount of light captured by the eye must be maximised to overcome low ambient illumination whilst the refractive index of water diminishes the refractive power of the cornea. Instead, a strongly curved and ball-like, high refractive index lens provides focusing power, combined with a GRIN distribution of broadly spherical form. The eyes of fish and cephalopods such as octopus contain strong index gradients, with index variation in the Octopuses *Octopus australis* and *Octopus pallidus* varying between N=1.509 to N=1.357 from centre to edge, likewise the goldfish *Carassius auratus auratus* shows an index variation from N=1.55-1.57 at the lens centre to N=1.35 at the lens edge [14]. The biological eye is also a known example of *convergent evolution*, whereby similar structures have evolved in organisms that do not share a common ancestor [15] (as is indeed the case for cephalopods and fish). Overall, the widespread use of GRIN in nature lends strength to the potential benefits of GRIN in human-made optics, with *biomimicry* often proving a successful engineering strategy

1.2.2. Early Design and Fabrication Approaches

Research in the second half of the 20th century saw identification of the aberration correction potential of GRIN optics. H. A. Buchdahl proposed a theoretical framework for the aberrations of rotationally symmetric GRIN systems, based on the method of quasi-invariants [16]. Buchdahl also raised the notion of an optical system whereby the number of optical surfaces tended to infinity, coining the term *continuous symmetrical optical system* [17]. This theoretical framework for the modelling of GRIN aberrations was later to prove vital to the work of numerous authors who developed the theory further, such as Sands [18], Bociort [19] and Moore [20]. Concurrently and crucially, the development of the electronic computer enabled much faster numerical raytracing and optimisation of GRIN materials. This approach allowed GRIN designs to break free of a narrow range of distributions that had analytical raytracing solutions. An early example of the use of GRIN to simplify the optical construction of imaging systems was published by Atkinson et al. [21], whereby a six-element double-Gauss photographic lens design was reduced to two radial-GRIN elements with equivalent performance. This design however; could not be fabricated using techniques available at the time.

In the same period, significant advances were made in the fabrication of GRIN lenses, with a plethora of techniques developed and published. Methods such as ion exchange [22, 23], ion stuffing [24], neutron irradiation [25] and chemical vapour deposition (CVD) [26] were all shown to successfully produce well controlled refractive index gradients within optical materials. The development of these methods saw the emergence of early commercial applications in GRIN optics, such as in the preparation of precision borescopes [27], as well as optical fibres and their connectors [28]. Axial-GRIN lenses for spherical aberration correction saw some commercial use. During this period however; numerous commercially viable methods to produce aspheric and diffractive optics were developed, such as computer numerical controlled

(CNC) polishing, single-point diamond turning (SPDT) and moulding. By contrast, contemporary GRIN manufacture techniques were energetically demanding and time consuming, with modest capability to enhance system performance. This limited commercial GRIN imaging to niche applications, where very thin rod-like lenses were required.

1.2.3. New Generation Gradient-Index Technologies

In the early 21st century, a resurgence of research activity into GRIN imaging optics has occurred. Enabling technologies such as additive manufacture [29–33], localised material modification [34–36], and nanolayer co-extrusion [37], have created new possibilities for the manufacture of reduced-SWAP-C GRIN optics. Such technologies now offer a path to GRIN lenses with greater diameter, index variation (known as ΔN), chromatic dispersion variation, lower cost, and reduced mass density. Additive manufacture processes mean it is now possible to design and manufacture GRIN lenses that have an essentially arbitrary distribution of refractive index, which can also consist of a large number of base materials. At the time of writing, non-rotationally symmetric "freeform" and array-based GRIN optics have been experimentally demonstrated [38].

Multilayer Coextrusion

The group of Eric Baer at Case Western Reserve University identified that extrusion of polymers of different refractive index into fine sub-wavelength layers had the potential to yield a production process for films of tunable effective refractive index [39]. This process is referred to as Layered-gradient-index or *LGRIN*. The LGRIN process is illustrated in Figures 1.1 and 1.2. A feedstock of two base polymers is melted into an extruder where the two plastics are forced into assembly with one another. This polymer extrudate is then cut and re-assembled together multiple times to produce increasingly fine layers. This process continues until the final film is extruded with individual layers of polymer that are much thinner than the wavelength range of visible light (approximately 50 nm thick), causing the polymer structure to behave as an effective medium with minimal scattering. By controlling the relative thickness of the fixed-index alternating layers, the effective index of the entire film can be tailored to a specific value (within the refractive index boundaries imposed by the base materials). A GRIN lens is then fabricated by first arranging a sequence of defined-index films into a stack, which is consolidated together at elevated temperature and pressure. Further moulding of this axial-GRIN preform can then be performed to generate a spherical (and potentially aspheric) GRIN preform. Finally, this GRIN preform is optically processed (typically by SPDT) into a GRIN lens. It is worth noting that the final optical surfaces need not be conformal with the contours of the GRIN distribution. We discuss the Optical Design of layered polymer GRIN lenses in greater detail in Chapter 5.
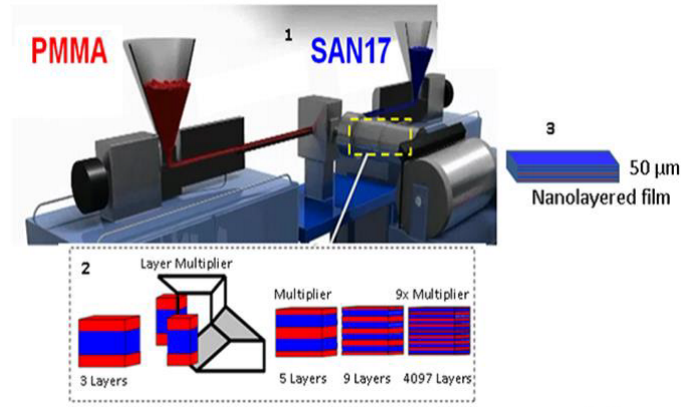
Figure 1.1: LGRIN multilayer extrusion process (from Fein and Ponting [1])
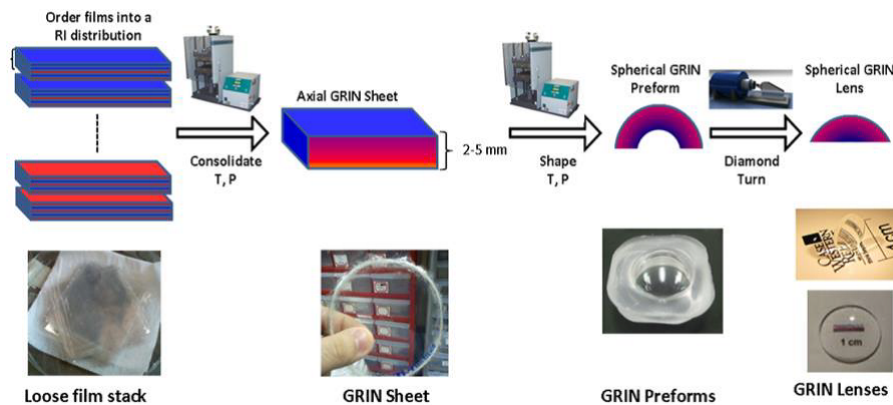
Figure 1.2: LGRIN lens moulding and turning process (from Fein and Ponting [1])

Additive Manufacture

Additive manufacture is a particularly promising means to generate GRIN lenses of arbitrary distribution, with the inherently localised nature of the process enabling the deposition of volumetric elements (known as voxels) of tailored-index material in a precise manner. Consequently, several authors have investigated this route to GRIN fabrication [29–33].

Significant progress in this field has been demonstrated by the *volumetric index of refraction gradient optics* (VIRGO) approach of Vadient Optics LLC (also known as NanoVox™). This approach uses multiple tailored-index, UV-curable inks that are inkjet printed in a spatially varying halftone pattern, where index variation is generated by doping with high (and low) index nanoparticles in the base inks. It is also possible to generate index variation by mixing different-index base monomers. ΔN in excess of 0.2 has been experimentally demonstrated via the VIRGO process [29]. Lenses manufactured via this route are not limited to a compositional gradient between only two materials, with a much larger *material space* possible through printing with three or more base materials. This allows spatial control of refractive index at multiple independent wavelengths, and therefore, rigorous control of chromatic aberrations.

The direct ink writing process of Dylla-Spears et al. [30] yields printed, glass-based GRIN material (in contrast to the nanoparticle-doped polymer VIRGO process). Via this approach, nanoparticles of glass precursors are blended into a printable slurry. Slurries with different refractive index precursors are mixed inside a printhead and deposited in a spatially varying

6
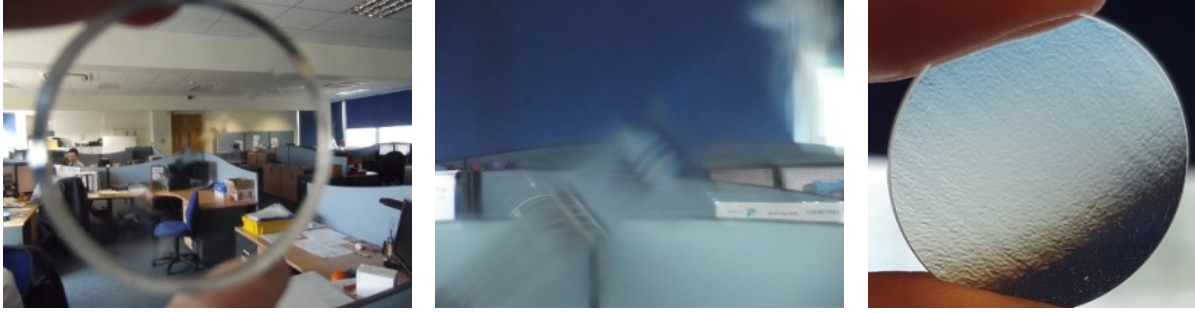
Figure 1.3: Left and centre: image defect through homogeneous 3D-printed window. "Stripe" effect caused by periodic inhomogeneity at the length scale of printed voxels. Right: localised inhomogeneity in 3D-printed GRIN distribution, highlighted by a defocused high-contrast image (credit A. Hurst).

distribution, being held in place by a UV-curable binder. The resulting "green" part is then dried and sintered to remove organic impurities and to densify the material to a glass. Such an approach similarly enables generalised GRIN, and also expands the capability of additively manufactured GRINs to glass materials. Glass materials are typically harder than polymers (with the trade-off of higher density). A glass approach potentially allows GRIN components to be used on the exterior surfaces of defence and aerospace optics that are frequently exposed to environmental stressors such as blown sand and dust. Furthermore, the higher melting point of glass GRIN optics potentially enables their use in high-energy applications (such as laser systems) where the low melting point (and sometimes photo-darkening) of polymers is not suitable.

Additively manufactured optics still face technical challenges at the time of writing in 2025. The "pixellated" approach via which materials are deposited leads to voxel-scale inhomogeneity in GRIN materials at length scales similar to the printer resolution. The mechanical and rheological properties of the inks must also retain a degree of similarity, as ultimately they must form a smooth spatially varying mixture. Figure 1.3 shows examples of localised inhomogeneity formed by optical 3D printing processes. These challenges are being addressed through progressively higher-resolution print systems and improved ink rheological properties that increase inter-diffusion between voxels during the print process.

Targeted Modification

Targeted Modification GRIN technologies exploit the fact that, under the right conditions, the refractive index of a homogeneous material may be modified. If this modification can be controlled as a smooth, spatial variation then a GRIN component can be fabricated. Furthermore, if the refractive index change can be locally controlled over a sufficiently short spatial length, then arbitrary GRIN distributions can be formed. At the time of writing, this approach has been demonstrated in the visible and infrared wavebands, by modification of polymers, nano-porous silica and silicon, and chalcogenide glasses.

In 2020, Ocier et al. [35] demonstrated significant changes in refractive index within photopolymer-doped silica networks using direct laser writing; known as the subsurface controllable refractive index via beam exposure (SCRIBE) process. Through this process, ΔN values of 0.3 at visible wavelengths were obtained, with sub-micron spatial index resolution, enabling the fabrication of a Luneburg lens at optical wavelengths.

Work undertaken at the University of Central Florida by Kang et al. revealed the possibility

to generate infrared GRIN lenses in chalcogenide glass, via forced, local recrystallisation of the glass [34, 40]. For an appropriate chalcogenide glass composition, a laser source can be used to locally force a material phase change within the glass, which upon further heat treatment causes the growth of high-index nanocrystals within the glass, generating a GRIN chalcogenide glass-ceramic hybrid material. Via this route, a spatially varying index change of 0.1 was demonstrated. Further development into such phase-change materials has shown the potential for very large index variation, for example in 2020, Delaney at al demonstrated an index change in Sb_2Se_3 of 0.77 [41]. In further work, Delullier et al. at ONERA demonstrated a GRIN Fresnel lens based on direct laser writing of chalcogenide glass with a ΔN of 0.055 [42].

Infrared Gradient-Index Lenses

A number of technologies are under investigation for the generation of GRIN media in infrared materials. Chalcogenide glasses in particular are appealing materials for the generation of index gradients due to their large glass forming regions, as well as other mechanisms via which their refractive index may be modified such as targeted modification. Work undertaken at Naval Research Labs [43], The University of Bordeaux [36] and The University of Central Florida [40] all demonstrate mechanisms via which chalcogenide GRIN lenses may be generated. It is also feasible to generate index gradients in certain crystalline materials. Pickering et al. [26] demonstrated the possibility to generate compositional gradients between zinc sulphide and zinc selenide. With the exception of the approach of Kang et al. previously outlined, these processes do not produce GRINs of arbitrary form. however, the application of GRIN to such materials has significant potential, even with a less general GRIN distribution. The dispersive properties and broad spectral transmission window of infrared GRIN materials potentially allow colour-corrected optics over multispectral wavebands, which we explore in Chapter 7.

1.3. Contemporary Optical Design Challenges and Approaches

The degrees of freedom provided by these new GRIN manufacture processes pose a new set of design challenges. The highly general nature of the GRIN materials offered by new manufacture processes presents a new and very broad design landscape that has been little explored by optical designers. Available GRIN distributions are now limited by imagination rather than the manufacturing process (within index and resolution limits). It is the design challenge of how to exploit these new degrees of freedom that this work seeks to address. Herein, we seek to produce innovations that may now be realised with generalised GRIN lenses, as well as design tools that provide valuable insights into the inner workings of such generalised GRIN lenses.

To date, two main design strategies have been employed to address the generalised GRIN design problem in the literature. These are *optical design* and *transformation optics*. The more classical optical design approach forms the basis of this work and has also been approached by a small number of authors at the time of writing in 2025 [38, 44–46]. This approach broadly makes use of geometrical optics and aberration theory to reach an eventual design by a combination of insight and optimisation. Transformation optics can in some cases be considered an attempt to invert the optical design problem, seeking a design solution by a coordinate transformation of an appropriate candidate system.

Transformation optics exploits the fact that Maxwell's laws are invariant under a coordinate

transformation. An object with a given permittivity and permeability may be "transformed" into a new curvilinear coordinate system, resulting in modified permittivity and permeability that increases where space has been compressed and vice-versa. This approach can be applied to a number of optical problems, including imaging systems. A useful intuitive example of the approach was demonstrated by Campbell et al. [47], whereby the transformation of a spherical lens into a plano-plano geometry yields a positively powered GRIN distribution within the lens.

Transformation optics has some limitations however. The coordinate transformations required in general may lead to materials that are anisotropic, magnetic, or require very strong index variation. All of which makes design for manufacture challenging, often requiring the use of novel metamaterials with electromagnetic properties not observed in natural materials. This limitation is partly addressed by disregarding magnetic contributions to the derived material (which are often very small). This is known as *quasi-conformal* transformation optics, published by Li and Pendry [48]. Notably, such transformations when applied to imaging applications may require further optimisation via raytracing. In this regard, transformation optics provides a useful design starting point. A further challenge in the application of transformation optics to imaging optics design is difficulty in applying it to multi-element lens assemblies. Transforming the set of discontinuous boundaries associated with lens surfaces tends to lead to discontinuities in the resulting GRIN medium [45].

A classical optical design approach to GRIN optics design benefits from the mature design infrastructure that exists in the form of optical design software. Such software is well-proven for raytracing GRIN media, and is typically customisable with macro code and user-defined GRIN features. This provides us with a foundation to solve a key challenge of this work, creating tools for the design of generalised GRIN lenses for manufacture. Whilst optical design software is capable of tracing and optimising a variety of refractive index distributions, it is not intrinsically able to express GRIN optical designs in terms of a manufacturing process, nor provide the key optimisation constraints required to ensure a physically valid result. These tools must be created by the optical designer, and we address that in this work.

1.4. Goals and Outline of this Thesis

This work proposes to answer a central research question: *Are there benefits to the SWAP-C of optical systems through the use of generalised GRIN lenses, and if so what are they*? In support of this central problem, we define the following objectives:

- Review and explore the design freedoms offered by new GRIN manufacture technologies, motivated by SWAP-C minimisation in defence and aerospace optics.
- Devise design tools that enable the modelling, optimisation, and analysis of GRIN lenses enabled by new manufacture technologies.
- Identify applications enabled by new GRIN manufacture technologies.
- Conclude whether the use of generalised GRIN optics has a future in SWAP-C-critical defence and aerospace applications.

Broadly, this work is separated into two themes. Chapters 2, 3, and 4 are aimed at establishing principles and methods for the design of generalised GRIN lenses. Chapters 5, 6, and 7 are subsequently aimed at the applications and possibilities for optimised SWAP-C optics using generalised GRIN media.

In Chapter 2, *Mathematical Characterisation of Inhomogeneous Optical Media*, we explore

mathematical representations for generalised GRIN media, particularly where the underlying GRIN consists of more than two base materials. We note that a succinct and well-adapted mathematical representation for GRINs can ease the process of design optimisation, allowing the design to be expressed in a manner indicative of the manufacturing process that can also simplify the passage of lens data to fabricators.

In Chapter 3, *Paraxial Analysis and Reconstruction of Gradient-Index Lens Systems*, we explore means to gain insight into the optical construction of generalised GRIN lenses, using the approximate form of raytracing known as *paraxial optics*. Using this approximation, we propose a method to convert existing homogeneous lens systems into continuous GRIN equivalents that serve as starting points for further optimisation. We propose this method as a means of filtering the solution space of generalised GRIN optics, leveraging the vast body of work performed in homogeneous optical design over the past century.

In Chapter 4, *Surface Curvature and the Abbé Sine Condition in Gradient-Index Lenses*, we explore the effect of plano-plano surface geometry on the aberration correction of GRIN lenses. For any lens system to be free from the aberration known as coma, rays propagating through the lens must satisfy the Abbé sine condition, which we show is impossible for a plano focusing lens of negligible thickness focused at infinity. We demonstrate that for a plano GRIN lens with a small, finite thickness, a generalised GRIN medium allows the lens to satisfy the Abbé sine condition, with the trade-off that the complexity and refractive index variation of the GRIN medium increases. Conversely, we show that combining surface curvature and a GRIN medium of much lower index variation and complexity also allows correction of coma.

In Chapter 5, *Optical Design of Layered GRIN lenses*, we explore the design degrees of freedom enabled by one modern GRIN manufacturing process, the layered gradient-index or LGRIN process. Such GRINs consist of contoured layers of customisable index material, typically with a spherical GRIN distribution. We compare the aberration correction potential of LGRIN lenses to other optical manufacture technologies.

In Chapter 6, *Optical Design of Freeform GRINs for Avionics*, we propose that the application of GRIN media of non-rotationally symmetric form are an effective degree of freedom in the optical design of tilted and off-axis HMDs. We show how GRINs may reduce the mass and component count of such systems whilst retaining optical performance, applying GRINs in an analogous manner to freeform surfaces whilst also considering their capacity to simultaneously address chromatic aberrations of HMDs.

In Chapter 7, *Optical design of athermal, multispectral GRINs*, we propose that GRIN optics are an effective means for SWAP-C minimisation of multispectral optical systems. Chromatic aberration correction is a well-noted application for GRIN lenses, whilst also being the most significant challenge for realisation of multispectral optics. We examine the optical performance potential of GRIN media based on common infrared materials and further implications for another key challenge in infrared design, athermalisation. Athermal optical systems have stable optical performance over an extended temperature range and GRIN materials show potential as a degree of freedom to correct defocus and aberrations induced by temperature changes. We show via a theoretical model, that for an idealised GRIN, thermal defocus is analogous to that of homogeneous lenses, depending only on the lens materials and focal power. The output of this model is used to design a SWIR and LWIR GRIN objective lens with a common focal plane, which demonstrates substantially improved performance, reduced lens count, and reduced tolerance sensitivity compared to a homogeneous baseline design.

Finally, the results and implications of the main chapters of this work are discussed in concluding Chapter 8, *Conclusions*.

1.5. Geometrical Optics, Imaging Systems, and Aberrations

The underlying physics of this work makes use of the theory of *geometrical optics*. The general physics of light is highly complex, with photons of light having particle-like and wave-like properties. Geometrical optics abstracts the properties of light into a convenient approximation that simplifies the analysis of optical systems known as a *ray*.

There is no single definition of a ray [49, Chapter 1.3], but one sufficient for this work is the normal to the wavefront of a propagating electromagnetic wave within an isotropic medium as the frequency of the wave tends to infinity. Under this assumption, the effect of diffraction becomes negligible. Another useful description is that a ray in an isotropic medium represents the path of flow of electromagnetic energy.

Ray trajectories in geometrical optics are elegantly described by Fermat's principle, which states that the optical path length (defined as distance multiplied by the refractive index) of any ray is a stationary point with respect to adjacent paths. An intuitive (yet limited) interpretation of this, is that light takes the path of least time between two points A and B. Fermat's principle is given by

$$\delta s = \delta \int_A^B N(\mathbf{r}) \, ds = 0, \tag{1.2}$$

where $N(\mathbf{r})$ represents the refractive index as a function of a position vector in space, $\mathbf{r}$, and s is the length parameter of the ray path. Refractive index is a dimensionless quantity associated with an optical material that scales the velocity and wavelength of light propagating through it. Fermat's principle can be used to generate an expression for the path of a ray within a GRIN medium via a Hamiltonian approach. This is explored within the narrow region adjacent to the optical axis known as the paraxial region in Chapter 3. A further consequence of Fermat's principle is the well-known Snell's law at the interface between two optical media of refractive indices N_1 and N_2

$$N_1 \sin(i) = N_2 \sin(r), \tag{1.3}$$

where i and r are the respective angles of incidence and refraction to the surface normal at the point of intersection by a ray. Raytracing in optical systems most commonly consists of sequential interaction with surfaces, followed by propagation through optical media, from a defined object to an image surface. These are most commonly spherical surfaces, however conic sections and aspheres are also frequently used for rotationally symmetric optical designs. The surface sagitta, $z_{asphere}$ of a rotationally symmetric even asphere with respect to the surface vertex is given by

$$z_{asphere} = \frac{c\rho^2}{1 + \sqrt{1 - (1+k)\,c^2\rho^2}} + \sum_{i=4,6,8\ldots} A_i \rho^i, \tag{1.4}$$

as a function of perpendicular distance from the optical axis, ρ. The quantity c is the reciprocal of the surface radius of curvature, R, such that

$$c = \frac{1}{R}, \tag{1.5}$$
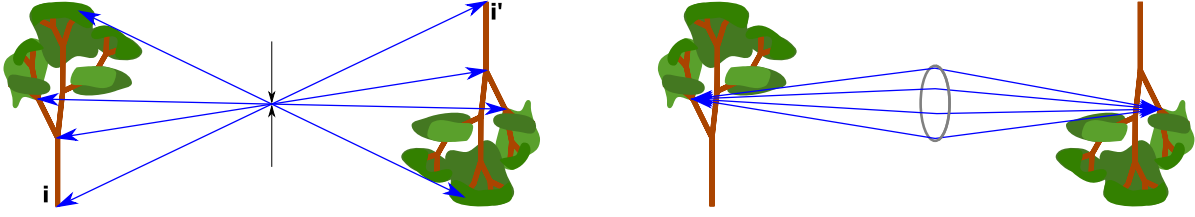
Figure 1.4: Left: the principle of stigmatic imaging for a pinhole camera. The blue arrows map points in the object space (left) to the image space (right). Right: stigmatic imaging through a finite pupil where all rays emanating from a point source that fit through the pupil focus on the same point in the image space.

k is the conic constant and A_i are aspheric surface coefficients. In the case of a spherical surface, k and all A_i are zero. Aspheric coefficients are typically only applied in powers of ρ^4 or higher to avoid degeneracy with the base conic.

The interaction of a general skew ray with a conic surface can be calculated analytically [50, Chapter 4]. However, more general optical surfaces such as aspheres have no such solution. Likewise, the propagation of a skew ray through a general gradient-index medium has no analytical solution (with the exception of some specific index distributions). Complex optical systems therefore rely heavily on numerical methods for raytracing.

A useful trait of ray-based optical models, is that some wave-like aspects of light can be retrospectively modelled with a high degree of accuracy. The effect of diffraction on the distribution of intensity formed by an image for example, can be modelled by applying the aberrations analysed via a ray-based model to a wave-based model defined by Fourier optics. This approach has enabled accurate performance predictions for complex optical systems for many decades and is very widely adopted by optical engineers.

1.5.1. Imaging Systems

Whilst geometrical optics can be applied to a wide range of optical problems, within this work we are primarily concerned with optical imaging systems. A primary concept behind such systems is that of *stigmatic imaging*. Imaging systems map information from a source in the object space, to a receiver in the image space (see Figure 1.4). A point **i** in the object space is mapped to a point **i′** in the image space by a factor, $\mathcal{M}$, the magnification

$$\mathbf{i}' = \mathcal{M}\mathbf{i}. \tag{1.6}$$

Figure 1.4 (left) illustrates the simplest optical system that can perform this task, the *camera obscura*. For an infinitesimally small pupil, geometrically perfect stigmatic imaging occurs. However, the small pupil causes diffraction to limit the resolution of the system (as per Equation 1.1) with negligible energy capture rendering such a system of little use for most modern imaging applications. In Figure 1.4 (right), a finite pupil size is illustrated where rays emitted from a point into a finite solid angle are captured and focused, which increases irradiance at the image. An optic is required to generate this focusing effect. The larger the size of the system pupil, the finer the diffraction-limited resolution of the system and the greater the amount of energy captured. In any given optical system, a limiting aperture known as the *aperture stop* limits the size of the axial pupil.

An important property of any imaging system is its *focal length*. A simplified definition of focal length is the distance from a thin lens to the image for an object plane located at infinity.
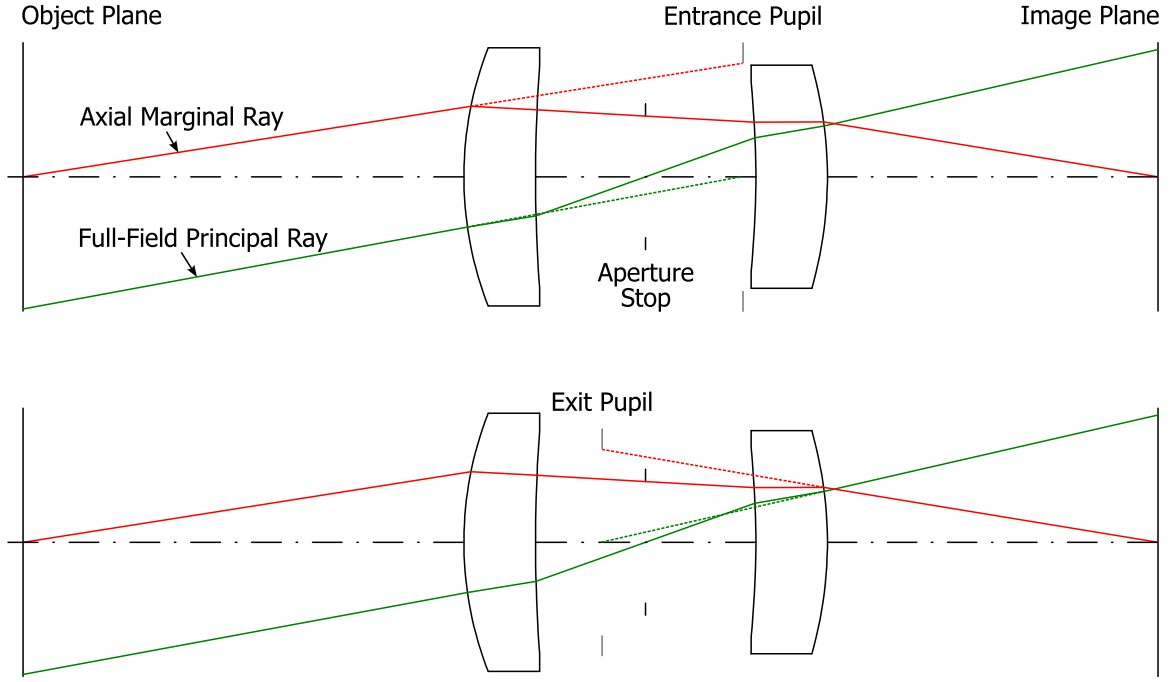
Figure 1.5: Pupil definitions for a notional optical system where the axial marginal ray show in red clips the edge of the aperture stop, while the full-field principal ray shown in green passes through the centre of the aperture stop, as well as the centre of the entrance and exit pupils. Top: Entrance pupil defined as the image of the stop in object space. Bottom: Exit pupil defined as the image of the stop in image space.

An analogous property of a lens is *focal power*, defined as the reciprocal of focal length. We denote focal length and power in this work with the symbols f and K respectively.

All nontrivial imaging systems also have a finite *field of view* (FOV), which is determined by the maximum size of the object or image as defined in Equation 1.6. Very commonly, the FOV of an imaging system is two-dimensional (such as the focal plane array of a camera). FOV is often expressed in terms of angle in object space for an object at an infinite distance. In this case, for an ideal stigmatic imaging system, the scalar image height, i', focal length, f, and the object angle, θ, are related by the formula

$$i' = f \tan \theta. \tag{1.7}$$

In addition to a definition of field, all optical systems have a finite *aperture*. Typically, one surface within a rotationally symmetric optical system limits the diameter of the axial field ray bundle. This surface we refer to as the *aperture stop*, with the outermost ray of the axial field bundle that just passes the stop referred to as the *axial marginal ray*. If we consider a bundle of rays originating at the aperture stop, we observe in Figure 1.5 that an image of the stop is formed on each side of it (shown by the intersection of the green dotted lines with the optical axis). These we refer to as the *entrance* and *exit pupils*, with the naming convention typically being aligned to the direction of light propagation, with light entering the system via the entrance pupil and vice-versa. The size of this image of the stop on the object side is known as the *entrance pupil diameter* or EPD. If we further stipulate that the ray passing through the centre of the aperture stop emanates from the outermost point of the object, then we refer to this ray as the *full-field principal ray*. A further common optical imaging system attribute related to focal length is the focal ratio or *F-number*, denoted as F/#. F/# is defined

for an object plane at infinity by

$$\text{F/\#} = \frac{f}{\text{EPD}}. \tag{1.8}$$

A lower F/# for a given focal length means a wider pupil, which outputs increased irradiance at the focal plane of the system. For photographic systems this results in a shorter exposure time required to capture an image, which has led to the industry parlance whereby lower F/# lenses are referred to as *faster*. Faster F/# systems also exhibit greater spatial resolution when diffraction limited, as well as decreased depth of focus (namely a smaller tolerance on defocus of the image before the blur spot increases to a given size).

More generally, the product of the entrance pupil area with the solid angle defined by the field of view, is proportional to the power throughput of an optical system for a uniform scene brightness (ignoring any losses due to absorption or surface reflectance). We refer to this product as the system *Étendue*. Broadly, the SWAP-C of an optical system scales nonlinearly with Étendue, and so it should be limited to the minimum necessary to execute a specified imaging task.

1.5.2. Paraxial Optics

An important approximation in the design and analysis of rotationally symmetric imaging systems is paraxial optics. Under this approximation, it is assumed that all ray angles within the system become very small such that $\sin\theta \approx \theta, \tan\theta \approx \theta$ [51, 52]. We may therefore also approximate Snell's law as

$$N_1 i = N_2 r. \tag{1.9}$$

The paraxial approximation also assumes that the sagitta of curved surfaces is zero. The first-order expansion of the sagitta of a spherical surface is given by

$$z_s = \frac{1}{2}c\rho^2, \tag{1.10}$$

for a displacement ρ from the optical axis. From inspection, this quadratically scaling quantity is negligible for very small ρ. Within the paraxial region, we gain insight into some fundamental properties of optical systems that define the *first-order* imaging properties of the system or *cardinal points*. In particular, the focal length and principal planes allow us to deduce the location and scale of an image (with knowledge of the object plane size and distance with respect to the optic). Furthermore, by paraxially tracing two key rays: the axial marginal ray and full-field principal ray, we can calculate the third-order aberrations of an optical system. We discuss paraxial optics in greater detail in Chapter 3. We refer to rays traced under the paraxial approximation as *paraxial rays*, whereas rays without this simplification are referred to as *finite rays*.

A further important formula for the paraxial properties of lenses is the lensmaker's equation for focal length, which for a thick lens in air is given by

$$K = \frac{1}{f} = (N-1)\left[c_1 - c_2 + \frac{(N-1)\,tc_1c_2}{N}\right], \tag{1.11}$$

where N is the lens refractive index**, t is its thickness, and c_1 and c_2 are the first and second curvatures respectively. A further useful approximation is where t is negligible, known as a

---

**The use of $N-1$ indicates the refractive index is relative to the medium in which the lens is embedded, which is generally air, though immersion in liquids is not uncommon in fields such as lithography and microscopy
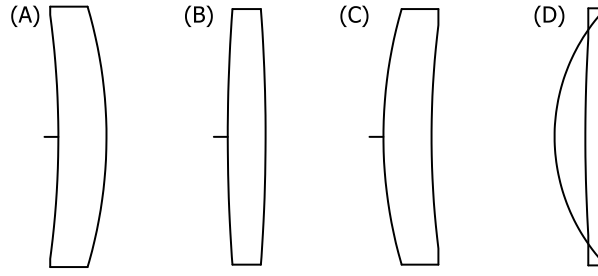
Figure 1.6: Positively powered singlet lenses of equivalent focal power with three different bending factors. Lens (A) with B=-3.0, lens (B) with B=0, lens (C) with B=3.0. (D) a positive lens of insufficient thickness where the surfaces have crossed over and produced a physically invalid negative edge thickness.

thin lens, giving a simplified formula for focal power:

$$K = \frac{1}{f} = (c_1 - c_2)(N - 1).$$ (1.12)

From inspection of Equations 1.11 and 1.12, it is clear that there are more degrees of freedom in the lens geometry than are required to solely control the lens focal power. A positive lens of constant focal power is illustrated in Figure 1.6, with three different bending factors, as defined by

$$B = \frac{c_1 + c_2}{c_1 - c_2}.$$ (1.13)

This additional control over lens shape through bending allows us to influence its aberrations while retaining a given focal power. A minimum value of lens thickness is required in the case of positively powered lenses to ensure the edge of the lens has a positive, physically valid thickness (or more practically, sufficient thickness for manufacturing feasibility). A counter-example of this is shown in Figure 1.6 (D). In some cases, substantial increases in the lens thickness are also useful to the designer for aberration correction.

1.5.3. Aberrations

Very few imaging systems produce geometrically perfectly stigmatic imagery (with some notable exceptions such as Maxwell's fisheye). The majority of optical designs have residual errors in the geometrical distribution of rays at the image. These errors degrade the image quality of the system and are known as *aberrations*. Aberrations generally scale as a polynomial function of the aperture size and field of view, making the design of systems with large aperture and field progressively more challenging for a given focal length or magnification. The correction and minimisation of aberrations using the degrees of freedom provided by the design parameters of an optical system, whilst retaining the necessary field and pupil size of the design requirement, is a key skill of the optical designer.

Aberrations can broadly be categorised into two types, chromatic and monochromatic.

Chromatic Aberrations

The primary chromatic aberrations are variation of the paraxial properties of an optical system with wavelength, due to the inherent variation of refractive index with wavelength in optical materials. There are two primary forms of chromatic aberration: *axial colour*, where the focus

of light varies with wavelength and *lateral colour*, where the scale of the image varies with wavelength. Both degrade image quality for a finite waveband. Correction of chromatic aberrations in refractive systems (including GRINs) generally requires the use of multiple materials with differing magnitudes of optical dispersion. We discuss chromatic aberration correction of GRIN optics in Section 1.7.3.

A well-known method to produce an optical system free from chromatic aberration is to use reflective optics. Reflective surfaces are intrinsically achromatic and fully-reflective optical systems have zero chromatic aberration; however this approach has significant trade-offs. The need to avoid obscuration from other reflective surfaces often restricts such designs to very narrow field of view applications such as telescopes, whilst the presence of a central obscuration can be unacceptable in infrared systems due to signal and resolution loss.

If the design decision is taken to use refractive optics, there are a number of options to implement chromatic aberration correction. Some common options used in defence and aerospace applications are illustrated in Figure 1.7. A well known and traditional route is to use a *cemented doublet* or *achromat*. This approach has been used successfully by optical designers since its invention in the 19th century. An achromatic doublet is formed when two or more lenses of different dispersion and optical power are cemented together (sharing a near-identical radius of curvature at the mating surface). The achromatic condition for a system of M thin lenses in contact is given by

$$\sum_{i=1}^{M} \frac{K_i}{V_i} = 0, \tag{1.14}$$

where K_i and V_i are the optical power and the well-known Abbé number [53, Chapter 10.1] respectively of the ith lens element. The Abbé V value describes the dispersion of a given material, defined by the refractive index at three wavelengths as

$$V = \frac{N(\lambda_{\text{mid}}) - 1}{N(\lambda_{\text{short}}) - N(\lambda_{\text{long}})}, \tag{1.15}$$

for three sequential defining wavelengths of the material ($\lambda_{\text{long}} > \lambda_{\text{mid}} > \lambda_{\text{short}}$). Achromatic doublets typically consist of a positively powered lens with high Abbé number (referred to as a crown) and a negatively powered lens with low Abbé number (referred to as a flint). One ubiquitous case of the Abbé number is V_{d}, which is defined by the Fraunhofer spectral lines C, d[†] and F (656.3 nm, 587.6 nm and 486.1 nm respectively). These defining wavelengths are an industry standard and are often quoted by optical material manufacturers to characterise visible waveband optical materials. The letter indication of a given Fraunhofer line is often used as a subscript to indicate a refractive index value is a that particular wavelength. Hence, an equation for V_d is often given by

$$V_d = \frac{N_d - 1}{N_F - N_C}. \tag{1.16}$$

It should be noted that satisfaction of Equation 1.14 alone does not necessarily make a good doublet. The variation of refractive index with wavelength in homogeneous optical materials is non-linear, hence when their optical powers are combined, residual chromatic aberration may remain in the form of *secondary spectrum*. Secondary spectrum is commonly quantified

---

[†]while commonly denoted as such in optical material catalogues, the d line is ambiguously defined, with the Fe line at 466.8 nm also referred to as 'd'. To avoid this, the He line at 587.6 nm is often referred to as 'D$_3$'.
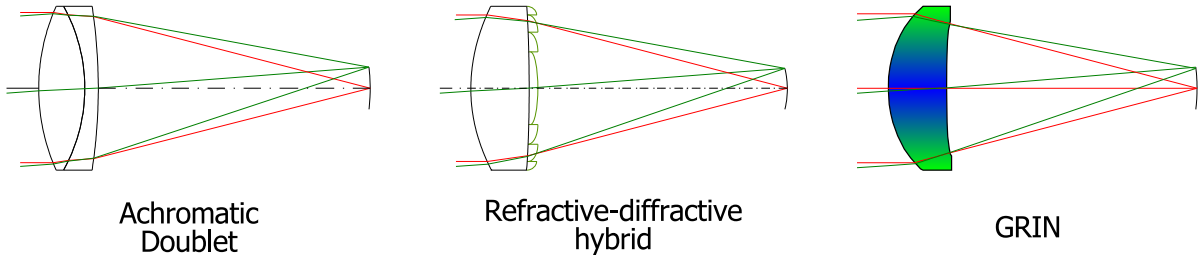
Figure 1.7: Left: Achromatic doublet based on cemented glass lenses, centre: diffractive hybrid lens (blaze profile not to scale), right: Achromatic GRIN lens

and controlled through the use of *relative partial dispersion*, which for the Fraunhofer g, F and C lines at 435.8 nm, 486.1 nm and 656.3 nm respectively is given by

$$P_{g,F} = \frac{N_g - N_F}{N_F - N_C}. \tag{1.17}$$

$P_{g,F}$ is a material property of specific wavelengths frequently used in the correction of visible waveband optics, although in principle, partial dispersion can be defined for any sub-band of the system waveband relative to the Abbé value. $P_{d,F}$ partial dispersion is also commonly used for visible waveband optics and is defined by

$$P_{d,F} = \frac{N_F - N_d}{N_F - N_C}. \tag{1.18}$$

Similarly to primary colour, secondary spectrum can be corrected for a system of thin lenses in contact by fulfilling the condition

$$\sum_{i=1}^{M} \frac{K_i P_i}{V_i} = 0, \tag{1.19}$$

where P_i is the partial dispersion of the ith lens element. This means that unless two materials are selected that have very similar partial dispersion, the correction of secondary spectrum generally requires a set of three materials. Lenses corrected for both primary and secondary chromatic aberration are often referred to as *apochromatic*.

Further to primary and secondary chromatic aberrations, each component in the doublet produces monochromatic aberrations, and chromatic variations thereof. The aberration correction of cemented doublets is often limited by the chromatic variation of spherical aberration known as spherochromatism. We discuss these themes in greater detail in Chapter 5.

The second option for chromatic aberration correction shown in Figure 1.7 (centre) is to use a diffractive hybrid surface. A diffractive surface with a parabolic blaze profile can create optical power with extremely strong negative chromatic dispersion ($V_d = -3.45$) [54]. As a result, diffractive surfaces can very easily remove the first-order chromatic aberration from optical systems. The addition of fourth-order or higher terms to the parabolic blaze profile also allows control of chromatic variations of monochromatic aberrations. A further SWAP-C benefit of diffractive surfaces is that they can be applied to a polymer substrate via single-point diamond turning (SPDT) or via moulding, with the lower density of a polymer compared to a glass cemented doublet providing a mass advantage. However, an important trade-off in the use of diffractive surfaces is their *diffraction efficiency*. Diffractive surfaces split light into multiple orders (an effect familiarly observed with diffraction gratings). In colour correcting diffractive optics, it is desirable for as much light as possible to be contained within a single

"design" order. Otherwise, light coupled into adjacent diffraction orders generates spurious "ghost" images that can be distracting to a user. Spurious diffraction orders also degrade image quality through loss of image contrast [55].

As the third and final option in Figure 1.7, GRIN represents a potentially ideal compromise. GRINs can be constructed from polymer materials to give a low-mass lens, whilst if a material blend with the right dispersion characteristics can be generated, a colour-corrected lens can be produced. We discuss the use of GRIN for colour correction applications widely in this thesis, as it is powerful application of the technology.

Monochromatic Aberrations

Monochromatic aberrations describe the deviation of the shape of an optical wavefront from the ideal spherical (or plano) case. Monochromatic aberrations are classified into types, identified by their effect on wavefront error as a function of field and aperture. Of the monochromatic aberrations, the five *Seidel aberrations* (named after the German mathematician Ludwig Von Seidel) are of particular importance for rotationally symmetric optical systems. These aberrations are of the fourth order in the wavefront, but are more often referred to as the third-order aberrations of the image. Correction of the Seidel aberrations alone does not guarantee a well-corrected system overall when analysed with finite rays, but generally all well-corrected optics have minimal amounts of the Seidel aberrations (with the potential exceptions of distortion and Petzval curvature depending on the system application).

Aberration coefficients do not provide an overall metric for system performance, rather, they provide *insight* into what limits the performance of a given design. A further useful aspect of the Seidel aberrations is that the total system aberration is equal to the sum of all surface contributions (and medium contributions for GRIN). By breaking down aberration contributions this way, surfaces that generate particularly large amounts of aberration can be identified as potential sources of nominal performance loss and sensitivity to manufacturing tolerances.

The five Seidel aberrations are characterised as follows:

Spherical aberration can be understood as the variation of focus with aperture. It has no field dependency.
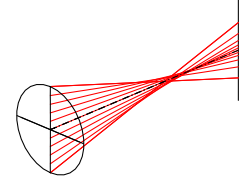
Coma is (broadly) the variation of magnification with aperture and has linear field dependency.
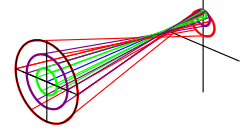
Astigmatism is the variation of focus between sagitta. It has quadratic field dependency.
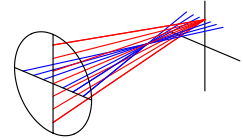
Petzval curvature causes the optimum focus to lie on a curve and not a plane. It has quadratic field dependency. Uniquely among the Seidels, its surface contributions do not depend on ray heights or angles and only on optical power divided by the refractive index (or $\mathcal{N}_2/\mathcal{N}_0^2$ for GRIN materials). See Chapter 3.
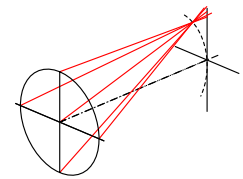
Distortion alters the geometry of an image and has no aperture dependency. As such distortion does not degrade image quality. It has cubic field dependency.
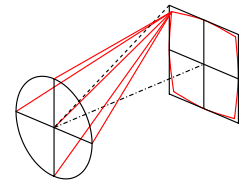
1.6. Optical Design - The Art and Science

In this work, we define optical design as the process of defining a system of optical components to meet a specification of optical requirements. This process typically makes use of geometrical optics (raytracing) combined with optimisation, followed by detailed analysis of optical performance, to determine the suitability of an optical solution to the design task.

The suitability of a given optical construction to the specification can be defined as a function of the wide range of possible system parameters. A *merit function* is defined based on a weighted sum of key performance metrics of the lens such as the geometric RMS spot size, expressed as a function of the lens design parameters such as surface radii of curvature and thickness. The optimisation goal is to minimise this function whilst typically retaining several design constraints, such as the space envelope and focal length.

The topology of the optical design merit function is highly complex and non-linear. As a result, the problem of optical design cannot easily be *inverted*. Raytracing of optical systems is generally performed in specialist optical design software such as CodeV® or Zemax®. Optimisation techniques are widely used to find solutions to optical imaging problems, with the Levenberg-Marquardt (damped least squares) algorithm being particularly ubiquitous [56][‡].

[‡]While based on this approach, most optical design programs are closed source and have proprietary, modified versions of this algorithm.

For optical systems of even modest complexity, multiple performance minima exist, with no simple way to determine if the solution found is the best overall global minimum. We refer to the abstract multidimensional space defined by the set of all parameters in a given optical design as *solution space*. Notably, the Levenberg-Marquardt algorithm is a *local* optimisation algorithm, descending into the nearest performance minimum based on the gradient of solution space at the starting point. Modern optical design programs also often feature *global* optimisation routines. These routines (that are often proprietary) attempt to move between different local minima of the solution space. They can be very effective but also have limitations. As the true global minimum of a non-trivial optical design problem cannot be known with certainty, it is difficult to determine the successful convergence of such an algorithm. Furthermore, higher-level design decisions such as the addition and removal of components or application of aspheres, GRINs or other degrees of freedom must generally be made outside the algorithm. An important intervention of the optical designer in the design process (for both local and global optimisation) concerns the selection of the starting solution from which the final design will be optimised. A poor starting solution often leads to a poor end solution, as it is difficult using optimisation techniques to jump between very different regions of the solution space. The inherent complexity of optical design solution spaces and presence of large numbers of local minima, combined with the trade-offs in system-level performance that many optimised solutions present (such as size versus optical performance), means that lens optimisation is seldom a straight forward process. Generally, lens systems are optimised in many stages, with local optimisations performed, followed by manual adjustment of the lens system variables (for example to freeze or vary aspheric coefficients), and adjustment of the optimisation parameters. A loop is formed between repeated optimisation and analysis until the lens reaches a satisfactory performance level, or the specification must be reconsidered.

Optical design is frequently referred to as both an art and a science, with successful execution of a design task requiring both a good understanding of the underlying optical theory, as well as significant intuition into the form and structure of optical systems. Imagination and determination are often required to tackle the most difficult design tasks. Real-world optical design tasks also require *engineering* knowledge. Often the desired performance from an optical specification is not feasibly achievable with real materials, processes and timescales. Pragmatic compromises with customers and other stakeholders within the design team of a wider *system* are often required to produce an optical system with optimal performance at a viable cost. The broad skill-set required of optical designers indicates that the job-role will not be co-opted by computers any time soon!

The author speculates that this principle similarly applies to more recent developments in artificial intelligence (AI), with the aforementioned engineering skills requiring a very general form of intelligence that must consider the wider context in which an optical design sits. The AI would require skills in negotiation, teamwork and leadership, while to produce truly original designs, the AI designer must somehow align its creativity with customer need. Another extremely challenging skill that an AI would also need to master to solve the most challenging design problems is the estimation of technical risk, which is often done on the basis of incomplete information. At present there is little substitute for decades of engineering experience as a prerequisite to excel at this. AI may however, serve as a means to develop more advanced global optimisation techniques, and already shows evidence of utility in lens starting solution selection and optimisation [57]. In time, AI may gain the capability to produce designs of increasing complexity and originality by controlling more advanced parameters such as the number of lens elements, aspheric surfaces, and even GRIN media. To do so however, the AI would need to be equipped with high quality information on relative costs or manufacturing

20

difficulty. This is also challenging information to provide, yet in recent years progress has been made through the development of computational models of lens manufacture processes [58].

It is easy to imagine a future where AI and optical designers work in harmony, with a greater role in global optimisation and analysis performed by the computer. However, the author cautions that this must not come at the expense of insight by the human designer. An understanding of optical constructions, aberrations, and what make some optical designs perform better than others (particularly under the effects of manufacturing tolerances) is a vital foundation to apply the higher-level engineering skills that will lead to great optical instruments and products.

1.6.1. Optical Figures of Merit

A wide range of methods to define optical quality exist, but in this work we are primarily concerned with imaging optics and make frequent reference to two key performance metrics, *modulation transfer function* (MTF) and *root-mean-squared (RMS) spot size*.

Modulation Transfer Function

The MTF describes how spatial frequencies of an object are transferred to an image by an optical system. It essentially describes the ability of a lens to transmit information. Usefully, it incorporates both the geometrical ray-based aspects of a system (aberrations) and the diffraction effects caused by the apertures of the lens system. MTF is particularly useful as a performance metric as it is readily measured for a real optical system. For this reason, optical performance specifications for lens systems are often expressed in terms of MTF. MTF is related to other quantities of interest, in particular (by its Fourier transform) the point spread function (PSF) and optical transfer function (OTF), with relations to MTF given by

$$\text{MTF} = \mathcal{F}\{\text{PSF}\}, \tag{1.20}$$

$$\text{MTF} = |\text{OTF}|. \tag{1.21}$$

MTF is typically calculated by an integral of the distribution of optical path difference in the exit pupil with respect to a reference sphere that defines a perfect image [59]. The aberrated wavefront is generally calculated by ray tracing. Conversely, MTF is generally measured through observation of the PSF (alternatively a line or edge-spread that is numerically deconvolved), followed by a numerical Fourier transform.

Root-Mean-Squared Spot Size

As the name implies, RMS spot size describes the size of the blurred spot generated by an optic as the root mean square of ray deviations from a centre point (that is typically the weighted average position of all rays under analysis). RMS spot size is a purely geometric measure of performance that neglects the effects of diffraction. This therefore limits the real-world use of this performance metric. RMS spot size is useful however within a theoretical optical design context. It is an easily calculated performance metric of a lens that allows for quick comparison between different solutions. For this reason, RMS spot size (or related RMS wavefront error) is often used as the basis of the optical design merit function.

A closely related quantity to the RMS spot size that accounts for diffraction is the point spread function (PSF), calculated by convolution of the ray distribution with the diffraction-limited spot
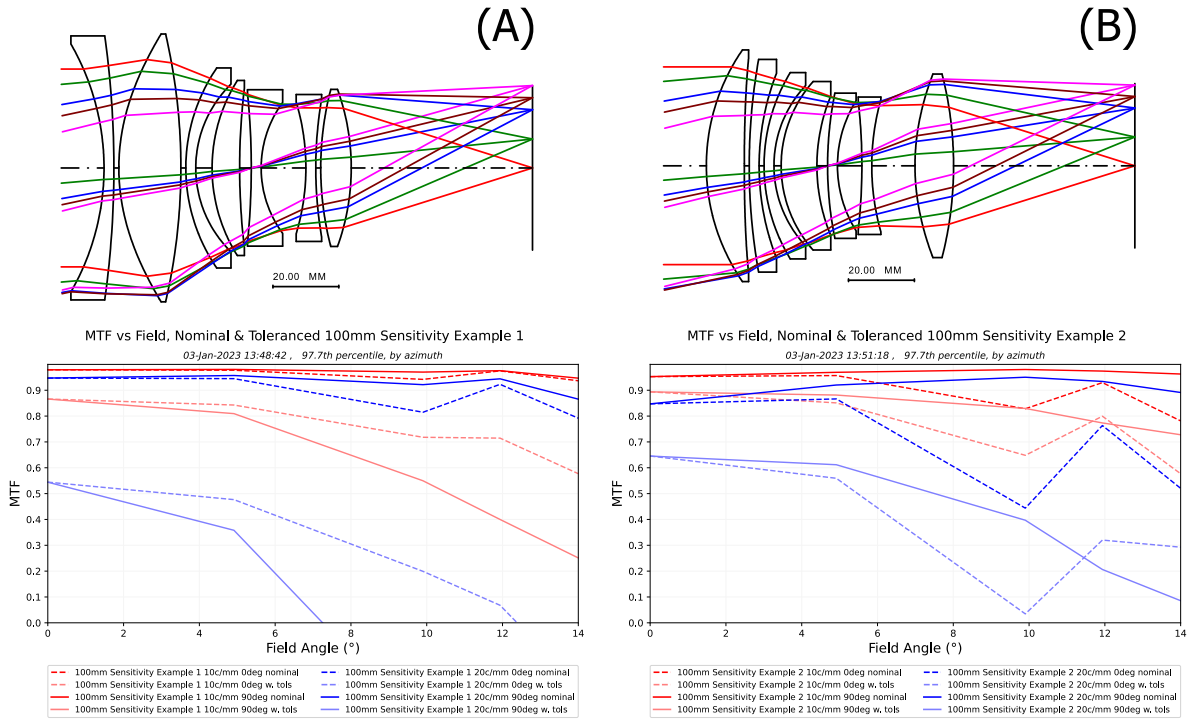
Figure 1.8: Contrasting tolerance sensitivities in a visible waveband 100 mm focal length lens. Lens geometry and MTF versus image height at 10.0 c/mm and 20.0 c/mm for two design examples where (A) represents naïve design based on best nominal performance and (B) represents best practice in lens desensitisation.

size predicted by Fraunhofer diffraction. From Equation 1.20, we note that image quality and information throughput is maximised by minimising the PSF. This is achieved by minimising the RMS spot size and maximising the pupil size (so as to reduce the contribution of diffraction to the PSF). These are often competing goals, with a larger aperture also transmitting more aberrations that degrade the RMS spot size or require more design degrees of freedom such as lens elements to correct. A key design decision therefore concerns selecting the aperture size, within the bounds of other system requirements such as cost and weight.

1.6.2. Design for Manufacture and Tolerances

Optical design generally has the end goal of producing a design that can be fabricated. It is at this point however, that design intent and the *as-built* optical system diverge! No optical component can be fabricated with perfect optical surface form, thickness, surface alignment (known as wedge), or refractive index. Likewise, it is not possible to assemble a system of lenses into perfect alignment. Tilts, decentres, air-spacing errors all alter the properties of the as-built design. Given that the nominal design is generally at a local minimum in the solution space, changes to the design upon fabrication statistically yield a net loss in optical performance.

Another important skill of the optical designer is to produce designs that are robust to small deviations in form caused by manufacturing tolerances. A well-known trap for the unwary comprises the generation of a design with very high nominal performance, but with high sensitivity to build errors. We consider two 100 mm lens designs prepared as examples for this work in Figure 1.8. Both designs have the same optimisable degrees of freedom, with two aspheric surfaces, variable curvatures, thickness and variable glass types over seven lens el-

ements. Design (B) has lower nominal performance than design (A), due to constraints on aspheric surface departure, angles of incidence, and the change in ray angles across lens components. If we consider theoretical *as-built* MTF performance however, analysed using a common set of optical tolerances in CodeV's wavefront-differential tolerancing routine, TOR, we observe that design (B) performs significantly better at the 97.7th percentile, as the afore-mentioned optimisation constraints have led to a solution with lower sensitivity to tolerances. Design (B) would perform significantly better than (A) in volume production, reducing cost by eliminating yield losses.

1.7. Fundamentals of Gradient-Index Optics

We define GRIN optics as any optical device that exploits the degrees of freedom available through use of a continuous and smoothly varying refractive index profile. This covers a broad set of applications including imaging, illumination and optical fibres. This contrasts to conventional homogeneous optics in which components have a constant refractive index, and rely upon interaction with optical surfaces to function. In GRIN optics, both the optical surfaces and optical media of a system can work in unison to provide improved optical correction, or potentially smaller and lighter optics for a given performance level.

GRIN materials generally consist of a variation between two or more basis materials. A frequently cited quantity associated with GRIN material combinations is *Delta N*, written as ΔN. This is the difference in refractive index between the maximum and minimum index of the given material combination. It is partly true that materials combinations offering larger ΔN values are more beneficial to the optical designer. However, this is significantly complicated by the chromatic properties of the GRIN we discuss in Section 1.7.3. A single figure of merit for a GRIN material combination is difficult to define, as it largely depends on the design task at hand.

1.7.1. Raytracing in Gradient-Index Optics

Numerous authors [19, 52, 60, 61] have addressed the derivation of an equation of motion for rays in GRIN media. A generally accepted form of the equation [62] is defined as

$$\frac{d^2\mathbf{r}}{dt^2} = \frac{1}{2}\nabla N^2(\mathbf{r}),\tag{1.22}$$

where $dt = ds/N$, and ds is an infinitesimal arc length along the ray, whilst $\mathbf{r}$ is the position vector of a point along the ray. $N(\mathbf{r})$ is the refractive index distribution. This equation is derived from geometrical optics principles in Appendix B. Generally this equation must be solved numerically, with only certain simple GRIN distributions (such as the spherical GRINs found in the Luneburg lens and Maxwell's fisheye) proving solveable analytically. The numerical solution of this second order differential equation is computationally intensive, with numerical optimisation of generalised GRIN systems also requiring that significant numbers of rays be traced. Numerous authors have addressed the problem of GRIN raytracing, with the procedure based on Runge-Kutta methods outlined by Sharma [63] seeing wide adoption in commercial optical design software.

A key parameter controlled by the designer when working with GRIN media is the stepping parameter assigned to the GRIN medium. This determines the step length over which the

Runge-Kutta methods are applied and generates a trade-off in trace precision versus speed, with larger stepping parameters tracing faster. It is useful to increase the stepping parameter whilst performing the bulk of optimisation and modification of an optical design. The loss in raytrace precision generally does not undermine the overall construction of an optical solution and the faster tracing speed allows more optimisation runs (and thus, potentially a broader exploration of the solution space) in a given timespan. Once an acceptable solution has been found, the stepping parameter can be decreased for a final optimisation run to generate a precise final result.

Due to the step-wise nature of GRIN raytracing, a further complication arises when GRIN rays intersect with optical surfaces. Runge-Kutta methods do not inherently produce a smooth curved trajectory, rather, they produce a set of points that each represent a numerically calculated approximation to a point on the ray. Interpolation is therefore required to accurately determine the ray-surface intersection point and incidence angle. This was addressed by Sharma by definition of an interpolating cubic from the ray positions and derivatives at the Runge-Kutta points, [64] and later improved by Stone and Forbes [65] by definition of a quartic interpolant that used additional information from the Runge-Kutta calculation.

These modern numerical GRIN raytracing techniques require (in addition to the starting vector of the ray) a function for the refractive index and its derivatives as a function of space. Only for the simplest GRIN distributions are these functions built in to optical design software (such as axial or spherical GRINs). Given the early developmental stage of the most advanced GRIN distributions at the time of writing, a key task of the optical designer is to mathematically define and program GRIN tracing equations that support generalised GRIN distributions. In this work, this is generally achieved through compiling a custom GRIN dynamic-link-library (.DLL) file or simple user "macro" code. Due to the aforementioned computational loads of tracing GRIN rays, offering a custom .DLL is generally a much more efficient way to trace rays and optimise a GRIN design (usually providing $> 10\times$ speed improvement), and is worth the additional effort for the majority of design tasks.

1.7.2. Common Refractive Index Distributions

Here, we define some common GRIN distributions and introduce a naming convention for GRINs of more general form. GRIN distributions mathematically describe the refractive index as a function of space ($N(\mathbf{r})$) within a region bounded by the optical surfaces and apertures of a GRIN lens. the GRIN distribution is described within a coordinate system whose origin may sit anywhere with respect to the GRIN lens (although it is frequently applied at a lens surface vertex).

Until recently, GRIN refractive index distributions (both theoretically and practically) tended to conform to one of three common types: axial, radial, or spherical. More generally, we may categorise these distributions as *one-dimensional* GRINs, as they are constrained to variation along one coordinate axis such as the radial axis of a cylinder or sphere. Whilst the goal of this work is to characterise more general GRIN lenses, there is significant utility in understanding the optical properties of these simpler distributions. Simple GRIN distributions may be considered to be a component part of a more complex general GRIN. For example, a general rotationally symmetric GRIN can be approximated as a stack of very thin radial GRINs.

GRIN distributions define a refractive index based on one or more index coefficients. In this work, we distinguish between refractive index coefficients and the refractive index of a

material by use of the calligraphic $\mathcal{N}$, i.e. $\mathcal{N}_{\text{coefficient}}$ and N_{material}. Refractive index coefficients have dimensions reciprocal to any term they are associated with, in order for the calculated refractive index to be dimensionless. For example, a coefficient pairing $\mathcal{N}_r S^r$ associated with a length, S, has a refractive index coefficient $\mathcal{N}_r$ of dimension (length)$^{-r}$.

General-Rotationally-Symmetric-Gradient-Index Media

We first define the most general case of smooth, rotationally-symmetric GRIN distribution. General-rotationally-symmetric GRINs may incorporate axial terms (parallel to the optical axis), radial terms (perpendicular to the optical axis) at even powers of ρ[§], and combinations of the two ($z^{m \geq 1} \rho^{n \geq 2}$) which we refer to as cross terms. The mathematical form of a general-rotationally-symmetric GRIN is given in Equation 1.23, with an example illustrated in Figure 1.9

$$
\begin{aligned}
N(\rho, z) = \sum_{i=0,2,4\dots}^{\infty} \sum_{j=0}^{\infty} \mathcal{N}_{ij} \rho^i z^j = & \left(\mathcal{N}_{00} + \mathcal{N}_{01}z + \mathcal{N}_{02}z^2 + \dots \right) \\
& + \left(\mathcal{N}_{20} + \mathcal{N}_{21}z + \mathcal{N}_{22}z^2 + \dots \right) \rho^2 \\
& + \left(\mathcal{N}_{40} + \mathcal{N}_{41}z + \mathcal{N}_{42}z^2 + \dots \right) \rho^4 + \dots
\end{aligned}
\tag{1.23}
$$

As general-rotationally-symmetric GRINs contain terms in ρ^2, the GRIN medium itself can generate optical power. A significant benefit of general-rotationally-symmetric GRIN distributions is the variation in linear optical power density, $dK(z)/dz \propto \mathcal{N}_2(z)$, along the optical axis, where the quantity $\mathcal{N}_2(z)$ represents a collection of all terms that are factors of ρ^2

$$
\mathcal{N}_2(z) = \sum_{j=0}^{\infty} \mathcal{N}_{2j} z^j.
\tag{1.24}
$$

Control of the optical power distribution over a thick GRIN lens is a very significant degree of freedom that theoretically enables optical systems to consist of just one GRIN lens, potentially making the continuous optical system envisioned by Buchdahl a reality. We explore this topic in greater detail in Chapters 2 and 3.
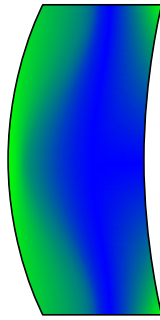
Figure 1.9: Diagram of a hypothetical general-rotationally-symmetric GRIN lens

---

[§]while it is possible to generate a GRIN medium with odd terms in ρ, it must be noted that the linear term renders the refractive index non-differentiable along the optical axis, and leads to changes in the optical wavefront that are non-conducive to imaging. Higher-order odd terms (such as ρ^3, ρ^5) may have some utility in optical design, but it is the even terms that most directly influence the optical power and aberrations.

Axial-Gradient-Index Media

Axial GRINs have variable refractive index parallel to a straight axis through an optical component. They can be conceptualised as a stack of infinitesimally thin layers of different refractive index. Their potential for aberration correction is comparable to that of an aspheric surface when applied to a lens surface with finite curvature [18]. The refractive index distribution of an axial-GRIN medium is given by Equation 1.23 in the specific case where only coefficients with $i = 0$ are non zero, yielding

$$N = \sum_{j=0}^{\infty} \mathcal{N}_{0j} z^j = \mathcal{N}_{00} + \mathcal{N}_{01} z + \mathcal{N}_{02} z^2 + \mathcal{N}_{03} z^3 + \mathcal{N}_{04} z^4 + \dots. \tag{1.25}$$

Axial GRINs influence the aberrations of a surface but impart no optical power of their own due to the absence of any radial index variation. A hypothetical axial GRIN is illustrated in Figure 1.10.
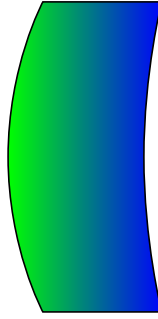
Figure 1.10: Diagram of a hypothetical axial-GRIN lens

Radial-Gradient-Index Media

Radial-GRIN lenses have cylindrically-symmetric index variation perpendicular to the optical axis, with zero index gradient parallel to the optical axis. They see widespread use in the form of optical fibres and their connectors, borescopes, and photocopier lens arrays [27]. Radial GRINs were the amongst the first GRIN lenses to be observed in nature [13] and were the first type of artificial GRIN lens to be fabricated in the laboratory [12]; the eponymous Wood lens. The refractive index distribution of a radial-GRIN lens is formed from Equation 1.23 in the case where only coefficients with $j = 0$ are non zero, giving

$$N = \sum_{i=0,2,4\dots}^{\infty} \mathcal{N}_{i0} \rho^i = \mathcal{N}_{00} + \mathcal{N}_{20} \rho^2 + \mathcal{N}_{40} \rho^4 + \mathcal{N}_{60} \rho^6 + \mathcal{N}_{80} \rho^8 + \dots \tag{1.26}$$

where ρ is the perpendicular distance from the optical axis of the GRIN. A radial GRIN can be conceptualised as a set of concentric tubes of different refractive indices and infinitesimal radial thickness. A hypothetical radial-GRIN lens is illustrated in Figure 1.11. It is particularly noteworthy that a quadratically varying radial GRIN has optical focusing power. Intuitively, this focusing power can be conceptualised as the propagating wavefront moving faster/slower (depending on the sign of optical power) at the optical axis compared to the edge of the lens, leading to a curved, focusing wavefront. The optical power, K_{GRIN} of a thin radial-GRIN

medium [60, Chapter 8.3] is given by

$$K_{\text{GRIN}} = -2\mathcal{N}_{20}(\lambda)\, t, \tag{1.27}$$

where t is the GRIN lens thickness. Despite the fact that our definition of GRIN power contains a thickness term, we still model it as a thin lens. This assumption is generally valid provided that $|K_{\text{GRIN}}|t^2 \ll 1$ [19, Chapter 4.1]. We note also that the index variation on the surfaces of a radial-GRIN lens does not affect the optical power [52, Equation 61]. Because the medium of a radial GRIN generates optical power, it is possible to generate a focusing lens with planar surfaces. This also means we can define the power of a thin, radial-GRIN lens with curved surfaces as the sum of surface power contributions and GRIN medium contributions as

$$K_{\text{lens}} = K_{\text{surf}} + K_{\text{GRIN}} = (c_1 - c_2)(\mathcal{N}_{00} - 1) - 2\mathcal{N}_{20}t, \tag{1.28}$$

where the axial index value, $\mathcal{N}_{00}$, contributes to the focal length of the surface (as it defines the index of the surface in the paraxial region).
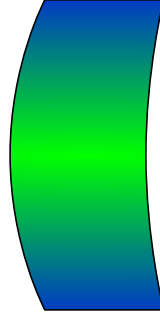
Figure 1.11: Diagram of a hypothetical radial-GRIN lens

Spherical-Gradient-Index Media

Spherical GRINs are one of the oldest types of GRIN used in an optical design; dating back to the formulation of Maxwell's fisheye lens in 1854 [10]. The inherent symmetry in spherical GRIN distributions has been exploited to theorise a number of perfect geometric imaging systems. Examples of such aberration free systems have been designed by Maxwell [10], Luneburg [11] and Shafer [66]. More recently, special cases of "offset" spherical GRINs have been manufactured, notably at Case Western Reserve [39], Rochester [67], and NRL [43] (specifically for infrared chalcogenide glass). In general, these processes involve creating an axial GRIN by fusion of multiple windows of constant, yet tailored, refractive index. This axial GRIN is then moulded into a curved preform that is cut into a lens geometry. A hypothetical spherical GRIN with geometry offset from the optical surfaces is shown in Figure 1.12.
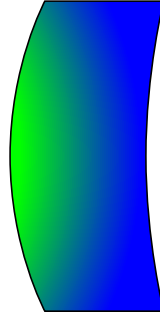
Figure 1.12: Diagram of a hypothetical spherical GRIN lens

Freeform-Gradient-Index Media

Within this work, we define freeform GRINs analogously to freeform surfaces, where the GRIN distribution lacks any axis of symmetry. A notional freeform GRIN is illustrated in Figure 1.13. As with freeform surfaces, a very wide range of mathematical representations exist that can define such a medium. Furthermore, due to the three-dimensional nature of GRIN distributions, a number of sub-categories of freeform GRIN also exist. A radial GRIN with additional odd terms in X and Y (perpendicular to the optical axis) fits the definition of a GRIN lacking any axes of symmetry, but a GRIN with further odd polynomial terms along the z-axis may be considered an even more general freeform GRIN. The variety of freeform GRIN representations was discussed by Lippman and Yang [46].

Like with freeform surfaces, such GRINs are near-exclusively applied to systems that themselves lack rotational symmetry. The tilt and decentre of powered optical components creates aberrations that are also asymmetric, with freeform degrees of freedom a notable means to correct them. A notable aerospace application of such asymmetric systems is in head-mounted and head-up displays for cockpit avionics. We discuss the application of freeform GRINs within this setting in Chapter 6.
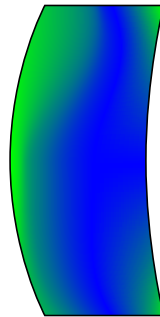
Figure 1.13: Diagram of a hypothetical freeform GRIN lens

Arbitrary-Gradient-Index Media

We reserve the term *arbitrary* for the most complex GRIN parts. With new manufacture approaches, it is not a strict necessity that the GRIN distribution remain a continuous function of position within the part. Novel components such as GRIN lens arrays and Fresnel lenses are possible. With recently developed additively manufactured GRINs, arrays of components can be generated where each lenslet is unique. Additive manufacture processes eliminate the

need for advanced tooling, which is often a cost driver of such optical components and can be prohibitive for smaller production runs. Arbitrary GRIN components have been demonstrated in the design of GRINs for structured illumination [68].

1.7.3. Chromatic Aberrations and Gradient-Index Lenses

Typically, all refractive materials have variable refractive index with wavelength and GRIN lenses are no exception. The transitional-blended nature of GRINs between two or more base materials generates some interesting properties however. Like with homogeneous materials, we can define a GRIN form of the Abbé V value [69, 70]. For a given material combination this is defined as:

$$V_{\text{GRIN}} = \frac{\Delta N(\lambda_{\text{mid}})}{\Delta N(\lambda_{\text{short}}) - \Delta N(\lambda_{\text{long}})},$$

(1.29)

for three defining sequential wavelengths, λ_{short}, λ_{mid}, and λ_{long}. This quantity may be highly positively or negatively dispersive or even infinite in the case where a constant ΔN with wavelength exists between the two defining GRIN materials (such a medium would contribute zero primary chromatic aberration). Table 1.1 shows notional examples of GRIN material combinations and their corresponding V_{GRIN} values for the commonly defined Fraunhofer C, d, and F lines[¶]. It is shown that combinations of common optical materials can generate a very wide range of chromatic dispersion values. It follows from Equation 1.29 that the same dispersion

Material 1	N_{D1}	V_{D1}	Material 2	N_{D2}	V_{D2}	ΔN	$V_{\text{D GRIN}}$
N-BK7	1.517	64.13	F4	1.616	36.60	0.100	11.35
S-FTM16	1.593	35.29	N-LAF21	1.788	47.46	0.195	-1012.92
N-PSK53A	1.618	63.36	LF5	1.581	40.83	0.037	-8.16

Table 1.1: Index, Abbé V values and GRIN properties for some example two-material combinations.

characteristics apply to the index gradient (by substituting ΔN for dN/ds). This implies that for a binary material combination, V_{GRIN} is constant at all points within the GRIN medium, irrespective of the GRIN distribution. Of particular note for a radial-GRIN lens, the distributed Abbé number can be obtained by the quadratic GRIN coefficient such that

$$V_{\text{20GRIN}} = \frac{\mathcal{N}_{20}(\lambda_{\text{mid}})}{\mathcal{N}_{20}(\lambda_{\text{short}}) - \mathcal{N}_{20}(\lambda_{\text{long}})}.$$

(1.30)

As the quadratic $\mathcal{N}_{20}$ GRIN coefficient is proportional to the power of a thin GRIN lens, we may also use the quantity $K_{\text{GRIN}}/V_{\text{GRIN}}$ in the colour correction of a GRIN lens. A widely used approach is to balance the optical power of the surfaces of a GRIN lens with that of the GRIN medium, giving an achromatic condition for a radial-GRIN lens

$$\frac{K_{\text{surf}}}{V_{\text{surf}}} + \frac{K_{\text{GRIN}}}{V_{\text{GRIN}}} = 0.$$

(1.31)

Equation 1.30 is also valid for GRINs consisting of three or more materials, however this must be considered with caution. In contrast to a binary GRIN combination, V_{GRIN} of a ternary or higher-order blend can be a function of position within the lens depending on the form of the relative composition distribution of each material.

[¶]Note that these combinations are not representative of manufacture GRIN blends, but notional combinations that illustrate key chromatic properties that can exist in GRIN materials.

It is also possible to deduce the value of V_{GRIN} for a given combination of two materials for which limited data (only a reference refractive index and Abbé value) are known, which allows a useful estimate for hypothetical GRIN combinations. Expanding Equation 1.29 for two underlying materials denoted by the subscripts A and B gives

$$V_{\text{GRIN}} = \frac{N_A(\lambda_{\text{mid}}) - N_B(\lambda_{\text{mid}})}{N_A(\lambda_{\text{short}}) - N_B(\lambda_{\text{short}}) - N_A(\lambda_{\text{long}}) + N_B(\lambda_{\text{long}})}. \tag{1.32}$$

Since

$$\begin{aligned} V_A &= \frac{N_A(\lambda_{\text{mid}}) - 1}{N_A(\lambda_{\text{short}}) - N_A(\lambda_{\text{long}})}, \\ V_B &= \frac{N_B(\lambda_{\text{mid}}) - 1}{N_B(\lambda_{\text{short}}) - N_B(\lambda_{\text{long}})}, \end{aligned} \tag{1.33}$$

we can rearrange Equation 1.32 to give

$$V_{\text{GRIN}} = \frac{N_A(\lambda_{\text{mid}}) - N_B(\lambda_{\text{mid}})}{(N_A(\lambda_{\text{short}}) - N_A(\lambda_{\text{long}})) - (N_B(\lambda_{\text{short}}) - N_B(\lambda_{\text{long}}))}. \tag{1.34}$$

By rearranging Equation 1.33 in terms of $N_A(\lambda_{\text{short}}) - N_A(\lambda_{\text{long}})$ and $N_B(\lambda_{\text{short}}) - N_B(\lambda_{\text{long}})$, we can therefore determine the Abbé V value of a two material combination in terms of $N(\lambda_{\text{mid}})$ and V of each material as

$$V_{\text{GRIN}} = \frac{N_A(\lambda_{\text{mid}}) - N_B(\lambda_{\text{mid}})}{\frac{N_A(\lambda_{\text{mid}})-1}{V_A} - \frac{N_B(\lambda_{\text{mid}})-1}{V_B}}. \tag{1.35}$$

Axial GRINs can also be used to correct chromatic aberration through a difference in dispersion between the front and rear surfaces of the lens, whereby the balance in optical power between the front and back surface can be used to solve for zero chromatic aberration as

$$\frac{K_{s1}}{V_{s1}} + \frac{K_{s2}}{V_{s2}} = 0, \tag{1.36}$$

where s1 and s2 represent the front and rear surfaces of the lens.

It is noted that general rotationally symmetric and freeform GRINs can have both axial and radial index variation, and thus both of these mechanisms of colour correction can occur in a single lens.

1.7.4. Monochromatic Aberrations of Gradient-Index Lenses

As previously noted, the aberration coefficients of optical systems allow the designer to gain significant insight into the inner workings of their designs. GRIN aberration theory has been addressed by several authors. Originally Buchdahl extended his theory of quasi-invariants to rotationally symmetric homogeneous media [16][Appendix F]. This was then expanded on by Sands [18] to provide Seidel aberration coefficients for both the surfaces and medium of GRIN distributions with the general-rotationally-symmetric form indicated in Equation 1.23.

The calculation of aberrations for GRIN components carries additional complexity in that both the surfaces and medium (or ray transfer) of the GRIN contribute to the total aberration. Surface contributions to the third-order aberrations are proportional to both axial and radial GRIN terms at the surface vertex ($d\mathcal{N}_0/dz$ and $\mathcal{N}_2$). Monochromatically, these are broadly

equivalent to the aberrations generated by an aspheric surface. The expressions for the ray-transfer contributions of the GRIN aberration theory developed by Buchdahl and Sands are integrals that in the majority of cases must be solved numerically. Moore produced a computational procedure for the calculation of GRIN aberrations based on said integrals [20]. More recently, formulas for the Seidel aberrations of GRINs were produced by Bociort for axial and radial GRIN lenses [19]. These contributions from the medium must be added to the surface contributions to obtain the total aberrations of the optical system. Contributions to the index gradient in the fourth power of aperture also act in a similar manner to aspheric coefficients.

We discuss in detail Seidel aberration calculation for both optical surfaces and media in Chapter 3.

2

Mathematical Representations of Inhomogeneous Optical Media

The contents of this chapter are derived and expanded from *"Optical design of multi-material, general rotationally symmetric GRIN lenses - Proc SPIE 10998, 2019"* [1, AMBproc].

2.1. Abstract

We present a model for the optical design of gradient-index (GRIN) media of general rotationally symmetric form, based on any number of constituent materials. This is achieved by modelling the relative composition of GRIN constituent materials as a function of space in a form that can be readily converted to refractive index and its derivatives, while being suitable for optimisation in lens design software. This model is used in the optical design of a singlet GRIN eyepiece where we demonstrate equivalent performance to a multi-element homogeneous design. We also show the potential of such media for correction of both chromatic and monochromatic aberrations by demonstration of a GRIN singlet with performance exceeding that of an apochromatic cemented triplet. We conclude that representation of generalised GRIN media by relative composition shows the potential for a powerful new class of imaging systems where the bulk of refractive power and aberration control is provided by the GRIN medium.

2.2. Refractive Index Distribution and Representation

The refractive index distribution is, quite naturally, a key defining feature of a GRIN lens. The choice of index distribution determines what aberrations are affected by the GRIN medium, and has very significant implications for how such a lens may be fabricated. A further nuance in the definition of GRIN lenses must also be considered. A given index distribution is described by a mathematical *representation*. It is possible for multiple mathematical representations to describe the same GRIN distribution. By analogy, it is possible to describe an aspheric surface using a range of mathematical surface representations (e.g. conventional asphere, Zernike polynomial, Forbes polynomial). In this chapter, we explore a GRIN representation for general rotationally symmetric GRINs consisting of multiple materials. We further impose that this

representation should be amenable to both optimisation and manufacture of the GRIN lens design.

2.3. Detailed Requirements for a Generalised Gradient-Index Representation

We specify the requirements for a generalised GRIN representation as follows.

Continuous	Whilst it is physically valid for optical rays to cross a discontinuous boundary (Snell's law), we cannot solve the GRIN raytracing equations at such a point as the index gradient is discontinuous. Any such discontinuities must be modelled as surfaces.
Differentiable	Similar to the requirement for continuity, the index medium must be spatially differentiable at all points within the clear aperture or the GRIN raytracing equation will not be accurately solved by the raytracing software. Whilst such a discontinuity in the derivative is physically possible, it must again be defined as an optical surface to be modelled correctly.
Suitable for the design of optical systems	We would ultimately like our representation to be put to use to design optical systems. It must therefore be suitable for controlling the paraxial optical properties and aberrations of the system.
Suitable for optimisation	Whilst a large number of different GRIN representations exist that can describe the same index distribution, some representations may be significantly better conditioned than others in convergence to a solution via numerical optimisation.
Definable in terms of the properties of component materials	GRIN media may be regarded as a spatially varying combination of a number of different component materials. We would like our GRIN representation to describe such a medium in terms of these components, and (where necessary) account for any non-linearity in the aggregate refractive index caused by interactions between the base materials.

2.4. Combination of Component Materials

The ability to fabricate an arbitrary GRIN distribution from multiple materials generates challenges in how the composite optical material is represented mathematically, as the example in Figure 2.1 shows. We consider two hypothetical GRINs, consisting of two and three materials respectively that are defined by the red points in the Abbé diagram, where N is the refractive index and V is the Abbé V value. In Figure 2.1 (a), we see that for two materials, the composite material sits on a curve in N-V space between the two base materials. There is a monotonic relationship between the refractive index at a given reference wavelength and the relative composition of the GRIN. The refractive index data is therefore useful to both the lens designer and the lens fabricator as it contains sufficient information for both raytracing and manufacture. For a three-material system however, refractive index at a reference wavelength cannot fully characterise the optical material, as a range of different dispersion values

33
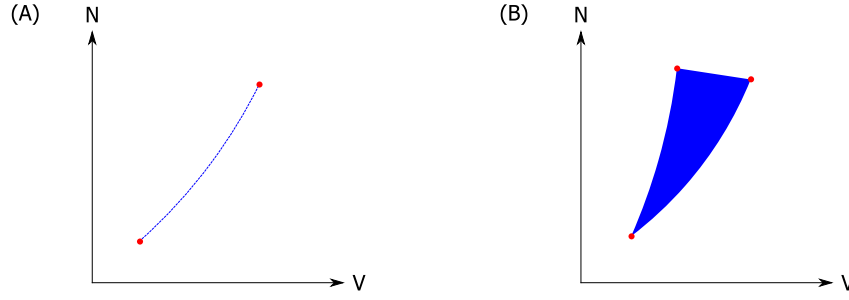
Figure 2.1: (a) Abbé diagram showing transition between two materials. (b) Abbé diagram showing the index and dispersion region covered by three materials.

are available to the designer for a given index value. In Figure 2.1 (b) we see that the range of possible N and V values covers the shaded blue area in N-V space. For a three-material GRIN system, this might be satisfactorily addressed in design by expressing composition of the GRIN in terms of both index and dispersion, but this approach carries some significant disadvantages. Firstly, we lose information about variation in partial dispersion from the base materials, which is required information to model and correct secondary spectrum. Secondly, an approach based on varying index and its derivatives is less amenable to optimisation, with a complex set of boundary constraints required for three or more materials to prevent the optimisation from returning an invalid N and V combination outside the blue shaded area. Such a result would need to consist of a negative fraction of a given base material, and is therefore unphysical. Such complex inequality constraints also generate a significant risk of the optimisation becoming ill-conditioned and unstable. The difficulties here outlined become further compounded for GRINs consisting of four or more base materials.

GRIN lens design relies heavily on wise selection of a mathematical representation that is amenable to optimisation and analysis, and that enables *design for manufacture*, which in this context means we are able to express and optimise the optical design in alignment with a chosen manufacture process, rather than a design that is optimal in the purely theoretical sense. The eponymous GRIN lens designs of Luneburg and Maxwell [10, 11] are counter-examples of design-for-manufacture. These designs both provide aberration free imaging, but were not designed with a fabrication process in mind and thus until very recently remained theoretical curiosities at optical wavelengths [35]. Broadly, without constraints on material properties, optimised GRIN lenses tend towards very large ΔN values and non-physical chromatic dispersion values that have little prospect of manufacture. Conversely, a representation that accounts for design for manufacture allows us to reach a solution that has the optimal performance the fabrication process can provide. It also helps us to understand the effects of variability in the manufacture process and tolerances it may introduce. The PhD thesis of Bentley [71, chapter 6] shows an example of this, with a design-for-manufacture approach employed in the optical design of a GRIN-based compact disc scanning lens. Two designs were produced, one with ideal theoretical performance, the other in terms of a GRIN diffusion model that strongly correlated with the manufacture process. Whilst the theoretically ideal design had slightly better performance, only the diffusion model based design could be manufactured.

Representations for a GRIN consisting of more than two materials were proposed by Mait et al. [72] and Beadie et al. [73], where the GRIN material is represented as a sum of partial compositions of the base materials, with the proportion of each base material required to add up to unity. Importantly, the representation described the GRIN medium in a form that is meaningful to an optical fabricator (*synthesis*), but similarly can be converted to a value of

refractive index and its gradient that is required to solve the differential ray tracing equations for GRIN media (*analysis*). Herein we propose a slight modification to Mait & Beadie's representation, with the relative fractions of each material normalised to allow greater flexibility in optimisation. More recently, Desai et al. [74] showed an example of a quaternary GRIN singlet medium, which using a material space enabled by 3D-printed nanoparticle-doped inks yielded a single lens corrected for chromatic aberration at five individual wavelengths.

In this chapter we show that it is possible to obtain the first-order *thin-lens* properties of multi-material GRIN media from a relative composition model. Furthermore, we show it is possible to decompose the first-order properties of a multi-material radial GRIN into those contributed by each of the constituent materials provided we can make some assumptions about the nature of the effective medium theory governing the combination of the lens materials. We call such a decomposition *partial power*. This technique yields insight into the means by which GRIN lenses can correct for chromatic aberrations by reformulating the material selection problem in a similar form to the thin-lens theory that can be used for homogeneous lenses. The resulting benefit of this is an efficient means to generate starting solutions for the design of achromatic GRIN lenses.

2.5. Representation of an N-Material Gradient-Index Medium by Relative Composition

2.5.1. Selection of a Coordinate System

Figure 2.2 shows the coordinate system for all formulae and optical designs in this chapter. We adopt a right-handed coordinate system where the z-axis is defined as the optical axis. We also define a quantity, ρ, where $\rho^2 = x^2 + y^2$ and represents the radial distance from the optical axis. Such a coordinate system is amenable to use within common optical design software packages.

2.5.2. Effective Medium Assumptions

Our choice of effective medium theory dictates how index scales for intermediate compositions between materials in our GRIN. This requires detailed consideration of the composition of the GRIN material at a sub-wavelength level, such as the size, shape and density of refractive-index-modifying dopants. This detail lies beyond the scope of this work. Rather we make
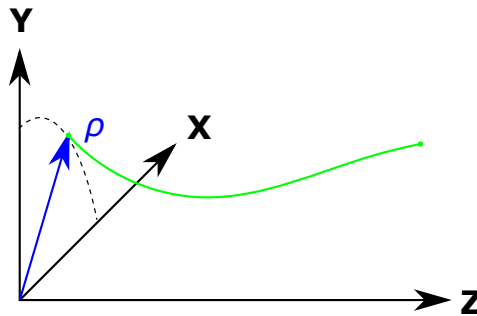
Figure 2.2: Defining coordinate system for general GRIN representations in this chapter. A notional GRIN ray propagating along the positive z-axis is shown in green.

the assertion that provided we can express the material in terms of a quantity that scales linearly with relative composition, and have a means to convert said quantity to refractive index, then the approach is useful. For this work, we consider two potential effective medium approaches: weighted average square refractive index (volumetric average permittivity for dielectric materials), and weighted average refractive index. Other models such as Maxwell-Garnett are also feasible to model, albeit more mathematically complex. In each case we show that it is possible to convert relative composition to a refractive index polynomial. In the simpler case of combination by average index, we may go even further and decompose the focal power into contributions by material. We discuss this concept further in Section 2.5.5.

In the literature we note two index scaling approaches in use by GRIN manufacturers. The average permittivity approach is adopted by Peak Nano LLC [75], whereas a linear index scaling with volumetric dopant fraction is observed by NanoVox [29].

2.5.3. Derivation of an Average-Refractive-Index Relative Composition Model

We define our GRIN as a combination of materials from a set of M base materials with refractive indices

$$\{N_\mu; \quad 1 \leq \mu \leq M\}. \tag{2.1}$$

We define a quantity m_μ, which is a compositional coefficient of material μ. The refractive index of the material mixture is then defined by

$$N(\rho, z) = \frac{1}{m_T} \sum_{\mu=1}^{M} N_\mu m_\mu(\rho, z). \tag{2.2}$$

where $m_T(\rho, z)$ represents the sum of all compositional coefficients at a given position, given by

$$m_T(\rho, z) = \sum_{\mu=1}^{M} m_\mu(\rho, z). \tag{2.3}$$

In the case of a given material, q, if $m_q \neq 0$ and all other m_μ are zero, the refractive index is N_q. We define $m_\mu(\rho, z)$ to be in the general rotationally symmetric form of Equation 1.23, given by

$$m_\mu(\rho, z) = \sum_{i=0,2,4\ldots}^{\infty} \sum_{j=0}^{\infty} m_{\mu ij} \rho^i z^j. \tag{2.4}$$

Our GRIN representation now provides two essential pieces of information. It provides relative composition data as a function of space for fabrication, as well as refractive index as a function of space for analysis. Such a representation has the potential to be useful to both the lens designer and the lens fabricator. We can also obtain some of the first-order and paraxial properties of a lens with such a distribution. Properties such as the GRIN medium optical power may provide useful diagnostic information to the designer. By substitution of Equations 2.3 into 2.2, we obtain

$$N(\rho, z) \sum_{\mu=1}^{M} m_\mu(\rho, z) = \sum_{\mu=1}^{M} N_\mu m_\mu(\rho, z). \tag{2.5}$$

Substituting $N(\rho, z)$ for its definition in Equation 1.23, $m_\mu(\rho, z)$ for its definition in Equation 2.4 and expanding with respect to ρ gives

$$\sum_{\mu=1}^{M} \sum_{i=0,2,4...}^{\infty} \mathcal{N}_i(z)\rho^i \sum_{l=0,2,4...}^{\infty} m_{\mu l}(z)\rho^l = \sum_{i=0,2,4...}^{\infty} \sum_{\mu=1}^{M} N_\mu m_{\mu i}(z)\rho^i, \tag{2.6}$$

where

$$\mathcal{N}_i(z) = \sum_{j=0}^{\infty} \mathcal{N}_{ij}z^j, \quad \text{and} \quad m_{\mu i}(z) = \sum_{j} m_{\mu ij}z^j. \tag{2.7}$$

By use of the Cauchy product of two infinite series given by

$$\sum_{p=0}^{\infty} a_p \sum_{q=0}^{\infty} b_q = \sum_{r=0}^{\infty} \sum_{p=0}^{r} a_p b_{r-p}, \tag{2.8}$$

we rearrange Equation 2.6 as

$$\sum_{i=0,2,4...}^{\infty} \sum_{k=0,2,4...}^{i} \sum_{\mu=1}^{M} \mathcal{N}_k(z)m_{\mu i-k}(z)\rho^i = \sum_{i=0,2,4...}^{\infty} \sum_{\mu=1}^{M} N_\mu m_{\mu i}(z)\rho^i. \tag{2.9}$$

Then, by collecting terms in ρ^i, we obtain an expression for the radial GRIN coefficents as a function of z

$$\sum_{k=0,2,4...}^{i} \sum_{\mu=1}^{M} \mathcal{N}_k(z)m_{\mu i-k}(z) = \sum_{\mu=1}^{M} N_\mu m_{\mu i}(z). \tag{2.10}$$

It is of particular use to expand the first two terms of Equation 2.10, as they yield the paraxial properties of a GRIN medium [76]. For a GRIN consisting of M base materials we have

$$\mathcal{N}_0(z) = \frac{\sum_{\mu=1}^{M} N_\mu m_{\mu 0}(z)}{\sum_{\mu=1}^{M} m_{\mu 0}(z)}, \tag{2.11}$$

$$\mathcal{N}_2(z) = \frac{\sum_{\mu=1}^{M} N_\mu m_{\mu 2}(z) - \mathcal{N}_0(z) \sum_{\mu=1}^{M} m_{\mu 2}(z)}{\sum_{\mu=1}^{M} m_{\mu 0}(z)}. \tag{2.12}$$

We make use of Equations 2.11 and 1.11 to deduce the power contribution from the lens surfaces, whilst we substitute Equation 2.12 into Equation 1.27 to obtain the local optical power of the GRIN medium*. Further simplification of these formulae is obtained in the case where $m_T(\rho, z) = 1$ at all points within the GRIN medium. In this case, where $\rho = 0$

$$\sum_{\mu=1}^{M} m_{\mu 0} = 1. \tag{2.13}$$

---

*This approach is valid to calculate optical power of a thin region within a general GRIN where $\mathcal{N}_2$ and ray heights do not vary greatly. For a thick, generalised GRIN, a full paraxial raytrace is required to robustly calculate the focal power of the entire lens.

At non-zero values of ρ it follows that

$$\sum_{\mu=1}^{M} m_{\mu 2} = 0. \tag{2.14}$$

In this case, the first two terms of Equation 2.10 in ρ simplify further to

$$\mathcal{N}_0(z) = \sum_{\mu=1}^{M} N_\mu m_{\mu 0}(z), \tag{2.15}$$

$$\mathcal{N}_2(z) = \sum_{\mu=1}^{M} N_\mu m_{\mu 2}(z). \tag{2.16}$$

Binary and Ternary Blends

Some common cases of GRIN material blends concern mixtures of two and three base materials. These combinations are frequently referred to in this work, where we define the binary case as $M = 2, \mu = 1 = A, \mu = 2 = B$, and the ternary case as $M = 3, \mu = 1 = A, \mu = 2 = B, \mu = 3 = C$. The refractive index as a function of position of respective binary and ternary blends is given by

$$N(\rho, z) = \frac{N_A m_A(\rho, z) + N_B m_B(\rho, z)}{m_A(\rho, z) + m_B(\rho, z)}, \tag{2.17}$$

$$N(\rho, z) = \frac{N_A m_A(\rho, z) + N_B m_B(\rho, z) + N_C m_C(\rho, z)}{m_A(\rho, z) + m_B(\rho, z) + m_C(\rho, z)}. \tag{2.18}$$

The $\mathcal{N}_0$ coefficients of such blends are for the binary and ternary respective cases are given by

$$\mathcal{N}_0(z) = \frac{N_A m_{A0}(z) + N_B m_{B0}(z)}{m_{A0}(z) + m_{B0}(z)}, \tag{2.19}$$

$$\mathcal{N}_0(z) = \frac{N_A m_{A0}(z) + N_B m_{B0}(z) + N_C m_{C0}(z)}{m_{A0}(z) + m_{B0}(z) + m_{C0}(z)}, \tag{2.20}$$

whilst the $\mathcal{N}_2$ coefficients are given by

$$\mathcal{N}_2(z) = \frac{N_A m_{A2}(z) + N_B m_{B2}(z) - \mathcal{N}_0(z) \left[m_{A2}(z) + m_{B2}(z) \right]}{m_{A0}(z) + m_{B0}(z)}, \tag{2.21}$$

$$\mathcal{N}_2(z) = \frac{N_A m_{A2}(z) + N_B m_{B2}(z) + N_C m_{C2}(z) - \mathcal{N}_0(z) \left[m_{A2}(z) + m_{B2}(z) + m_{C2}(z) \right]}{m_{A0}(z) + m_{B0}(z) + m_{C0}(z)}. \tag{2.22}$$

Applying the condition $m_T(\rho, z) = 1$ yields further simplified expersions by applying Equations 2.13, 2.14, 2.15, and 2.16. In this case the refractive index as a function of position is given by

$$N(\rho, z) = N_A m_A(\rho, z) + N_B m_B(\rho, z), \tag{2.23}$$

$$N(\rho, z) = N_A m_A(\rho, z) + N_B m_B(\rho, z) + N_C m_C(\rho, z), \tag{2.24}$$

with axial coefficients

$$\mathcal{N}_0(z) = N_A m_{A0}(z) + N_B m_{B0}(z), \tag{2.25}$$

$$\mathcal{N}_0(z) = N_A m_{A0}(z) + N_B m_{B0}(z) + N_C m_{C0}(z), \tag{2.26}$$

and likewise quadratic radial index coefficients

$$\mathcal{N}_2(z) = N_A m_{A2}(z) + N_B m_{B2}(z), \tag{2.27}$$

$$\mathcal{N}_2(z) = N_A m_{A2}(z) + N_B m_{B2}(z) + N_C m_{C2}(z). \tag{2.28}$$

2.5.4. Derivation of an Average Permittivity Relative Composition Model

By similar logic to that employed in Section 2.5.3, we can represent a multi-material GRIN by the average of the square of the refractive index of the constituent materials (relative permittivity for dielectric base materials). This represents an alternative to the linear index combination outlined in Chapter 2.5.3 and is dependent on the physics of how GRIN basis materials combine for a given manufacture process. Such an approach adapts the optical design process to the manufacture process, enabling improved design for manufacture by ensuring designs are representative of what can be made. For the same material set denoted in Equation 2.1, the compositional scaling law for a GRIN based on average relative permittivity is given by

$$N^2 = \epsilon_{eff} = \frac{\sum_{\mu}^{M} m_\mu \epsilon_\mu}{\sum_{\mu}^{M} m_\mu}, \tag{2.29}$$

where ϵ_i represents the permittivity of the μth material. We seek a GRIN distribution of the form

$$N^2(z, \rho) = \eta_0(z) + \eta_2(z)\rho^2 + \eta_4(z)\rho^4 + \dots. \tag{2.30}$$

This form of GRIN distribution is amenable to the calculation of optical power and the Seidel aberrations [77]. We use the letter $\eta(\rho, z)$ to distinguish coefficients in permittivity from the $\mathcal{N}(\rho, z)$ terms used in GRINs with a weighted average index combination law. Following an analogous derivation to that of Chapter 2.5.3 we obtain the following coefficients for η_0 and η_2:

$$\eta_0(z) = \frac{\sum_{\mu=1}^{M} \epsilon_\mu m_{\mu 0}(z)}{\sum_{\mu=1}^{M} m_{\mu 0}(z)}, \tag{2.31}$$

$$\eta_2(z) = \frac{\sum_{\mu=1}^{M} \epsilon_\mu m_{\mu 2}(z) - \eta_0(z) \sum_{\mu=1}^{M} m_{\mu 2}(z)}{\sum_{\mu=1}^{M} m_{\mu 0}(z)}. \tag{2.32}$$

These two coefficients in particular are useful as they fully describe the paraxial properties of the GRIN medium . The η_0 and η_2 coefficients describe the optical power of a thin radial-GRIN lens of thickness, t, in N-squared form [78], given by

$$K_{\text{GRIN}} = -\frac{\eta_2}{\sqrt{\eta_0}} t. \tag{2.33}$$

2.5.5. Partial Power

The linear index compositional scaling rule of Equation 2.2 allows significant insight into the properties of the GRIN by separating the optical power into contributions by each of the component materials. For a multi-material GRIN, we suppose that it can be replaced by a stack of thin, radial-GRIN lenses in contact, with optical power as given by Equation 1.28. Each lens of this stack consists of only one component material of the GRIN, with the others
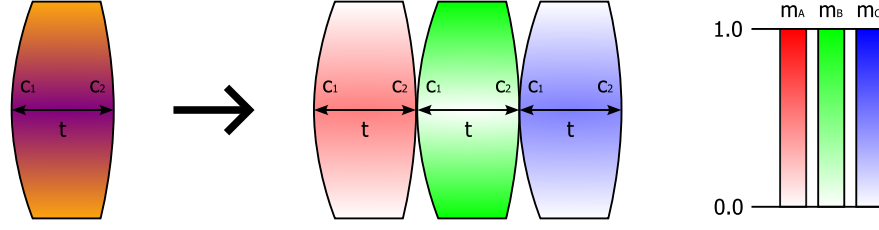
Figure 2.3: Separation of a ternary-material GRIN (left) into three thin GRIN lenses of identical geometry that blend between a given component material and air.

replaced by air (N=1). Each lens in the stack has the same thickness and surface curvatures. This hypothetical lens is illustrated in Figure 2.3 for a ternary blend. We shall show that the combined optical power of this stack of thin GRIN lenses is equivalent to the combined multi-material GRIN. We assume $m_T = 1$ to simplify the derivation through use of Equations 2.15 and 2.16, which we sum over all materials after making all but a given material ν have refractive index $N = 1$. The power of the νth lens in this thin lens stack is given by

$$K_\nu = (c_1 - c_2) \left[N_\nu m_{\nu 0} + \sum_{\mu=1}^{M} m_{\mu 0} - m_{\nu 0} - 1 \right] - 2t \left[N_\nu m_{\nu 2} + \sum_{\mu=1}^{M} m_{\mu 2} - m_{\nu 2} \right]. \quad (2.34)$$

Using equations 2.13 and 2.14 to simplify, then summing over all ν we obtain

$$\sum_{\nu=1}^{M} K_\nu = (c_1 - c_2) \sum_{\nu=1}^{M} [N_\nu m_{\nu 0} - m_{\nu 0}] - 2t \sum_{\nu=1}^{M} [N_\nu m_{\nu 2} - m_{\nu 2}], \quad (2.35)$$

where the optical power contribution from material ν is

$$K_\nu = (N_\nu - 1) [m_{\nu 0}(c_1 - c_2) - 2t m_{\nu 2}]. \quad (2.36)$$

We refer to the contribution of each material as its *partial power*.

   Partial power shows that the optical power of a multi-material GRIN lens can be represented as the sum of individual material contributions. These formulae represent a simple means for a designer to gain insight into the behaviour of a multi-material GRIN system, particularly through the use of common thin-lens theory for achromatic lenses. By use of Equations 1.14 and (if required) 1.19, we can determine whether the material combination in a GRIN is useful for correction of primary and secondary chromatic aberrations. Crucially, this can be achieved without resorting to more time-consuming finite raytracing and detailed optical design by solving the achromatic condition for a set of M given materials, which is given by

$$\sum_{\mu=1}^{M} \frac{K_\mu}{V_\mu} = 0. \quad (2.37)$$

2.6. Optical Designs Using a Relative Composition Representation

A key desirable property of our GRIN representations is that they be amenable to optimisation in optical design software. In this section we demonstrate some examples of the relative

composition approach applied to optical design problems. We first demonstrate the simplified case of a two-material GRIN. We then expand the approach to a three-material radial GRIN to achieve apochromatic correction, before demonstrating optimisation of GRIN systems with multiple materials and a generalised rotationally symmetric distribution.

2.6.1. Design of a Two-Material Gradient-Index Achromat
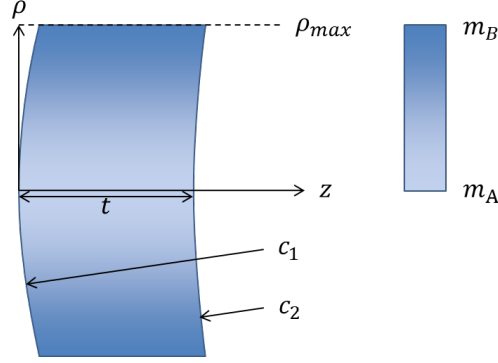
Figure 2.4: Geometry of a two-material radial-GRIN lens

We first consider the simplified case of a two-material radial GRIN ($M=2$, $\mu=1=A$, $\mu=2=B$). Prior to optimisation, we generate an analytical starting solution by calculating the relative composition of the lens as a function of ρ and the difference in the lens surface curvatures. We assume that the lens consists entirely of material A along the optical axis and entirely of material B at the aperture edge, ρ_{max}. The radial GRIN distribution is independent of z. It is also assumed to be quadratic and therefore terms in ρ^4 or greater are zero. The lens has thickness t and surface curvatures c_1 and c_2. This GRIN geometry is illustrated in Figure 2.4. The refractive index is given by Equation 2.23 where the coefficients for material A are

$$
\begin{aligned}
m_A(\rho) &= m_{A0} + m_{A2}\rho^2, \\
m_{A0} &= 1, \\
m_{A2} &= \frac{-1}{\rho_{\text{max}}^2},
\end{aligned}
\tag{2.38}
$$

and for material B

$$
\begin{aligned}
m_B(\rho) &= m_{B0} + m_{B2}\rho^2, \\
m_{B0} &= 0, \\
m_{B2} &= \frac{1}{\rho_{\text{max}}^2}.
\end{aligned}
\tag{2.39}
$$

The partial power of materials A and B is obtained by substitution of the concentration coefficients into Equation 2.36 for each respective material. We obtain partial powers for each material given by

$$
K_A = (N_A - 1)\left[(c_1 - c_2) + \frac{2t}{\rho_{\text{max}}}\right],
$$

$$
K_B = -\frac{2t(N_B - 1)}{\rho_{\text{max}}^2}.
\tag{2.40}
$$

Summing these partial powers gives an expression for the optical power of the lens

$$K_{\text{lens}} = (c_1 - c_2)(N_A - 1) + \frac{2t(N_A - N_B)}{\rho_{\text{max}}^2}. \tag{2.41}$$

We define an achromatic GRIN lens by invoking the achromatic condition of Equation 2.37 using the Abbé V values of the base materials, V_A and V_B. The Abbé V values effectively define the waveband of our system. In this case, the system defining wavelengths are 633, 546 and 436 nm. This condition gives us sufficient information to generate equations for the lens thickness, t and the difference in lens curvatures, $\tau = (c_1 - c_2)$, noting that only the *difference* in surface curvatures determines focal length of a thin lens. The lens thickness is given by

$$t = \frac{\rho_{\text{max}}^2 K_{\text{lens}}}{2\,(N_B - 1)\left(\frac{V_A}{V_B} - 1\right)} \tag{2.42}$$

$$\tau\,(N_A - 1) = K_{\text{lens}}\left[1 - \frac{(N_A - N_B)}{(N_B - 1)\left(\frac{V_A}{V_B} - 1\right)}\right] \tag{2.43}$$

Selection of a total power, $K_{\text{lens}} = 0.05$ and semi-diameter, $\rho_{\text{max}} = 5$ along with hypothetical lens materials** N-BK7 and SF6 return the GRIN and surface curvature parameters in Table 2.1.

ρ_{max}	5.0 mm
K_{lens}	0.05 mm^{-1}
t	0.465 mm
τ	0.117 mm^{-1}
$R_1 = -R_2$	17.030 mm
K_{GRIN}	-0.011 mm^{-1}
K_{surf}	0.061 mm^{-1}
K_A	0.080 mm^{-1}
K_B	-0.030 mm^{-1}
M_{A0}	1.00
M_{A2}	-0.040 mm^{-2}
M_{B0}	0.000
M_{B2}	0.040 mm^{-2}

Table 2.1: Lens parameters for an N-BK7 and SF6 achromatic GRIN lens, derived via spreadsheet calculation

This first-order lens model was constructed in the CodeV optical design software, as shown in Figure 2.5 (a). The value of τ was converted to individual surface curvatures by assuming a biconvex lens geometry, namely $c_1 = -c_2$. Our GRIN employs an average-index effective medium model. We see excellent agreement for the focal power versus wavelength of an N-BK7, SF6 GRIN lens with linear index scaling, as shown in Figure 2.6. It is noted that the first-order model returns a very thin GRIN lens with negative edge thicknesses. This is

---

**Materials are selected to demonstrate the theory. This combination has not been experimentally generated.

addressed in our CodeV model by increasing the thickness inversely to the GRIN m_{A2} and m_{B2} coefficients. Alternatively, edge thickness can be increased through optimisation by the imposition of weighted constraints. The coefficients and thickness of Figure 2.5 (a) were scaled by a factor of 1/5 and 5 respectively. The starting lens of 2.5 (a) has significant spherical aberration, but this is readily reduced by optimisation of the bending factor and GRIN coefficients of the lens. Optimisation, with variable radii of curvature and m_{A0}, m_{A2}, m_{B0} and m_{B2} coefficients returns the optimised design in Figure 2.5 (b). Performance of the optimised lens is limited by fifth-order spherical aberration balanced by third-order spherical aberration, with some residual axial colour.
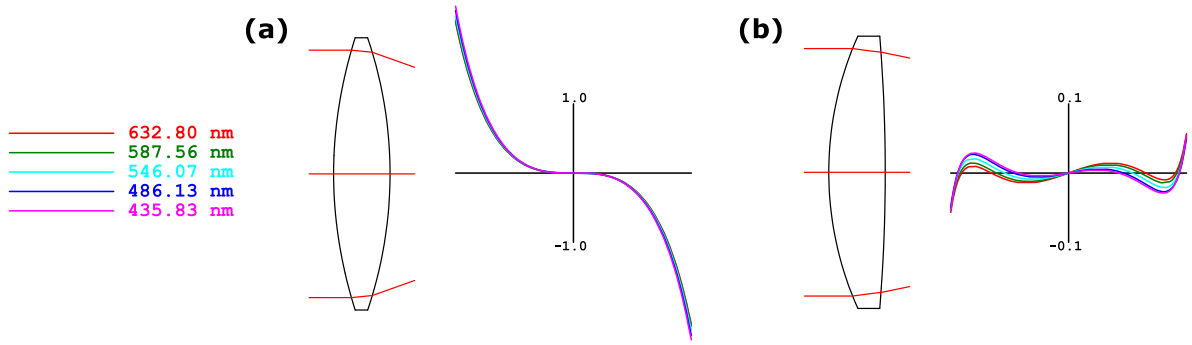
Figure 2.5: (a) N-BK7 SF6 GRIN singlet from first-order model with thickness and GRIN coefficients scaled to avoid negative edge thickness. The transverse ray errors for this starting solution show well-corrected chromatic aberration and residual primary spherical aberration. (b) Optimised singlet corrected for chromatic and spherical aberration (note change of scale).
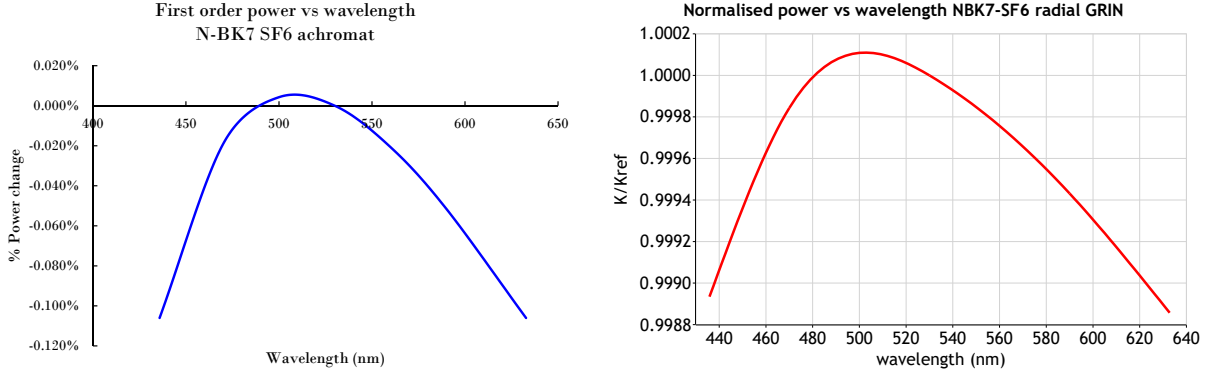
Figure 2.6: Normalised power vs wavelength for first-order calculation (left) and CodeV model (right).

2.6.2. Design of a Three-Material Radial-Gradient-Index Apochromat

We apply the relative composition model to the optical design of an apochromatic GRIN singlet lens. We will then compare the construction and performance of this GRIN lens to a cemented triplet design consisting of the same materials. The specification to which these lenses are designed is listed in Table 2.2.

The apochromatic condition is met when the focal length is the same at three distinct wavelengths. Achieving this condition generally requires the use of three separate materials (or alternatively two materials with equivalent partial dispersion). We model our apochromatic

F/#	6.0
Focal length	50 mm
Waveband	435.8-632.8 nm, uniform weighted
Semi-FOV	0.25°
RMS spot size	to be minimised

Table 2.2: Apochromatic lens specification.

system as three thin lenses in contact, consisting of materials, A, B, and C, each providing their own optical power contribution, given by

$$K_{\text{lens}}(\lambda) = K_A(\lambda) + K_B(\lambda) + K_C(\lambda), \tag{2.44}$$

where $K_A(\lambda)$, $K_B(\lambda)$, $K_C(\lambda)$ are the optical powers of materials A, B, and C respectively, effected either via surface curvature or by a quadratically varying radial GRIN medium. We can expect equivalent colour correction via either route as chromatic aberration is a first-order property of the material selection. We now define three distinct wavelengths, λ_1, λ_2, and λ_3 which form the waveband of our apochromatic system. The apochromatic condition is given by

$$K_{\text{lens}}(\lambda_1) = K_{\text{lens}}(\lambda_2) = K_{\text{lens}}(\lambda_3). \tag{2.45}$$

From Equation 2.36, we observe that for both GRIN partial power and homogeneous lenses, the optical power is proportional to $(N(\lambda) - 1)$, with all other terms in the equation being independent of wavelength. We therefore define an optical power coefficient, $\mathcal{K}$, which for the νth material is given by

$$\mathcal{K}_\nu = \frac{K_\nu}{N_\nu - 1}. \tag{2.46}$$

For a thin, homogeneous lens

$$\mathcal{K}_\nu = c_1 - c_2 = \tau, \tag{2.47}$$

and for material ν within a GRIN lens

$$\mathcal{K}_\nu = m_{\nu 0}(c_1 - c_2) - 2tm_{\nu 2} = m_{\nu 0}\tau - 2tm_{\nu 2}. \tag{2.48}$$

The optical power of each lens in the three-material apochromat in terms of $\mathcal{K}$ is given by

$$\begin{aligned}
K_A(\lambda) &= \mathcal{K}_A(N_A(\lambda) - 1) \\
K_B(\lambda) &= \mathcal{K}_B(N_B(\lambda) - 1) \\
K_C(\lambda) &= \mathcal{K}_C(N_C(\lambda) - 1).
\end{aligned} \tag{2.49}$$

We can now find $\mathcal{K}_A$, $\mathcal{K}_B$, and $\mathcal{K}_C$ to solve Equation 2.45 by solving a system of three equations, which expressed as a matrix equation is given by

$$\begin{pmatrix} N_A(\lambda_1) - 1 & N_B(\lambda_1) - 1 & N_C(\lambda_1) - 1 \\ N_A(\lambda_2) - 1 & N_B(\lambda_2) - 1 & N_C(\lambda_2) - 1 \\ N_A(\lambda_3) - 1 & N_B(\lambda_3) - 1 & N_C(\lambda_3) - 1 \end{pmatrix} \begin{pmatrix} \mathcal{K}_A \\ \mathcal{K}_B \\ \mathcal{K}_C \end{pmatrix} = \begin{pmatrix} K_{\text{lens}} \\ K_{\text{lens}} \\ K_{\text{lens}} \end{pmatrix}. \tag{2.50}$$

We solve 2.50 for a known apochromatic combination of three Schott glasses: N-BK7, N-SF6 and N-KZFS8[†]. The residual chromatic aberration is shown in Figure 2.7. Partial powers for

---

[†]As before, this material blend is notional to demonstrate the theory and is not based on fabricated GRIN material.

each material are listed in the central column of Table 2.4. Further calculation is then required to convert partial powers to values of c_1, c_2, t, and m_{v0}, m_{v2} for each constituent material. Firstly, the value of τ is calculated. We divide Equation 2.36 by $N_v - 1$ for each material to obtain $\mathcal{K}_v$, then sum over the three materials to obtain

$$\mathcal{K}_A + \mathcal{K}_B + \mathcal{K}_C = \tau (m_{A0} + m_{B0} + m_{C0}) - 2t (m_{A2} + m_{B2} + m_{C2}), \qquad (2.51)$$

where because $m_{A0} + m_{B0} + m_{C0} = 1$ and $m_{A2} + m_{B2} + m_{C2} = 0$, we can simplify the bracketed terms to solve for τ, given by

$$\tau = \mathcal{K}_A + \mathcal{K}_B + \mathcal{K}_C. \qquad (2.52)$$

As with the two-material case, we simplify selection of the surface curvatures by making $c_1 = -c_2$. From here, the designer must select values of the free parameters m_{v0} and t to produce a physically valid solution. If poorly selected, it is possible to obtain a solution where $m_v(\rho)$ becomes negative within the lens, while still producing the correct $K(\lambda)$. Clearly t must be positive; it must also be sufficiently thick to ensure values of $|m_{v2}|$ remain sufficiently small to ensure positive $m_v(\rho)$ over the lens aperture. To select optimal values for these parameters, a two-stage process is undertaken. Firstly, for any material where $m_{v2} > 0$, m_{v0} is set to zero. Secondly, to maximise the diameter at which $m_v(\rho) = 0$, we choose the values of m_{v0} to be $\mathcal{K}_v$ divided by the sum of all positive $\mathcal{K}$, namely

$$m_{v0} = \frac{\mathcal{K}_v}{\sum_{i,\,\mathcal{K}_i>0}^{M} \mathcal{K}_i}, \qquad (2.53)$$

for a set of M materials (where M=3 for this lens design). Applied to the N-BK7, N-SF6, N-KZFS8 example lens, we note from Table 2.4 that N-BK7 and N-SF6 have positive $\mathcal{K}$. This yields the required values for m_{v0} which are shown in Table 2.3. Once the values for $\mathcal{K}_v$, m_{v0},

t	1.5	
τ	0.0667	
ρ_{max}	8.333	
$\mathcal{K}_A$	$\mathcal{K}_A$	$\mathcal{K}_A$
0.164	0.064	-0.162
m_{A0}	m_{B0}	m_{C0}
0.719	0.281	0
m_{A2}	m_{B2}	m_{C2}
-0.03878	-0.01514	0.05391

Table 2.3: Apochromatic lens parameters for A=N-BK7, B=N-SF6, C=N-KZFS8 GRIN lens.

and τ are known, we can readily obtain a value for $m_{v2}t$ by rearranging Equation 2.36

$$m_{v2}t = \frac{m_{v0} - \mathcal{K}_v}{2}. \qquad (2.54)$$

While the value of t can be selected by the designer, it is instructive to show the minimum value that yields all positive $m_v(\rho)$ over the lens aperture. For a lens of semi-aperture ρ_{max}, m_v at the clear aperture is given by

$$m_v(\rho_{\text{max}}) = m_{v0} + m_{v2}\rho_{\text{max}}^2. \qquad (2.55)$$

Rearranging Equation 2.55 in terms of $m_{\nu 2}$ and substituting into Equation 2.54 gives an expression for the value of t that returns a GRIN lens with zero concentration of materials with positive partial power at the lens edge, provided the process of Equation 2.53 has been followed

$$t \geq \rho_{\max}^2 \frac{\mathcal{K}_\nu - m_{\nu 0}\tau}{2m_{\nu 0}}, \tag{2.56}$$

where t can (and generally should) be greater to provide some leeway for optimisation of higher-order compositional coefficients $m_{\nu 4}, m_{\nu 6}, \ldots$. Once t is selected, $m_{\nu 2}$ is easily calculated by rearranging Equation 2.54

$$m_{\nu 2} = \frac{m_{\nu 0} - \mathcal{K}_\nu}{2t}. \tag{2.57}$$

These parameters were used to define our GRIN optimisation starting solution, which was modelled in CodeV. The RMS spot size was then optimised to yield the solution shown in Figure 2.8. Surface curvatures, the lens centre thickness and back focal distance were all variables in the optimisation. Additionally, the front surface was made aspheric with variable fourth and sixth-order coefficients, with GRIN relative composition terms for each material in ρ^0, ρ^2, and ρ^4 also variable. The end result is that the lens was able to correct for spherical aberration and spherochromatism, with the only residual aberrations being higher-order axial chromatic aberration. The resulting performance was diffraction limited with a transmitted polychromatic wavefront error of 0.0067 waves RMS over a uniform-weighted waveband between 436 nm and 633 nm. Concurrently, a cemented triplet lens consisting of N-BK7, N-KZFS8 and N-SF6 was designed to the same optical specification by optimisation of the lens surface curvatures and by trial-and-error ordering of the materials in the triplet to minimise the RMS spot size. This lens solution is illustrated in Figure 2.10. Transverse rays errors for this design are shown in Figure 2.11. The spherical surfaces of the design result in significant spherochromatism, which limits the optical correction of the lens to 0.038 waves RMS. The performance of the homogeneous design can be improved to that of the GRIN design by optimising aspheric terms on all of the optical surfaces that comprise the lens (noting that this would entail manufacture of six aspheric surfaces in total). We deduce by comparison of these lens designs, that ternary GRIN media with full control of relative composition as a function of aperture are extremely powerful components in the correction of chromatic aberrations, being essentially limited to the paraxial chromatic aberration of the underlying material selection. While the materials in this exercise were fictitious and not representative of any particular manufacture approach, it is clear that if the underlying material palette of the GRIN process has sufficient variability in refractive index, dispersion, and partial dispersion, then such well colour corrected lenses can be made a reality.

Material	K_{partial} **(First-order model)**	K_{partial} **(Optimised lens)**
$K_{\text{N-BK7}}$	0.0862	0.0922
$K_{\text{N-SF6}}$	0.0532	0.0534
$K_{\text{N-KZFS8}}$	-0.1194	-0.1256
K_{total}	0.02000	0.01997

Table 2.4: First-order partial powers for an N-BK7, N-SF6, N-KZFS8 apochromat.

Normalised power vs wavelength
N-BK7, N-SF6, N-KZFS8 apochromat
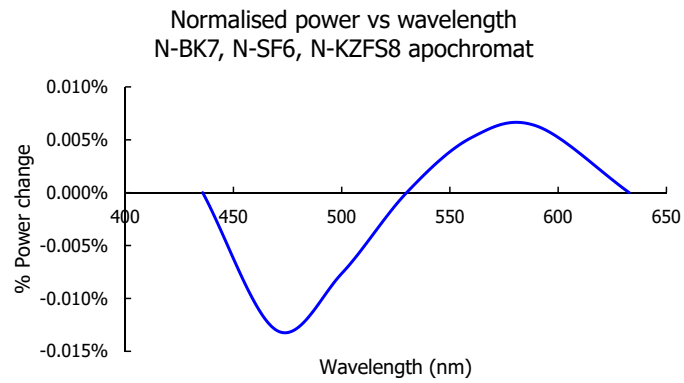
Figure 2.7: Normalised power of an N-BK7, N-SF6, N-KZFS8 apochromat.
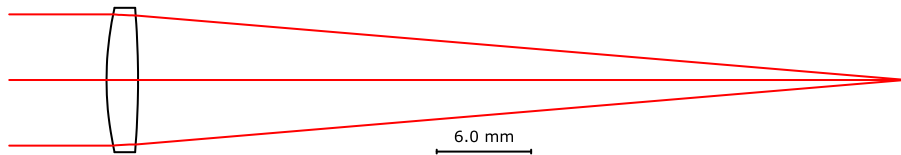
Figure 2.8: Optical design of an N-BK7, N-SF6, N-KZFS8, F/6 ternary GRIN singlet.

Ray aberration, μm
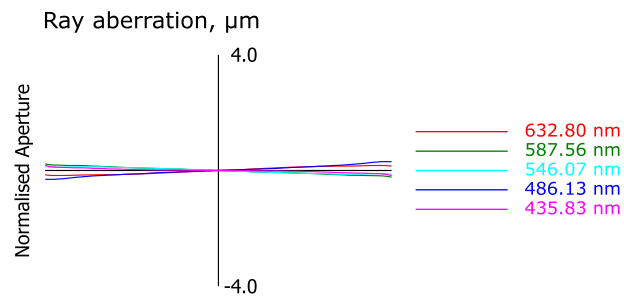
Figure 2.9: Transverse ray errors for a N-BK7, N-SF6, N-KZFS8 ternary GRIN singlet.
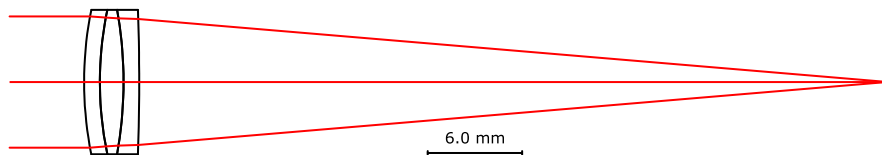
Figure 2.10: Optical design of an N-BK7, N-SF6, N-KZFS8, F/6 cemented triplet with spherical surfaces.

47
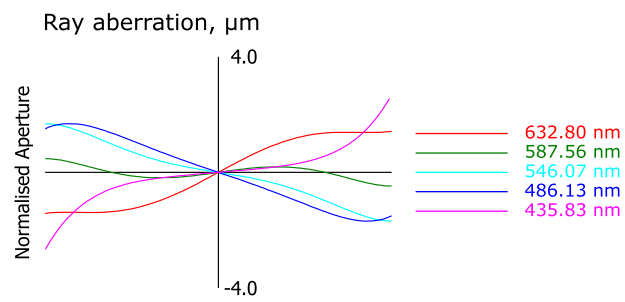
Figure 2.11: Transverse ray errors for a N-BK7, N-SF6, N-KZFS8 cemented triplet with spherical surfaces.

2.7. Optical Design of a Ternary-Material, General-Rotationally-Symmetric-Gradient-Index Magnifier

We demonstrate that the relative composition representation may be applied to the optical design and optimisation of more general GRIN distributions. A magnifier optical design exercise was performed for a micro-OLED (organic light emitting diode) display, where we compare a generalised GRIN solution to a homogeneous design. The intent of this design exercise was to determine whether there are sufficient degrees of freedom in general-rotationally-symmetric GRIN media to perform an equivalent role to multiple aspheric and diffractive surfaces. The magnifier specification is detailed in Table 2.5.

We generalise our GRIN distribution to incorporate terms in ρ, z, and cross terms ($\rho^{n>0} z^{m>0}$). Such a GRIN distribution has the degrees of freedom to allow optical power to vary along the z-axis of the GRIN. If our GRIN lens is sufficiently thick, these degrees of freedom may be very powerful in the correction of optical aberrations. The composition coefficient of the µth material is given by

$$m_\mu = m_{\mu 00} + m_{\mu 01} z + m_{\mu 02} z^2 + (m_{\mu 20} + m_{\mu 21} z + m_{\mu 22} z^2)\rho^2 + (m_{\mu 40} + m_{\mu 41} z + m_{\mu 42} z^2)\rho^4, \quad (2.58)$$

where the refractive index of the GRIN medium is obtained by combining the contributions of all materials as per Equation 2.2. A reference design was generated for intended fabrication using state-of-the-art optical technologies that are widely deployed in industry, which includes cemented doublets, polymer lenses, and aspheric refractive-diffractive hybrid surfaces that can be produced via diamond turning.

Field of view	30°
Entrance pupil diameter	10 mm
Display size	640x512, 15 µm pixel pitch
Eye relief	30 mm
Clear aperture	23 mm (vignetting permitted)
Waveband	Photopic

Table 2.5: GRIN magnifier cardinal point requirements

2.7.1. Homogeneous Solution

A conventional magnifier design was optimised from a starting solution typical of high-performance designs. The optical construction is shown in Figure 2.12 (top). An N-LASF31A, S-NPH2 doublet provides some colour correction whilst introducing small contributions to the Seidel aberrations due to the very high refractive indices and dispersion difference of these glasses. This doublet is followed by two acrylic lenses. The first of these features a hybrid refractive-diffractive surface. Hybrid surfaces enable highly effective colour correction, due to their strongly negative dispersion, but the presence of parasitic diffraction orders also increases the risk of stray light and may reduce the system contrast [55]. Each acrylic lens also features aspheric terms to enable correction of astigmatism and higher-order aberrations.

The overall level of correction of this lens over the field and full pupil is sufficient to execute the display viewing task specified. MTF at 35 cycles/mm (approximately the Nyquist spatial frequency of the specified micro-OLED display) is greater than 0.5 across the entire field

(shown in Figure 2.14 (left)). Transverse ray error plots are shown in Figure 2.13 (left). The Seidel aberrations are substantially corrected and are balanced against higher-order aberrations, with the design limited by a small amount of spherical aberration and lateral/axial colour. This design represents a useful baseline with which we can compare our GRIN designs.

2.7.2. Gradient-Index Solution Optimisation

A magnifier starting solution for optimisation was generated via the partial power method previously outlined. Our material selection this time is more complex than previous examples, as our lens design now has a larger FOV and aperture. In addition to correction of primary chromatic aberrations, we would like the magnifier to provide an image with minimal Petzval curvature, which as noted in Chapter 1.5.3 depends on the optical power and axial refractive index of a lens. As a result, three different materials are required in the starting solution to give degrees of freedom to solve for focal power, chromatic aberration, and Petzval curvature. For a homogeneous lens, the Petzval curvature has the relationship

$$S4_{\text{hom}} \propto \frac{K_{\text{lens}}}{N_{\text{lens}}}, \tag{2.59}$$

While for a GRIN lens, we have

$$S4_{\text{GRIN}} \propto \frac{K_{\text{GRIN}}}{\mathcal{N}_0^2}. \tag{2.60}$$

In the partial power model, the amount of optical power from each material can be provided by both the optical surface and GRIN medium, which complicates the calculation of a flat-field starting solution. Pragmatically, we assume that all optical power is provided by the GRIN medium such that

$$\frac{K_A}{N_A^2} + \frac{K_B}{N_B^2} + \frac{K_C}{N_C^2} = 0, \tag{2.61}$$

while noting that a thicker GRIN lens has the ability to influence Petzval curvature through the *distribution* of optical power in the lens. We assume that a flat-field all-GRIN starting point found via first-order theory is sufficiently close to the optimised solution that will combined surface and GRIN optical power. With any three materials, we have sufficient degrees of freedom to find a power construction that gives achromatic performance (corrected at two wavelengths) and a correct focal power, given by

$$\frac{K_A}{V_A} + \frac{K_B}{V_B} + \frac{K_C}{V_C} = 0 \tag{2.62}$$

and

$$K_A + K_B + K_C = K_{\text{lens}}. \tag{2.63}$$

This now defines a system of three equations, which written in matrix form is given by

$$\begin{pmatrix} 1 & 1 & 1 \\ \frac{1}{V_A} & \frac{1}{V_B} & \frac{1}{V_C} \\ \frac{1}{N_A^2} & \frac{1}{N_B^2} & \frac{1}{N_C^2} \end{pmatrix} \begin{pmatrix} K_A \\ K_B \\ K_C \end{pmatrix} = \begin{pmatrix} K_{\text{lens}} \\ 0 \\ 0 \end{pmatrix}. \tag{2.64}$$

Equation 2.64 can then by solved by substituting multiple materials combinations[‡]. We must then apply one further condition to select our materials from the large number of possible

---

[‡]As with previous examples, the materials are notional examples to demonstrate the design theory and process, and are not representative of real, manufactured GRIN material.

solutions. We would like the monochromatic aberrations of the system to be minimised to obtain good imaging performance. We achieve this by reducing the magnitude of the power of each material in the system. We therefore filter material combinations by the root-sum-of-squares (RSS) optical partial power in each material. These conditions generally lead us to select glass combinations that consist of a high refractive index, low-dispersion "crown", with a combination of high and low index dispersive "flints". A combination of N-LAK9, N-KF9 and N-SF10 was eventually selected, as it had a low normalised-RSS power of 7.60 and a sufficient ΔN of 0.210. By comparison, the previous combination of N-BK7, N-SF6 and N-KZFS8 had a normalised-RSS power of 22.89. A more extreme material combination of N-LASF31A, N-SF66 and N-KF9 provides even further reduced power balance, but requires a very large ΔN of 0.411. Calculation of the lens curvatures, thickness, and GRIN coefficients was then calculated using the procedure outlined in Section 2.6.2.

Optimisation of the GRIN lens was then undertaken from the first-order starting solution to minimise the RMS spot size over a weighted average of each field angle. The lens GRIN coefficients, aspheric coefficients, curvatures and centre thickness were all variables in the optimisation. The centre thickness of the GRIN was limited to the axial length of the homogeneous solution optics.

Material	K_n	Material	K_n	Material	K_n
N-BK7	-6.96	N-LAK9	5.94	N-LASF31A	4.38
N-SF6	-10.91	N-SF10	-1.26	N-SF66	-1.37
N-KZFS8	18.87	N-KF9	-3.69	N-KF9	-2.00
K_{RSS}	22.88	K_{RSS}	7.60	K_{RSS}	5.01
ΔN	0.297	ΔN	0.210	ΔN	0.411

Table 2.6: Example flat field achromatic GRIN combinations

Optimisation of the GRIN-based solution with a generalised distribution yielded the solution shown in Figure 2.12 (bottom). A good level of correction is achieved in a single component. The transverse ray errors of the GRIN solution are shown in Figure 2.13 (right). Performance is limited by small amounts of higher-order aberrations. MTF performance is shown in Figure 2.14 (right). We achieve improved colour correction on axis, as the GRIN provides better correction of secondary spectrum than the diffractive variant. Performance at wider field angles is broadly comparable between the two approaches.

2.7.3. Relative Composition Plots

It is important that we verify that any optimised GRIN design is physically valid. For a relative composition representation we need to verify that there is no negative proportion of any material within the design. The relative compositions of each material over a cross-section of the lens were plotted. Figure 2.15 shows three sample plots for the singlet magnifier design. The colour of the plot fades to white as the amount of a given material approaches zero. However if the amount of the material becomes negative, the relevant region of the plot turns black to highlight this fact. An example of a compositional violation is shown in Figure 2.16. Relative composition plots also give us an intuitive perspective of how the GRIN is achieving correction of the optical system. The distribution of N-LAK9 in Figure 2.15 is concentrated at the front optical surface, and forms a positively powered GRIN through the bulk of the lens, whilst the distribution of N-KF9 becomes more strongly negatively powered towards the back
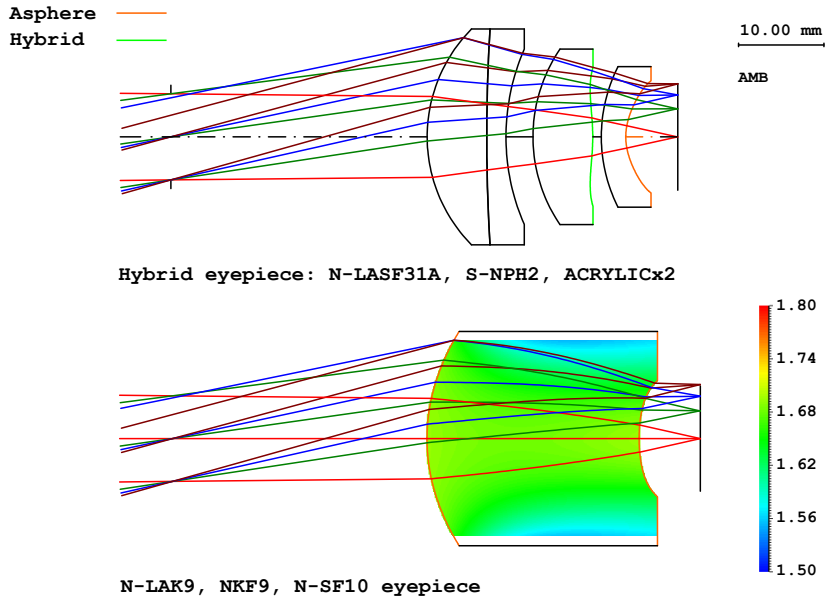
Figure 2.12: Cross sections of magnifier designs. Top, conventional design featuring a cemented doublet, an asphero-diffractive hybrid and an aspheric lens. Bottom, continuous GRIN magnifier composed of N-LAK9, N-KF9 and N-SF10.
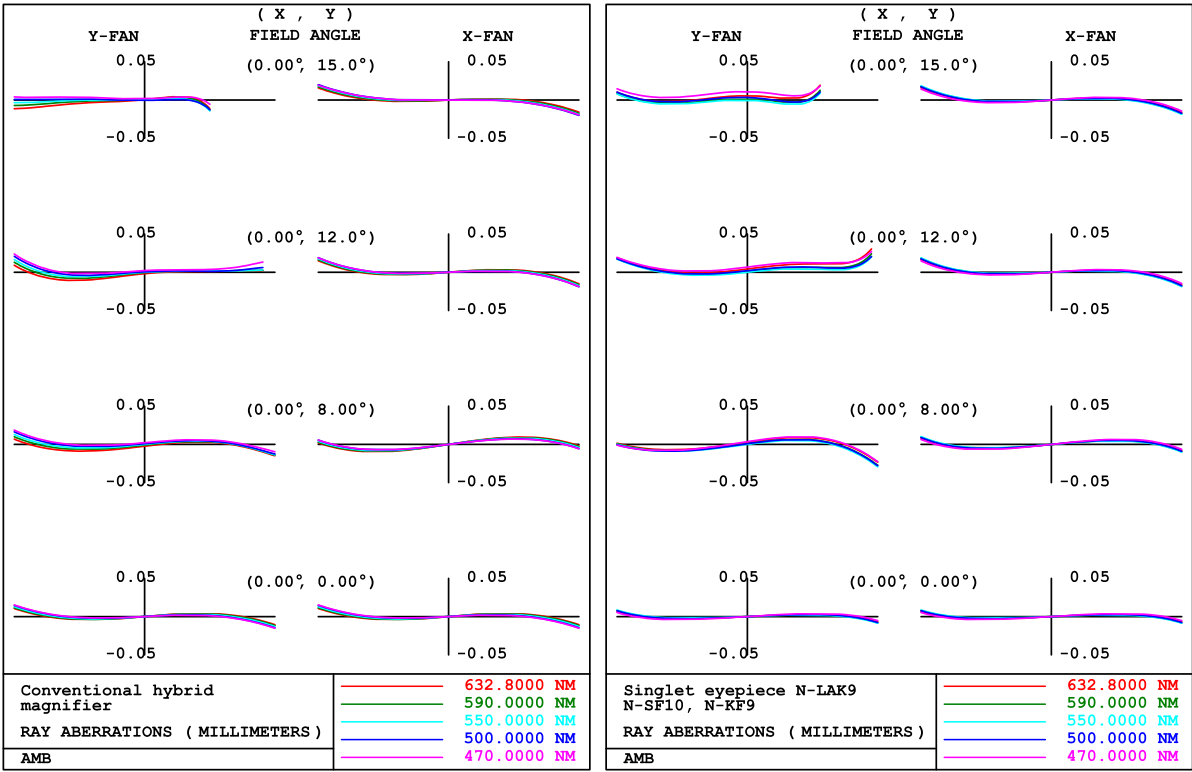
Figure 2.13: Magnifier design transverse ray error plots. Left, conventional asphero-hybrid design. Right, continuous GRIN design.

of the lens. This is typical of a magnifier construction, with strong positive power as close as possible to the entrance pupil and negative power near the image plane to flatten the field.
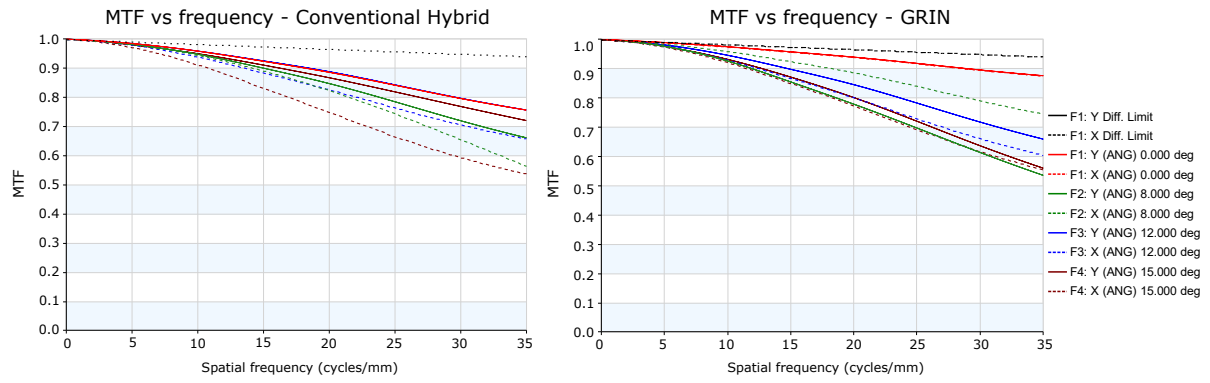
Figure 2.14: Magnifier design MTF vs. frequency plots. Left, conventional asphero-hybrid design. Right, continuous GRIN design.
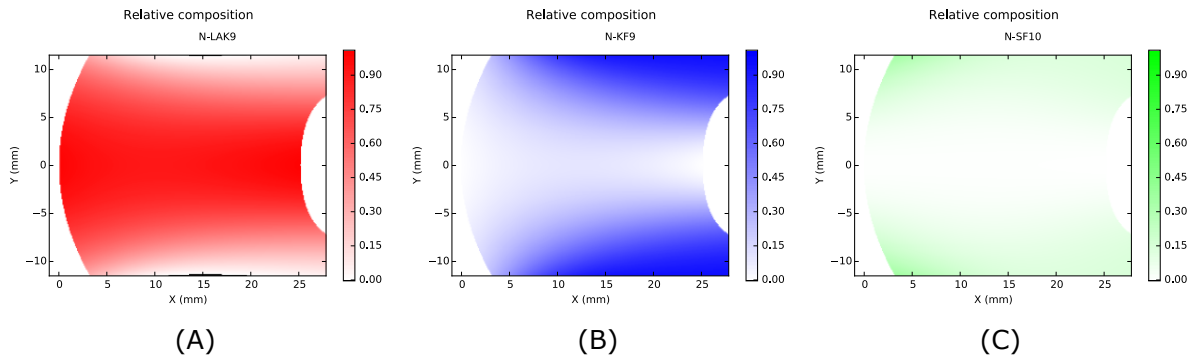
Figure 2.15: Relative composition plots by material for N-LAK9, N-SF10, N-KF9 singlet eyepiece design
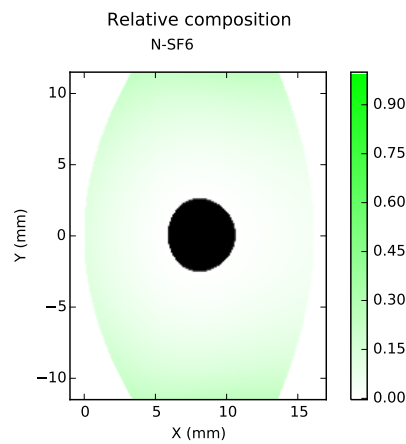
Figure 2.16: Example relative composition plot showing a compositional violation in black.

2.8. Conclusions

In this chapter we have demonstrated a mathematical representation for the optical design of GRIN media of multiple constituent materials. In particular we have shown an effective approach for combinations of three or more base materials. This representation is applied to optical design examples of radial and general rotationally symmetric GRIN lenses, however in principle this approach could be applied to any other GRIN distribution. We propose that such an approach is well suited to the design-for-manufacture of GRIN lenses made via additive manufacture or similar routes, as it is easy to link to commonly made effective medium theory approximations. Effective medium theories based on volumetric average permittivity and average index are addressed, as these are confirmed by the observations of two GRIN lens manufacturers.

When the assumption is made that the refractive index scales linearly with relative composition, it was demonstrated that it is possible to decompose the optical power of GRIN lenses into contributions from each underlying material, known as partial power. Through the use of partial power, we can solve for known material combinations via thin lens theory. This technique enables us to efficiently search for material combinations without the need for successive material substitution and optimisation via finite raytracing, using a figure of merit based on the residual chromatic aberrations and the RSS sum of optical powers. This search technique was used to select base materials for a range of optical designs ranging from two and three material radial GRIN singlets to general rotationally symmetric GRINs that show equivalent performance to multi-element homogeneous optical designs. In particular, a thick singlet magnifier design was generated based on a ternary blend of glass materials that showed superior performance to a four element magnifier design consisting of a cemented doublet, an acrylic asphero-hybrid and an acrylic asphere.

A key discussion point relating to this design concerns the selection of materials. The current material selection was based on glasses in the Schott catalogue, which combined to allow a GRIN that provides good colour correction with a small RSS sum of partial powers. This choice of materials was fictitious due to a lack of refractive index data for nanoparticle doped polymer materials available at the time of design. We note that a glass solution would have significantly higher density and would potentially undermine the SWAP-C benefits of a continuous GRIN. More recently however, the required level of index variation to produce this design has been demonstrated by NanoVox LLC [29] through the use of titania and zircona-based nanoparticle dopants into a polymer matrix.

An area of study that may demonstrate further benefits is to consider GRIN solutions consisting of two lens elements. The generation of an air gap in the centre of the optic offers potentially greater degrees of freedom for aberration correction and mass reduction, however it carries with it the trade-off of additional polishing and assembly operations, with the need for alignment of the lens elements introducing a potential performance penalty.

3

Paraxial Analysis and Reconstruction of Gradient-Index Lens Systems

The contents of this chapter are derived and expanded from *"Paraxial reconstruction: conversion of homogeneous lens forms to continuous gradient-index media - Applied Optics 63, 7252-7261 (2024)"* [1, AMBref].

3.1. Abstract

We present a technique for the optical design of generalised-distribution GRIN lenses. Multi-element homogeneous lens designs are reconstructed as single GRIN media via smoothing of the homogeneous lens paraxial ray paths. These continuous optical systems successfully replicate the first-order properties of their homogeneous parent lens systems and serve as starting points for further optimisation. When the technique is applied at several wavelengths, the chromatic aberration correction of the homogeneous parent lens is also converted. The paraxial reconstruction, finite-ray optimisation and evaluation of several lens designs is demonstrated.

3.2. Introduction

Several of the new GRIN manufacture methods described in Chapter 1 enable the manufacture of GRIN lenses of arbitrary refractive index distribution. Such manufacture approaches allow multiple lens components (and potentially entire optical assemblies) to consist of a single GRIN lens, where the optical work performed by several homogeneous optical surfaces is instead performed by a continuous GRIN medium. We refer to such optics as *Continuous Optical Systems*, abbreviated to COS herein. COS were first coined by Buchdahl [17] as an example of an optical system where the number of surfaces tends to infinity. However, an historical lack of suitable manufacture processes and computational power required for design optimisation means only a handful of published designs exist at the time of writing in 2024.

56

The combination of the degrees of freedom for aberration correction provided by GRIN optics, with scalable yet flexible additive manufacture, promises a new route to fabricate improved SWAP-C optics. The reduced need for custom tooling required by an additive approach may also enable reduced development cycle time to deployment and engineering non-recurring expenditure (NRE), significantly lowering the cost and time barriers to the use of bespoke optical systems in a range of applications. There is therefore a strong motivation to develop optical design tools for COS.

In the development of any optical product, the optical design process forms a substantial part of the engineering NRE. Optical design can be a challenging task, with significant skill required to optimise a design and ensure adequate performance while accounting for the effects of manufacturing tolerances. A key decision in the optical design process is the selection of a starting solution*, which due to the complexity and topology of optical design solution spaces has a very significant effect on the end solution that is reached by optimisation. The starting point, if chosen well, leads to a high performing and cost-effective final design over an efficient development time scale. Conversely, a poor starting solution may quickly lead to a poor local minimum after optimisation of the design, resulting in a poorer performing product and accruing significant extra cost over an extended production run.

Due to the relative novelty of generalised GRIN technology, few such starting solutions exist for COS, with the design landscape relatively unexplored. In addition, such lens optimisation problems have a very large number of complex degrees of freedom, accounting for the variation in refractive index coefficients at multiple powers of lens aperture as described in Equation 1.23. For more complex optical systems such as wide-angle lenses or telecentric relay lenses, manual construction of a starting solution by manipulation of GRIN coefficients becomes extremely difficult.

Our objective for this work is to devise a method to generate COS starting solutions derived from the optical constructions of homogeneous optical designs. Previous works in the literature have addressed the problem of reconstructing a GRIN lens from a conventional optic. In the field known as *transformation optics*, components such as homogeneous lenses are converted to GRIN media by a coordinate transformation of the lens geometry [48]. Given that Maxwell's equations are invariant under such a coordinate transformation, the compression or expansion of the space within an optical component yields a spatially varying (and anisotropic) permittivity and permeability. The magnetic and anisotropic contributions are often small and disregarded to yield a simpler all-dielectric solution (known as quasi transformation optics or qTO). Whilst this is a powerful technique, it is difficult to apply to multi-element lens systems, with the boundaries between lens elements leading to discontinuities in the resulting GRIN [45].

Several authors have addressed the inverse problem of refractive index distribution construction via a geometrical optics approach. Nemoto and Makimoto [79] first demonstrated a method to solve for a GRIN distribution given a known ray curve, noting that in such a case, numerous paraxially-equivalent index distributions exist for a single ray path. In 2022, Kochan et al. [80] demonstrated a method of reconstructing individual homogeneous surfaces as GRIN media, by use of a sigmoid function GRIN distribution. In 2023, Gomez-Correa et al. [81] demonstrated a means to solve for the GRIN distribution given a finite ray path, exploiting an invariant quantity that arises when Fermat's principle is solved via a Lagrangian approach. This invariant quantity was shown to enable analytical solutions to ray paths within

---

*See also Chapter 1.6 for a discussion of the importance of starting points.

spherical and cylindrical gradient-index media.

In this work, we present a method for the conversion of multi-element homogeneous lens systems to a single GRIN medium that serves as a starting solution for further finite-ray optimisation. We propose that the paths of two defining paraxial rays (non-degenerate in field and aperture) contain sufficient information to reconstruct the first-order optical properties of a homogeneous lens system as a COS.

3.3. Paraxial Raytracing in GRIN lenses

To achieve a GRIN reconstruction of a homogeneous lens design, we use paraxial raytracing. The paraxial approximation assumes that all rays in the system travel along a narrow, thread-like region about the optical axis, allowing us to substitute all trigonometric functions for the first-order terms in their series expansions. In the case of Snell's law we state

$$N \sin i \approx N i, \tag{3.1}$$

for an incidence angle i and refractive index, N. We also assume that the sagitta of a curved surface is negligible, as it is proportional to the square of the (assumed very small) lens aperture. In essence, the paraxial approximation simplifies finite raytracing of an optical system to a linear form, allowing significant insight into its properties. In addition to the first-order properties of an optical system, a paraxial raytrace of the axial marginal and full-field principal rays also contains sufficient information to calculate the third-order aberrations for both GRIN and homogeneous surfaces and media [77]. We define a paraxial COS in Figure 3.1. The quantity y represents the height of a paraxial ray. The quantity u represents the paraxial ray angle in the anti-clockwise trigonometric convention such that $u \approx \dot{y}$, where dotted quantities represent differentiation with respect to the optical axis, z. The optical system itself is represented by the green box labelled ABCD. Barred quantities are those associated with the paraxially traced full-field principal ray, whereas unbarred quantities are of the paraxial marginal ray. The subscripts O and I represent quantities in the object and image planes respectively.
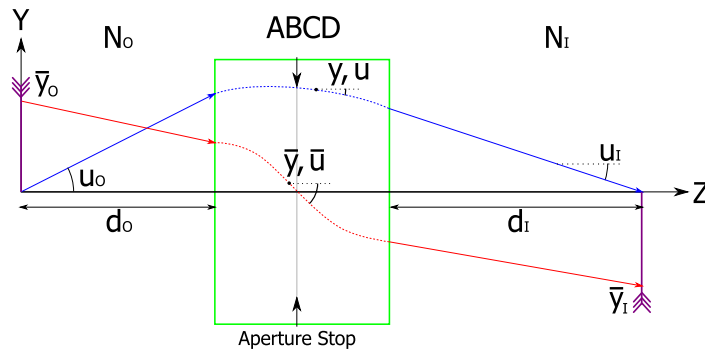
Figure 3.1: Schematic of a paraxial COS, ABCD. Rays traced are indicated in blue (marginal ray) and red (principal ray). barred quantities refer to the principal ray. The refractive index of the object and image spaces is indicated by N_O and N_i respectively. The aperture stop is labelled thus.

The linearisation of raytracing in the paraxial region allows us to represent the optical system as a 2x2 matrix that relates the height and optical direction cosine of a paraxial ray in the object space to the image space. In Equation 3.2, we represent the optical system of Figure 3.1 in this way, treating the object and image space conjugate distances, d_O and d_I, with respective homogeneous refractive indices, N_O and N_I, separately. We have

$$\begin{pmatrix} y_I \\ N_I u_I \end{pmatrix} = \begin{pmatrix} 1 & d_i/N_i \\ 0 & 1 \end{pmatrix} \begin{pmatrix} A & B \\ C & D \end{pmatrix} \begin{pmatrix} 1 & d_o/N_O \\ 0 & 1 \end{pmatrix} \begin{pmatrix} y_O \\ N_O u_O \end{pmatrix}, \tag{3.2}$$

where the quantities A,B,C,D fully characterise the first-order properties of the system. In particular, the quantity -C is equivalent to the focal power (the inverse of the focal length). It is also possible to break the ABCD matrix down into contributions from individual surfaces and ray transfer events between surfaces, representing the system as a product of elemental matrices. We assume a general-rotationally-symmetric GRIN distribution of the form defined in Equation 1.23. The equation of propagation for a GRIN paraxial ray in the plane $x = 0$ within such a GRIN is given by

$$2\mathcal{N}_2(z)y(z) - \frac{d}{dz}\left[\mathcal{N}_0(z)u(z)\right] = 0. \tag{3.3}$$

Equation 3.3 is derived in Appendix B.2. In the general-rotationally-symmetric case, the transfer matrix of a GRIN has no analytical solution [76]. The paraxial raytrace of the GRIN was therefore performed by slicing the COS into thin slices, as illustrated in Figure 3.2. Following the derivation of Sands [76], the ray path in a thin GRIN slice is then evaluated locally about a point, z, based on a Taylor series expansion of the $\mathcal{N}_0$ and $\mathcal{N}_2$ coefficients

$$\mathcal{N}_0(z + \delta z) = \mathcal{N}_0(z) + \dot{\mathcal{N}}_0(z)\delta z + \frac{1}{2}\ddot{\mathcal{N}}_0(z)\delta z^2 + \dots$$
$$\mathcal{N}_2(z + \delta z) = \mathcal{N}_2(z) + \dot{\mathcal{N}}_2(z)\delta z + \frac{1}{2}\ddot{\mathcal{N}}_2(z)\delta z^2 + \dots, \tag{3.4}$$

where δz is the small, finite thickness along the optical axis of an elemental GRIN located at z. We also expand the first and second terms of Equation 3.3 as a series

$$y(z + \delta z) = y(z) + u(z)\delta z + \frac{\dot{u}(z)}{2}\delta z^2 + \dots,$$

$$\mathcal{N}_0(z + \delta z)u(z + \delta z) = \mathcal{N}_0(z)u(z) + \frac{d}{dz}\left[\mathcal{N}_0(z)u(z)\right]\delta z + \frac{d^2}{dz^2}\frac{\left[\mathcal{N}_0(z)u(z)\right]}{2}\delta z^2 + \dots. \tag{3.5}$$
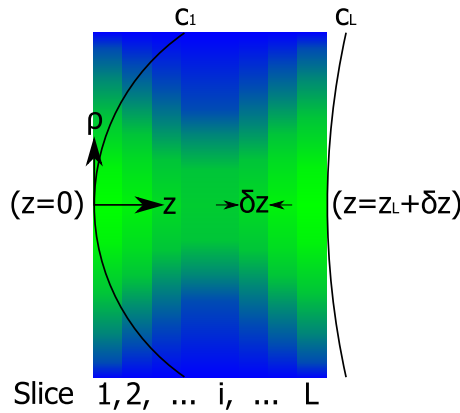
Figure 3.2: General-rotationally-symmetric GRIN decomposed into planar, thin, elemental GRINs of thickness δz.

The solution to the thin ray transfer matrix has the general form for the ith slice within the GRIN located at z_i

$$y(z_i + \delta z) = A_i y(z_i) + B_i \mathcal{N}_0(z_i) u(z_i),$$

$$\mathcal{N}_0(z_i + \delta z) u(z_i + \delta z) = C_i y(z_i) + D_i \mathcal{N}_0(z_i) u(z_i).$$

(3.6)

Our goal is therefore to express the equation for the ray trajectory in terms of $y(z)$ and $\mathcal{N}_0(z)u(z)$. To achieve this, we find expressions for $\dot{u}$, $d/dz(\mathcal{N}_0(z)u(z))$ and $d^2/dz^2(\mathcal{N}_0(z)u(z))$, which we substitute into Equation 3.5. Expanding Equation 3.3 yields

$$2\mathcal{N}_2(z)y(z) - \dot{u}(z)\mathcal{N}_0(z) - \dot{\mathcal{N}}_0(z)u(z) = 0,$$

(3.7)

which solved for $\dot{u}$ is

$$\dot{u} = \frac{2\mathcal{N}_2 y - \dot{\mathcal{N}}_0 u}{\mathcal{N}_0}.$$

(3.8)

We then substitute Equation 3.8 into Equation 3.5. We simplify the second derivative terms using Equation 3.3 by substituting $\frac{d}{dz}[\mathcal{N}_0(z)u(z)]$ for $2\mathcal{N}_2(z)y(z)$. This gives

$$y(z + \delta z) = y(z) + u(z)\delta z + \frac{\mathcal{N}_2 y - \frac{1}{2}\dot{\mathcal{N}}_0 u}{\mathcal{N}_0}\delta z^2 + \dots,$$

$$\mathcal{N}_0(z + \delta z)u(z + \delta z) = \mathcal{N}_0(z)u(z) + 2\mathcal{N}_2(z)y(z)\delta z + [\mathcal{N}_2(z)u(z) + \dot{\mathcal{N}}_2(z)y(z)]\delta z^2 + \dots.$$

(3.9)

Collecting terms in $\mathcal{N}_0(z)u(z)$ and $y(z)$ and expanding to the quadratic order then yields

$$y(z + \delta z) = \left[1 + \frac{\mathcal{N}_2(z_i)}{\mathcal{N}_0(z_i)}\delta z^2\right]y(z) + \left[\frac{\delta z}{\mathcal{N}_0(z_i)} - \frac{1}{2}\frac{\dot{\mathcal{N}}_0(z_i)}{\mathcal{N}_0(z_i)^2}\delta z^2\right]\mathcal{N}_0(z)u(z)$$

$$\mathcal{N}_0(z + \delta z)u(z + \delta z) = \left[2\mathcal{N}_2(z_i)\delta z + \dot{\mathcal{N}}_2(z_i)\delta z^2\right]y(z) + \left[1 + \frac{\mathcal{N}_2(z_i)}{\mathcal{N}_0(z_i)}\delta z^2\right]\mathcal{N}_0(z)u(z).$$

(3.10)

By inspection of Equation 3.6, it is clear that the square bracketed terms of Equation 3.10 correspond to A, B, C, and D of an elemental GRIN ray-transfer matrix to the quadratic order

$$A_i = 1 + \frac{\mathcal{N}_2(z_i)}{\mathcal{N}_0(z_i)}\delta z^2,$$

$$B_i = \frac{\delta z}{\mathcal{N}_0(z_i)} - \frac{1}{2}\frac{\dot{\mathcal{N}}_0(z_i)}{\mathcal{N}_0(z_i)^2}\delta z^2,$$

$$C_i = 2\mathcal{N}_2(z_i)\delta z + \dot{\mathcal{N}}_2(z_i)\delta z^2,$$

$$D_i = 1 + \frac{\mathcal{N}_2(z_i)}{\mathcal{N}_0(z_i)}\delta z^2.$$

(3.11)

The full system ABCD matrix (as per Equation 3.2) of the COS divided into L slices is given by

$$\begin{pmatrix} A & B \\ C & D \end{pmatrix} = \begin{pmatrix} 1 & 0 \\ c_L(N_I - \mathcal{N}_0(z_L)) & 1 \end{pmatrix} \prod_{i=0}^{L} \begin{pmatrix} A_i & B_i \\ C_i & D_i \end{pmatrix} \begin{pmatrix} 1 & 0 \\ c_1(\mathcal{N}_0(0) - N_O) & 1 \end{pmatrix},$$

(3.12)

where the leftmost and rightmost matrices are due to refraction across the optical surfaces at each end of the COS. As each internal elemental GRIN is planar (excluding the end surfaces), the surface refraction contribution is the identity matrix and is disregarded. The quantity $-C_i$ gives the focal power of a GRIN ray transfer matrix, yielding the well-known formula for the focal power of a thin, radial GRIN medium, $K_{\text{GRIN}} = -2\mathcal{N}_2\delta z_i$, for a GRIN of thickness, δz_i. From this, the distribution of $\mathcal{N}_2(z)$ can be intuitively interpreted as the *linear optical power density* of a COS.

The use of a numerical paraxial tracing approach means it is necessary to ensure that enough thin slices are used to avoid numerical errors in ray height and angle. Accuracy of the fit is diagnosed by calculating the determinant of the system ABCD matrix which should have negligible deviation from unity (in the Nu ray direction convention used), with the two mitigation options for insufficient accuracy being to add additional Taylor expansion terms or finer GRIN slices. Expansion of Equation 3.7 to the quadratic order in δz is generally sufficient. For the lens reconstructions in this work, L=2500 slices, which achieved a determinant error less than 10^{-6} in all cases.

3.3.1. Location of the Aperture Stop and Pupil Size

In order to define the Étendue and calculate the aberrations of a paraxial lens system, it is necessary to define or calculate (depending on design approach) a position along the optical axis as the aperture stop. Two conditions are met at the aperture stop. Firstly, the height of the paraxial full-field principal ray is zero, secondly, the clear semi-aperture of the stop is equal to the paraxial marginal ray height at the stop surface. Definition of the stop is partly dependent on how the designer chooses to set up the optical system. For example, the designer may define a specific stop location and diameter and solve for rays that satisfy the above conditions, or they may equally calculate the location and diameter of the stop based on a specific set of input rays. For simplicity, we shall assume that the designer wishes to define a), a fixed entrance pupil diameter b), a stop location on the optical axis and c), a fixed angular field of view.

As the height of the paraxial principal ray must be zero at the stop, this determines the ray-aiming of the paraxial principal ray in the object plane. If the field of the optic is defined as the object plane angle, then $N_O\bar{u}_O$ is constrained, meaning we must determine the principal ray height in the object plane, $\bar{y}_O$, that gives $\bar{y} = 0$ at the stop surface. To do this, we define a sub-matrix of the system, consisting of all surfaces from the object plane to the stop, where the ray vector of the full-field principal ray at the stop surface is given by

$$\begin{pmatrix} 0 \\ N_{\text{stop}}\bar{u}_{\text{stop}} \end{pmatrix} = \begin{pmatrix} A_{\text{stop}} & B_{\text{stop}} \\ C_{\text{stop}} & D_{\text{stop}} \end{pmatrix} \begin{pmatrix} 1 & d_O \\ 0 & 1 \end{pmatrix} \begin{pmatrix} \bar{y}_O \\ N_O\bar{u}_O \end{pmatrix}. \tag{3.13}$$

With a known value of $N_O\bar{u}_O$, this equation can be solved for the necessary value of $\bar{y}_O$ to intersect the centre of the stop

$$\bar{y}_O = \frac{-N_O\bar{u}_O\left(A_{\text{stop}}d_O + B_{\text{stop}}\right)}{A_{\text{stop}}}. \tag{3.14}$$

By rearrangement of Equation 3.14, we can also solve for the object space slope of the principal ray, $N_O\bar{u}_O$, when the principal ray height in the object plane, $\bar{y}_O$, is constrained.

Next, we must define the paraxial marginal ray based on the entrance pupil diameter. For a system with an object plane at infinity, this is a trivial calculation, as the value of $N_O u_O$ is

zero, and so $y_O = \text{EPD}/2$. For an entrance pupil at finite conjugates, we must determine the entrance pupil location, which we obtain by finding the point at which the paraxial principal ray crosses the optical axis, as given by

$$d_{\text{EP}} = \frac{-\bar{y}_O}{\bar{u}_O}. \tag{3.15}$$

For such a finite conjugate system, $y_O = 0$ and the paraxial marginal ray angle in object space is given by

$$u_O = \frac{\text{EPD}}{2d_{\text{EP}}}. \tag{3.16}$$

By similar logic, paraxial principal ray heights and angles can be determined for alternative field and pupil specifications in the image plane, such as paraxial image height or image F/#. The only prerequisite is that both the field and aperture of the system be defined in some way.

Once defined as shown in the preceding section, our paraxial COS can be considered a "template" from which we can reconstruct a parent system by finding appropriate values of c_1, c_L, $\mathcal{N}_0(z)$, and $\mathcal{N}_2(z)$.

3.4. Paraxial Reconstruction

Our approach shall be to identify a GRIN distribution in the form of Equation 1.23, such that the ABCD matrix of a conventional system is approximately replicated within the same axial length. To achieve a smooth GRIN distribution, we will convert the discrete and segmented trajectory of two paraxially traced rays (typically the axial marginal and full-field principal rays) within a homogeneous optical system to a smooth ray path indicative of a GRIN medium. An example of this ray smoothing concept is shown in Figure 3.3. From these smoothed and fitted rays, we then solve for the refractive index distribution. To avoid the requirement for a GRIN medium in the object and image space, we bound the GRIN region by the first and last surfaces of the optic.

Assuming the paraxial ray height $y(z)$ and its derivatives with respect to z are known from the reconstruction of the ray, we must devise a procedure to reconstruct the axial and parabolic radial GRIN coefficients, $\mathcal{N}_0(z)$ and $\mathcal{N}_2(z)$ at any point along the optical axis of the lens. Rearrangement of Equation 3.3 gives an expression for the value of $\mathcal{N}_2(z)$

$$\mathcal{N}_2(z) = \frac{\dot{u}(z)\mathcal{N}_0(z) + \dot{\mathcal{N}}_0(z)u(z)}{2y(z)}, \tag{3.17}$$

where from inspection, in addition to the ray paths, we must determine the values of $\mathcal{N}_0(z)$, and its derivative with respect to z, $\dot{\mathcal{N}}_0(z)$. To achieve this, we make use of the Lagrange invariant, a conserved quantity of any optical system loosely related to energy throughput. The Lagrange invariant is defined as

$$H = \mathcal{N}_0(z) \left[\bar{u}(z)y(z) - u(z)\bar{y}(z) \right], \tag{3.18}$$

where barred quantities refer to the full field principal ray. The numerical value of H is inherited from the paraxial rays of the parent homogeneous optical system. This, in combination with the reconstructed ray trajectories gives us sufficient information to calculate $\mathcal{N}_0(z)$ from Equation 3.18. $\dot{\mathcal{N}}_0(z)$ is determined by differentiation of the Lagrange invariant as

$$\dot{\mathcal{N}}_0(z) \left[\bar{u}(z)y(z) - u(z)\bar{y}(z) \right] + \mathcal{N}_0(z) \left[\dot{\bar{u}}(z)y(z) - \dot{u}(z)\bar{y}(z) \right] = 0. \tag{3.19}$$
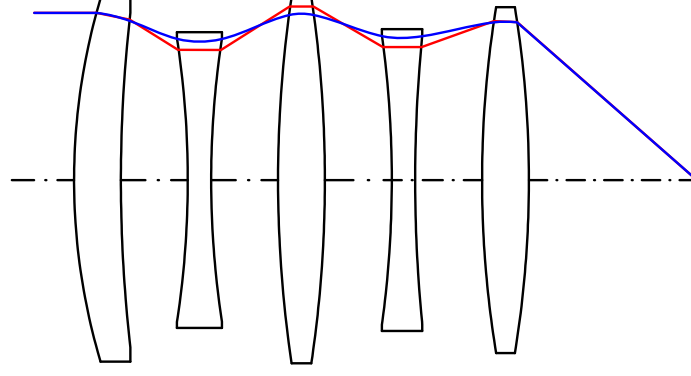
Figure 3.3: Reconstruction of a notional paraxial ray within a lens system (red lines, not to scale) to a continuously differentiable GRIN trajectory (blue dashed line). The ray positions and derivatives in both cases are matched at first and last surfaces of the lens system.

By rearranging Equations 3.18 and 3.19 we obtain the following expressions for $\mathcal{N}_0(z)$ and $\dot{\mathcal{N}}_0(z)$:

$$\mathcal{N}_0(z) = \frac{H}{\bar{u}(z)y(z) - u(z)\bar{y}(z)}, \tag{3.20}$$

$$\dot{\mathcal{N}}_0(z) = \frac{-\mathcal{N}_0^2(z)\left[\dot{\bar{u}}(z)y(z) - \dot{u}(z)\bar{y}(z)\right]}{H}. \tag{3.21}$$

Once $\mathcal{N}_0(z)$, $\dot{\mathcal{N}}_0(z)$, and the smoothed ray paths are known, we calculate $\mathcal{N}_2(z)$ from Equation 3.17 for each elemental GRIN slice within the COS.

3.5. Selection of a Mathematical Representation for Reconstructed Ray-paths

A key decision in paraxial reconstruction concerns selection of a tool for the smoothed ray fit. A number of candidate mathematical constructions were considered based on three key requirements:

- The fitted curve must match the position and slope of the discrete ray path at the endpoints to correctly account for refraction at the end surfaces. This condition ensures that the first-order properties will be accurately reconstructed.

- The curve must be smooth and continuous to at least the second derivative in z to avoid discontinuities in the distribution of $\mathcal{N}_2$.

- The fitted curve should not rely upon least-squares numerical fitting, which adds complexity to the process and does not guarantee a good fit can be found for more complex distributions of refractive index, being vulnerable to over-fitting effects such as Runge Phenomenon.

Bézier curves were identified as ideal candidates based on these criteria. Bézier curves are parametric polynomials in the Bernstein basis [82, chapter 1.3.4] that are widely used in

graphics and product design due to their user-friendly application and numerical stability. Bézier curves are defined by a set of control points, which in paraxial reconstruction are based on the paraxial ray paths of the parent system, allowing us to avoid numerical least-squares fitting routines. The polynomial order of a Bézier curve is equal to the number of control points minus one. The position and derivative of the curve endpoints are defined by the first and last control point segments, fulfilling the first criterion. A set of at least three control points yields a curve for which a second derivative exists that is continuous**. Furthermore, Bézier curves do not interpolate intermediate control points exactly, but approximate them with the property of *diminished variation*. This property minimises over-fitting effects and the resulting index gradients of the reconstruction. Further information on Bézier curves is provided in Appendix C.

3.6. Computational Implementation

The paraxial reconstruction approach was implemented using the Python programming language. Specifically, the "bezier" library[83] was used to model the Bézier curves required for reconstructing the rays, whilst elements of the "scipy" library [84] were used for various other aspects such as spline fitting the resulting index coefficient curves.

An example Double-Gauss lens from the CodeV software was used as a homogeneous "parent" lens system. Its basic optical properties are listed in Table 3.1. A raytrace cross section of this design is shown in Figure 3.4.

Parameter	Value
F/#	2.0
Focal Length	100 mm
Waveband†	486.1-656.3 nm
Back focal clearance	61.1 mm
Axial length	139 mm
Semi-field of view	14°

Table 3.1: Basic parameters for the parent Double-Gauss lens.
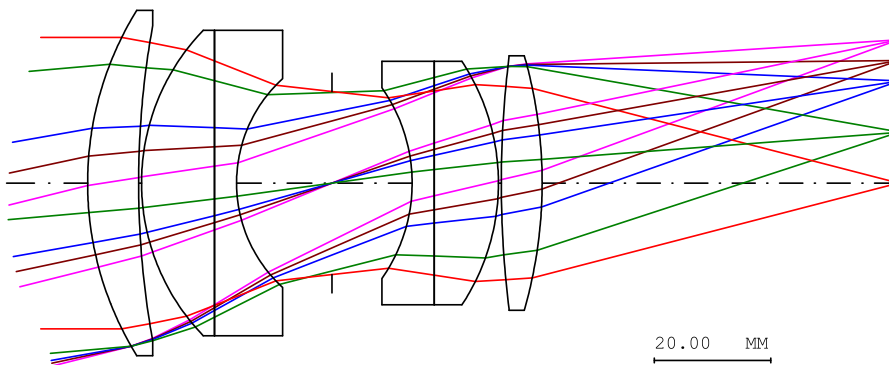
Figure 3.4: Finite raytrace of homogeneous parent Double-Gauss lens.

**A Bézier curve of only two points would define a straight line, which would not be able to represent the curved ray trajectories of a GRIN

†The paraxial reconstruction of this lens was carried out monochromatically at a wavelength of 587.6 nm.
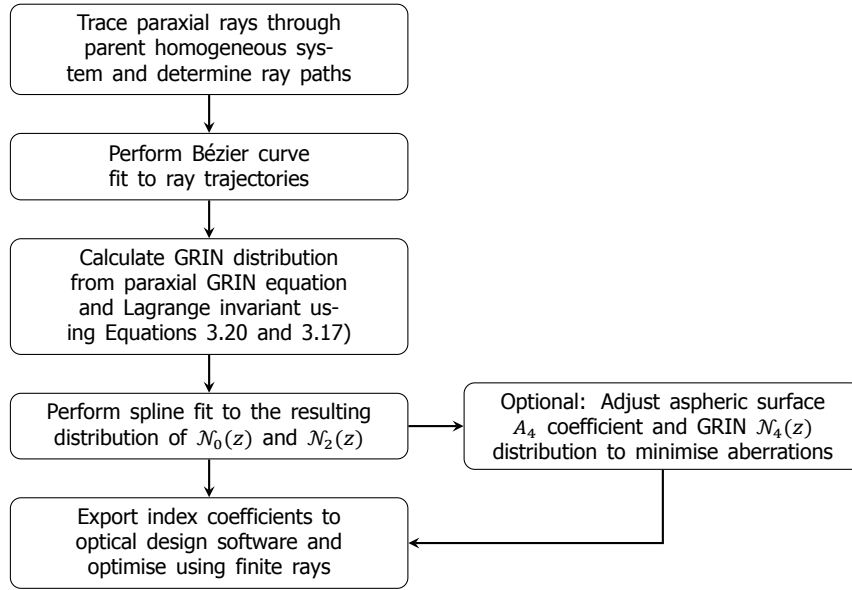
Figure 3.5: Flowchart for the paraxial reconstruction process

Paraxial reconstruction was implemented via the procedure summarised in Fig. 3.5. The discrete ray paths of the parent optical system were converted to piecewise linearly interpolated functions. Sets of evenly spaced control points were defined along each linearly interpolated ray path that define the Bézier curves. The closeness of the reconstructed ray paths to the parent rays is affected by the number of control points, which for the designs in this work was notionally set to twice the number of optical surfaces of the parent system. Increasing the number of control points results in reconstructed rays that more closely track the parent ray path. This increases the curvature of these rays, resulting in a greater magnitude of $\mathcal{N}_2$ and therefore increased index modulation in the reconstructed design. The choice of control points is therefore a trade-off between how precisely the paraxial GRIN rays track those of the parent solution, and reduction of index variation in the reconstructed design, which is worthy of investigation in further work. Note that the first-order properties of the design are unaffected by this choice, as the constrained ray slopes and positions at the endpoints of the lens determine this.

Following Bézier fits of the ray paths, these curves were input to Equations 3.7, 3.20, and 3.21. The output of these calculations was another set of curves defining $\mathcal{N}_0(z)$ and $\mathcal{N}_2(z)$. It was then necessary to further fit these curves in a form more amenable to optical design software. Whilst Bézier curves are an optimal mathematical form to reconstruct the ray path, the number of control points required depends on the number of lens elements in the parent system. Furthermore, the large number of control points invariably leads to a large number of refractive index coefficients required in optimisation, which slows the optimisation process of the finite-ray traced design. For this reason, a cubic spline fit was made to the reconstructed $\mathcal{N}_0(z)$ and $\mathcal{N}_2(z)$ distributions. The number of spline knots required depends on the complexity of the optical design being reconstructed, but is generally much smaller than the number of control points in the Bézier curves.

A further benefit of a spline-distributed GRIN lies in its ability to locally and stably control the axial distribution of GRIN coefficients. For polynomial GRIN distributions of a high degree in the optical axial coordinate, z, it is very difficult to locally control the GRIN distribution at the

65
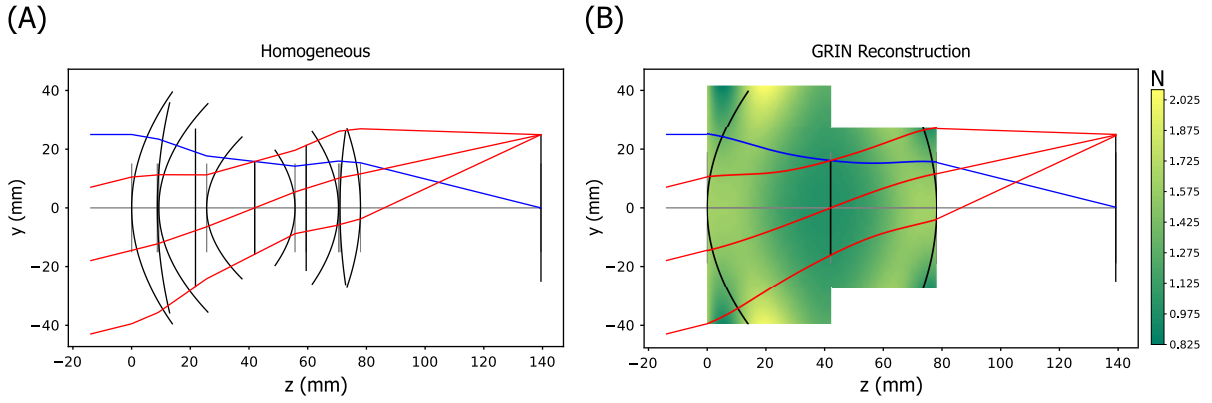
Figure 3.6: Left: paraxial raytrace of parent homogeneous system based on CodeV example F/2 Double-Gauss lens. Right: paraxial reconstruction raytrace of the same lens. The paraxial upper marginal ray is shown in blue. Full-field paraxial rays are show for the upper, centre (principal ray), and lower pupil in red.

far end of a thick GRIN lens, relying on the balancing of several polynomial terms. Whereas, for a spline GRIN, tactile and local adjustments can be made by changing only a single control point, leading to better conditioning of the finite ray optimisation problem.

An immediate question that follows the use of a secondary spline fit to the refractive index coefficients is: "why not use splines for the ray path fit?". While this is a valid technique, it suffers from worse over-fitting effects compared to Bézier curves, with much greater index variation in the fitted curves. Unlike Bézier curves, splines are not bounded by the convex hull of the control points, which means values of $\mathcal{N}_0(z) < 1.0$ can be formed in the fit. These are non-physical, cause raytrace errors in the reconstructed system, and importantly cannot be rectified by simply reducing the lens field or aperture. Using a Bézier fit followed by a secondary spline fit gives us the "best of both worlds", allowing us to start from the more optimal shape of the Bézier fit, but with the convenience of splines in optical design software.

A paraxial reconstruction example of the Double-Gauss lens is shown in Figure 3.6. The Bézier curve fits of the paraxial marginal and principal rays are shown in Figure 3.7. From these ray paths, $\mathcal{N}_0(z)$ and $\mathcal{N}_2(z)$ were calculated. These distributions are shown in Figure 3.8. It is observed that the axial refractive index distribution broadly follows that of the parent design, with $\mathcal{N}_0$ being close to 1 inside the central air gap of the Double-Gauss lens. Similarly, the $\mathcal{N}_2$ distribution correlates well with the expected distribution of optical power density (Note that linear optical power density is proportional to $-\mathcal{N}_2$). The regions at each end of the system contain positive optical power density, whereas the central region of the paraxial reconstruction contains negative power density. This leads to the familiar "hourglass" profile of the axial marginal ray we observe in the Double-Gauss solution. The focal length of the GRIN was 99.7 mm, a very close match to the parent design focal length of 100 mm. Spline fits to the reconstructed $\mathcal{N}_0(z)$ and $\mathcal{N}_2(z)$ distributions are also shown in Figure 3.8. $\mathcal{N}_0(z)$ shows the distribution of the axial refractive index, whilst $\mathcal{N}_2(z)$ is related to the distribution of linear optical power density, being related by the equation $dK/dz = -\mathcal{N}_2(z)$. A natural cubic spline fit with ten knots placed at the Chebyshev-Lobatto nodes provides a sufficiently accurate fit to these reconstructed distributions with minimal oscillations.
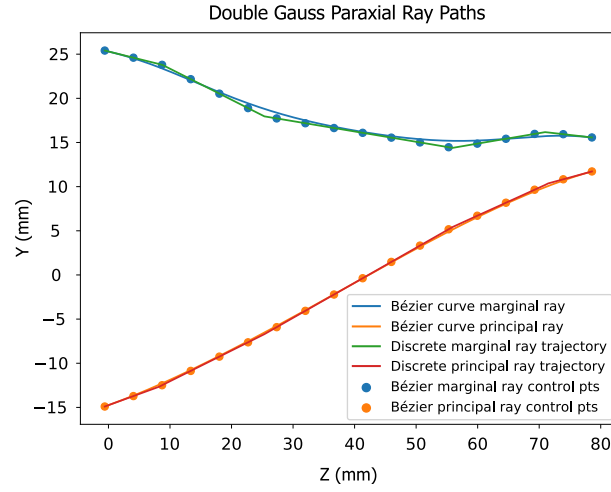
Figure 3.7: Homogeneous segmented ray paths, control points, and their Bézier reconstructions for the paraxial marginal and full field principal rays. Double Gauss F/2 example lens. Plot coordinate system origin sits at the lens front vertex.
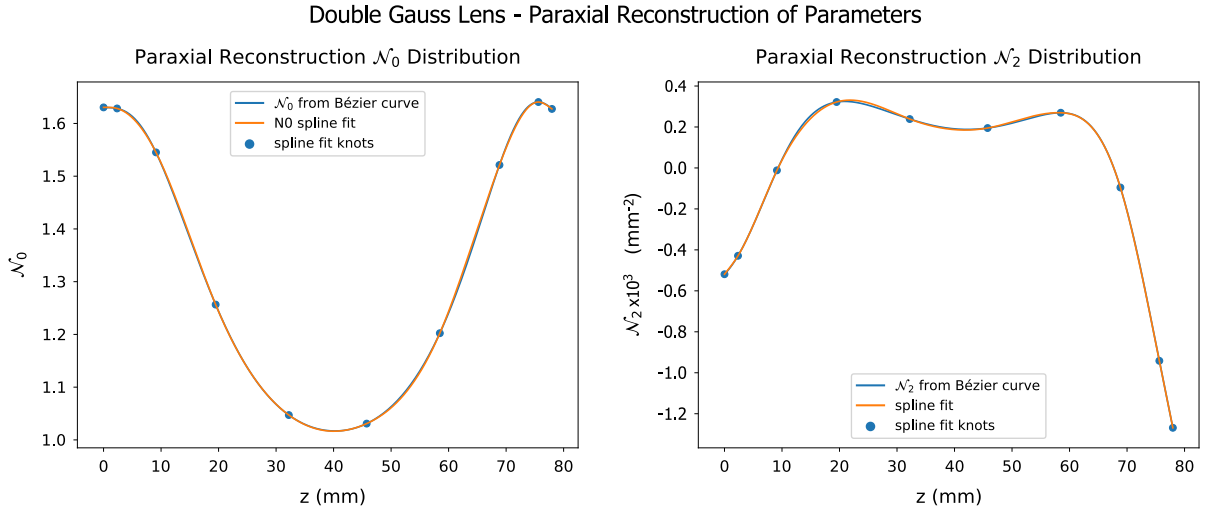
Figure 3.8: Reconstructed GRIN coefficients for the Double Gauss design example. Left: reconstructed distribution for the axial index, $\mathcal{N}_0$. Right: reconstructed distribution for the quadratic radial coefficient, $\mathcal{N}_2$.

3.6.1. Seidel Aberration Calculation

It is informative to calculate the Seidel aberrations of both the homogeneous parent and paraxially reconstructed designs. Paraxial reconstruction does not guarantee the resulting system will have equivalent third-order aberrations to the parent system. In addition to the standard Seidel aberration contributions of the refractive surfaces, GRIN lenses produce two additional Seidel contributions for each of the Seidel aberrations. These consist of an additional surface contribution, and also a *transfer* contribution generated as rays pass through the GRIN medium. For a COS, the magnitude of the transfer contributions can be very significant compared to the that of the optical surfaces.

In extreme cases, the Seidel aberrations of reconstructed designs may require some preliminary correction, if they are of a magnitude that seriously affects finite raytracing. Several authors have shown methods to calculate the Seidel coefficients of GRIN lenses [18, 77]. The calculation of aberrations of a COS is complicated by the varying index coefficients and ray heights and angles. We therefore outline a procedure by which they can be calculated.

The total aberrations of a COS for the nth Seidel coefficient are given by

$$\mathrm{Sn} = \mathrm{Sn}_{\mathrm{hom1}} + \mathrm{Sn}_{\mathrm{gs1}} + \mathrm{Sn}_{\mathrm{gt}} + \mathrm{Sn}_{\mathrm{homL}} + \mathrm{Sn}_{\mathrm{gsL}}. \tag{3.22}$$

The terms $\mathrm{Sn}_{\mathrm{hom1}}$ and $\mathrm{Sn}_{\mathrm{homL}}$ represent the homogeneous surface contributions of surfaces s1 and sL, which are equivalent in form to the Seidel aberration contributions of a homogeneous refractive lens, with the exception that we substitute the refractive index, N, of a homogeneous lens for the values of $\mathcal{N}_0(z)$ at the applicable lens surface. These homogeneous contributions, for a surface of radius of curvature c and refractive index N, are given by [50]

$$\mathrm{S1}_{\mathrm{hom}} = -A^2 H \Delta \left(\frac{u}{N} \right)$$

$$\mathrm{S2}_{\mathrm{hom}} = \frac{\bar{A}}{A} \mathrm{S1}_{\mathrm{hom}}$$

$$\mathrm{S3}_{\mathrm{hom}} = \frac{\bar{A}}{A} \mathrm{S2}_{\mathrm{hom}} \tag{3.23}$$

$$\mathrm{S4}_{\mathrm{hom}} = -H^2 c \Delta \left(\frac{1}{N} \right),$$

$$\mathrm{S5}_{\mathrm{hom}} = \frac{\bar{A}}{A} \mathrm{S3}_{\mathrm{hom}} + \frac{\bar{A}}{A} \mathrm{S4}_{\mathrm{hom}}.$$

Δ indicates the change in a quantity after refraction at the surface. The quantities A and $\bar{A}$ are known as the refraction invariants for the marginal and principal rays respectively. These are given by

$$A = N \left(yc + u \right) = Ni$$
$$\bar{A} = N \left(\bar{y}c + \bar{u} \right) = Ni, \tag{3.24}$$

where i represents the angle of incidence as stipulated in Equation 3.1. The terms of Equation 3.22, $\mathrm{Sn}_{\mathrm{gs1}}$ and $\mathrm{Sn}_{\mathrm{gsL}}$, represent the GRIN surface contributions, and $\mathrm{Sn}_{\mathrm{gt}}$ represents the

GRIN transfer contribution. Following Sands [18], the surface contributions are influenced by both $\mathcal{N}_0$ and $\mathcal{N}_2$ at the corresponding lens surface

$$
\begin{aligned}
\text{S1}_{\text{gs}} &= \kappa y^4 \\
\text{S2}_{\text{gs}} &= \kappa y^3 \bar{y} \\
\text{S3}_{\text{gs}} &= \kappa y^2 \bar{y}^2 \\
\text{S5}_{\text{gs}} &= \kappa y \bar{y}^3
\end{aligned}
\tag{3.25}
$$

where the factor κ is due to the axial and radial index gradients at the surface vertex.

$$
\kappa = -c\Delta \left(2\mathcal{N}_2 + \frac{1}{2}c\dot{\mathcal{N}_0} \right).
\tag{3.26}
$$

Note that the GRIN surface contributions do not affect S4. Monochromatically, the GRIN surface contributions have equivalent dependency on the paraxial ray heights and angles to those contributions generated by an aspheric surface. A subtle difference between GRIN and aspheric surface contributions however, is that the chromatic variation of the aberrations generated can differ if the GRIN has a different V_{GRIN} compared to the homogeneous case. More significantly, the aberrations induced at the surface of a GRIN are proportional to curvature. A planar surface does not have third-order GRIN surface aberration contributions.

Sands [18] produced a set of integrals for the calculation of the GRIN transfer contributions to the Seidel aberrations of general-rotationally-symmetric GRIN media. These depend on the distributions of $\mathcal{N}_0(z)$, $\mathcal{N}_2(z)$, and $\mathcal{N}_4(z)$ within the lens[‡] and are given by

$$
\text{S1}_{\text{gt}} = \frac{1}{2}\Delta\left[\mathcal{N}_0 y u^3\right] + \int_0^{z_L} \left[4\mathcal{N}_4 y^4 + 2\mathcal{N}_2 y^2 u^2 - \frac{1}{2}\mathcal{N}_0 u^4 \right] dz
$$

$$
\text{S2}_{\text{gt}} = \frac{1}{2}\Delta\left[\mathcal{N}_0 y u^2 \bar{u}\right] + \int_0^{z_L} \left[4\mathcal{N}_4 y^3 \bar{y} + \mathcal{N}_2 y u \left(y\bar{u} + \bar{y}u \right) - \frac{1}{2}\mathcal{N}_0 u^3 \bar{u} \right] dz
$$

$$
\text{S3}_{\text{gt}} = \frac{1}{2}\Delta\left[\mathcal{N}_0 y u \bar{u}^2\right] + \int_0^{z_L} \left[4\mathcal{N}_4 y^2 \bar{y}^2 + 2\mathcal{N}_2 y\bar{y}u\bar{u} - \frac{1}{2}\mathcal{N}_0 u^2 \bar{u}^2 \right] dz
\tag{3.27}
$$

$$
\text{S4}_{\text{gt}} = H^2 \int_0^{z_L} \left[\frac{\mathcal{N}_2}{\mathcal{N}_0^2} \right] dz
$$

$$
\text{S5}_{\text{gt}} = \frac{1}{2}\Delta\left[\mathcal{N}_0 y \bar{u}^3\right] + \int_0^{z_L} \left[4\mathcal{N}_4 y \bar{y}^3 + \mathcal{N}_2 \bar{y}\bar{u} \left(y\bar{u} + \bar{y}u \right) - \frac{1}{2}\mathcal{N}_0 u\bar{u}^3 \right] dz,
$$

where H is the Lagrange invariant. These integrals must be integrated numerically over the thickness of the GRIN lens, which we perform via the trapezium rule, using the ray heights and angles at z and $z + \delta z$ for each of the thin, elemental GRIN slices of thickness δz to define trapezia. The contributions for each elemental GRIN are then summed over the thickness of the COS.

To allow for a more meaningful comparison of the aberrations between GRIN and homogeneous systems in this work, we show the *cumulative* Seidel aberrations of the system,

---

[‡]$\mathcal{N}_4(z)$ is initially set to zero during the reconstruction process, $\mathcal{N}_4$ terms are shown in Equation 3.27 for completeness

illustrating the ebb and flow of the aberrations as influenced by the construction of a given optic. Cumulative aberrations are calculated for a given surface by a sum of the aberration contributions of that surface with those of all preceding surfaces in the system. For the GRIN transfer contributions, cumulative contributions are calculated by performing the integrals of Equation 3.27 from $z = 0$ to an intermediate point, z, within the lens. The Seidel aberration contributions of both the homogeneous Double Gauss and COS reconstruction are shown in Figure 3.9. It is observed that while the cumulative distribution of the Seidel aberrations bears some similarity between the homogeneous and COS paraxial reconstruction, there is a gradual divergence of aberrations for the COS solution which results in significant Seidel contributions at the image plane. Whether this is problematic for use of the paraxial reconstruction as an optimisation starting point depends on the aperture, field and total amount of aberration, but it is sometimes useful to control the Seidel aberrations of the starting point to allow finite ray tracing for optimisation. Generally, reconstructed lens systems can be brought out of ray-failure by reduction of the field and aperture until they trace successfully, with the aperture and field restored by gradually increasing them with successive optimisations. Pre-correction of the Seidels is useful in cases where a particularly severe reduction in field and aperture is required that could result in a significant change to the lens construction when optimised to recover the field and aperture (such as very wide-angle lens systems that require significant barrel distortion to raytrace successfully).

If control of the third-order aberrations is required, then additional degrees of freedom are available to the designer prior to optimisation with finite rays. Firstly, aspheric surface terms can be applied to compensate for surface GRIN contributions. Secondly, the quartic GRIN coefficient, $\mathcal{N}_4(z)$ can be used to control aberrations.

There are two options for controlling GRIN surface aberration contributions. Firstly to constrain the gradient of the axial index distribution to zero at the lens vertices, and secondly to introduce A_4 aspheric surface coefficients (as defined in Equation 1.4) to correct the aberrations induced by the index gradient (only the fourth order of an asphere or conic surface is meaningful in Seidel aberration calculation). In this work we have adopted the latter approach to avoid further complicating the paraxial reconstruction approach. Such aspheric surfaces can be retained in the final design (as many modern GRIN processes yield materials that are amenable to the production of aspheric surfaces via diamond turning), or progressively optimised out of the system by use of a weighted constraint that pushes the A_4 aspheric coefficient towards zero.

From Sands [18][Equations 31-32] we note that the surface contributions of a generalised GRIN lens have equivalent dependency on the incident ray heights and angles to a fourth-order aspheric term. We therefore define a value of the fourth-order aspheric term, A_4, as per Equation 1.4, that causes the GRIN surface Seidel contributions to be equal and opposite to the surface aspheric Seidel contributions. When this condition is satisfied, the end surfaces of the paraxial reconstruction have equivalent aberration contributions to the parent system. The value of A_4 with GRIN-equivalent surface aberration is given by

$$A_4 = \frac{\kappa}{4\Delta\mathcal{N}_0}. \tag{3.28}$$

Control of the GRIN medium contributions (with the exception of S4) can be achieved by numerical optimisation of the $\mathcal{N}_4(z)$ spline coefficients. This can be performed without repeated tracing of the GRIN paraxial reconstruction, as the $\mathcal{N}_4(z)$ coefficients do not affect the paraxial ray trace.
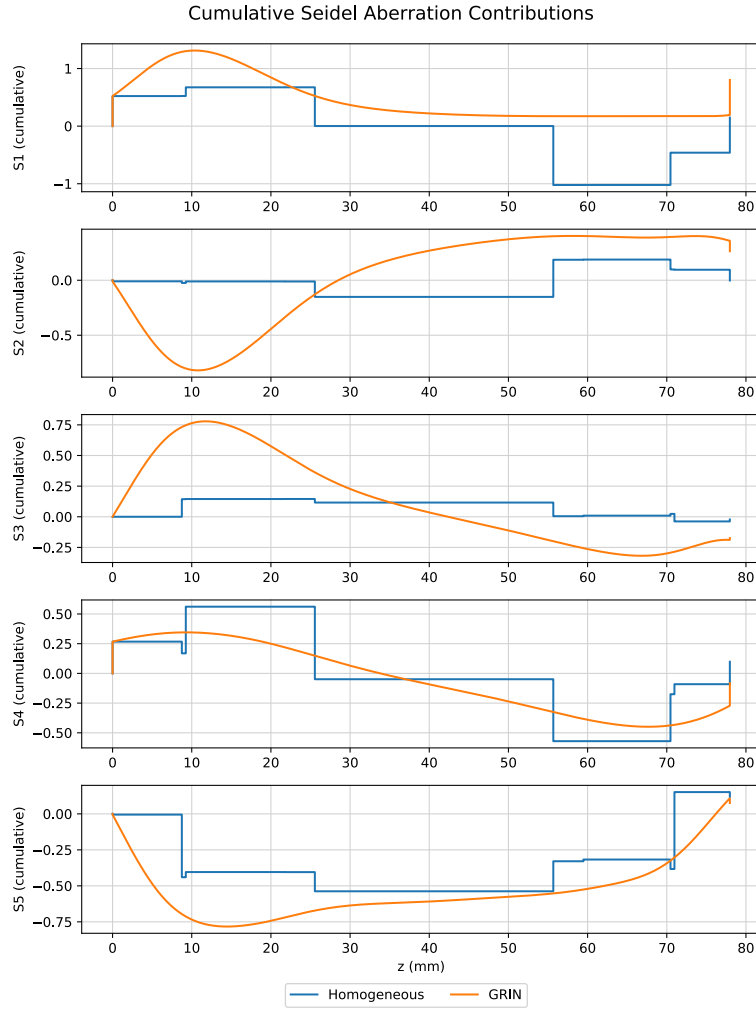
Figure 3.9: Cumulative Seidel aberration contributions for the F/2 Double-Gauss lens (blue) and its COS paraxial reconstruction (orange). S1-5 represent the usual Seidel aberration coefficients of spherical aberration, coma, astigmatism, Petzval curvature and distortion. The discontinuous changes in cumulative aberration are caused by the discrete Seidel contributions of optical surfaces.

71
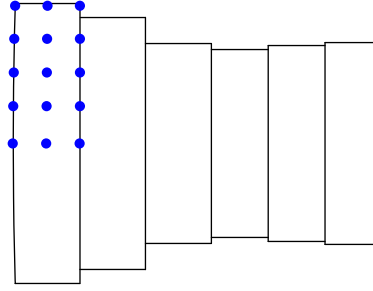
Figure 3.10: Illustrated 3x5 grid of control points assigned over the first of six sub-elements of a rotationally symmetric GRIN lens.

3.6.2. Lens Optimisation and Analysis

Once the paraxial reconstruction process was completed, the model was exported as a CodeV command sequence file. It was necessary to produce custom raytracing DLLs to enable tracing of a general GRIN distribution in the CodeV optical design software. These DLLs take the defined $\mathcal{N}_n$ coefficients of the optical model and return refractive index and its derivative in x, y, and z for a given point within the lens. Additionally, coefficients for the sixth and eighth power of ρ, $\mathcal{N}_6(z)$ and $\mathcal{N}_8(z)$, were added to allow for optimisation and control of higher-order aberrations. Raytracing DLLs for a spline-based GRIN distribution were written and compiled from source code in the C programming language.

The resulting paraxially reconstructed double Gauss starting point was optimised in CodeV using the damped-least-squares "AUT" option. Overarching constraints on the refractive index limits were imposed by first slicing the GRIN into six sub-lenses, then calculating the minimum and maximum refractive index over a grid of points as illustrated in Figure 3.10. Segmenting the GRIN in this way allows us to avoid over-estimating the clear aperture of the lens (and therefore over-constraining the GRIN distribution) in the central "bottleneck" of the design. Care must be taken to ensure the grid is sufficiently dense to capture local variation (in this case 11x11 points over the lens aperture). For this example, the refractive index was constrained to lie between 1.4 and 1.75. These limits are not indicative of current manufacture technology, rather, they are chosen constraints to demonstrate the paraxial reconstruction method. The curvature of the rearmost surface was constrained to be convex to preserve back focal clearance (a typical space envelope constraint for photographic lenses). The Back focal distance was kept identical to the homogeneous parent solution.

The lens was optimised in stages, with only the $\mathcal{N}_2$ terms made variable at first. The $\mathcal{N}_0$, $\mathcal{N}_4$ and higher-order radial terms were varied progressively after the lens was allowed to optimise to the local minimum for each order. Introducing too many variables too soon tended to lead to poor local minima. A raytrace cross-section is shown in Figure 3.11 with overlaid GRIN distribution.

The RMS spot size (at 587 nm wavelength) of the GRIN solution was smaller than that of the homogeneous lens, which is shown for reference in Table. 3.2, however one must consider with caution that making a direct comparison of performance is not a fair test, as the parent design was corrected for chromatic aberrations, and was presumed to be optimised accordingly, while the GRIN was not.

72
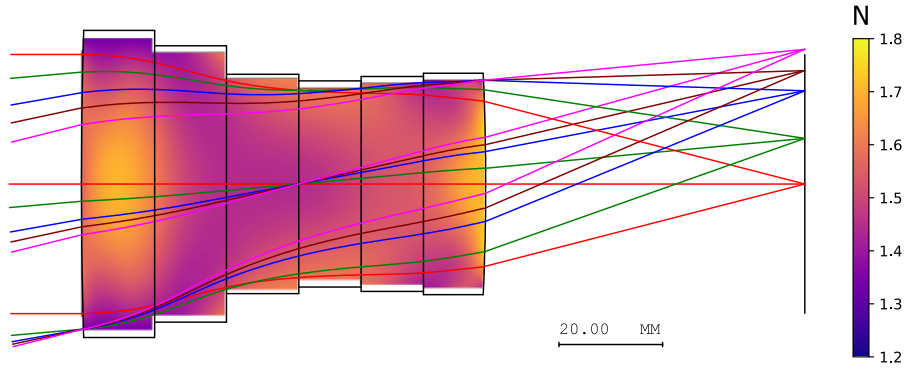
Figure 3.11: Finite raytrace of optimised COS from paraxially reconstructed starting point.

Field (°)	Homogeneous RMS Spot size (μm)	GRIN RMS Spot size (μm)
0.0	26.4	7.6
10.0	29.8	11.0
14.0	42.6	17.3

Table 3.2: RMS spot size over field for homogeneous and GRIN reconstructed-optimised Double Gauss solutions.

3.7. Further Examples

To reduce the risk of fitting the paraxial reconstruction method to a specific problem, the approach was applied to a wider range of design examples. These systems were selected to represent some of the diversity of common imaging lens systems. Paraxial reconstructions of these solutions are shown in Figure 3.12. Good fidelity of the reconstructed focal length is observed for all designs with error in the focal length within 5% in all cases (see Table 3.3). It is noted that some designs incur negative refractive index around the lens edges. This is generally due to rays in the paraxial region significantly exceeding the ray heights of the finite ray design. This is due to vignetting factors in other design examples such as the previous double-Gauss lens and the 300 mm telephoto design of Figure 3.12. A further example of a fisheye lens (not shown) produced very negative refractive indices, as the extreme barrel distortion of such a lens is not observed in paraxial rays. These low index regions are broadly resolved on a return to finite raytracing with appropriate vignetting factors and distortion, and can be further mitigated by temporarily reducing field and aperture if they persist.

Lens	Nominal Focal Length (mm)	Reconstructed Focal Length (mm)
Zeiss Sonnar	49.82	50.60
Telephoto Lens	295.04	304.88
Eyepiece (Warmisham)	25.05	25.15

Table 3.3: Focal lengths of further parent and reconstructed design examples.

Zeiss Sonnar
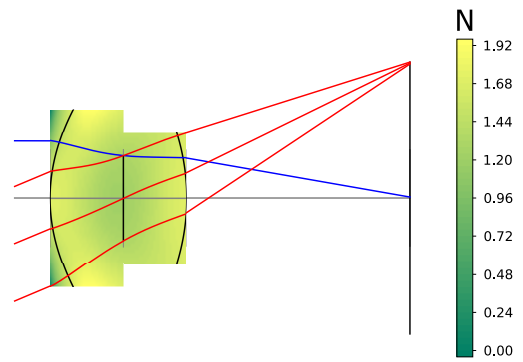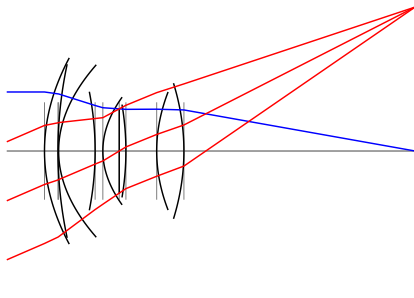
Telephoto lens - 300mm
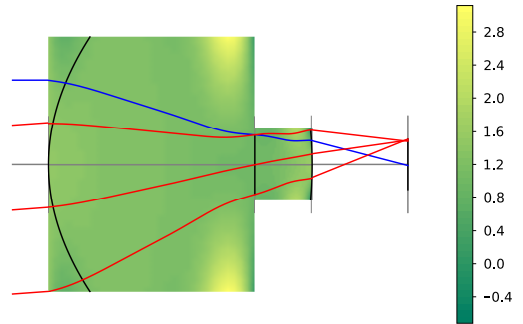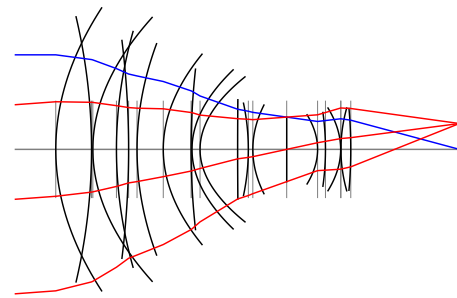
Eyepiece - Warmisham
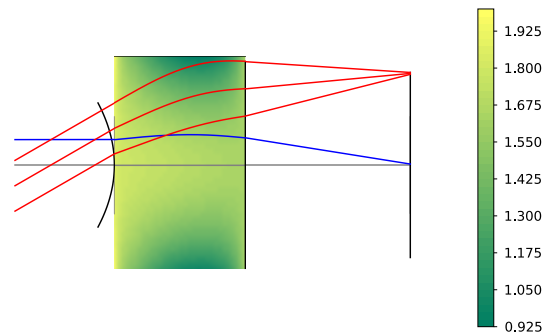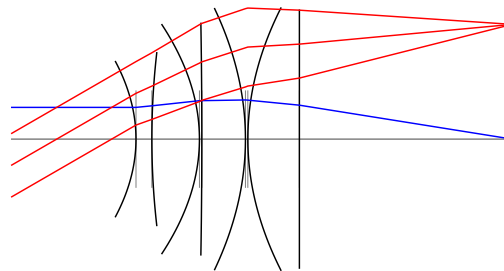
Figure 3.12: Paraxial reconstructions of additional lens designs.

3.8. Further Worked Example - Lithographic Lens Design

We demonstrate the strength of paraxial construction as a method of starting point generation by conversion of a complex lithographic lens design [85]. Such lens designs feature large numbers of lens elements of modest optical power and produce ray structures that closely resemble the curved ray trajectories of a GRIN. A fourteen-element stepper lens of NA=0.2, 589 nm reference wavelength, and 50 mm image diameter at -1 magnification was paraxially reconstructed as a GRIN (see Figure 3.13 top). Paraxial traces of the homogeneous parent system and paraxial reconstruction are illustrated in Figure 3.14. Strong left-right symmetry is observed about the aperture stop surface in both the parent and reconstructed solutions. Distortion and telecentricity of such optical systems are of paramount importance to the lithographic process. The paraxial reconstruction approach maintains the telecentric entrance and exit pupil locations with a strong degree of fidelity, with both the entrance and exit pupils located over 50 metres from the lens vertices.

The reconstructed system was then optimised in CodeV. To maintain low distortion and to guide the optimisation away from poor local minima, bilateral symmetry about a plane through the aperture stop was initially forced into the design optimisation. This was achieved by constraining variables each side of the stop to have equivalent values. This has the additional benefit of reducing the size of the optimisation problem by halving the number of variable coefficients. The GRIN distribution consisted of 20 spline knots as illustrated in Figure 3.15, with individual knots placed at the Chebyshev-Lobatto nodes (this particular distribution of knots being more concentrated at the ends of the GRIN where more structure exists in the distribution). As was the case for the previous Double Gauss example, initial optimisation runs allowed only the $\mathcal{N}_0$ and $\mathcal{N}_2$ coefficients to vary to avoid poor local minima, with the exception of $\mathcal{N}_4$ coefficients closest to the aperture stop to control spherical aberration. Once the optimisation had converged for these lower order coefficients, higher-order coefficients were gradually made variable. The resulting design is shown in Figure 3.13 (bottom). Distortion, telecentricity error (defined as the principal ray incidence angle at the image plane), RMS spot size, and RMS wavefront error are all comparable to the parent solution, as listed in Table 3.4.

Image Height (mm)	Hom. Telecentricity (°)	Hom. RMS Spot Size (µm)	Hom. RMS Wavefront Error (Waves at 589 nm)	Hom. Distortion (%)
0.0	0.0000	0.309	0.0056	0.0000
5.0	0.0705	0.303	0.0096	-0.0328
10.0	0.1243	0.939	0.0328	-0.0290
17.5	0.1347	1.688	0.0780	-0.0180
25.0	0.0018	1.743	0.0432	0.0000
Image Height (mm)	GRIN Telecentrity (°)	GRIN RMS Spot Size (µm)	GRIN RMS Wavefront Error (Waves at 589 nm)	GRIN Distortion (%)
0.0	0.0	0.271	0.0063	0.0000
5.0	0.0799	0.306	0.0066	-0.0237
10.0	0.1351	0.455	0.0088	-0.0199
17.5	0.1134	0.984	0.0290	-0.0089
25.0	0.1271	1.819	0.0450	-0.0091

Table 3.4: Telecentricity, RMS spot size, and RMS wavefront error with image height for the optimised paraxially reconstructed GRIN and homogeneous parent solution

The cumulative Seidel aberration contributions of the parent and reconstructed starting system are shown in Figure 3.16. Spherical aberration is not corrected by the reconstruction approach but can be corrected in near isolation by changing the $\mathcal{N}_4$ coefficient spline knot close

75
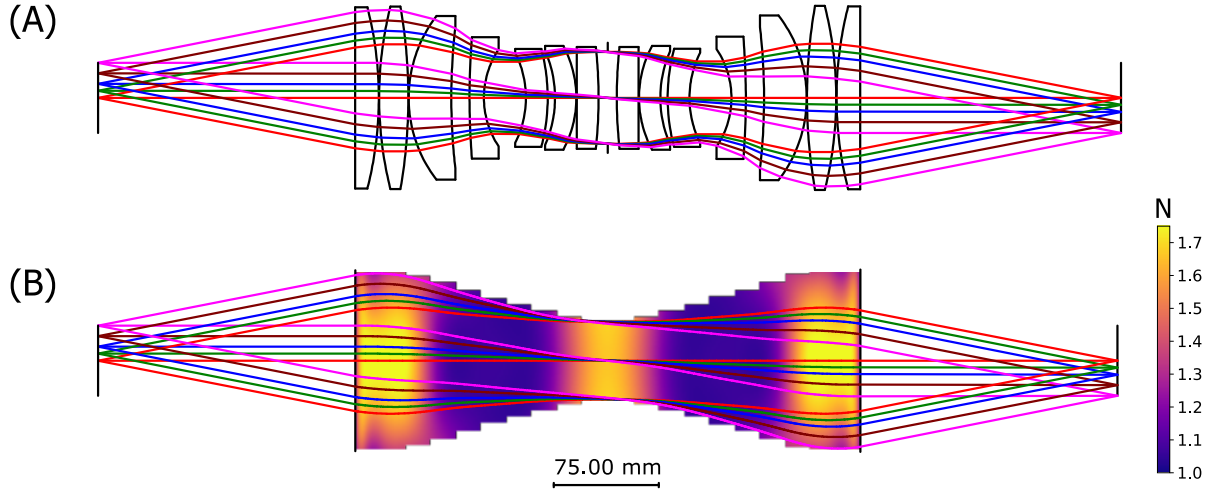
Figure 3.13: Finite ray trace of parent homogeneous lithographic lens (A) and optimised COS solution from parax-ially reconstructed starting point, with overlaid GRIN distribution (B).
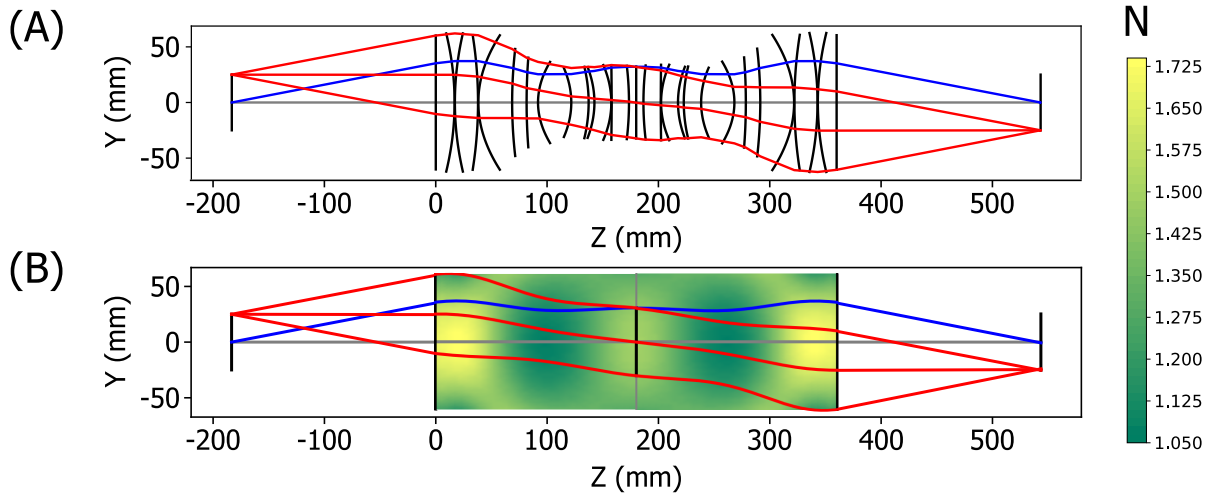
Figure 3.14: Paraxial trace of lithographic lens (A) and GRIN paraxial reconstruction (B).
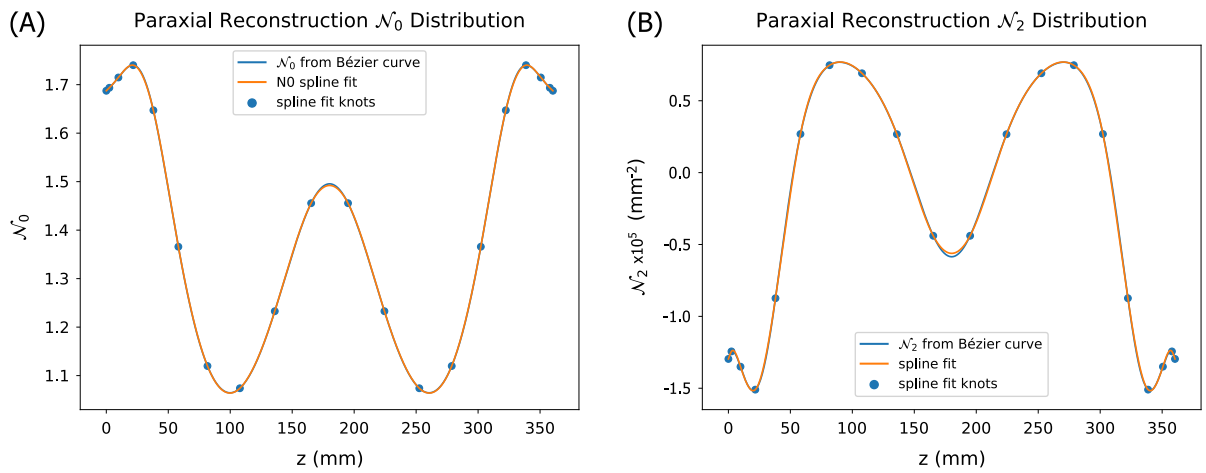
Figure 3.15: Lithographic lens paraxial reconstruction outputs. (A): $\mathcal{N}_0$ distribution and associated spline fit. (B): $\mathcal{N}_2$ distribution and associated spline fit.
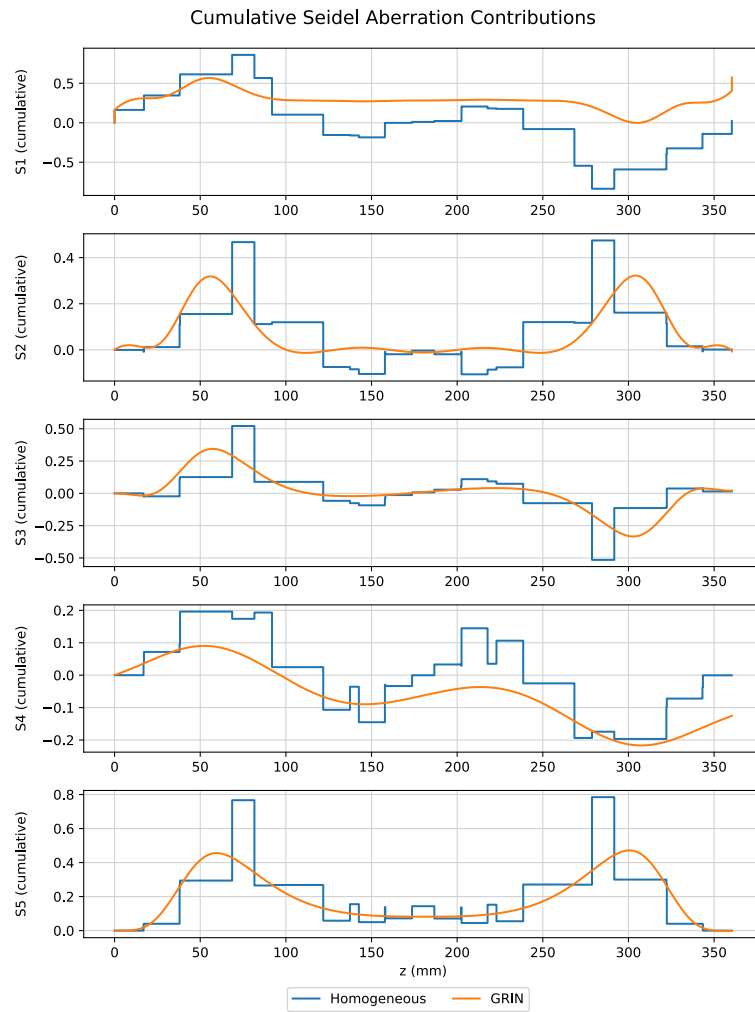
Figure 3.16: Cumulative Seidel aberrations of the paraxially reconstructed lithographic lens (orange series) and homogeneous parent design (blue series).

to the aperture stop of the system. Coma and distortion are well corrected by the symmetry of the lens. Astigmatism is also corrected in each half of the lens, although the causal mechanism (if any) is not currently known as symmetry alone does not guarantee astigmatism correction in a lens. Petzval curvature is observed to gradually diverge from the homogeneous solution, despite a very similar power construction. This is due to a fundamental difference in aberration theory between powered GRIN media and refractive homogeneous lenses [77]. In Equation 3.29 we note that for a thin, radial GRIN medium, Petzval curvature is proportional to power divided by the square of the axial index $\mathcal{N}_0$, whereas for homogeneous lenses the dependency is optical power divided by the lens refractive index.

$$S4_{\text{GRIN}} = -H^2 \frac{K_{\text{GRIN}}}{\mathcal{N}_0^2}$$

$$S4_{\text{hom}} = -H^2 \frac{K_{\text{lens}}}{N_{\text{lens}}}.$$

(3.29)

The result of this difference in aberration theory is a change in the power construction of the GRIN solution following optimisation of the paraxially reconstructed starting point. On visual inspection of Figure 3.13, it is observed that the ray paths of the homogeneous solution show three "bulges" where ray heights from the optical axis reach local maxima. By contrast, only two such bulges are shown in the GRIN solution. It is surmised that this is caused by the use of the optical power distribution to correct Petzval curvature. In microcosm, this principle can be demonstrated by a simple objective lens consisting of two lens elements of equal refractive index and opposite optical power. According to Equation 3.29, this lens system has zero Petzval curvature, however if modelled as thin lenses in contact, the system has zero optical power. Spatially separated however, the lens system has net positive optical power. The optical power of a system of two thin lenses of optical powers K_1 and K_2, separated by a distance, d, is given by

$$K_T = K_1 + K_2 - dK_1 K2. \tag{3.30}$$

If $K_1 = -K_2$, then the net optical power of this zero-Petzval-curvature lens system is given by

$$K_T = dK_1^2. \tag{3.31}$$

A paraxial raytrace of an optical system of this form is shown in Figure 3.17 (A). While Petzval curvature is corrected, the lens does not demonstrate the symmetry shown in the Lithographic designs of Figure 3.13. Rather, we must place two copies of the lens in Figure 3.17 (A) end to end, and place the aperture stop between them in order to generate bilateral symmetry in the design and ensure coma, lateral colour, and distortion are corrected. This combined lens is shown in Figure 3.17 (B) and now illustrates a "double bulge" construction. A similar solution exists where the powers of the positive and negative lenses are reversed, which leads to a compact design, yet it is much harder to correct for aberrations of the field such as astigmatism. In highly complex lithographic relay designs, multiple bulges can be observed in the ray paths as the lens corrects for multiple orders of all aberration types. It is surmised that the change in relationship between Petzval curvature and the axial refractive index between the homogeneous and GRIN solution types has led to the structural change in the optical solution from three bulges to two. It is however difficult to prove this definitively (as for any complex lens design), as the system is optimised for a construction that corrects multiple orders of all aberration types.
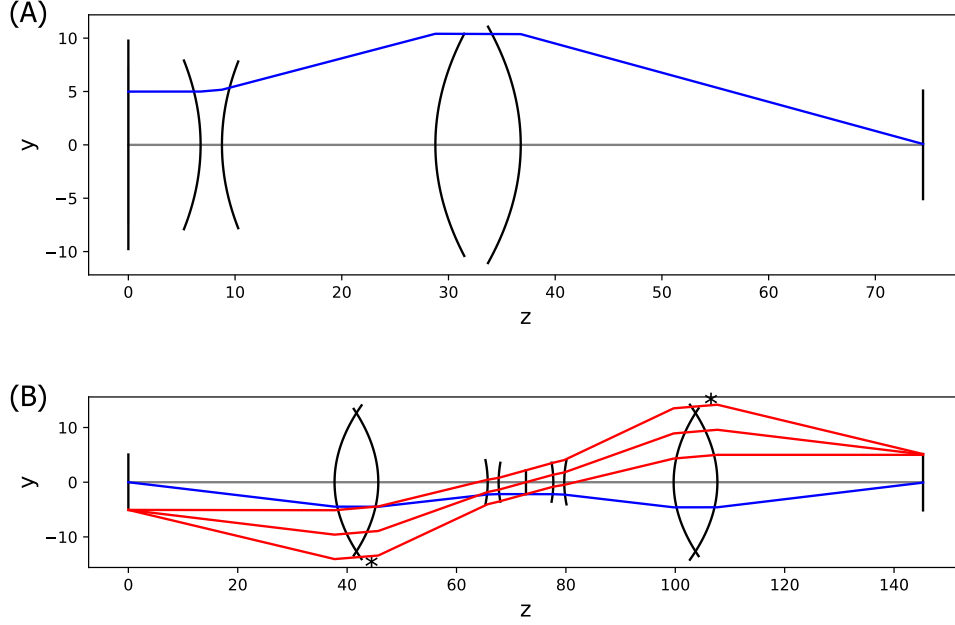
Figure 3.17: (A) Paraxial trace on axis of two separated lenses with equal and opposite optical power displaying net positive focusing power for an object at infinity. (B) Paraxial trace of two copies of the same lens placed end to end. Locations of the characteristic ray bulges are denoted by an asterisk.

3.9. Chromatic Paraxial Reconstruction to a Three Material GRIN

GRIN lenses are frequently used to enhance the chromatic aberration correction of optical systems. Thus, there is a strong motive to apply the paraxial reconstruction method to polychromatic systems. Such a conversion may be achieved by paraxially reconstructing at three defining wavelengths that span the operating waveband of the system. With these three paraxially-reconstructed systems we define two key quantities, the axial dispersion $\mathcal{N}_{0\lambda}$ and the distributed GRIN second order dispersion $\mathcal{N}_{2\lambda}$, defined as

$$\mathcal{N}_{0\lambda} = \mathcal{N}_0(\lambda_{\text{long}}) - \mathcal{N}_0(\lambda_{\text{short}}), \tag{3.32}$$

$$\mathcal{N}_{2\lambda} = \mathcal{N}_2(\lambda_{\text{long}}) - \mathcal{N}_2(\lambda_{\text{short}}). \tag{3.33}$$

For a GRIN where the ΔN is constant with wavelength, the distributed Abbé value according to Equation 1.29 is infinite. The spatial distribution of chromatic dispersion as a function of z in a GRIN lens may frequently pass through zero, which implies an infinite Abbé number. This leads to asymptotes in the V_{GRIN} distribution, making a mathematical fit very challenging. Therefore we use dispersion, which is inversely related to the Abbé number.

Once the required values of dispersion from the paraxial reconstruction are known, we fit the reconstructed $\mathcal{N}_0$, $\mathcal{N}_2$, $\mathcal{N}_{0\lambda}$, and $\mathcal{N}_{2\lambda}$ profiles to a basis of constituent materials that form the GRIN starting solution. Fitting a GRIN to a spatial distribution of base materials enables improved design for manufacture by expressing the GRIN lens in terms of what can be made. For a GRIN consisting of two base materials, V_{GRIN} is a constant (with paraxial reconstruction at a single wavelength all that is required). A three material GRIN is required to fit $\mathcal{N}_0$, $\mathcal{N}_2$, $\mathcal{N}_{0\lambda}$, and $\mathcal{N}_{2\lambda}$.

Previous works (Chapter 2, [72]) have outlined mathematical representations for the refractive index of GRIN lenses consisting of three or more materials as a weighted average of the

constituent material refractive indices. We define the refractive index of a three-base-material GRIN lens as per Equation 2.24. For such a GRIN, $\mathcal{N}_0(z)$ and $\mathcal{N}_2(z)$ are given by Equations 2.26 and 2.28. Calculation of $\mathcal{N}_0(z, \lambda_{\text{long}}) - \mathcal{N}_0(z, \lambda_{\text{short}})$ and $\mathcal{N}_2(z, \lambda_{\text{long}}) - \mathcal{N}_2(z, \lambda_{\text{short}})$ yields the GRIN dispersion equations

$$\mathcal{N}_{0\lambda}(z) = N_{A\lambda} m_{A0}(z) + N_{B\lambda} m_{B0}(z) + N_{C\lambda} m_{C0}(z), \tag{3.34}$$

$$\mathcal{N}_{2\lambda}(z) = N_{A\lambda} m_{A2}(z) + N_{B\lambda} m_{B2}(z) + N_{C\lambda} m_{C2}(z), \tag{3.35}$$

where $N_{A\lambda}, N_{B\lambda}, N_{C\lambda}$ are the dispersion values of the base materials given by

$$\begin{aligned} N_{A\lambda} &= N_A(\lambda_{\text{long}}) - N_A(\lambda_{\text{short}}) \\ N_{B\lambda} &= N_B(\lambda_{\text{long}}) - N_B(\lambda_{\text{short}}) \\ N_{C\lambda} &= N_C(\lambda_{\text{long}}) - N_C(\lambda_{\text{short}}). \end{aligned} \tag{3.36}$$

Equations 2.13, 2.14, 2.26, 2.28, 3.34, and 3.35 form a system of six equations that allow us to solve for the distribution of $m_{A0}(z), m_{B0}(z), m_{C0}(z)$ and $m_{A2}(z), m_{B2}(z), m_{C2}(z)$ for each material once the refractive index and dispersion of the base materials, as well as $\mathcal{N}_0(z), \mathcal{N}_2(z)$, $\mathcal{N}_{0\lambda}(z)$, and $\mathcal{N}_{2\lambda}(z)$ of the system (via paraxial reconstruction), are known. This system of equations can be represented as two 3x3 matrix equations, given by

$$\begin{pmatrix} 1 & 1 & 1 \\ N_A & N_B & N_C \\ N_{A\lambda} & N_{B\lambda} & N_{C\lambda} \end{pmatrix} \begin{pmatrix} m_{A0} \\ m_{B0} \\ m_{C0} \end{pmatrix} = \begin{pmatrix} 1 \\ \mathcal{N}_0 \\ \mathcal{N}_{0\lambda} \end{pmatrix}, \tag{3.37}$$

$$\begin{pmatrix} 1 & 1 & 1 \\ N_A & N_B & N_C \\ N_{A\lambda} & N_{B\lambda} & N_{C\lambda} \end{pmatrix} \begin{pmatrix} m_{A2} \\ m_{B2} \\ m_{C2} \end{pmatrix} = \begin{pmatrix} 0 \\ \mathcal{N}_2 \\ \mathcal{N}_{2\lambda} \end{pmatrix}. \tag{3.38}$$

We define a quantity, ϕ, which is the determinant of the matrices in Equations 3.37 and 3.38 and is given by

$$\phi = N_A N_{B\lambda} - N_A N_{C\lambda} - N_B N_{A\lambda} + N_B N_{C\lambda} + N_C N_{A\lambda} - N_C N_{B\lambda}. \tag{3.39}$$

Equations 3.37 and 3.38 have solutions provided ϕ is non-zero. Solution by Cramer's rule then gives the following equations for the relative composition coefficients of each material:

$$m_{A0}(z) = [N_B N_{C\lambda} - N_C N_{B\lambda} + \mathcal{N}_0(z)(N_{B\lambda} - N_{C\lambda}) - \mathcal{N}_{0\lambda}(z)(N_B - N_C)]\phi^{-1},$$

$$m_{B0}(z) = [-N_A N_{C\lambda} + N_C N_{A\lambda} - \mathcal{N}_0(z)(N_{A\lambda} - N_{C\lambda}) + \mathcal{N}_{0\lambda}(z)(N_A - N_C)]\phi^{-1},$$

$$m_{C0}(z) = [N_A N_{B\lambda} - N_B N_{A\lambda} + \mathcal{N}_0(z)(N_{A\lambda} - N_{B\lambda}) - \mathcal{N}_{0\lambda}(z)(N_A - N_B)]\phi^{-1},$$

$$m_{A2}(z) = [\mathcal{N}_2(z)(N_{B\lambda} - N_{C\lambda}) - \mathcal{N}_{2\lambda}(z)(N_B - N_C)]\phi^{-1}, \tag{3.40}$$

$$m_{B2}(z) = [-\mathcal{N}_2(z)(N_{A\lambda} - N_{C\lambda}) + \mathcal{N}_{2\lambda}(z)(N_A - N_C)]\phi^{-1},$$

$$m_{C2}(z) = [\mathcal{N}_2(z)(N_{A\lambda} - N_{B\lambda}) - \mathcal{N}_{2\lambda}(z)(N_A - N_B)]\phi^{-1}.$$

Computationally, these coefficients were determined via an analogous method to that outlined for monochromatic paraxial reconstruction. $\mathcal{N}_0(z)$ and $\mathcal{N}_2(z)$ were calculated via the fitting of Bézier curves to the paraxial rays of the parent optical system at three separate

wavelengths. The trace at the central reference wavelength was used to define $\mathcal{N}_0(z)$ and $\mathcal{N}_2(z)$, whilst the difference between the short and long wavelength systems was used to define $\mathcal{N}_{0\lambda}(z)$ and $\mathcal{N}_{2\lambda}(z)$. The resulting functions $\mathcal{N}_0(z)$, $\mathcal{N}_2(z)$, $\mathcal{N}_{0\lambda}(z)$, and $\mathcal{N}_{2\lambda}(z)$ were then input to Equation 3.40 to solve for the relative composition coefficients of the lens, $m_{A0}(z)$, $m_{B0}(z)$, $m_{C0}(z)$, $m_{A2}(z)$, $m_{B2}(z)$, $m_{C2}(z)$. Spline knots were then fitted to these functions of z, these knots forming the input to a spline-based, three-material GRIN tracing DLL. Three materials and their associated properties were defined as input parameters for the reconstruction. In principle, any three unique materials with non-identical refractive index and dispersion can be used to fit relative composition, however the refractive index and dispersion space defined by materials A, B and C should be comparable to or larger than that defined by the materials of the parent system. If the range of refractive index and dispersion values differ significantly between the parent lens and GRIN reconstruction, then regions of unphysical negative concentration may result from the paraxial reconstruction process. Whilst such regions are generally simple to address through optimisation, correction of excessive material errors can lead to poor local minima in the optimised design.

A Cooke triplet example lens system was reconstructed over a finite waveband to demonstrate this technique. The specification of this lens is listed in Table 3.5. For consistency, the GRIN basis materials A, B and C were equivalent to the parent system (N-SK16, N-F2 and air). Whilst this design is not indicative of any current GRIN manufacture approach, it is used to demonstrate the technique and the first-order equivalence of the reconstructed solution. The relative composition of the paraxially reconstructed GRIN starting point is shown in Fig-

Focal Length	50.00 mm
F/#	5.0
Field of view	40°
Wavelengths (nm)	486.1, 546.1, 656.3
Glass Types	N-SK16, N-F2, N-SK16
Back focal clearance	38.71 mm
Overall length	57.55 mm

Table 3.5: Optical specification for the Cooke triplet parent lens design.

ure 3.18. Notably, there are regions of negative concentration in N-F2 (material B), with a corresponding excess of N-SK16 (material A). This is due to the very similar refractive index between these two materials. Such negative concentration errors are corrected through the imposition of constraints during finite-ray optimisation. The similar index of these materials allows restoration of only positive material concentration distributions without a change in the merit function of a magnitude that would cause significant disruption to the optimisation process.

The paraxially converted starting point is shown alongside a paraxial trace of the parent solution in Figure 3.20. The focal length of the converted system (at the centre wavelength) matches the parent solution very closely, at 49.62 mm compared to 50.00 mm. The focal length versus wavelength of the paraxial reconstruction and parent design is shown in Figure 3.19. It was observed that the chromatic aberration successfully replicates that of the parent solution.

Optimisation was again performed in CodeV. The merit function comprised the RMS spot size, with constraints to ensure the focal length of 50 mm was maintained. Grid constraints

Paraxially Reconstructed Relative Composition
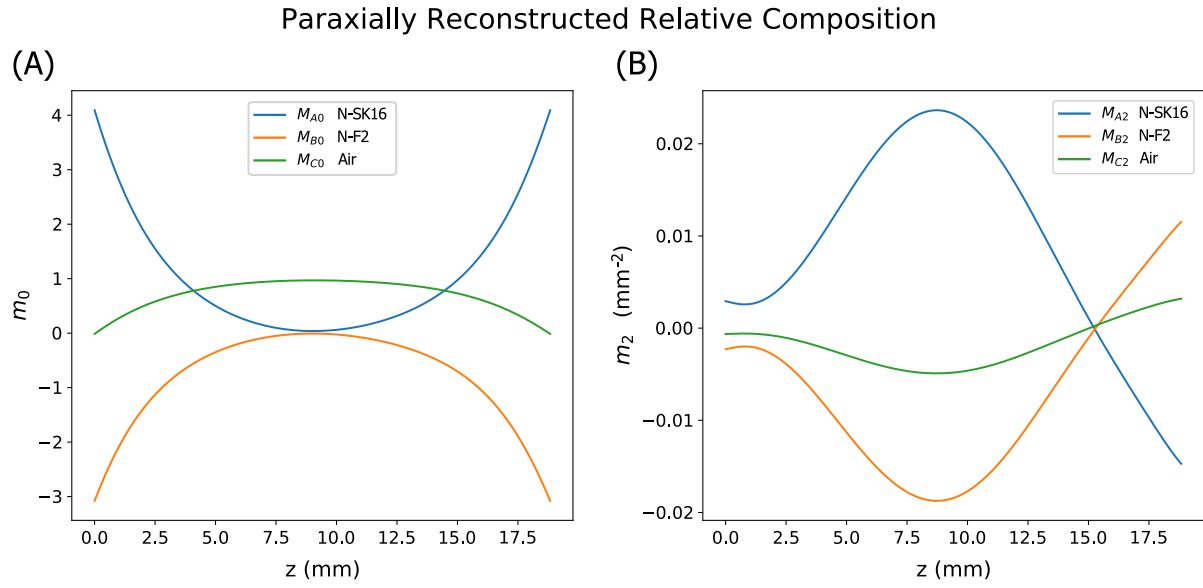
Figure 3.18: Reconstructed relative composition distribution of Cooke triplet parent design. (A): axial relative composition $m_0(z)$ for each constituent material. (B): second order $m_2(z)$ distribution for each constituent material.
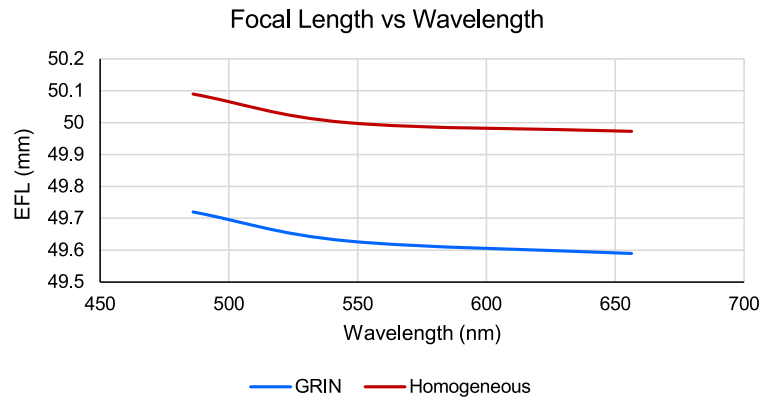
Figure 3.19: Focal length versus wavelength of the paraxial reconstructed GRIN Cooke triplet lens and its homogeneous parent.

	RMS Wavefront error (waves at 546.1 nm)	
Field angle (°)	Homogeneous Parent	GRIN Optimised
0.0	0.1266	0.0527
7.0	0.2916	0.0717
14.0	0.7771	0.1398
17.0	0.7859	0.1151
20.0	0.2788	0.1644

Table 3.6: RMS wavefront of Cooke triplet homogeneous parent lens and optimised GRIN solution from paraxially reconstructed starting point.
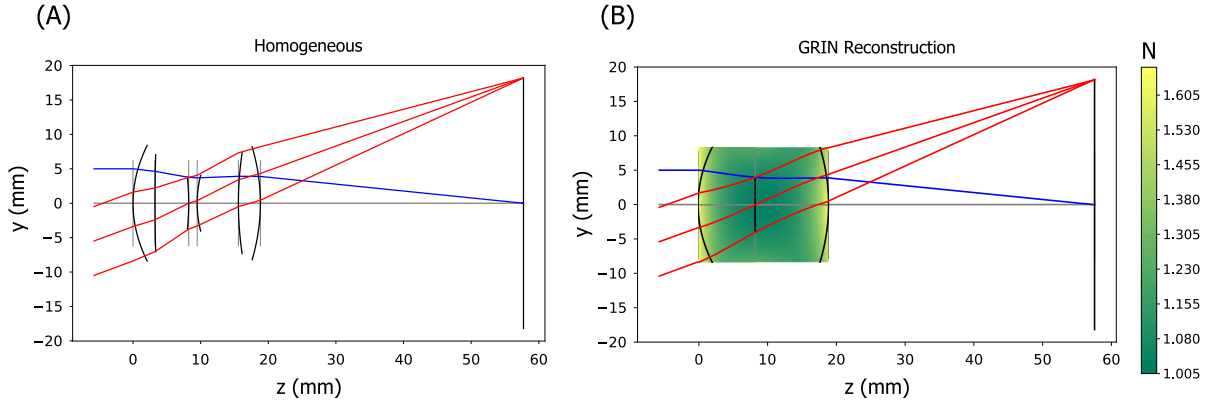
Figure 3.20: Conventional Cooke triplet paraxial raytrace (A). Paraxially reconstructed GRIN paraxial raytrace (B).

analogous to those used for the Double Gauss converted design were implemented, this time being used to ensure the concentration of any of the constituent materials did not become negative within the clear aperture of the lens. As before, to ensure these constraints were not applied over an excessive aperture, the GRIN was sliced into 12 segments. Initially, only the $m_0(z)$ and $m_2(z)$ coefficients were allowed to vary for each material, with additional orders progressively made variable after convergence of the previous optimisation run to avoid poor local minima. The overall thickness of the GRIN was kept constant at an equivalent value to the axial length of the parent homogeneous solution. Likewise, the back focal distance was frozen at an identical value to the homogeneous parent lens.

The optimised GRIN system and homogeneous parent lens are shown in Figure 3.21. RMS wavefront error of the GRIN solution is significantly better than the homogeneous starting solution (listed in Table 3.6), however it must be noted that the GRIN design has significantly more degrees of freedom than the homogeneous solution and is not based on any current GRIN technology. Rather, this solution is intended to demonstrate the utility of the paraxial reconstruction technique, yielding a GRIN analogue to a conventional design with high performance and without the need for time consuming global optimisation. The relative composition of the optimised GRIN solution is shown in Figure 3.22. The distribution of material within this lens remains strongly analogous to the homogeneous parent solution, with a higher concentration of N-SK16 close to the two refractive surfaces at each end of the lens, and a negatively powered central region. One notable difference is the shift of concentration of N-F2 from the centre of the lens to the lens surfaces. The large central region of the lens dominated by air indicates that should a smaller ΔN GRIN combination be required for manufacturing feasibility, the solution may function well as two lenses separated by an air gap containing the aperture stop.
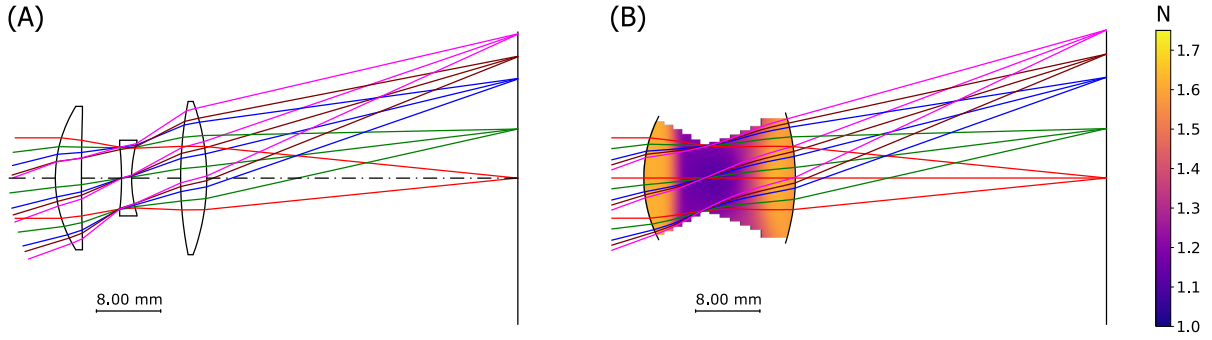
Figure 3.21: (A): conventional Cooke triplet design. (B): Converted and optimised COS design.
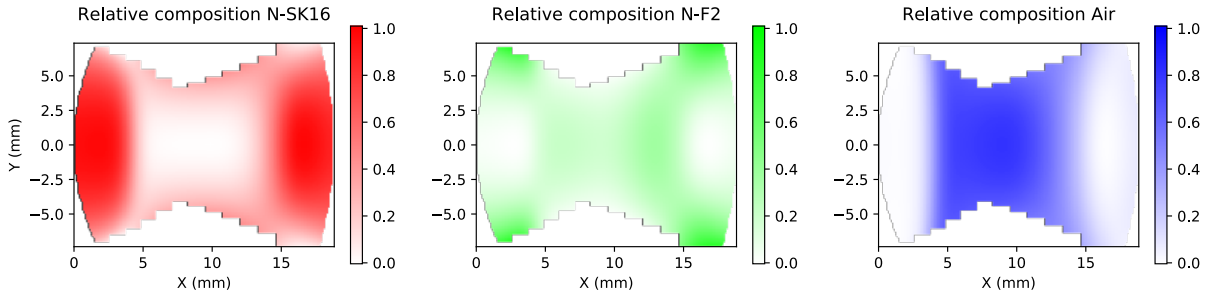
Figure 3.22: Relative composition of optimised COS reconstructed from the Cooke triplet.

3.10. Conclusions

The optical design of generalised GRIN continuous optical systems (COS) is a significant optical design challenge, due to a very large parameter space and computationally intensive raytracing. As a result, selection of a suitable starting solution is a critical step in the production of a high-performance optical design. We have demonstrated a method to generate starting solutions for COS, based on the chosen assumption that the optical constructions of homogeneous lens systems are broadly analogous to their COS form. This was achieved by smoothing of the discrete, segmented, paraxial ray paths of homogeneous systems to target paraxial GRIN ray trajectories, followed by calculation of the requisite GRIN properties from the paraxial raytracing equation for GRINs and the Lagrange invariant, a technique we refer to as paraxial reconstruction. These converted designs successfully replicate the first-order optical properties of the parent design with high fidelity.

We have demonstrated several paraxial reconstructions of common optical lens system types, yielding COS with comparable optical performance to their homogeneous parent solutions following finite-ray optimisation. Furthermore, we have shown that paraxial reconstruction can be used to convert the chromatic properties of the parent system. This was demonstrated for a Cooke triplet that showed excellent agreement in chromatic aberration properties between the paraxial reconstruction and homogeneous parent solution.

In its current state of development, the following limitations are noted in the paraxial reconstruction technique

- The process frequently leads to solutions with large amounts of index modulation. This is often induced by the presence of air gaps and edges. This can be an issue where the index modulation greatly exceeds that of the intended GRIN manufacture process.

- The process assumes that the input homogeneous solution is a good starting point for optimisation in the first place.

- Aberrations of the parent solution are not reconstructed, and in this work, sometimes required numerical optimisation of the fourth-order refractive index coefficient, $\mathcal{N}_4(z)$, to correct them where their magnitude caused finite raytracing failures that were not easily addressed by temporary reduction in field and aperture.

- Paraxial reconstruction does not find inherently new distributions of optical power that may lead to new COS-based designs. The final optimised solution must be sufficiently similar to the reconstructed starting solution to be found via local optimisation.

- The paraxial reconstruction process inherently produces lenses that are very thick, which may if incorrectly applied increase the optical mass of the finished optical design.

It is planned to address the limitation of large index variation in future work. It was observed that large index variation in reconstructed designs was predominantly caused by large air gaps and "air edges" caused by two lenses with adjacent convex surfaces. The large index variation can be addressed by quite simply dividing the paraxial reconstruction into multiple sub-systems where such large air gaps and edges are bounded by optical surfaces. This concept is illustrated for a hypothetical lens system in Figure 3.23. The large air gap between doublets of Figure 3.23 (A) results in a region of low refractive index in the paraxial reconstruction of Figure 3.23 (B). The overall index variation of the reconstruction can be reduced by either paraxially reconstructing the two doublets independently, or by inserting an air gap into the paraxial reconstruction and solving the surface curvatures such that the first-order properties of the lens system are retained (Figure 3.23 (C)). Such an approach may represent a more harmonious use of GRIN lenses in combination with optical surfaces, where GRIN media are highly effective for correcting chromatic and monochromatic aberrations, yet require a large ΔN to produce substantial focusing power that could be applied more simply with optical surfaces.

Performing paraxial reconstruction on regions of lenses within a wider system would also mitigate any potential increases in system mass while maximising the other SWAP-C benefits GRIN can bring. High-performance lens systems in particular can contain regions with a high density of air-spaced lens elements (similar to the lithographic relay lens example of this chapter). These regions often contain sequences of alternating positive and negatively powered lenses, which can generate high cost due to tight surface form and assembly alignment tolerances. Substitution of such regions of an optical system for a COS could yield significant simplification and cost reduction (provided sufficiently economical GRIN material can be produced).

Development of an analytical method to correct the Seidel aberrations of the reconstructed system would also be of significant benefit, as it would reduce the need for numerical fitting of $\mathcal{N}_4(z)$ or temporary reduction of field and aperture in the paraxial reconstructed optimisation starting solution. Promisingly, if this technique is augmented by a fitting approach for a finite marginal ray on axis, in a manner similar to those outlined in references [79, 81], then a deterministic procedure for a starting solution corrected for spherical aberration and coma is possible (by constraining the image plane ray to fulfil the Abbé sine condition[§]). With continuing development, paraxial reconstruction may serve as the foundation of a powerful suite of techniques to simplify generalised GRIN design and optimisation problems.

[§]We define and derive the Abbé sine condition in Chapter 4.
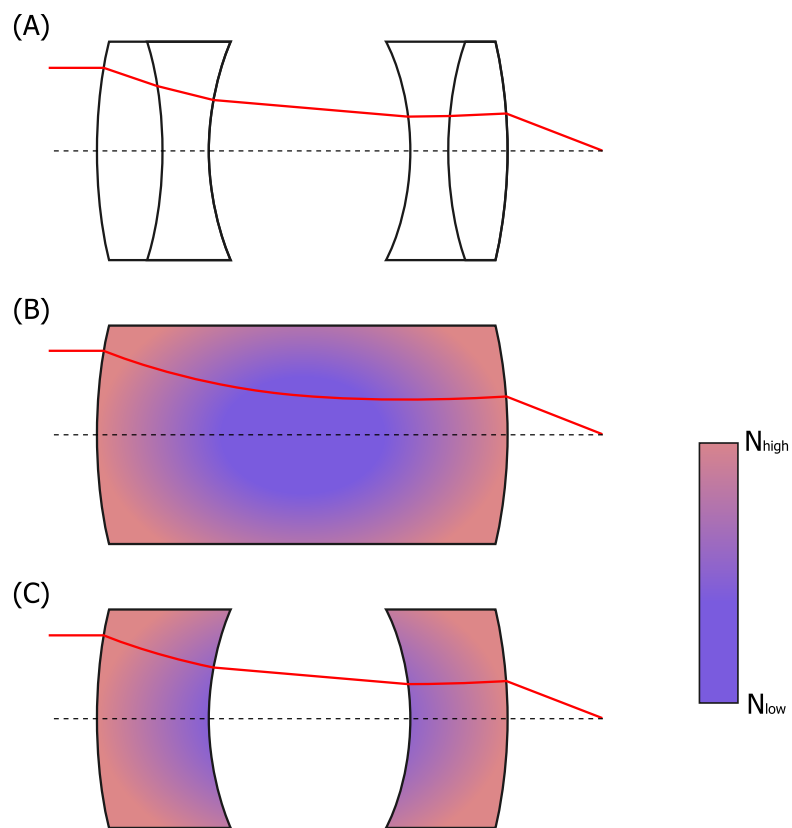
Figure 3.23: Conceptual lens system (A) paraxially reconstructed as a single lens (B) and as two separate GRIN lenses (C).

4

Surface Curvature and the Abbé Sine Condition in Gradient-Index Lenses

4.1. Abstract

The Abbé sine condition is a well-known requirement for optical imaging systems to be free from coma. We derive the Abbé sine condition from geometrical optical principles, before exploring its implications for GRIN lenses. In particular, we explore the consequences of plano and curved surfaces for the correction of coma in GRIN lenses. We find that general-rotationally-symmetric GRIN distributions have the potential to correct coma in a plano lens geometry, but with the trade-off that the complexity and ΔN of the GRIN distribution must increase compared to a Wood lens, while similar performance can be achieved with much simpler GRIN distributions when the lens surface can be curved.

4.2. Introduction

It is well proven both theoretically and experimentally, that radial GRIN lenses can generate optical focusing power despite having planar surfaces [12, Chapter 4]. This has the potential to be very convenient in the optical processing of the lens surfaces, as plano surfaces can be manufactured readily in large volumes, while their surface metrology using an interferometer or similar device is relatively simple to implement. This often leads to the question of whether the degrees of freedom conferred by generalised GRIN media supersede the need for surface curvature on GRIN lens elements. To evaluate this possibility, we must investigate the aberration correction properties of such planar GRIN lenses, as it is ultimately influence over aberrations that drives utility of GRIN as a technology for imaging optics. A key requirement of a hypothetical flat surface imaging GRIN lens is the correction of coma (assuming the lens requirement has a finite field of view). To correct coma, it is fundamentally necessary that the lens satisfy the Abbé sine condition. The Abbé sine condition was one of the earliest developments in aberration theory, and led to significant improvements in the image quality of telescope lenses [86]. We first derive the Abbé sine condition before investigating whether

it is possible for flat GRIN lenses of general distribution to satisfy it. We then compare this approach to the use of surface curvatures, a known technique for satisfying the same.

4.3. Derivation of the Abbé Sine Condition

We follow the derivation of the Abbé sine condition outlined by Braat [86]. We define a "black box" rotationally symmetric optical system as illustrated in Figure 4.1. Herein, unprimed and primed quantities are associated with the object and image space respectively. A ray emanating from a point, P, along the optical axis is imaged by the system to a point, P'. This axial image is assumed to be aberration free. This ray propagates with a direction defined by the vectors $\mathbf{r}$ and $\mathbf{r}'$ in the object and image space respectively, with respective angles U and U' with the optical axis. These ray vectors therefore have components given by

$$\mathbf{r} = (0, \sin U, \cos U), \tag{4.1}$$

$$\mathbf{r}' = (0, \sin U', \cos U'). \tag{4.2}$$

The object space and image space have homogeneous refractive indices, N and N' respectively. We also define a neighbouring ray, which travels from the point Q to the point Q', which emanates from a point an infinitesimal distance away from P, given by a displacement vector

$$\delta\mathbf{s} = (0, \delta y, 0). \tag{4.3}$$

We in turn define a displacement vector in the image space between the two rays

$$\delta\mathbf{s}' = (0, \delta y', 0) \tag{4.4}$$

This second ray is assumed parallel to the first ray in object and image space. We now wish to derive under what condition the image quality at Q' is identical to that of P'. If the image point defined by the first ray is perfect, then this is assumed to be a first-order optical system, where we can obtain the corresponding change in position in the image plane between P' and Q' by use of the paraxial transverse magnification, $\mathcal{M}$. The magnification gives us a relationship between the object and image displacements [50, Chapter 3.4], given by

$$\delta y' = \mathcal{M}\delta y. \tag{4.5}$$

In order for the image quality of the paths PP' and QQ' to be identical, the optical path length through the system must be identical for any direction of the ray vector, $\mathbf{r}$, that reaches the
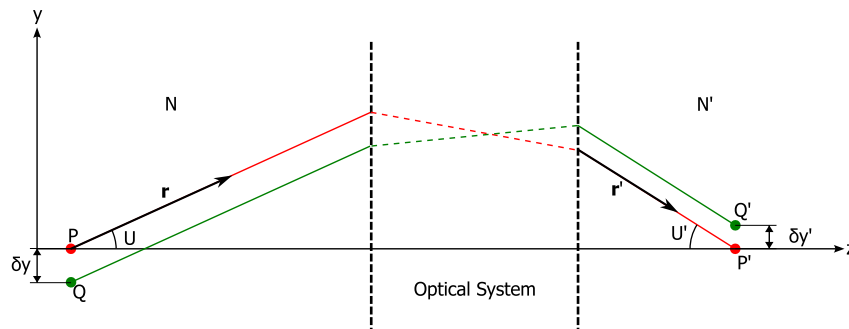
Figure 4.1: Finite rays from two object plane points passing through a notional rotationally-symmetric optical system.

entrance pupil of the optical system. We therefore evaluate an optical path difference, ΔW, between the two rays and observe under what condition it is zero. In the object space, the optical path difference is given by

$$\Delta W_O = -N\mathbf{r} \cdot \delta\mathbf{s} = -N\delta y \sin U, \tag{4.6}$$

while in the image space it is given by

$$\Delta W_I = N'\mathbf{r}' \cdot \delta\mathbf{s}' = N'\delta y' \sin U'. \tag{4.7}$$

Adding these two optical path length differences, and stipulating that the sum be zero gives

$$\delta W = N'\delta y' \sin U' - N\delta y \sin U = 0. \tag{4.8}$$

We then substitute the primed quantities using Equation 4.5 to give

$$\delta W = N'\mathcal{M}\delta y \sin U' - N\delta y \sin U = 0, \tag{4.9}$$

which after cancelling δy gives

$$\sin U' = \frac{N \sin U}{N'\mathcal{M}}. \tag{4.10}$$

We assert that this condition is equally true in the paraxial region, and substitute a paraxial ray angle, u, in a manner as discussed in Chapter 1.5.2, which is given by

$$u \approx \sin U, \tag{4.11}$$

and

$$u' \approx \sin U'. \tag{4.12}$$

The relationship between these paraxial rays is again determined by the system magnification where

$$\frac{Nu}{N'u'} = \mathcal{M}. \tag{4.13}$$

We can then substitute Equation 4.13 into Equation 4.10, giving

$$\frac{\sin U}{u} = \frac{\sin U'}{u'}, \tag{4.14}$$

which is the form the Abbé sine condition is most commonly expressed in. The implication of this condition is that the optical system has zero coma. This is because under this condition, the derivative of the wavefront error with respect to object height is zero, and coma is the only third-order aberration with a linear dependency on field. Deviation from this condition is referred to as *offence against the sine condition*. When the axial image is perfect, and the Abbé sine condition satisfied, the image is said to be *aplanatic*.

4.4. Plano GRIN Lenses and the Abbé Sine Condition

Let us consider an optical system focused at infinity with a planar surface, as illustrated in Figure 4.2. Both object and image are in air such that $N = N'$. Such a lens could not practically consist of a single refractive surface. Rather, it could consist of a diffractive optical surface, metasurface, or Fresnel lens, where we assume the optical path length change of the surface is generated by an infinitesimally thin structure with infinite refractive index, known
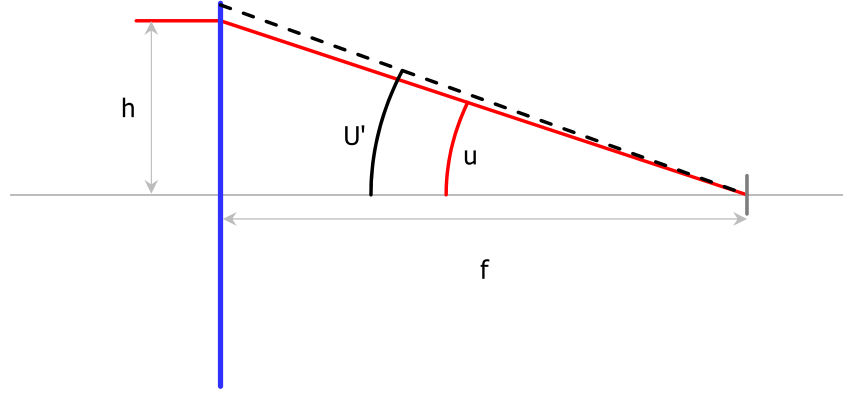
Figure 4.2: A planar lens of focal length f. The red line indicates the path of the axial marginal ray, while the black dashed line indicates the angle that would be required of the same ray to satisfy the Abbé sine condition.

as the Sweatt approximation [87]. For a lens focused at infinity, the distance $d \rightarrow \infty$, in which case

$$\lim_{d \to \infty} u = U, \tag{4.15}$$

therefore

$$\lim_{d \to \infty} \frac{\sin U}{u} = 1, \tag{4.16}$$

and we can therefore modify Equation 4.14 such that

$$\sin U' = u'. \tag{4.17}$$

From paraxial optics, we determine that $u' = h/f$, which we susbtitute into the expression to give the aplanatic condition for a lens focused at infinity

$$\sin U' = \frac{h}{f}. \tag{4.18}$$

We now observe that for the lens in Figure 4.2, the ray paths form a right-angled triangle, and therefore

$$\tan U' = \frac{h}{f} = u'. \tag{4.19}$$

It is clear from Equation 4.19 that $\sin U' \neq u'$, and that such an optic must generate offence against the sine condition. The required finite ray angle, U', in image space to satisfy the sine condition is indicated in Figure 4.2 by the black dashed line. To satisfy the sine condition, it is necessary that the sagitta of the blue surface be adjusted such that it intersects the black dashed line at a height, h. It is further noteworthy that such a flat lens generates offence against the sine condition irrespective of the position of the aperture stop, as the ray height, h, does not change with stop location. Only at unity magnification (which would be an optically powerless window for an infinite object distance) can a thin, plano lens be aplanatic, due to bilateral symmetry of the optical system about the aperture stop. In summary, curvature of such a thin lens is fundamentally necessary to correct coma.

4.4.1. Non-Aplanatic Wood lens

The situation for plano-surface GRIN lenses is more complex, as no GRIN lens truly has zero thickness. Equation 1.27 indicates that the focal power of a radial GRIN lens is proportion to
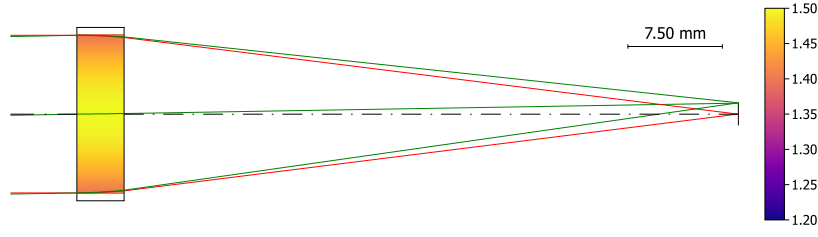
Figure 4.3: Raytrace of 50 mm focal length, F/4 Wood lens.
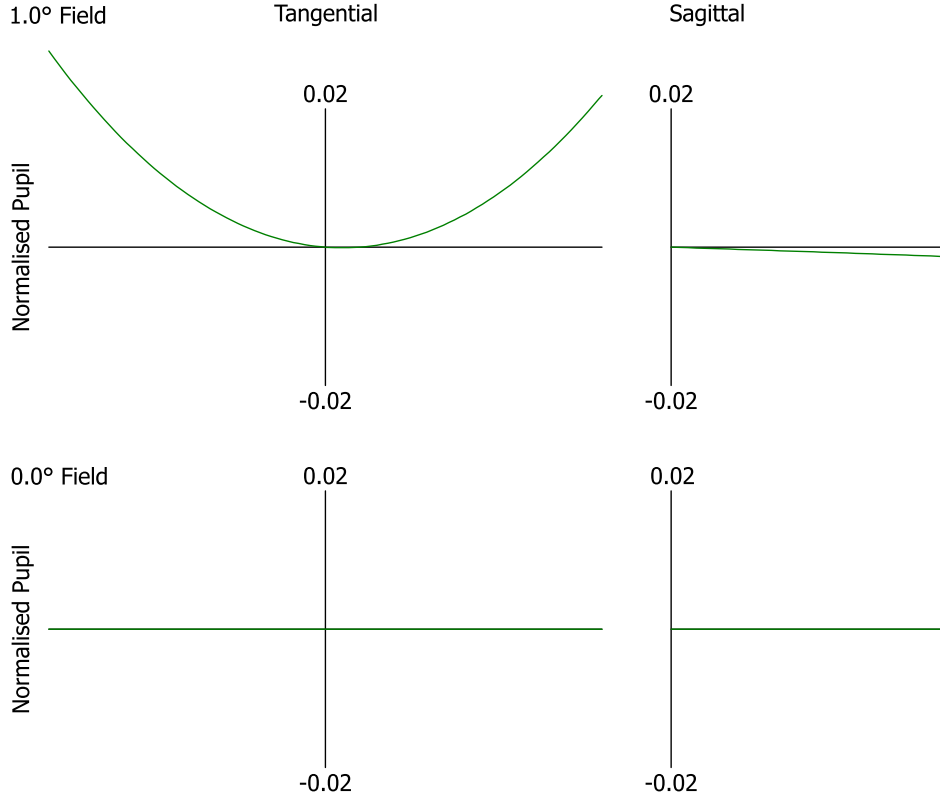
Figure 4.4: Transverse ray errors for 50 mm focal length, F/4 Wood lens. Substantial coma is present at 1 ° field, which is observed as a quadratic contribution with aperture in the tangential section.

its thickness, and so tends to zero as the lens thickness does. It is known that a thin Wood lens lacks the degrees of freedom to satisfy the sine condition and correct coma. An example of this is shown in Figure 4.3, illustrating an F/4 Wood lens of 50 mm focal length, whose GRIN distribution is of the form shown in Equation 1.26. Even after optimisation of the $\mathcal{N}_4$ coefficient, this lens cannot correct coma, while spherical aberration is well-corrected (Figure 4.4). The GRIN lens has a ΔN of 0.1043.

4.4.2. Aplanatic, Homogeneous Singlet

By contrast to the plano Wood lens, homogeneous lenses are readily able to correct coma by means of the lens bending factor (as described in Equation 1.13). Figure 4.5 shows an aspheric singlet consisting of N-BK7 (N_D=1.518). Bending of a lens with spherical surfaces gives sufficient degrees of freedom to minimise spherical aberration while correcting coma, while for an N-BK7 singlet, fourth and sixth-order aspheric terms are required to eliminate third

91
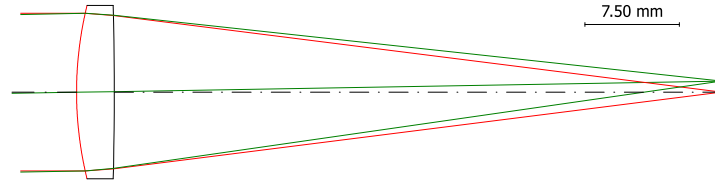
Figure 4.5: Raytrace of 50 mm focal length, F/4 homogeneous singlet lens. An aspheric surface is illustrated in red.
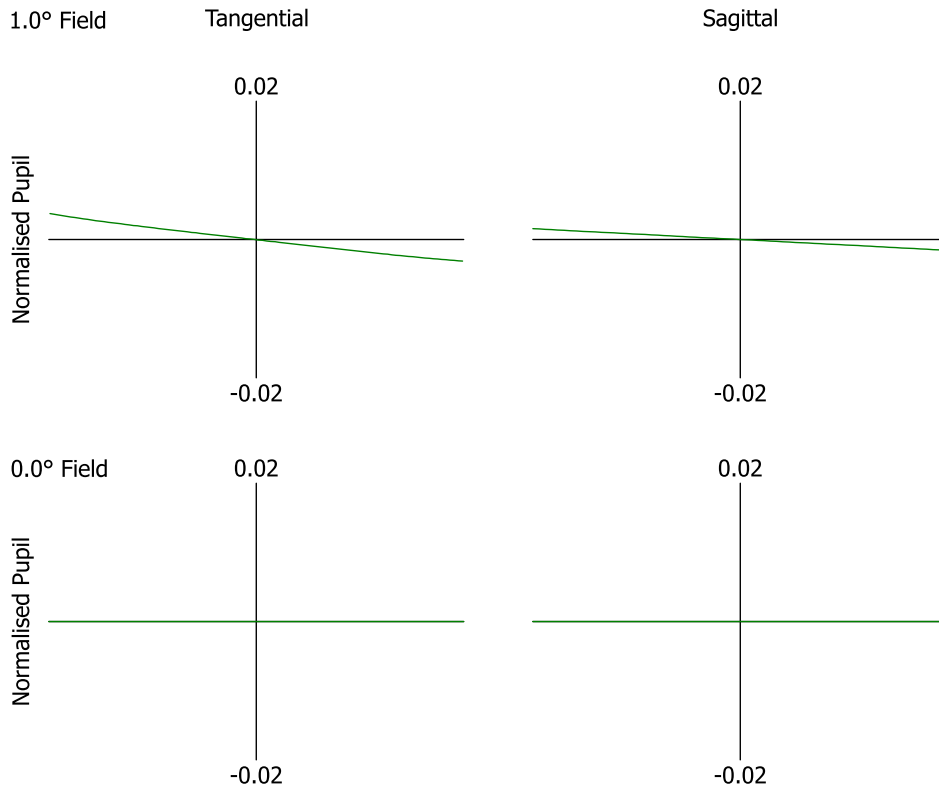
Figure 4.6: Transverse ray errors for 50 mm focal length, F/4 homogeneous lens. Coma is corrected and performance is limited by astigmatism and field curvature at 1 ° field.

and fifth-order spherical aberration. Transverse ray errors (Figure 4.6) indicate that the optical correction of the lens is limited by astigmatism and Petzval curvature, which a homogeneous singlet at the stop does not have the degrees of freedom to correct. Notably, astigmatism has a quadratic dependency that is unaffected by the presence of a very small field angle, and so satisfying the Abbé sine condition has no effect on its correction. The question remains, whether variation in the properties of the GRIN as a function of position along the optical axis, z, allows for satisfaction of the sine condition, and furthermore, what role surface curvature may play in the aberration correction of GRIN lenses.

4.4.3. Plano, Aplanatic, Generalised-GRIN Lenses

A generalised GRIN with the same thickness as the Wood lens of Figure 4.3 was optimised from the very same starting solution. The solution was optimised to minimise the RMS spot size, with radial and axial GRIN coefficients of progressively higher orders in z and ρ added
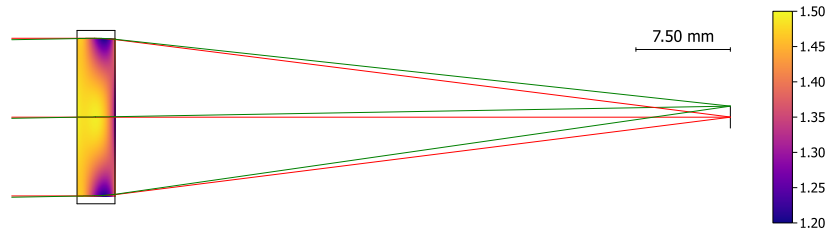
Figure 4.7: Raytrace of 50 mm focal length, F/4 general rotationally symmetric GRIN lens.

until the solution would improve no further. The GRIN was of the form described in Equation 1.23, with the coefficients shown in Table 4.1. The resulting design is shown in Figure 4.7. The

	z^0	z^1	z^2	z^3	z^4	z^5
ρ^0	1.5000	-7.773×10^{-2}	8.206×10^{-2}	-2.533×10^{-2}	0.000	0.000
ρ^2	-2.334×10^{-3}	4.154×10^{-3}	-8.930×10^{-3}	2.896×10^{-3}	0.000	0.000
ρ^4	3.401×10^{-5}	2.953×10^{-6}	-5.56×10^{-6}	-3.317×10^{-6}	0.000	0.000
ρ^6	-1.056×10^{-8}	1.066×10^{-8}	0.000	0.000	0.000	0.000
ρ^8	6.336×10^{-12}	0.000	0.000	0.000	0.000	0.000

Table 4.1: GRIN coefficients of optimised 50 mm, F/4, aplanatic lens.

GRIN distribution is now significantly more complex, and has a much greater ΔN of 0.2986. The lens is, however, now capable of correcting coma as shown in Figure 4.8, being limited by astigmatism in a similar manner to the aspheric singlet of Figure 4.5, with a very small amount of higher order spherical aberration present on axis. Notably, the much larger ΔN of this design has ramifications for its manufacturability.

93
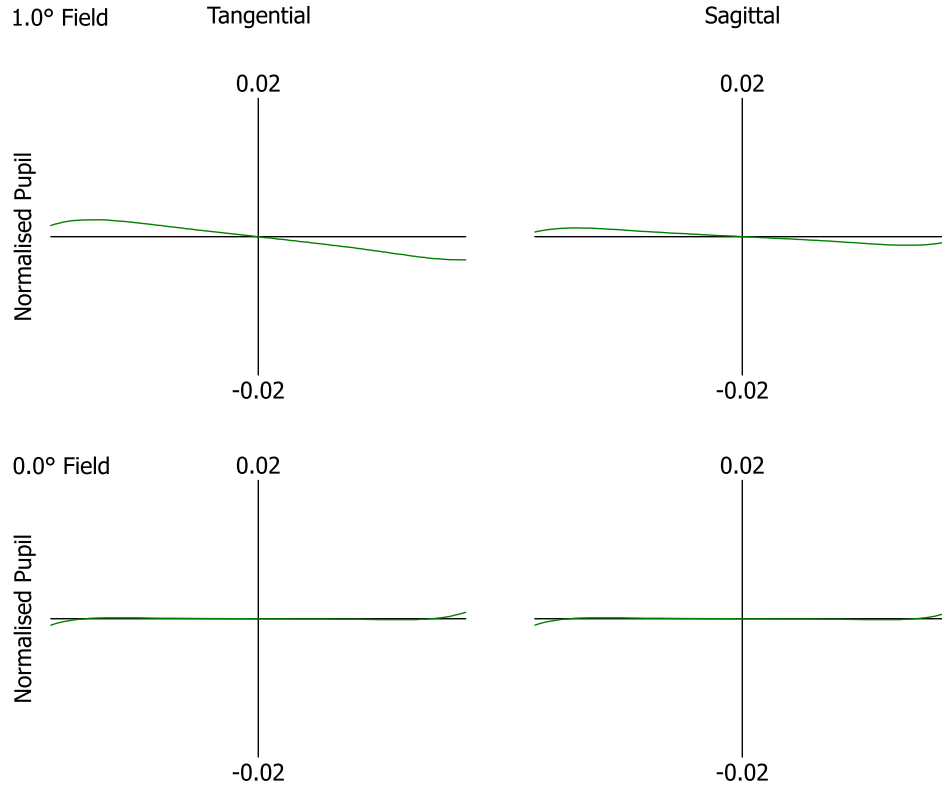
Figure 4.8: Transverse ray errors for 50 mm focal length, F/4 general rotationally symmetric GRIN lens. Coma is corrected and performance is limited by astigmatism and field curvature at 1 ° field.

We next consider the effect of increasing the thickness of the GRIN lens, which as per Equation 1.27, theoretically allows smaller GRIN coefficients to achieve the same focal power, which in turn reduces the ΔN of the lens. The lens thickness was varied in optimisation with an upper bound of 6 mm, double that of the previous solution. Due to the increased thickness, coefficients with a higher power in z were varied to yield the solution shown in Table 4.2. A raytrace of the resultant lens is shown in Figure 4.9. The ΔN of the lens has reduced significantly from 0.2986 to 0.0897. As with the thinner case, the lens is aplanatic, as shown in Figure 4.10. The trade-off with this design however, is that the thicker lens doubles its volume (and would generally be expected to increase its mass). We therefore consider whether there is benefit in a combined approach, using a curved optical surface in conjunction with the GRIN medium.

	z^0	z^1	z^2	z^3	z^4	z^5
ρ^0	1.499	-2.896×10^{-3}	-4.365×10^{-4}	1.734×10^{-4}	9.213×10^{-6}	-1.990×10^{-6}
ρ^2	-1.580×10^{-3}	1.009×10^{-4}	-1.034×10^{-4}	1.640×10^{-5}	-2.354×10^{-7}	3.222×10^{-9}
ρ^4	1.080×10^{-5}	-7.017×10^{-7}	-7.410×10^{-7}	-3.919×10^{-10}	0.000	0.000
ρ^6	-5.754×10^{-11}	7.893×10^{-11}	1.088×10^{-10}	0.000	0.000	0.000
ρ^8	-4.084×10^{-11}	3.026×10^{-12}	2.811×10^{-12}	0.000	0.000	0.000

Table 4.2: GRIN coefficients of optimised 50 mm, F/4, aplanatic lens.

94
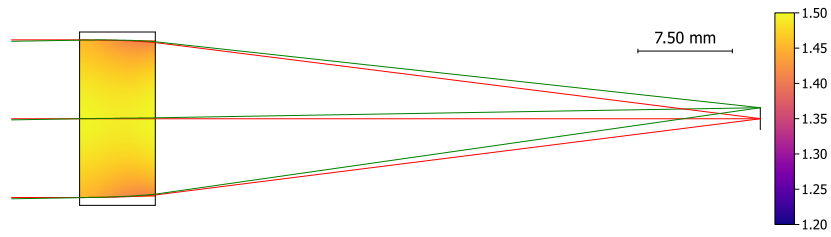
Figure 4.9: Raytrace of 50 mm focal length, F/4 general rotationally symmetric GRIN lens with increased thickness.
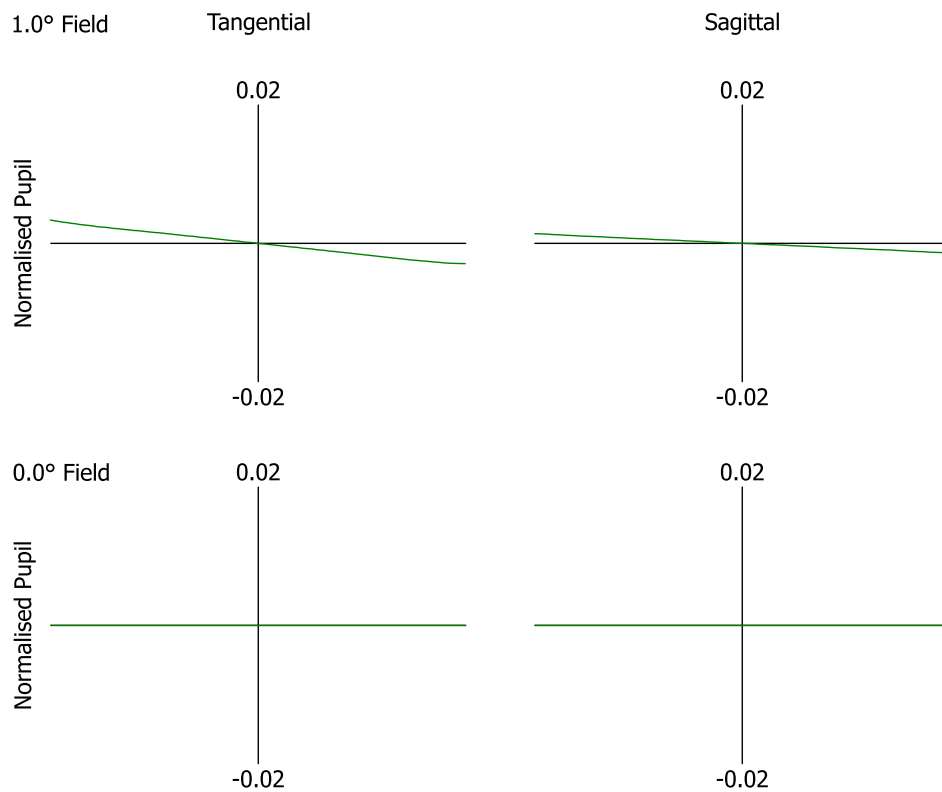
Figure 4.10: Transverse ray errors for 50 mm focal length, F/4 general rotationally symmetric GRIN lens with increased thickness. Coma is corrected and performance is limited by astigmatism and field curvature at 1 ° field.

95

4.4.4. Curved, Aplanatic, Radial GRIN Lens

We now evaluate the performance of a radial GRIN lens with a spherical curved surface on one side. From a Wood lens starting solution, the curvature of the first surface was varied in optimisation with the $\mathcal{N}_{20}$, $\mathcal{N}_{40}$, and $\mathcal{N}_{60}$ coefficients of a radial refractive index distribution as defined in Equation 1.26. The optimised solution is shown in Figure 4.11. The lens is well corrected on axis and has negligible coma as per Figure 4.12. As in the other aplanatic design cases, performance is limited by astigmatism and Petzval curvature. The ΔN of this lens is much smaller than for a plano GRIN lens of the same performance, with a total ΔN of 0.0312, while the lens thickness is the same as the lens illustrated in Figure 4.7.
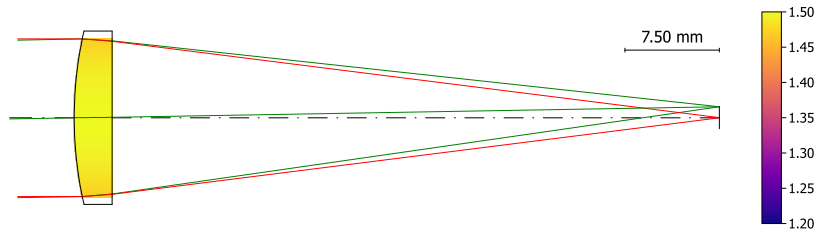
Figure 4.11: Raytrace of 50 mm focal length, F/4 radial GRIN lens with curved front surface.
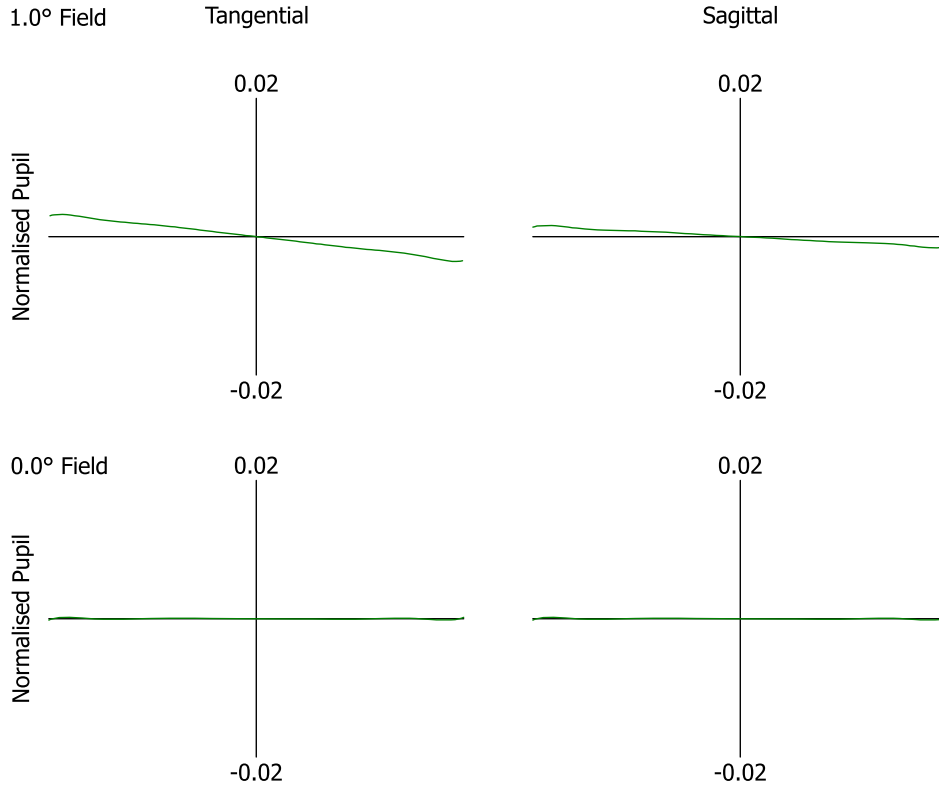
Figure 4.12: Transverse ray errors for 50 mm focal length, F/4 radial GRIN lens with curved front surface. Coma is corrected and performance is limited by astigmatism and field curvature at 1 ° field.

4.5. Conclusions

Via the method published by Braat [86] we have derived an expression for the Abbé sine condition, which must be fulfilled to yield a lens design free from coma. We have shown that in the case of a plano singlet optic (of the type which could be generated by a diffractive lens, metasurface or Fresnel lens), it is impossible to fulfil this condition for an object at an infinite distance. We have shown that a similar effect applies to a Wood lens, which while not infinitesimally thin, has very little principal ray height variation over its length and lacks the necessary degrees of freedom in the GRIN distribution to control coma.

By contrast, general-rotationally-symmetric-GRIN distributions are shown to have sufficient degrees of freedom for coma correction in the case of an F/4 singlet, producing similar aberration correction to an aspheric homogeneous singlet. The side effect of this however is a very large ΔN within the GRIN distribution when the lens is thin, or, a much thicker GRIN lens. By contrast, when a curved surface and a radial GRIN distribution are combined, an aplanatic lens is obtained with a much smaller ΔN.

One caveat that must be applied to all results is that they only concern correction of coma within a single lens element, while the combined effect of multiple lens elements (that would ordinarily not fulfil the Abbé sine condition on their own) can correct coma when arranged correctly. Third-order aberration contributions can be summed over each surface (and GRIN medium) of an optical system to give the total aberration coefficients for the system. It follows that a positive coma contribution from one component can be combined with a negative contribution of equal magnitude from another component to give zero overall contribution.

However, while on first thought this effect may be considered to be an easy solution to aberration correction, the designer must also consider the effect of higher-order aberrations, which themselves can be *induced* at optical surfaces and media by the presence of existing third-order aberrations. As a consequence, the *control*, if not correction of aberrations for a given component within a multi-element optical system is of great importance to minimise fifth and higher-order aberrations, strengthening the requirement for aplanatic components within more complex optical systems.

The consequence of this study for GRIN lens design and manufacture must be treated with pragmatism. While new GRIN manufacture technologies are enabling progressively larger ΔN values and more general GRIN distributions, this entails increased manufacturing complexity, while generation and polishing of a spherical surface is a very mature technology and can be applied at low cost. An alternative approach of using a thicker, general GRIN distribution to achieve lower ΔN achieves the same imaging result, but with a corresponding size and mass penalty as the lens must be thicker. While the cost of a general GRIN lens with plano surfaces may eventually be less than that of a curved homogeneous lens, this is not presently the case, and as a result, there is little commercial argument to migrate to the new technology for this reason alone. Rather, it is more sensible to use GRIN lenses in harmony with curved surfaces, and identify applications where such curved and general GRIN lenses have a high comparative advantage over homogeneous optics. This could include applications where the core function of the optical device is impossible without GRIN, or where GRIN imparts a major SWAP-C benefit, such as improving the aberration correction of a lens within a highly-constrained volume. We explore such applications in the next three chapters.

5

Optical Design of Layered GRIN lenses

The contents of this chapter are derived and expanded from *'Layered Polymer GRIN Lenses and their Benefits to Optical Designs - Andrew Boyd, Michael Ponting & Howard Fein, Advanced Optical Technologies Vol. 4, pp. 429-443, 2015'* [2, AMBref], in addition to internal R&D work undertaken at Qioptiq. Optical design work is my own, with material and process data provided by my co-authors.

5.1. Abstract

We discuss the findings of an optical design study into layered polymer gradient-index (LGRIN) lenses. A range of GRIN singlet lenses were designed for various aperture and field of view configurations. Their optical performance was compared to polymer refractive-diffractive hybrid lenses and glass cemented doublets (with both spherical and aspheric surfaces) designed to the same specification. We find that LGRIN lenses offer comparable performance to achromatic doublets and hybrid elements over a significant aperture and field of view range. We also find that the correction potential of GRIN solutions is substantially increased when: the bulk GRIN Abbé value (V_{GRIN}) is negative, the GRIN distribution is radial, or the index range (ΔN) of the GRIN is increased significantly.

5.2. Introduction

It is of key interest in the imaging optics industry to generate products which provide good image quality at reduced size, mass and cost. Optical design greatly influences this. Opto-mechanical modules often comprise the majority of the size and mass of an imaging system. Traditionally, optical systems have used one of three methods to correct chromatic and spherical aberrations (as illustrated in Figure 1.7). Firstly, the classical doublet enables colour correction through balancing the wavelength dependent powers of two lenses of different materials cemented together. It is a well-understood and effective solution but involves the use of glass lenses which are denser than polymer lenses and requires that two lenses be first manufactured, then precisely aligned during a cementing operation. Secondly, a hybrid

99

refractive-diffractive lens enables colour correction through use of a highly dispersive, blazed surface that removes the chromatic aberration generated by the underlying refractive surfaces. This blaze can be generated on a polymer substrate via SPDT or moulding, enabling the generation of a lightweight, well-corrected solution which is easy to manufacture. However diffractive lenses have limitations due to the stray light effects of spurious diffraction orders, which can become problematic in broad wavebands or high dynamic range imaging. A GRIN lens made from a polymer substrate has the potential to reduce the mass of an optical system by eliminating denser glass material while maintaining chromatic aberration correction (and without introducing significant stray light).

One major barrier to widespread adoption of GRIN technology has been the cost and complexity of manufacture. Recent developments in layered polymer GRIN technology (known as LGRIN) have the potential to overcome this barrier. Developed over the early 2000s, LGRIN materials rely on the forced assembly of a very large number of sub-wavelength thickness polymer films of two or more materials with different refractive indices [88]. Due to their negligible optical thickness, the layers act as an effective medium for visible or longer wavelengths. By controlling the relative thickness of the fixed-index alternating layers, the refractive index of the medium can be modified spatially. This approach enables the generation of polymer lens preforms with axial, spherical, and even aspheric GRIN profiles. Two polymers are currently used to generate LGRINs: poly (methyl methacrylate) (PMMA) and styrene acrylonitrile (SAN17). These are suitable for single-point diamond turning (SPDT) which enables economical generation of aspheric surfaces on the finished lens. These surfaces need not necessarily be conformal with the polymer nano-layers.

The LGRIN manufacturing process is summarised in Figure 1.1 and Figure 1.2 [37]. Two materials are co-extruded through a layer multiplying process to generate 50 µm thick films of constant, yet customisable, refractive index. Index customisation is achieved by varying the proportional thickness of the input layers via in-line precision melt pumps calibrated to control the relative polymer material feed rates down to 0.3%. Quality assurance refractive index testing is routinely performed on processed 475 m long × 0.5 m wide nano-layered film rolls to ensure the target refractive index is achieved. Based on the developed nano-layered film refractive index testing procedures averaged from 750 unique measurements over the entire roll, a refractive index variation tolerance of less than 2.5×10^{-4} must be met to qualify the material for continued processing into GRIN optics. Once qualified, these films are then used to populate an inventory of available index values. The films are then selected and stacked subject to the design of the GRIN profile. This film stack is then consolidated into a single GRIN sheet. From here, the axial GRIN may be moulded further into a spherical (potentially aspheric) GRIN preform. The optical surface quality of the spherical preforms is sufficient to allow optical alignment of preforms to diamond turning lathes.

5.3. Modelling of Layered GRIN Lenses

Polymer GRINs are not subject to the same manufacturing constraints that diffusion-driven GRIN manufacture methods are limited by. This method of GRIN manufacture requires a new optical design modelling approach. A simple spherical GRIN distribution is defined as

$$N(R) = \mathcal{N}_0 + \mathcal{N}_1 R + \mathcal{N}_2 R^2 + \mathcal{N}_3 R^3 + \dots, \tag{5.1}$$

where R defines the distance from the centre of the GRIN distribution of a surface of constant refractive index, while $\mathcal{N}_0, \mathcal{N}_1, \dots$ are refractive index coefficients. While in principle Equation
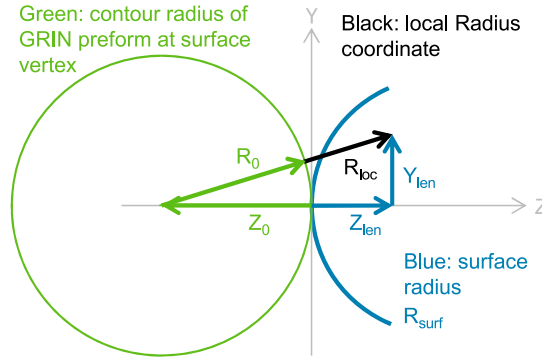
Figure 5.1: Coordinate transform for optimisation of spherical polymer GRINs.

5.1 can be used for the design and optimisation of a polymer spherical GRIN, it can be put into a form much more amenable for optimisation in optical design software. Typically, for LGRIN lenses, the centre of the spherical GRIN distribution is a significant distance away from the lens surfaces along the optical axis, a position along the optical axis we define as z_0 as shown in Figure 5.1. This distance is a necessary constraint of the moulding process, as indicated in Figures 1.2 and 5.3. The value of z_0 is also typically an optimisation variable, as it has a significant impact on the optical power of the GRIN. The form of Equation 5.1 is very poor for optimisation, as changes in z_0 cause the GRIN distribution to move relative to the lens vertex. The result of this approach is lens optimisations frequently become "stuck", as multiple variables must change simultaneously to improve the lens. It is much more preferable to separate the variation of z_0 and the GRIN polynomial terms, and furthermore, place the origin of the GRIN polynomial at the lens vertex. To perform this separation, we define a local radius, R_{loc}, given by

$$R_{\text{loc}} = R - z_0. \tag{5.2}$$

We then change the variable of our GRIN polynomial to R_{loc},

$$N\left(R_{\text{loc}}\right) = \mathcal{N}_0 + \mathcal{N}_1 R_{\text{loc}} + \mathcal{N}_2 R_{\text{loc}}^2 + \mathcal{N}_3 R_{\text{loc}}^3 + ... \tag{5.3}$$

Figure 5.1 shows an example of such an offset spherical GRIN representation. The origin of the spherical GRIN iso-indicial contours lies outside the lens. x_{len}, y_{len} and z_{len} represent the Cartesian coordinates of any point inside the GRIN with respect to the origin of the lens surface, as will generally be used by commercial optical design software such as CodeV or Zemax. At a given point within the lens, the GRIN iso-indicial contour radius is given by

$$R_{\text{contour}}^2 = x_{\text{len}}^2 + y_{\text{len}}^2 + \left(z_{\text{len}} - z_0\right)^2. \tag{5.4}$$

Expressing the refractive index as a function of R_{loc} decouples the origin which controls the contour curvature from the origin which controls the index polynomial, and allows much more stable optimisation. In order to model accurately a GRIN lens made from any two known materials (say A and B), one must also consider chromatic dispersion effects. LGRIN can be modelled as a mixture of the two constituent materials where the index varies linearly with the volumetric proportion of each material between the properties of A and B, as outlined in Section 2.5.5. Experimentally, such a linear scaling law has been shown to be valid [39] within the repeatability of the LGRIN fabrication process. Due to the fact this refractive index change is linear with relative composition, it is possible to generate a wavelength-dependent scaling coefficient, $C(\lambda)$, defined as the ratio of the index change at a given wavelength to the index

101

change at a reference wavelength

$$C(\lambda) = \frac{\Delta N(\lambda)}{\Delta N(\lambda_{\text{ref}})}, \tag{5.5}$$

where

$$\Delta N(\lambda) = N_B(\lambda) - N_A(\lambda). \tag{5.6}$$

We then define the refractive index polynomial as a base material, $N_A(\lambda)$ plus an index variation as a function of space multiplied by $C(\lambda)$, given by

$$N(R_{\text{loc}}, \lambda) = N_A(\lambda_n) + C(\lambda) \left[\mathcal{N}_0 + \mathcal{N}_1 R_{\text{loc}} + \mathcal{N}_2 R_{\text{loc}}^2 + \mathcal{N}_3 R_{\text{loc}}^3 + \ldots \right]. \tag{5.7}$$

$C(\lambda)$ is required to model the GRIN at any wavelength other than λ_{ref}. In the case where $\lambda = \lambda_{\text{ref}}$, $C = 1$. The refractive index coefficients $\mathcal{N}_0, \mathcal{N}_1, \ldots$ therefore define the GRIN at $\lambda = \lambda_{\text{ref}}$. In the case where the square bracketed term of Equation 5.7 equals $\Delta N(\lambda_{\text{ref}})$, $N(\lambda) = N_B(\lambda)$.

For optimisation it is useful to add a variable $\mathcal{N}_0$ term. This essentially changes the starting material at $R_{\text{loc}} = 0$. An $\mathcal{N}_0$ value equal to $\Delta N(\lambda_{\text{ref}})$ represents a full transition to material B, whilst retaining the correct dispersion properties. The index variation generated by the bracketed term must be constrained to within $\Delta N(\lambda_{\text{ref}})$ over a GRIN lens volume to avoid the design of an un-manufacturable material.

5.4. Trade-off Study of Colour Correction Methods

To investigate the aberration correction properties of LGRIN lenses, a lens parameter study was undertaken into the performance of simple, single-element systems of various F/# and field-of-view (FOV) configurations. Sets of GRIN, spherical doublet, aspheric doublet and diffractive lenses were designed according to a basic specification listed in Table 5.1. The material combination used for the GRIN lenses was PMMA-SAN17 (ΔN=0.085, V_{GRIN}=6.16). The effectiveness of GRIN lenses is heavily dependent upon the lens thickness, therefore to ensure a fair comparison between lenses, the axial thicknesses of each lens was held constant at 10 mm.

Parameter	Value(s)
Focal Length	50 mm
Entrance Pupil Diameter (EPD)	5, 10, 15, 20, 25 mm
Field of View	0, 4, 8°
Waveband	450-650 nm, uniform spectral weighting
Image Plane Curvature	Curved image plane permitted
Lens Thickness	10 mm max
RMS Spot Size	To be minimised

Table 5.1: Colour correction trade study lens specification

5.5. Optimisation

Material selection for the glass doublets was limited to commercially available glasses from Schott and Ohara. The CodeV macro "glassexpert.seq" was used to efficiently find optimal glass choices, thicknesses and curvatures over the full range of fields and apertures of the trade study (30 glass designs in total). The material pairings chosen were required to be thermally stable by means of a tolerance on glass coefficient of thermal expansion (CTE) mismatch. Any doublet glass combination which demonstrated a deviation greater than 0.1µm/K over the clear aperture was rejected.

The RMS spot size of the trial GRIN lenses was optimized using the CodeV automatic design (AUT) option. It was necessary to control the refractive index limits of the GRIN lenses during optimization to prevent un-manufacturable solutions from being generated. This was done via user-defined constraints within the optimiser. Maximum and minimum refractive index limits were defined as the pure forms of each constituent material of the GRIN. For computational simplicity, the refractive index profile was constrained at the optical axis and the clear aperture (Figure 5.2). This was generally effective as the index extremes within the GRIN lenses tended to occur along the optical axis and at the clear aperture. The index control process was further simplified by the rotational symmetry of the system. It was also important to control the GRIN contour origin offset, z_0. Left unconstrained this had a tendency to produce solutions with the origin of the GRIN contours internal to the lens itself which is infeasible to manufacture via the LGRIN process. A basic moulding feasibility constraint was added, which did not allow the GRIN curvature origin, z_0, any closer to the lens vertex than the size of the adjacent clear semi-aperture. This avoids the scenario shown in the left-hand side of Figure 5.3. Finally, as both surfaces of the GRIN lens are diamond turned, variable aspheric terms were added to combine with the GRIN properties for monochromatic aberration correction. The number of variable aspheric terms was increased progressively until the optimization process stagnated.
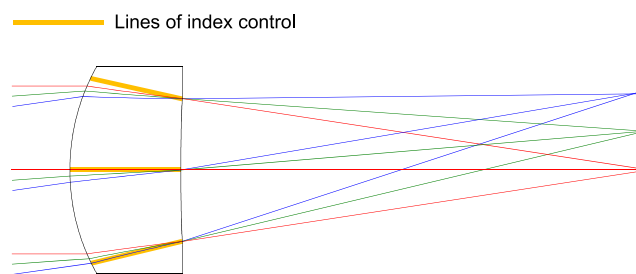
Figure 5.2: Regions of a GRIN lens where the index is constrained in optimisation along the optical axis and at the lens clear aperture.
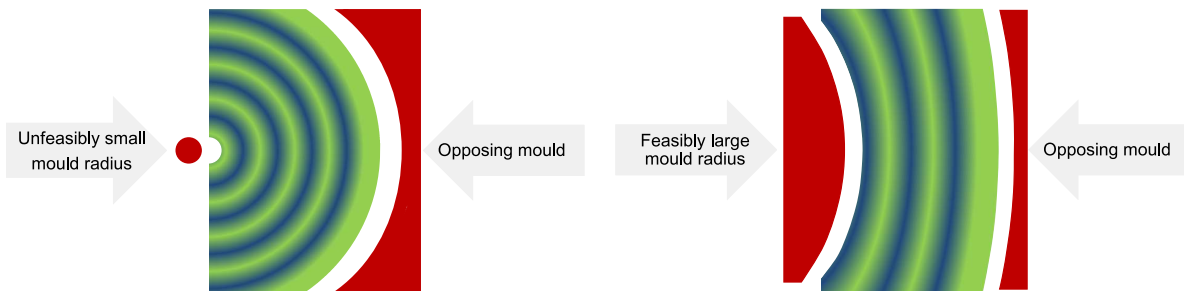
Figure 5.3: Large and small mould radius scenarios.

5.6. Results

The RMS spot size over the field of view was recorded for each trade space lens. The lens designs and RMS spot size values are shown in Figures 5.4 and 5.5 for the axial lens specification, 5.6 and 5.7 for the 4° field specification, and 5.8 and 5.9 for the 8° field specification.

Non-linear growth was observed in the axial RMS spot size versus entrance pupil diameter (EPD) of each solution type with the exception of the diffractive solution. Particularly rapid growth was seen in the RMS spot size of the spherical doublet solutions. At the edge of the field of view, the performance of each solution type is broadly similar. For the widest angle solutions with a field of view of 8°, some greater variation in spot size is observed with the diffractive and GRIN lenses outperforming the doublet lenses. The spherical doublets show particularly rapid growth in on-axis spot size due to the onset of spherical aberration. As colour correction is a key objective of GRIN lens use, the percentage variation of the focal length against wavelength was recorded for each solution type (Figure 5.10).

Achromatic correction was observed for the 5 mm, 10 mm and 15 mm EPD GRIN lenses. This comes in the form of a U-shaped variation of focal length with wavelength. Beyond 15 mm EPD a progressive breakdown in the level of correction occurred. The variation of focal length with wavelength becomes gradually more "hockey stick" shaped, with a progressively smaller region of the waveband corrected for two wavelengths. Chromatic aberration remains well-controlled by both the spherical and the aspheric doublets over the full aperture range. The diffractive solution shows a fixed level of secondary spectrum for all EPD values. Note that the secondary spectrum profile is inverted due to the negative chromatic dispersion of the diffractive surface. All solutions showed a steady loss in off-axis performance due to astigmatism which cannot be corrected in simple lenses located at the aperture stop.
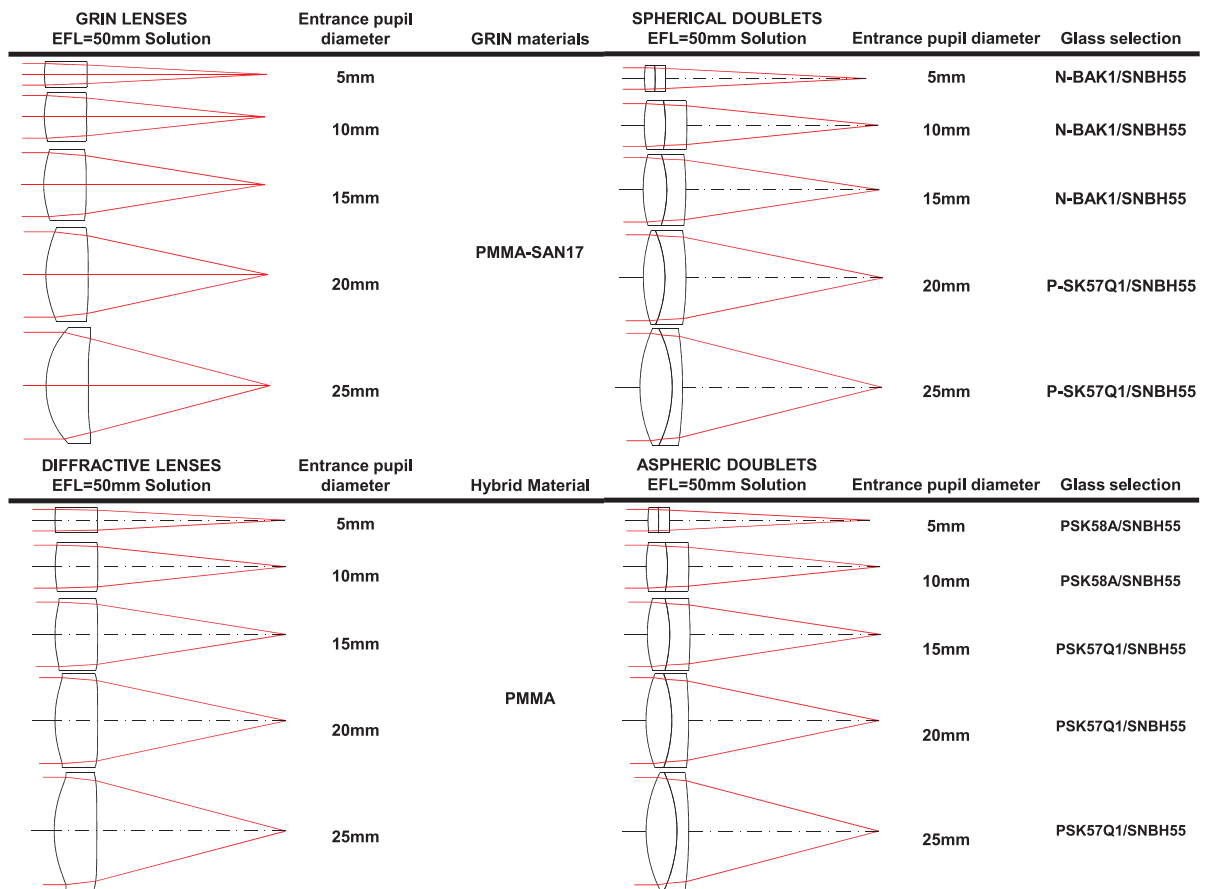
Figure 5.4: Trade study lens designs for the axial specification.
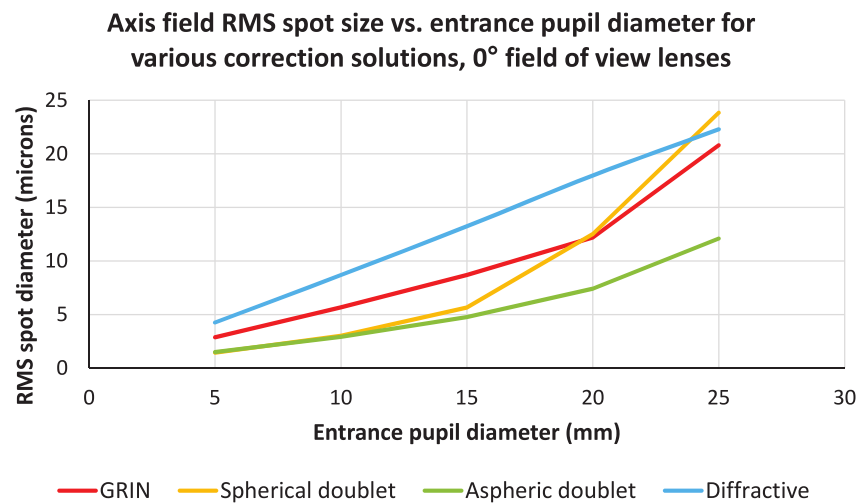
Figure 5.5: Trade study RMS spot sizes for the axis-only field of view specification.

Figure 5.6: Trade study optical designs for the 4° field of view specification.
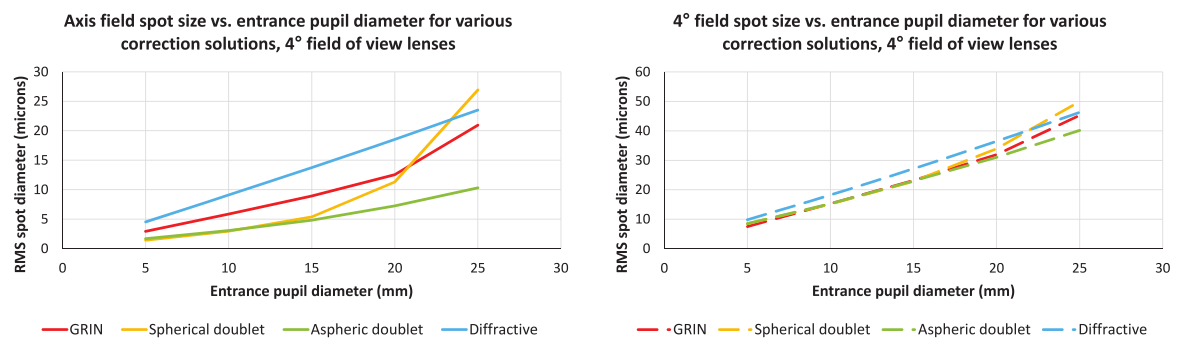
Figure 5.7: Trade study RMS spot sizes for the 4° field of view specification.
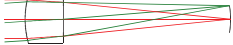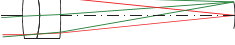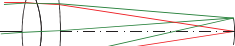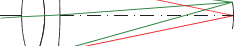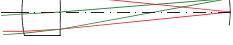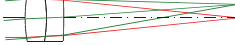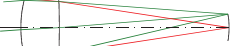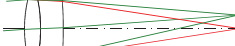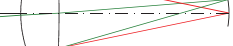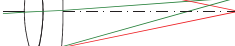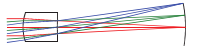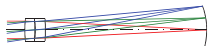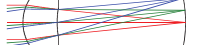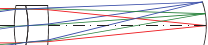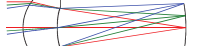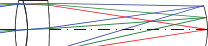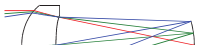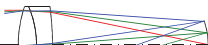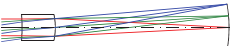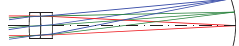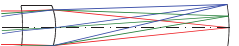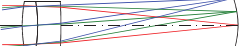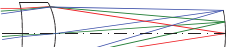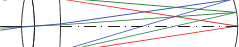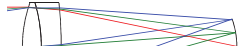
GRIN LENSES EFL=50mm Solution	Entrance pupil diameter	GRIN materials		SPHERICAL DOUBLETS EFL=50mm Solution	Entrance pupil diameter	Glass selection
	5mm				5mm	N-SK2HT/SNBH55
	10mm				10mm	N-SK2HT/SNBH55
	15mm				15mm	N-SK2HT/SNBH55
	20mm	PMMA-SAN17			20mm	N-SK2HT/SNBH55
	25mm				25mm	N-LAK12/SNBH55

DIFFRACTIVE LENSES EFL=50mm Solution	Entrance pupil diameter	Hybrid Material		ASPHERIC DOUBLETS EFL=50mm Solution	Entrance pupil diameter	Glass selection
	5mm				5mm	PSK58A/STIH23
	10mm				10mm	PSK58A/STIH23
	15mm				15mm	PSK58A/STIH23
	20mm	PMMA			20mm	PSK58A/STIH23
	25mm				25mm	PSK58A/STIH23

Figure 5.8: Trade study optical designs and for the 8° field of view specification.

Axis field spot size vs. entrance pupil diameter for various correction solutions, 8° field of view lenses

4° field spot size vs. entrance pupil diameter for various correction solutions, 8° field of view lenses

8° field spot size vs. entrance pupil diameter for various correction solutions, 8° field of view lenses
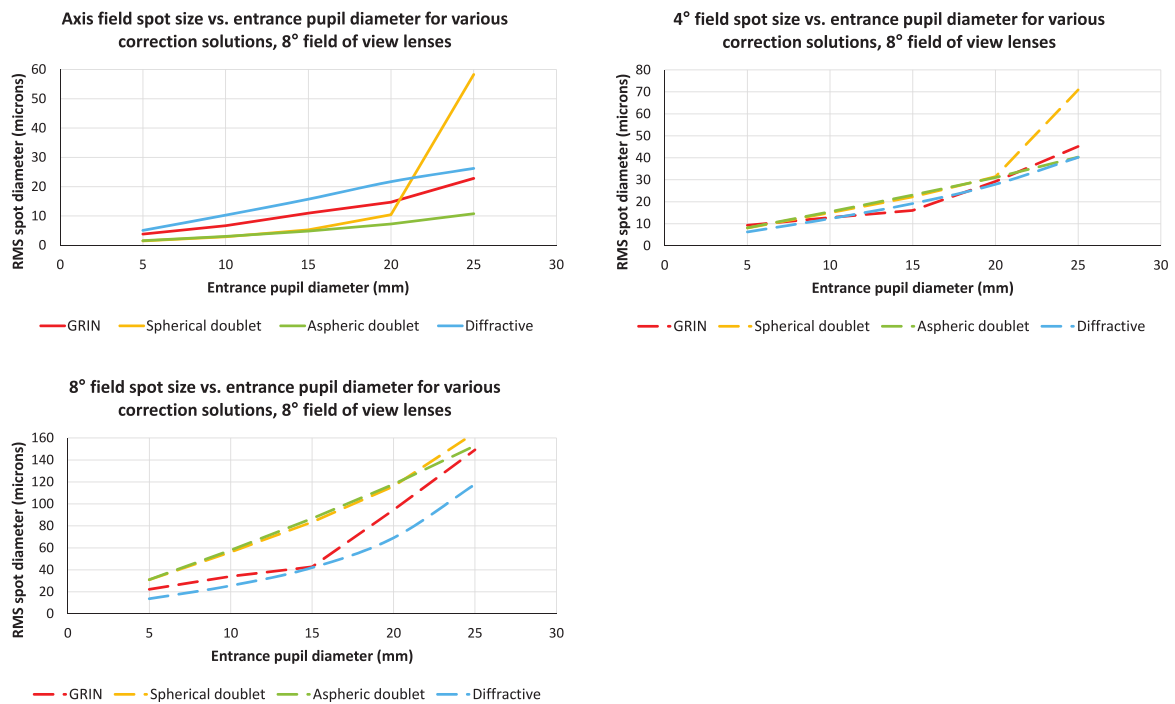
Figure 5.9: Trade study RMS spot sizes for the 8° field of view specification.
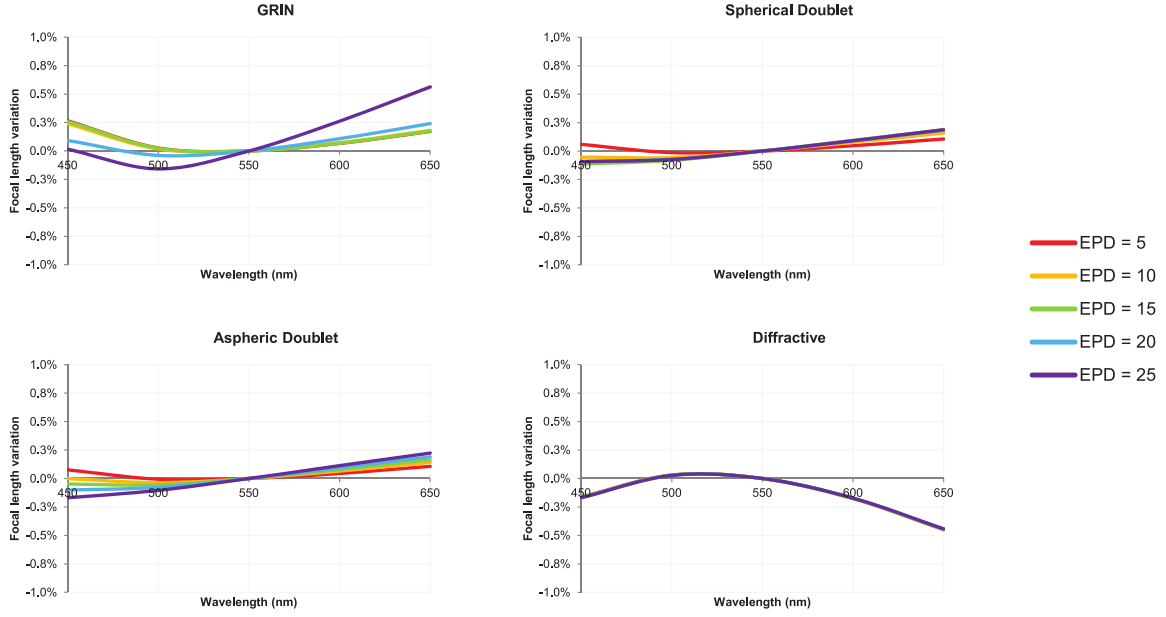
Figure 5.10: Percentage focal length variation of axial field 50 mm designs for several entrance pupil diameters.

5.7. Discussion

It was observed that it is possible to correct axial colour for GRIN, diffractive and doublet designs at modest aperture values (EPD=5-15 mm, corresponding to F/10-3.33). Within this range, the spherical doublet surfaces are capable of controlling spherical aberration and coma to an adequate degree. We observe better RMS spot size performance from the doublet at these smaller apertures due to reduced secondary spectrum. This is due to the fact that the glass doublet solutions have the design freedom to select an optimal material combination, whereas the diffractive-refractive hybrid and GRIN solutions are constrained in their material selection.

At the full aperture of 25 mm, each solution type is limited by different aberrations. These are apparent when one observes the transverse ray errors for the axial field (see Figure 5.11). The GRIN optic is limited by loss of colour correction whilst providing some compensation through control of spherical aberration and spherochromatism. The spherical doublet no longer has the ability to control spherical aberration due to the lack of an aspheric surface. The hybrid-diffractive lens controls spherical aberration and chromatic aberration well, but is limited by the secondary spectrum caused by combining a diffractive (that has linear dispersion and $P_{g,F} = 0.3$) with refractive optical power from the PMMA substrate ($P_{g,F} = 0.53$). There are also practical limits to manufacturing a diffractive component due to the fact that as the aperture expands the zone spacing becomes progressively smaller, eventually becoming impractical. For zone spacings of ≈ 10 wavelengths or less, the thin phase approximation used in their design begins to break down, leading to a requirement for highly complex, rigorous diffraction analysis of the lens or the risk of ghosting and efficiency loss. The best overall performer was the aspheric doublet which can suppress secondary chromatic aberration and spherical aberration, being limited by a small amount of spherochromatism. Such a solution could prove costly however if the aspheric surfaces cannot be generated by an economical process such as precision moulding (that also requires a suitable glass type).

Axial transverse errors of GRIN,
hybrid and doublet 4° singlets (mm)

	650.0000 nm
	600.0000 nm
	550.0000 nm
	500.0000 nm
	450.0000 nm

GRIN

Doublet

Hybrid
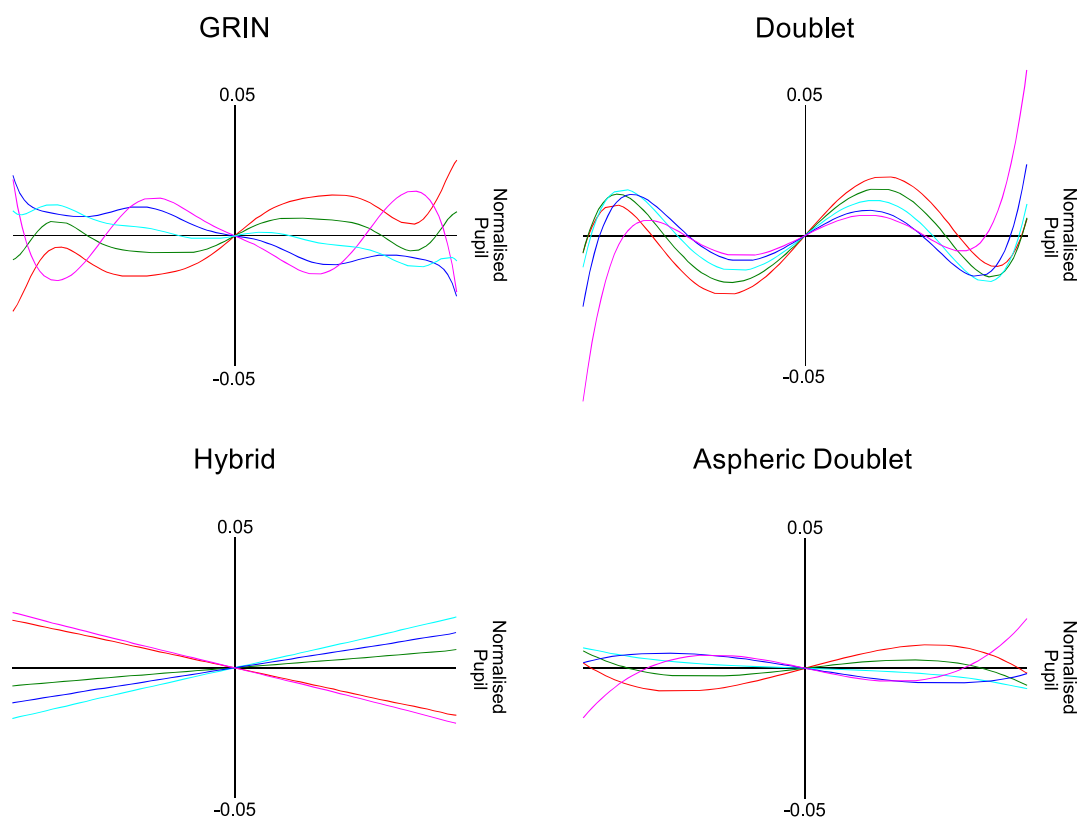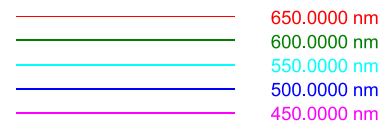
Aspheric Doublet

Figure 5.11: Transverse ray aberrations of GRIN, doublet, diffractive and aspheric doublet 4° FOV designs (EPD=25 mm).

The loss of colour correction for a spherical GRIN depends on two factors. Firstly, the loss of surface-based correction due to the changing shape of the lens and secondly, the loss of correction from the GRIN transfer contributions due to the limited ΔN and gradual decrease in curvature of the GRIN contours. The second factor occurs due to the need to retain an aspect ratio of the GRIN that is feasible for moulding, as shown in Figure 5.3.

5.7.1. Challenging the F/# limits of GRIN Correction

By considering the current limitations of GRIN materials, we propose some future developments which can offer improvements in performance at faster F/#s. Three candidate technologies were considered:

- Negative V_{GRIN} materials
- Increased ΔN material combinations
- Radial GRIN distributions

Each of these technologies were considered in turn and applied to the 25 mm EPD, 4° FOV design.

Negative V_{GRIN} GRINs are generated by selecting a pair of compatible materials whereby the higher index material has lower dispersion than the low index material. We recall and inspect Equation 1.29 for the Abbé value of a GRIN material. Zero-dispersion GRIN occurs where the ΔN is identical at long and short wavelengths, and dispersion becomes negative when the high index material is less dispersive than the lower index material. Take for example the glasses N-LAK14 and F2 (shown in Figure 5.12). Traversing the glass chart in from top left to bottom right generates a GRIN with a negative V_{GRIN} dispersion value of -17.559 as opposed to the opposite diagonal where a combination of SK5 and N-BASF64 gives a V_{GRIN} value of 13.894.

This approach shows particularly strong potential for aberration correction as it allows the reduction of chromatic aberration using positive power. This allows reduction of the surface curvatures of the lens which in turn reduces monochromatic aberrations. A design was generated where the GRIN was composed of polycarbonate and a hypothetical material of equivalent dispersion characteristics to the Schott glass N-LAK7*. This GRIN had a V_{GRIN} value of -5.25 and a ΔN of 0.064. In Figure 5.13 we observe reduced aspheric departure in the optical surfaces of the negative V_{GRIN} design compared to the positive V_{GRIN} case. This leads to reduced contributions from higher-order aberrations which generally limit the performance of lenses at wider apertures. In Figure 5.14, reduced axial colour and spherochromatism was observed as a result of the improved power balance.

Another effective approach to improve aberration correction of an LGRIN lens at faster F/# is to increase the available index difference between the low and high index material. One such possibility for increased ΔN was prototyped at Polymerplus LLC. A mixture of PVDF and PMMA was used to reduce the refractive index of the low index GRIN material. Pure PVDF is a crystalline material which is unsuitable for extrusion, but when blended correctly with PMMA forms a low-index, low-dispersion starting material which can be extruded. This approach extends the ΔN to 0.129 from the 0.085 available with a PMMA-SAN17 GRIN.

---

*This combination is not directly representative of manufactured GRIN material, however similar optical properties have been demonstrated by NanoVox [29].
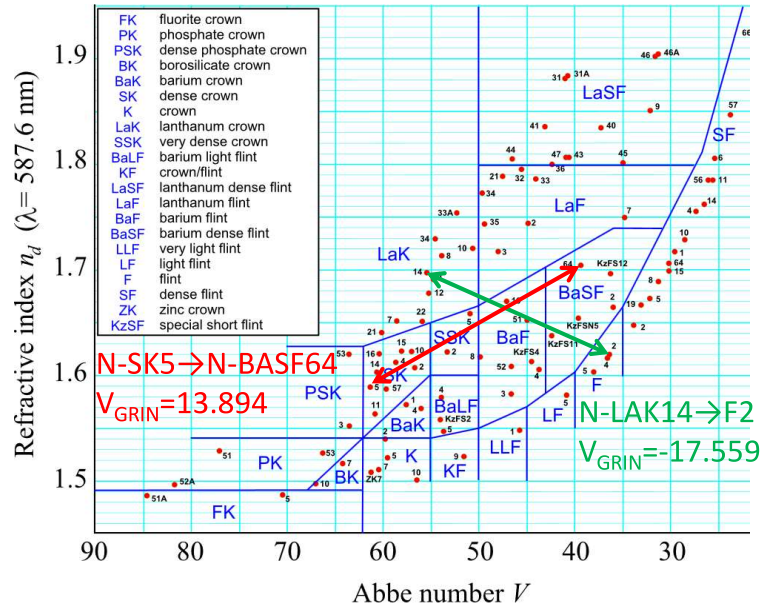
Figure 5.12: Illustration of both negative and positive V_{GRIN} material combinations. [2]

PMMA-SAN17, ΔN=0.085

Polycarbonate-NLAK7, ΔN=0.064
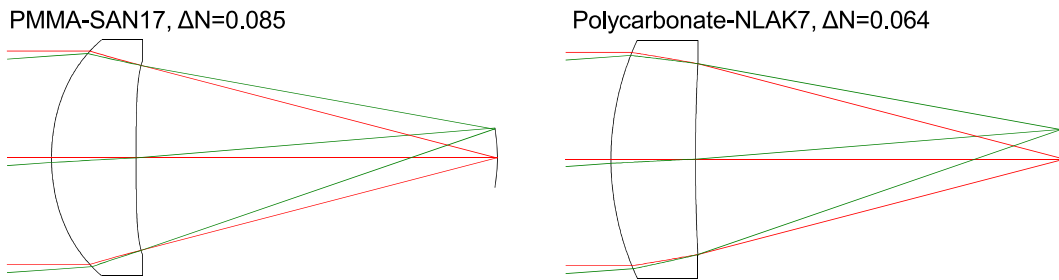
Figure 5.13: Optical design cross sections of positive and negative V_{GRIN} solutions, EPD=25 mm

Axial transverse errors (mm) of positive and negative V_{10}, 4° lenses (50mm EFL, 25mm EPD)

650.0000 nm
600.0000 nm
550.0000 nm
500.0000 nm
450.0000 nm

PMMA-SAN17

V_{10}=6.16

PCARB-NLAK7

V_{10}=-5.25
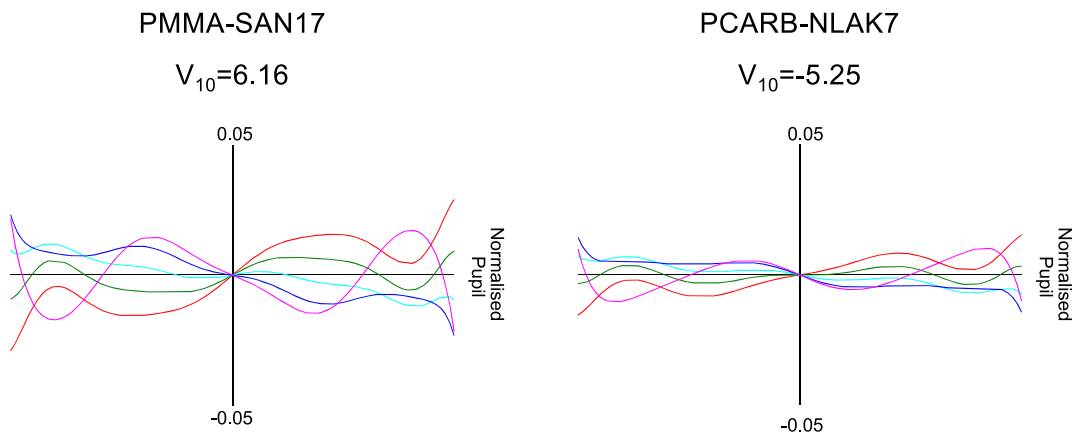
Figure 5.14: Transverse ray aberrations of positive and negative V_{GRIN}, 4° FOV designs.

111

PMMA-SAN17, ΔN=0.085

PVDFb-SAN17, ΔN=0.129
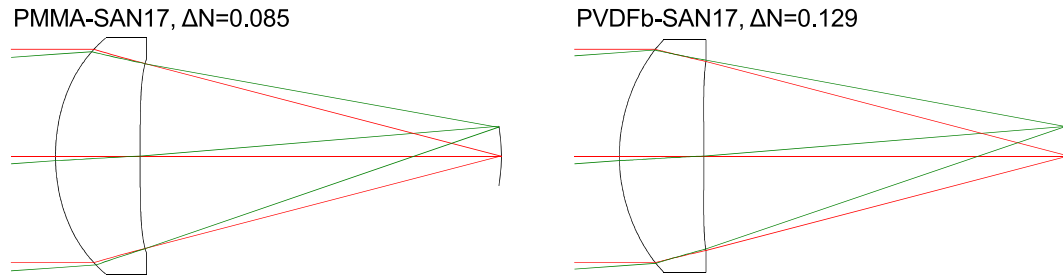
Figure 5.15: Optical design cross sections of PMMA-SAN17 and PVDFb-SAN17 GRINs

Axial transverse ray errors (mm) of
PMMA-SAN17 and PVDFb-SAN17 4°
GRIN lenses (50mm EFL, 25mm EPD)

650.0000 nm
600.0000 nm
550.0000 nm
500.0000 nm
450.0000 nm

PMMA-SAN17
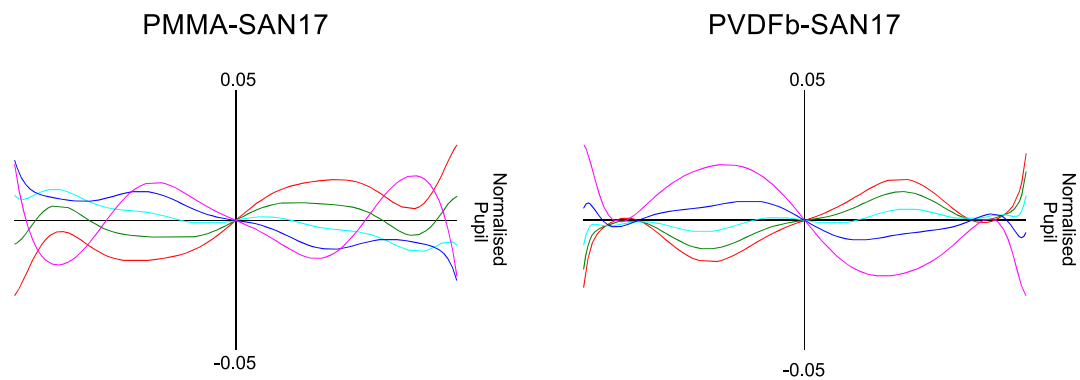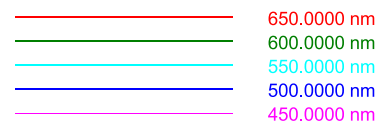
PVDFb-SAN17

Figure 5.16: Transverse ray aberrations of PMMA-SAN17 and PVDFb-SAN17 4° FOV designs.
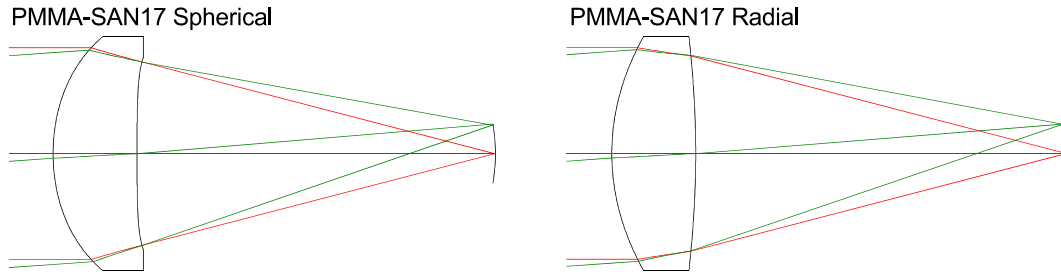
Figure 5.17: Optical design cross sections of PMMA-SAN17 spherical and radial GRINs, 4° FOV.
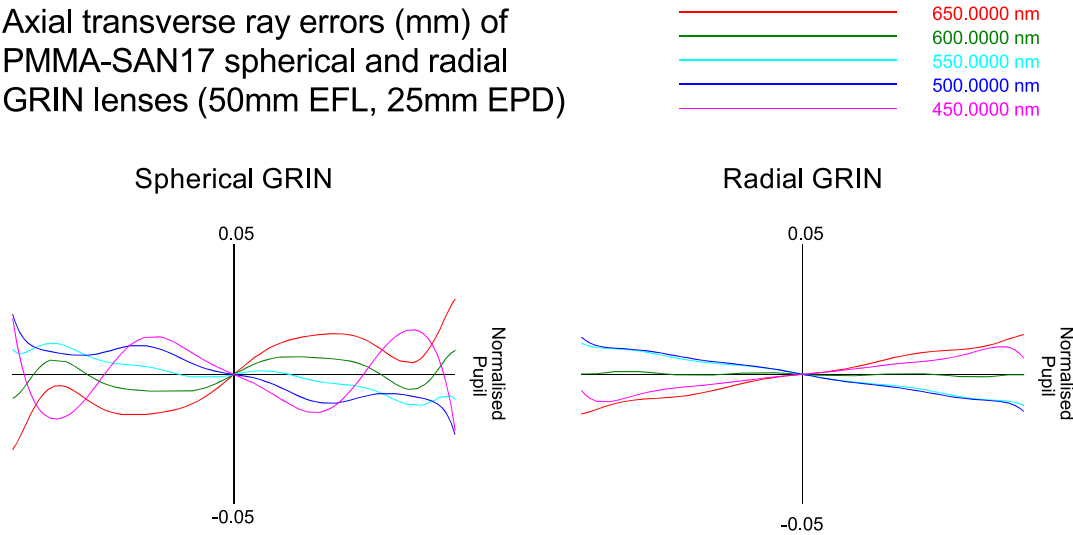
Figure 5.18: Transverse ray aberrations of PMMA-SAN17 spherical and radial GRINs, 4° FOV.

Figure 5.15 demonstrates the effect of a larger ΔN on the optical design. In this case the starting material on the convex first surface has lower index. This leads to this particular aspheric surface having a tighter base radius of curvature of 20.22 mm, reduced from 24.38 mm. In Figure 5.16 the effect of this higher ΔN, lower V_{GRIN} dispersion GRIN on image quality is exhibited. The lower dispersion reduces the influence of the GRIN on colour correction and has resulted in increased axial colour. This has been balanced with spherochromatism in the solution. Such a component may be useful in improving systems limited by spherochromatism, an aberration which is difficult to correct with conventional lenses.

Finally, changing the GRIN geometry inside the lens can have a significant effect upon its correction capability. In the case of our singlet components, the curvature of the spherical GRIN tends toward the tightest possible value subject to our moulding rule outlined in Figure 5.3. This implies the GRIN needs to be more radial in nature as defined in Equation 1.26. Radial GRINs are currently not supported in LGRIN manufacture, but we can nonetheless model the optical properties such a solution would provide. A radial GRIN was therefore designed with an index distribution in the form of Equation 1.26 and with the same PMMA and SAN17 base materials as the LGRIN solutions.

The change in lens form of the radial GRIN solution is shown in Figure 5.17. It was observed that the aspheric departure of the GRIN optical surfaces had reduced as well as the lens "bending factor", yielding a biconvex component. Surface one aspherically departs by 0.1397 mm compared to 0.2250 mm for the LGRIN solution; surface two now departs from spherical

113

Axial RMS spot size of F/2 lens correction solutions
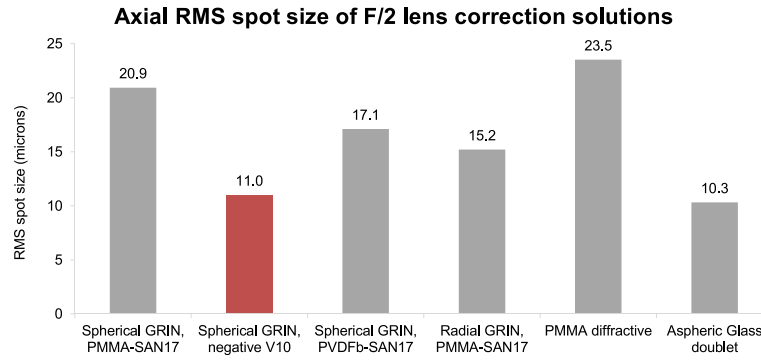
Figure 5.19: Comparison of axial RMS spot size for future and current aberration correction methods.

by 0.0398 mm compared to 0.2182 mm. Figure 5.18 demonstrates the effect of a radial profile on the transverse ray errors. It is observed that the level of spherochromatism has been dramatically reduced, leaving the system limited by secondary spectrum only. This is intrinsic to the material selection of the lens. If anomalous dispersion plastics could be developed for LGRIN materials, the level of correction could be improved further yet. Radial GRINs show great potential to correct aberrations over an extended field of view, they are particularly effective in eyepiece designs where there is significant pupil separation over the lens surfaces, as demonstrated by Visconti et al. [89].

The efficacy of these next generation GRIN technologies was compared to current technology by evaluation of the axial RMS spot size. In Figure 5.19 we observe that negative V_{GRIN} shows the greatest aberration correction potential. A spherical GRIN of PVDFb and SAN17 comes in second place, followed closely by a radial GRIN of PMMA and SAN17. Significantly we observe that all GRIN solutions produce a spot size smaller than that of a diffractive surface turned onto a PMMA aspheric lens.

5.8. Conclusion

GRIN lenses offer great potential to improve optical systems with respect to their size and mass. Polymer GRIN lenses give the optical designer a new degree of freedom to correct chromatic aberrations within visible optical systems. It was shown that spherical GRINs composed of PMMA-SAN17 can provide aberration correction comparable to achromatic doublets or hybrid refractive-diffractive lenses. This similarity was demonstrated over a range of fields of view from 0-8° and a range of entrance pupil diameters from 5-25 mm. This GRIN correction capability currently degrades with faster F/# due to the GRIN geometry and magnitude of the ΔN and V_{GRIN} dispersion values. Further development of the underlying polymers that form the GRIN material to incorporate negative V_{GRIN} properties and greater ΔN values will improve this further by allowing a greater proportion of aberration correction to take place within a single lens element. Development in this area has the potential to enable GRIN lenses to become the optical correction solution of choice for lightweight, high-performance imaging systems.

6

Optical Design of Freeform-GRIN Lenses for Avionics

The contents of this chapter are derived and expanded from *"Optical design of a freeform, gradient-index, head-mounted display - Optical Engineering Vol. 62, No. 7, Jul 2023"* [3, AMBref].

6.1. Abstract

We present the results of an optical design study into the performance benefits of non-rotationally-symmetric "freeform" gradient-index (GRIN) media on a pupil-relay head-mounted display (HMD). A range of design variants are presented based on freeform-GRIN lenses consisting of ternary base material combinations, enabled by recent developments in additive manufacture. The optical performance of these designs is compared to homogeneous solutions comprising combinations of spherical, aspheric, toric and freeform surfaces. We show that freeform-GRIN media represent powerful degrees of freedom for aberration correction in tilted and off-axis optical systems, performing comparably to homogeneous freeform optics whilst illustrating significant potential reductions in lens count and mass.

6.2. Introduction

The recent development of new GRIN manufacuture methods, particularly additive manufacture techniques [29, 30, 35], demonstrate the potential to manufacture visible waveband GRIN lenses of arbitrary distribution with rotational symmetry about an optical axis no longer a constraint. Concurrently, there is also significant interest in freeform surfaces that lack any axis of symmetry. Freeform surfaces are well documented as a degree of freedom suitable for the correction of aberrations in asymmetric systems caused by the tilt and decentre of optical components [90, 91].

Helmet and Head-Mounted Displays (HMDs) are two system types in particular that obtain optical performance benefits from freeform optics. HMD systems see broad applications such as avionics for defence and aerospace applications and mixed-reality goggles. HMDs typically
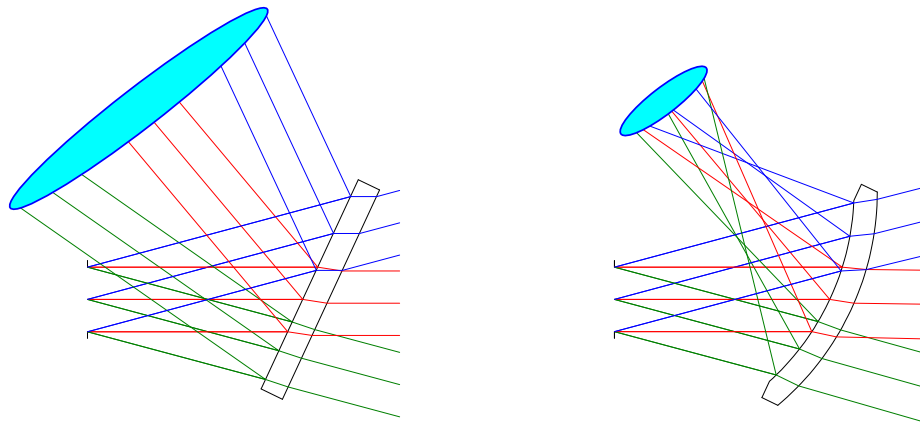
Figure 6.1: Two types of combiner surface interacting with a remote pupil. Left: the planar combiner introduces no aberration but the necessary collection aperture for relay optics (shown in aqua) is very large. Right: the use of a curved combiner creates an intermediate image which significantly reduces the collection aperture of the relay optics, but the powered and tilted surface introduces aberrations.

project information into the eye of a user via a semi-reflective component known as a combiner. The outside world is simultaneously transmitted through the combiner, allowing symbology to be overlaid for the user. For the optics not to clash with the user's head, it is fundamentally necessary to break rotational symmetry of the optical system.

It is often beneficial to the size and mass of the projection optics to make the combiner curved, giving it converging optical power in reflection. This approach is illustrated in Figure 6.1. On the left, ray bundles from the eye box continue to diverge following reflection off a planar combiner, and thus require a much larger collection aperture for the projection optics (illustrated approximately as a cyan ellipse). Such a collection optic becomes larger and heavier than powered alternatives and may not conform to the often challenging space envelopes required of avionic systems. The right-hand side of Figure 6.1 illustrates the effect of a powered combiner. The bundles of rays now converge to an intermediate image and subsequent relayed pupil, requiring a significantly smaller collection aperture than a planar combiner. A curved combiner of uniform thickness also generates a small amount of optical power in transmission that affects perception of the outside world. This effect is minimised by making the combiner as thin as practical whilst being constructed from a low refractive index material. Alternatively, the curved combiner surface may be "buried" at the interface between two lenses with planar exterior surfaces or even implemented as a volume hologram.

There is a trade-off associated with the use of a tilted, powered combiner however, as a highly aberrated intermediate image is generated. These aberrations must be equal and opposite to the relay optics in order to provide satisfactory image quality to the user. The rotational asymmetry of these aberrations necessitates asymmetry in the optics of the relay lens. Due to the inherent difficulty in the manufacture of non-rotationally-symmetric optical surface geometries, this is conventionally achieved through the use of multiple tilted and decentred spherical (and aspheric) lenses.

Cylindrical and toric surfaces are also a powerful degree of freedom for the correction of asymmetric aberrations. Their two radii of curvature in separate azimuths make them particularly apt for the correction of astigmatism, whilst their geometrical form retains an axis of symmetry that makes them more amenable to conventional optical polishing and turning

116

processes than true freeform surfaces.

True freeform surfaces lack any degree of rotational symmetry. This represents both a powerful design degree of freedom and a manufacturing challenge. Their usefulness in the correction of aberrations of tilted and decentred optical systems as well as head-mounted displays has been widely demonstrated in the literature [90, 92]. Their lack of rotational symmetry prevents their manufacture by conventional lap polishing processes, with techniques such as CNC grinding and polishing required to generate the required departure in form and slope from a sphere. A further challenge in freeform manufacture lies in the required metrology processes. The lack of an axis of symmetry requires precise alignment of the part under test with respect to a sufficient number of datum features to constrain fully translation and rotation.

Cylindrical, toric, and freeform surfaces can also be applied to the reflective combiner surface [92]. This approach has advantages and disadvantages. From an aberration correction standpoint, it is beneficial to reduce the aberrations of the combiner where they are generated, reducing the magnitude of aberrations that must be corrected in the projector optics, and potentially simplifying their construction. This method is not a panacea however, with significant remaining aberration transfer between the combiner and projector that must be corrected by correspondingly non-rotationally-symmetric degrees of freedom. One must also note that application of a freeform or similar surface form to one side of a combiner necessitates that the same surface deformation be applied to the other, to avoid distortion and parallax of the outside world, which may add manufacturing complexity compared to a spherical combiner.

A further significant design challenge for HMDs concerns the correction of chromatic aberrations. The relay lenses of HMD systems are generally refractive in nature, whilst modern LED light sources emit a finite waveband. The chromatic dispersion of lens elements leads to axial and lateral colour over the lens field of view, whilst prismatic effects due to the tilt and decentre of lens elements also introduce field-constant lateral colour; all of these chromatic aberrations degrade system resolution. More recently, requirements for full-colour HMDs compound the necessity for chromatic aberration correction. Conventionally, chromatic aberrations in HMD systems are corrected by the combination of lens elements with dissimilar Abbé V values and opposing signs of optical power. Whilst effective, this adds optical components and mass. Diffractive optical elements may also be used in HMD systems. Diffractive optical elements (DOEs) generate extreme optical dispersion with a negative Abbé V value that is highly effective in the removal of chromatic aberrations. They may also be applied to polymer materials via diamond turning or moulding, reducing mass significantly. However, DOEs also diffract light into spurious higher and lower orders. For avionic applications, such diffraction can cause veiling glare and multiple "ghost" images, with a risk that such artefacts can be hazardously misleading to a pilot under challenging environmental conditions.

Another design approach in HMD displays that has been the subject of significant research is the use of pupil-replicating waveguides. Such components function by replicating a collimated pupil over one or more dimensions, via diffraction gratings or alternative mechanisms such as polarisers or microprism arrays [93]. The SWAP-C benefits of waveguides are potentially very significant, as the accompanying optics may be vastly reduced in scale and rotationally symmetric, as the waveguide effectively replaces the combiner. This approach introduces trade-offs however. The pupil replication effect in waveguides means a correspondingly higher luminance must transmit through the projection optics. This higher energy density within the optical system introduces challenges in heat management and athermalisation, with added technical risk attached to the use of polymer lenses due to their lower melting points and

susceptibility to yellowing with time under intense light. The waveguide projection optics must also be very well corrected and collimated, to avoid errors "cascading" over the multiple pupil replications in the waveguide. Furthermore, the efficiency of a waveguide itself must be carefully calibrated over the pupil and field of view for different wavelengths. Otherwise, there is a significant risk of non-uniformity in the colour and brightness over the pupil and field of view of the system, as well as the potential for ghost imaging.

In this work, we examine the application of freeform-GRIN media to HMD optics. We define freeform-GRIN media as continuously varying gradient-index materials that lack any axes of rotational symmetry. A freeform refractive index distribution within a lens of finite thickness causes an optical path difference to transmitted light that is analogous to the function of one or more freeform surfaces (depending on thickness, distribution and index variation). Freeform GRINs have only recently been applied to imaging problems of non-rotationally-symmetric systems . Lippman et al. defined and demonstrated simulations of non-rotationally symmetric GRIN representations, showing their influence on aberrations within imaging systems [46]. Yang et al. demonstrated experimentally that freeform-GRIN lenses can reduce the aberrations of a tilted, spherical mirror [38], while both Yee et al. and Desai et al. showed the promise of the technology in the design of a freeform-GRIN prismatic display [44], and a novel spectrographic GRIN lens that produces a well-corrected image spatially separated by wavelength [94].

Radial-GRIN lenses are a well-known strategy to correct chromatic aberrations [95]. The combination of different materials within a GRIN leads to the generation of a combined Abbé number or V_{GRIN} as defined in Equation 1.29. V_{GRIN} may assume radically different values to homogeneous materials, with highly dispersive values such as $V_{GRIN} < 10$ and even negative dispersion a possibility. As a result of such extreme dispersion characteristics, GRIN media with only modest optical power can be used to correct the chromatic aberrations of optical systems. The development of GRIN polymer materials also enables colour correction in a low-mass component. In this work, we also investigate the colour correction potential of GRINs in HMD systems.

GRIN lenses of freeform distribution have the potential to address a wide range of design problems simultaneously. A single GRIN lens can have attributes of an aspheric/freeform surface and achromatic doublet within a single optical medium. This multiplexing of lens properties has the potential to significantly reduce SWAP-C of HMD optics, by reducing the size and number of lens components.

It is noted that replacing freeform surfaces with freeform media has an effect on the optical manufacture approach, with some transfer of complexity from the optical surfaces to the optical medium. At the time of writing, freeform-GRIN components have been fabricated [38], however significant challenges remain with respect to manufacture of non-planar surfaces, as well as metrology and alignment of the GRIN distribution with respect to the optical surfaces of the GRIN component and during assembly into a multi-element optical system.

6.3. Mathematical Representation of Freeform Surfaces and Gradient Index Media.

We define a coordinate system as the basis for subsequent freeform surfaces and GRIN media in Figure 6.2. In this basis we define a freeform optical surface in Equation 6.1. We represent
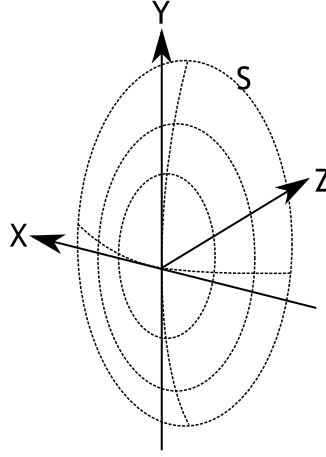
Figure 6.2: Coordinate system definition for optical surfaces in our system. The vertex of each surface is locally defined at the origin of a left-handed Cartesian coordinate system. The z-axis defines surface sagitta and the local optical axis.

a freeform surface with an x-y polynomial appended to a base conic. Whilst the number of potential freeform representations for both GRIN and surfaces is vast and merits further research [46, 96], such an exploration was not possible in this work due to time constraints, with an x-y polynomial considered sufficient for proof of concept of freeform-GRIN media, whilst also being simpler to implement computationally as a GRIN tracing routine. The surface sagitta, $z_{\text{surf}}(x,y)$, of this freeform surface is given by

$$z_{\text{surf}} = \frac{c\rho^2}{1 + \sqrt{1 - (1+k)\,c^2\rho^2}} + \sum_{i=0}\sum_{j=0} B_{ij}x^iy^j, \tag{6.1}$$

where $\rho^2 = x^2 + y^2$ defines the distance from the optical axis, z, k is the conic constant, and B_{ij} are coefficients of non-rotationally-symmetric freeform terms. Herein, we also explore the use of toric surfaces in the optical design of an HMD. Toric surfaces have some of the benefits of a freeform surface, namely by allowing optical power to be split into x and y components. We define a toric surface by rotation of a circle of radius, $r_x = 1/c_x$ in the x-z plane about the y-axis over a radius $r_y = 1/c_y$. The surface sagitta of such a "y-toric", z_{toric}, is given by [97]

$$z = r_x - \left[\left(\sqrt{r_y^2 - y^2} + r_x - r_y\right)^2 - x^2\right]^{\frac{1}{2}}, \tag{6.2}$$

where r_x and r_y are the x and y axis radii of curvature respectively. Both the x-y polynomial and toric surface representations can be modelled in CodeV without customisation.

To define a freeform GRIN distribution, we follow a broadly analogous approach to the x-y polynomial surface, which we adapt to a multi-material GRIN representation in three dimensions. In Chapter 2, a mathematical representation was outlined for such a general multi-material GRIN whereby the refractive index is computed based on the relative composition of a number of constituent materials. The refractive index at a point, P, for a combination of three base materials: A, B, and C of respective refractive indices: $N_A(\lambda)$, $N_B(\lambda)$, and $N_C(\lambda)$ is given by

$$N(P,\lambda) = \frac{N_A(\lambda)m_A(P) + N_B(\lambda)m_B(P) + N_C(\lambda)m_C(P)}{m_T(P)}, \tag{6.3}$$

where $m_T(P) = m_A(P) + m_B(P) + m_C(P)$ and the quantity $m_\mu(P)/m_T(P)$ describes the relative composition of the μth material at a given point within the lens. $m_\mu(P)$ must be positive at all points within the lens. To impart freeform degrees of freedom, $m_\mu(P)$ was defined as a polynomial in even powers of ρ plus an x-y polynomial (analogously to Equation 6.1) about the surface vertex of the GRIN lens. Furthermore, as freeform GRINs can have refractive index variation in three dimensions, each $m_\mu(P)$ coefficient was allowed to vary as a function of z, giving

$$m_\mu(P) = m_\mu(x, y, z) = \sum_{\mu=1}^{M} \sum_{k=0} z^k \left(\sum_{l=0} m_{\mu l k} \rho^l + \sum_{i=0} \sum_{j=0} m_{\mu i j k} x^i y^k \right). \tag{6.4}$$

Here, we apply an additional sum of rotationally symmetric terms defined by the $m_{\mu l k}$ coefficients. At first the additional rotationally symmetric terms defined by the $m_{\mu l k}$ coefficients appear degenerate as, for example, $\rho^4 = x^4 + 2x^2y^2 + y^4$. However, if used correctly, they are important for improving the conditioning of the freeform GRIN optimisation problem. It is often useful to constrain multiple terms to vary in unison to address specific aberrations (for example, variation in ρ^4 near to the aperture stop of a lens allows control of spherical aberration). If left to vary independently, three terms in an x-y polynomial (coefficients of $x^4, 2x^2y^2, y^4$) must vary together to achieve this, which increases the risk of descent into a poor local minimum and increases computation time as three finite differences must be computed by raytracing the system. In the ρ^4 basis, the same can be achieved by varying a single coefficient*. Such an approach also allows a starting solution to be designed with rotational symmetry, before applying tilts and decentres to surfaces such as the combiner.

Of all the terms in Equation 6.4, many can also be redundant depending on the symmetry of the design problem. For example, for an optic with symmetry about the y-z plane (as is the case for the designs in this work), there is little utility in terms that contain odd powers of x. Such redundancy was significant due to a limit on the number of optimisable coefficients that could be applied to a GRIN material in CodeV. At the time of writing, CodeV (version 2022.03) had a limit of 150 optimisable user-defined GRIN coefficients. The usefulness of these coefficients was therefore maximised by removing a) any coefficients that were odd powers of x and b) removing one coefficient per even power of aperture to eliminate the degeneracy with ρ^n terms previously discussed. The number of base materials was limited to three, as this was shown to be effective in Chapter 2 for correcting both chromatic and monochromatic aberrations. Coefficients were budgeted to a higher order in x and y than for z, as such terms perpendicular to the optical axis tend to have a greater effect on aberration correction, with z-axis terms tending to vary less over the lens volume. Potentially variable coefficients using this GRIN distribution are shown in Table 6.1. In this case, y-z plane symmetric freeform terms to the quintic order were possible for three materials whilst meeting the CodeV 150 GRIN coefficient limit.

These equations were then used to write and compile user-defined raytracing DLLs in the C programming language. GRIN raytracing is computationally intensive compared to conventional homogeneous surfaces. For asymmetric problems such as HMD design, this issue is compounded by the requirement to trace a larger number of field angles to sufficiently sample the entire field of view. Further yet, such complex systems have a very large number of optimisation variables that require the system to be traced a greater number of times to compute all variable derivatives for optimisation via finite differences. Compilation of raytracing

---

*This can also be achieved by use of "coupling codes" or "pickups" in optical design software that constrain coefficients to be a factor of one another, however this was not possible at the time of writing for GRIN materials in CodeV and had to be implemented via additional coefficients.

m_n

z^0	ρ^0	ρ^2	ρ^4	ρ^6	ρ^8
	✓	✓	✓	✓	✓

	y^0	y^1	y^2	y^3	y^4	y^5
x^0		✓	✓	✓	✓	✓
x^1						
x^2		✓		✓		
x^3						
x^4	✓	✓				
x^5						

m_n'

z_1	ρ^0	ρ^2	ρ^4	ρ^6	ρ^8
	✓	✓	✓	✓	✓

	y^0	y^1	y^2	y^3	y^4	y^5
x^0		✓	✓	✓	✓	✓
x^1						
x^2		✓		✓		
x^3						
x^4	✓	✓				
x^5						

m_n''

z_2	ρ^0	ρ^2	ρ^4	ρ^6	ρ^8
	✓	✓	✓	✓	✓

	y^0	y^1	y^2	y^3	y^4	y^5
x^0		✓	✓	✓	✓	✓
x^1						
x^2		✓		✓		
x^3						
x^4	✓	✓				
x^5						

Table 6.1: Variant coefficients for the µth material of an x-y-z polynomial GRIN distribution. Only even powers in x are variable.

DLLs significantly improves optimisation time (compared to macro code within CodeV) and enables a more interactive design process, with the capability to explore a greater number of solutions within a given time frame.

6.4. Material Selection and Colour Correction

Base material data in this study were provided by NanoVox LLC. These materials are UV-curable, nanoparticle-doped polymers with significant variation in refractive index, making them suitable for additive manufacture of GRIN lenses via an inkjet printing approach (known as the Volumetric Index of Refraction GRIN Optic process or VIRGO [29]).

Material	N_d	V_d	$P_{d,F}$	Density (g cm^{-3})
VYIX1060	1.45621	24.0	0.643	1.42
VZBX2000	1.62308	46.7	0.703	1.15
VZAX1500	1.70432	18.6	0.718	1.44

Table 6.2: Basic properties of NanoVox base materials.

Refractive index and Abbé V values for the base materials are shown in Table 6.2 for the Fraunhofer d, F, and C lines as defined in Chapter 1.5.3. Their properties relative to Schott catalogue glasses are shown in Figure 6.3. The large ΔN of the GRIN combination provides a significant level of design freedom. The low mass-density of these polymers ensures a lightweight design is achievable. At the time of writing, these are developmental inks that are not in production.

The set of three materials outlined in Table 6.2 yields three possible GRIN combinations. The optical properties of these combinations are shown in Table 6.3.

These three materials were selected to maximise the area of an inverted pyramid formed in N-V space. In Chapter 2 it was identified that such a combination of GRIN base materials enables chromatic correction, a large ΔN that minimises GRIN thickness, and a flat field corrected for primary field curvature. The thickness of the GRIN lens and the ΔN of the GRIN have a very strong influence on aberration correction potential and manufacturing feasibility. Smaller ΔN GRINs require increased thickness to impart the same optical path length change, whilst printing of thicker GRINs incurs greater manufacturing difficulty. If the ΔN is too small, the GRIN may not be able to impart sufficient optical function, even if it occupies the majority
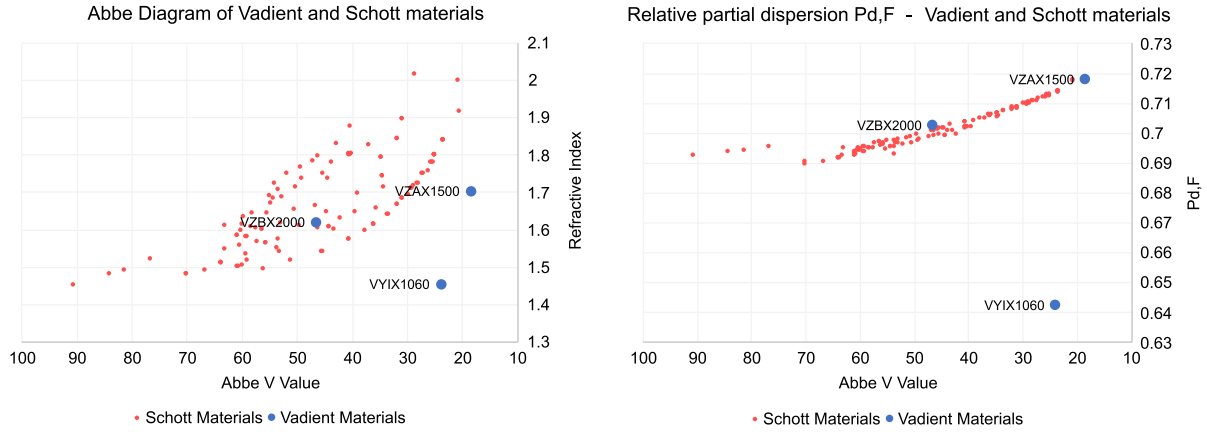
Figure 6.3: Left: Abbé diagram showing GRIN base materials laid over the Schott catalogue glasses for comparison. Right: short-end partial dispersion plot showing the same material sets.

of the available track length of the lens. Conversely, larger ΔN GRINs can be more difficult to manufacture due to the challenges associated with printing inks with higher nanoparticle loadings. The large ΔN and variable dispersion of the material combinations listed enable very powerful degrees of freedom for the aberration correction of GRIN lens systems.

The first combination of VYIX1060 and VZBX2000 has a large ΔN and relatively weak negative dispersion. This combination can be usefully combined with weakly positive optical dispersion contributions from the lens surfaces to effect optical power that is distributed between the surface and the medium. Distributing the power of a lens in this way enables an achromatic lens with reduced monochromatic aberrations. The second and third GRIN combinations both have high optical dispersion with varying ΔN values. Such GRIN combinations allow strong, negative chromatic aberration contributions with only a small negative contribution to the optical power of the GRIN. It is also noteworthy in Figure 6.2 (right) that the base material VYIX1060 has highly anomalous partial dispersion compared to conventional Schott glasses and the other materials in the GRIN. This indicates that a composite "flint" generated by negative optical power contributions balanced between VYIX1060 and VZAX1500 has the potential to correct for secondary spectrum generated by positive power contributions from VZBX2000. This extreme partial dispersion difference between VYIX1060 and VZBX2000 also leaves the potential for residual secondary spectrum, however this effect is offset by the benefits to monochromatic aberration correction of the increased ΔN.

Material Combination	ΔN_d	V_{GRIN}
VYIX1060-VZBX2000	0.167	-29.52
VYIX1060-VZAX1500	0.248	13.16
VZBX2000-VZAX1500	0.081	3.32

Table 6.3: Combinatorial GRIN properties of NanoVox base materials.

6.5. Colour Helmet-Mounted Display Optical Design Study

To assess the benefits of freeform-GRIN media, we define a lens specification upon which comparative designs are based. A schematic of a HMD device is shown in Figure 6.4. A combiner component sits in front of the user's eye. This combiner has a partially reflective
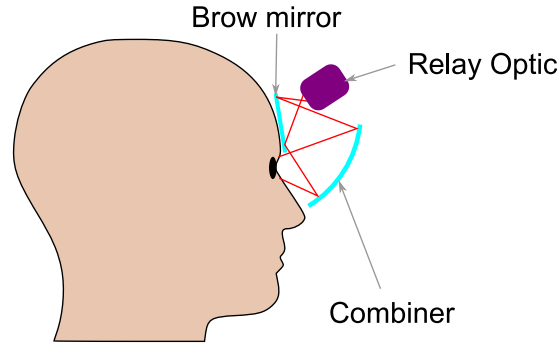
Figure 6.4: Basic construction of a head-mounted display device.

Field of view	40° circle truncated to 30° vertical
Eyebox diameter	10 mm
Axial combiner distance	40 mm
Combiner tilt angle	20°
Waveband	486.1-656.3 nm (uniform weighted)
Display size	800x600 pixels, 15 µm pitch
Temperature range	Ambient only

Table 6.4: Specification parameters for hypothetical HMD requirement

coating that transmits the majority of light from the outside world, whilst also reflecting key wavelengths of interest from the projection system of the HMD. Another reflective component is located at the forehead of the user, known as the brow mirror, this redirects light from the relay lens away from the user's head and towards the combiner. Due to the strong positive optical power of the tilted combiner surface, a highly aberrated intermediate image exists between the combiner and the brow mirror. It is the purpose of the relay lens to generate aberrations opposite to this intermediate image to enable projection of high-resolution images to the user from a notional microdisplay.

A set of basic optical requirements for the system are listed in Table 6.4. The field of view and display combination corresponds to a focal length of approximately 16.5 mm and F/# of 1.65 for an equivalent rotationally-symmetric system. This yields an indicative diffraction-limited spot size (given by $\nu = 1.22 f \lambda / D$) of 1.15 µm. Illustrations of key construction dimensions are also shown in Figure 6.5. These dimensions form the system-human interface, with sufficient clearance from the forehead and ergonomic placement of the eyebox needed in any real-world HMD design. Dimensions of the combiner and brow mirror are also constructed such that sufficient clearance exists for a notional lens housing. These dimensions are however, not indicative of any real-world design requirement, but rather, they serve as a standard comparator to assess the aberration correction potential of the GRIN and homogeneous designs. An equivalent amount of aberration is generated by the tilted combiner for each solution.

Our performance metric for each optical design in this work was RMS spot size over the field of view for the full eyebox, as traced from the eyebox to the display. This is only a basic performance metric; adopted both for brevity and due to time constraints on this work. Tracing in this manner simplifies the optimisation of the design as ray-aiming through the accessible pupil is far simpler, reducing the risk of ray failures and ill-conditioned optimisation.

FRONT ELEVATION

DISPLAY

BROW MIRROR

13.18

3°

COMBINER

EYEBOX

10.00

20°

40.00

10.00   MM

PLAN

COMBINER

R=50

BROW MIRROR

EYEBOX

DISPLAY
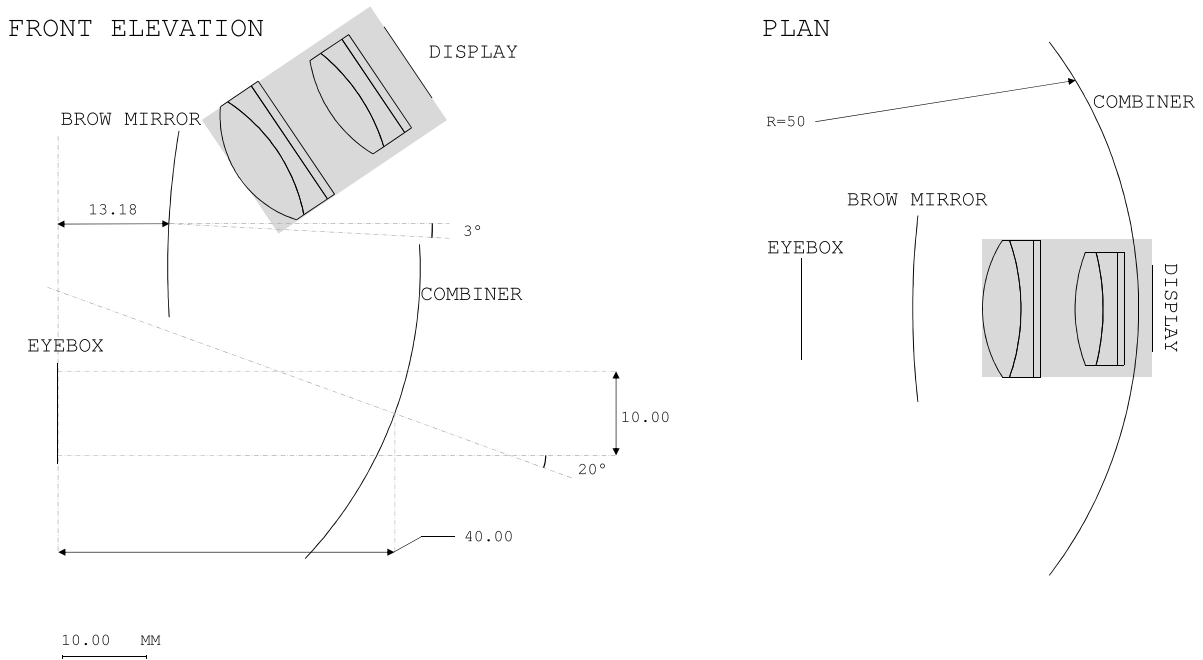
Figure 6.5: Key dimensions of HMD basic construction. Left, the front elevation of the design (the head viewed from the side). Right: The plan view of the space envelope (view from the top of the user's head).

The fine optimisation and analysis of HMD optical designs is a complex process, requiring consideration of a large number of eye sub-pupils within the total eyebox as well as effects on accommodation (and parallax where the system will be applied to both eyes) [98]. Performing such analysis over a large number of designs would be time consuming, and whilst delivering a more detailed answer, would only be marginally more useful in assessing the overall usefulness of GRIN degrees of freedom in HMD design.

Where applicable, packaging constraints were applied to the lens elements, constraining air gaps between surfaces to be greater than 1 mm (at any point over the lens surface). Length of the relay lens from the brow mirror to the centre of the display was constrained to 36 mm or less. The focal length of the design was constrained by forcing the horizontal field to fill the horizontal axis of the display. Distortion of the design was not constrained in optimisation, under the assumption that it may be corrected by "pre-distorting" the image on the display electronically, such that it is compensated by the projection optics.

Optimisation was performed using the CodeV automatic design (AUT) local optimiser. Weighted constraints and inequality constraints were defined to satisfy the requirements of the previously outlined specification, as well as case-specific constraints for GRIN and homogeneous designs outlined below. To minimise the risk of the optimised lens designs becoming stuck in poor local minima, degrees of freedom such as coefficients for aspheres, freeforms, and GRINs were added progressively in successive optimisation runs, starting with lower orders and progressing to the higher-order terms. For all solutions, the brow mirror was made aspheric, with coefficients allowed to vary.

To provide a subjective analysis of each design, the transverse ray errors of each solution were computed and evaluated for the axial field, as well as fields that represented the horizontal and vertical edges of the field of view. Additionally, the optical mass of each solution was estimated. The boundary of each lens was defined by the clear aperture. Whilst real

124

lenses have additional "overage" added to enable mechanical integration, a full mechanical design was not feasible within the bounds of this study and so mass estimates should be considered as comparative rather than absolute. Mass estimation of the GRIN components was simplified by assuming each consisted of homogeneous VZAX1500, the densest of the three base materials.

6.6. Non-GRIN Optical Designs

To determine if freeform-GRIN media are beneficial to the design of HMD systems, we require non-GRIN baseline designs to form a comparison. The solutions shown in this section were generated by a process of material and surface type substitution followed by multiple local optimisations until a good solution was found. Glass and plastic materials were both used in the design, as well as judicious use of special surfaces such as aspheres, torics and freeforms. Six lens elements were used in the relay of each homogeneous solution.

6.6.1. Non-GRIN with aspheres and torics

A design variant was optimised that made use of aspheric and toric surfaces (illustrated in Figure 6.6). Such surfaces represent the state of the art in (non-freeform) HMD optics. A set of tilted and decentred lenses provide aberration correction inverse to that introduced by the combiner surface. A cemented doublet component is incorporated to provide colour correction. A toric surface is applied close to the intermediate pupil to assist in correction of field-constant astigmatism.

Optical performance of this variant is shown in Figure 6.7. Performance on axis is limited by spherical aberration, with a comparatively small chromatic aberration residual. Performance at the outermost x-fields suffers from some astigmatism and coma.

Optical materials (in order from closest to the brow mirror, to the display) were Zeonex E48R, Schott N-LAK9, Schott N-PSK53A cemented to Ohara S-NPH1, Ohara S-LAM60 and Schott N-PSK53A. The optical mass of the solution was estimated to be 3.70 grams. This estimate was performed by applying rectangular and elliptical clear apertures that efficiently surround the system rays, followed by calculation of the volume of each component in CAD software.
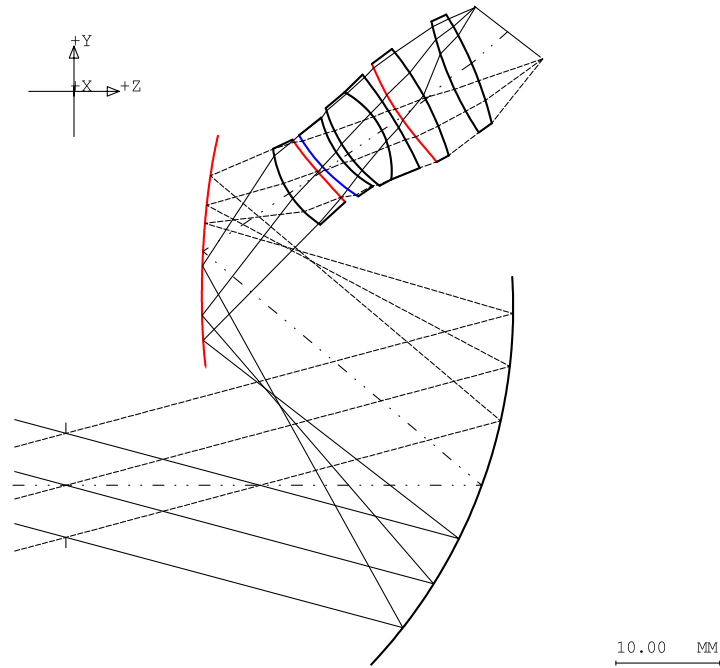
Figure 6.6: Raytrace of conventional HMD variant featuring aspheric surfaces (red) and a single toric surface (blue).
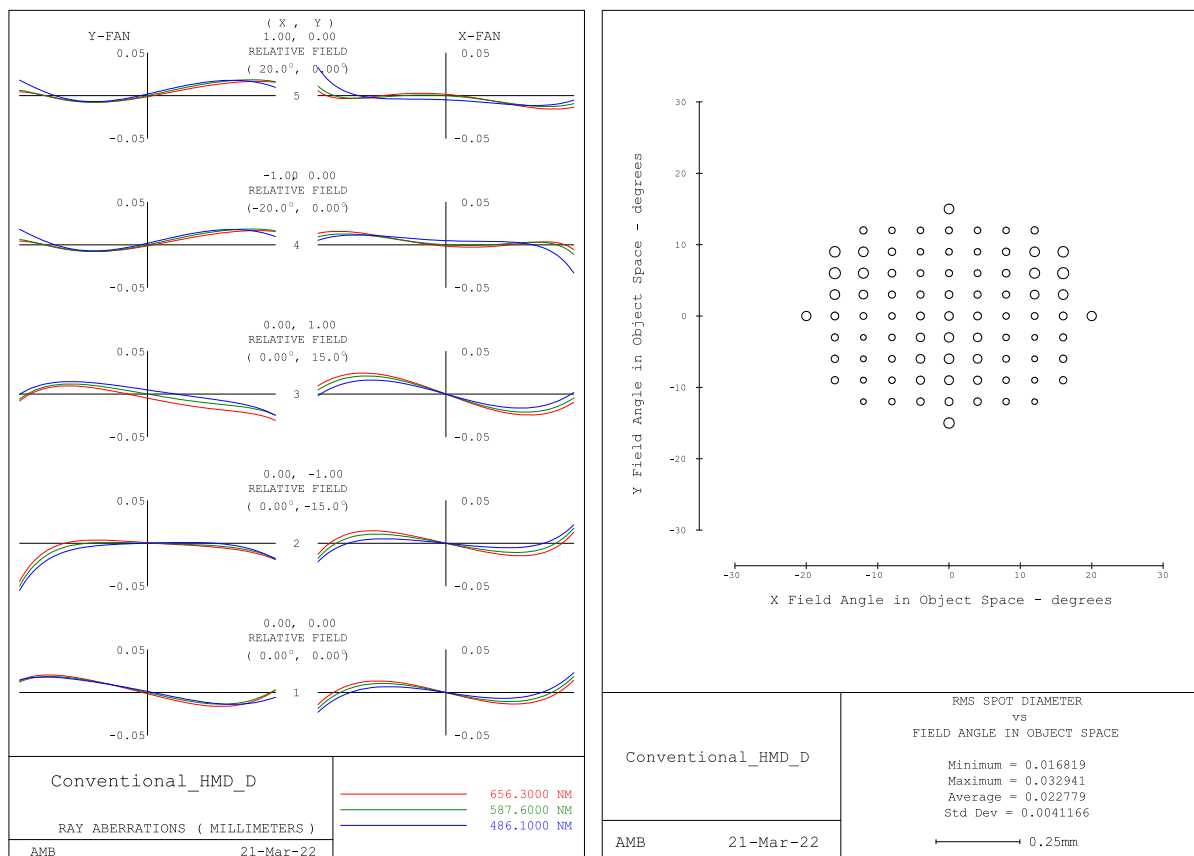
Figure 6.7: Left: transverse ray errors for the aspheric and toric non-GRIN HMD design. Right: RMS spot size over the field of view.

126

6.6.2. Non-GRIN with Freeform surfaces

Freeform surfaces were added to the baseline design on lenses 2 and 6, as illustrated in green in Figure 6.8. The first of these replaced the toric surface of the baseline design whilst the second replaced a spherical surface. These locations allow freeform degrees of freedom to be applied close to the intermediate pupil and display, to address aberrations with different field and pupil dependencies. The two aspheric surfaces from the baseline design were retained. Freeform terms up to and including the quartic order were added to each surface. RMS spot size over the field of view is illustrated in Figure 6.9. The average RMS spot size is substantially reduced to 11.9 μm. Furthermore, the spot size is very consistent over the field of view, with a standard deviation of 1.9 μm. Aberrations of the system are shown in Figure 6.7. Performance is limited by a combination of aberrations over the field of view, principally coma and astigmatism at wider field angles. The same set of materials were used for this design as the toric-based solution, resulting in an approximate optical mass of 4.0 grams.

127
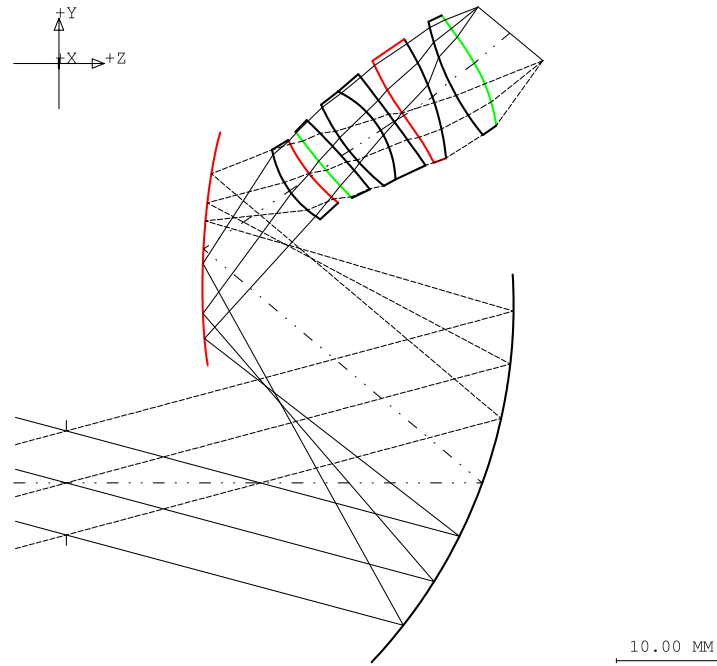
Figure 6.8: Raytrace of conventional HMD variant with twin freeforms. Aspheric surfaces are highlighted in red. Freeform surfaces are highlighted in green.

Figure 6.9: Performance data for the twin-freeform homogeneous variant. Left: Transverse ray errors over the X and Y field angles. Right: RMS spot size over full entrance pupil vs field.

128

6.7. GRIN Optical Designs

GRIN base materials were derived from the 3D printing VIRGO process of NanoVox as discussed in Section 6.4, for which refractive index data was provided in support of this work. These material data were selected based on the fact that the 3D printing VIRGO process is capable of producing an arbitrary refractive index distribution required for freeform-GRIN components.

The relative composition mathematical representation of Equation 6.3 allows for unphysical results if the relative composition of any material m_n becomes negative. The optimiser tended to produce negative material composition when unconstrained. To prevent this, grid constraints were placed over the lens volume. These constraints return the minimum value of material concentration for each material over a set of sample points covering the lens bulk. An example of such a constraint grid is illustrated in Figure 6.10. These constraint grids were constrained slightly above zero in optimisation (in this case 0.005 relative composition), to ensure that regions between the grid points did not drop below zero. For each design, validity of the relative composition was verified by plotting it over a fine grid of points. In this work, the grid points were aligned in polar coordinates about the optical axis, however it is considered that an evenly spaced grid in x and y may be a simpler and more effective means for future work, as a polar grid is somewhat sparse at the lens edge whilst excessively dense close to the optical axis.
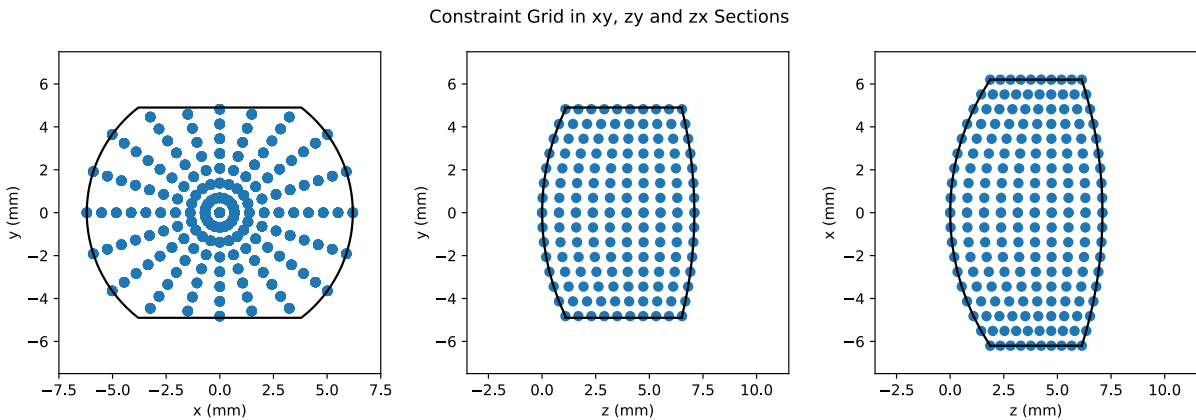
Figure 6.10: Constraint grid for a freeform-GRIN lens. Shown in x-y section (left), z-y section (centre) and z-x section (right).

6.7.1. Six-Element GRIN Solution

To enable a more direct comparison of the effectiveness of freeform GRIN relative to its homogeneous analogue, a design based on the preceding twin-freeform variant was produced, with substitution of the freeform surfaces for freeform GRINs. All other design variables were equivalent, with an identical set of radii, thickness and aspheric coefficients allowed to vary. The freeform surfaces of the homogeneous twin-freeform variant were replaced with spherical surfaces. As the GRIN lenses were relatively thin, an x-y polynomial GRIN formula of the form shown in Table 6.1 was used that featured terms constant in z only.

The optimised solution is illustrated in Figure 6.11. The GRIN lenses are shown by an overlay of their refractive index distribution, being lenses 2 and 6 of the overall system. The overall appearance of the solution is very similar to the twin-freeform-surface variant. Optical performance of the design is illustrated in Figure 6.12. RMS spot size is, on average, fractionally larger than the freeform-surface variant at 12.3 μm RMS compared to 12.1 μm RMS. Chromatic aberration correction is noticeably improved for the GRIN design, with the difference in RMS spot size due to increased monochromatic aberrations. Inspection of the transverse ray errors of Figure 6.12 indicated this was due to marginally increased coma. The modification of two lens components to a lower density polymer material reduced the approximate optical mass to 2.7 grams (from 4.0 grams for the homogeneous variant).

The refractive index distribution of this design is illustrated in Figure 6.13. the distribution of lens 2 shows only slight asymmetry, with the distribution largely resembling a decentred radial GRIN. The index distribution of lens 6 is significantly more freeform, using the entire allowable ΔN of the materials and with notable asymmetry between the X and Y axes. Relative composition is illustrated in Figure 6.14, illustrating that for lens 2, the GRIN heavily favours the low dispersion combination of VZBX2000 and VYIX1060, whilst lens 6 favours a more general blend of the three materials, but with a notably larger contribution at the lens edges from the high index and high dispersion material, VZAX1500, to correct lateral colour at wider field angles.

130
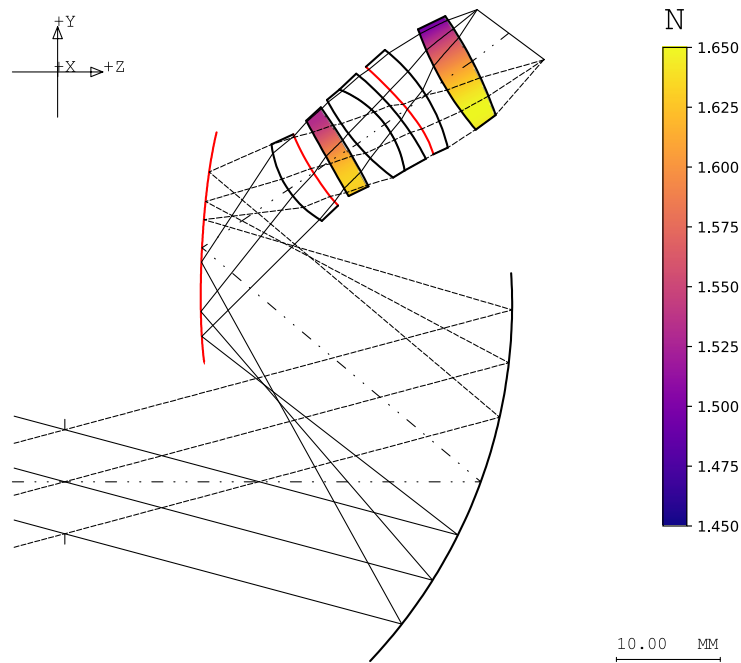
Figure 6.11: Raytrace of the six-element GRIN variant, where two freeform surfaces are replaced by freeform-GRIN media. Aspheric surfaces are illustrated in red. GRIN lenses are indicated by the shading of their refractive index distribution. (Patent Pending [1, AMBpat])
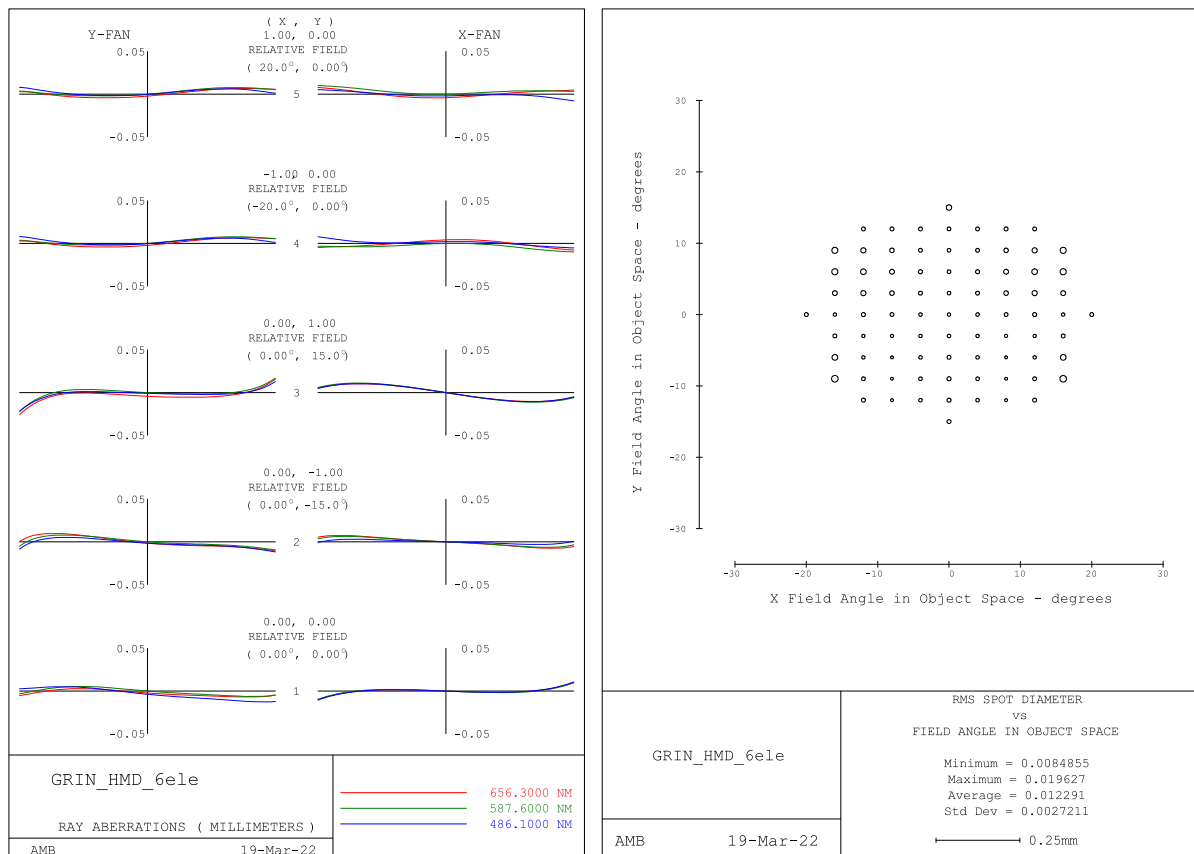
Figure 6.12: Performance data for the six-element GRIN lens variant. Left: Transverse ray errors over the X and Y field angles. Right: RMS spot size over full entrance pupil vs field.

Refractive Index Distribution - XY Section
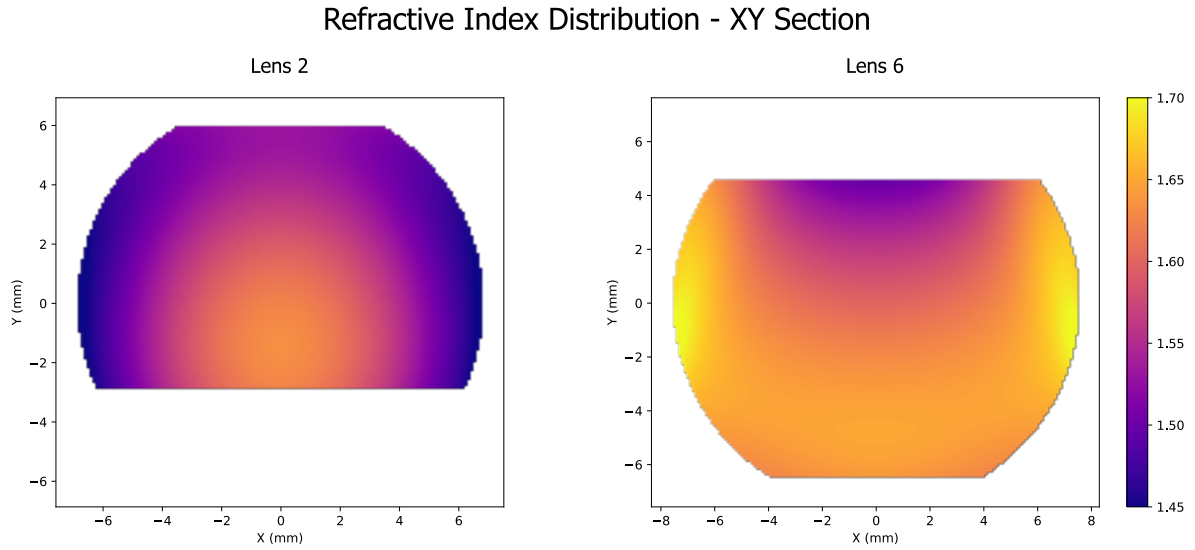
Figure 6.13: Refractive index cross-section for both GRIN lenses of the six-element GRIN solution. Coordinates are with respect to the local surface vertex.

Relative Composition over XY section - GRIN HMD Six Element
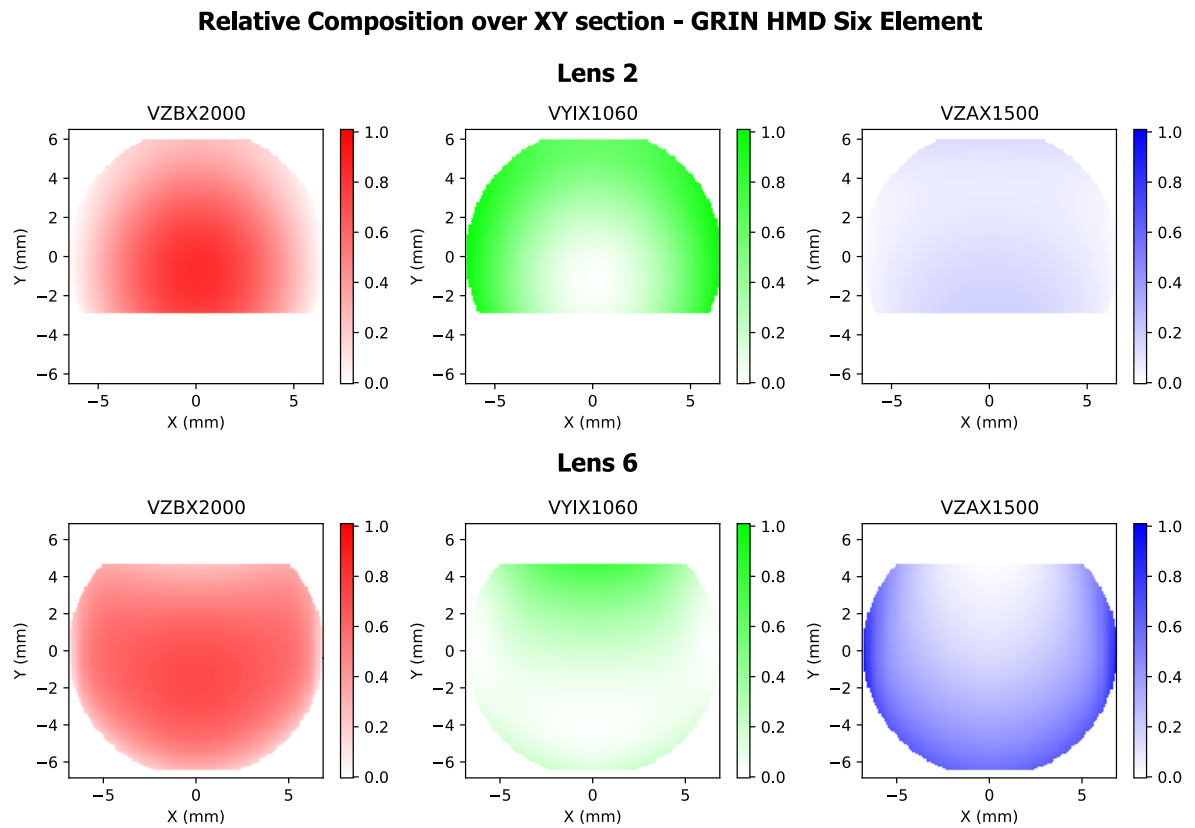
Figure 6.14: Normalised relative composition by material in x-y cross-section for both GRIN lenses of the six-element GRIN solution. Coordinates are with respect to the local surface vertex.

6.7.2. Two-Element GRIN Solution

Whilst the preceding six-element GRIN design demonstrates that a freeform-GRIN medium can be used as a direct substitute for a homogeneous freeform lens, we would like to explore design concepts that incorporate GRIN from the outset. In particular, constructing the design from thicker GRIN lenses that allow the GRIN medium to exert more influence over the design is of interest.

A solution based on two GRIN lenses was optimised. The placement of the GRIN lenses was targeted for maximal impact on the aberration correction of the system, with the first GRIN placed approximately at the intermediate pupil of the relay, whilst the second was placed close to the display to address aberrations of the field. The GRIN distribution of each lens was a y-plane symmetric distribution (as shown in Table 6.1) featuring radial terms to the 6th power of aperture and yz-plane-symmetric terms to the 5th power of aperture. The refractive index distribution was again independent of z. The GRIN lenses each had one variable aspheric surface to assist in the correction of rotationally-symmetric aberrations.

The two GRIN lenses of this solution share a common axis through their optical surface vertices. This is of significant benefit for the alignment and assembly of the GRIN. The coaxial symmetry of the end surfaces in the relay means the GRIN lenses may be aligned during assembly based on reflection off the lens surfaces and run-out of the lens edges, whilst the rotational alignment of the GRIN distribution about the optical axis may be performed by rotation of the lens elements. This opto-mechanical simplification may have benefits for the cost of such a system.

The optimised two-element GRIN design is illustrated in Figure 6.15. Optical performance is illustrated in Figure 6.16. Excellent chromatic aberration correction is shown over the field of view due to the ternary GRIN blend. RMS spot size is limited by monochromatic aberrations, with some residual astigmatism present along the optical axis. Despite the simplified coaxial geometry, average RMS spot size is improved over the baseline solution, at 18.1 µm compared to 22.8 µm. Approximate mass of this solution is significantly reduced, at 1.8 grams.

Cross-sections of the refractive index distribution and material concentration profile are shown in Figure 6.17 and Figure 6.18 respectively. It is observed that the GRIN distributions have significant asymmetry, deviating strongly from a radially symmetric distribution. The relative composition of lens 1 indicates a gradual transition from VZBX2000 at the centre to VZAX1500 at the edge, this is a negatively powered and highly dispersive combination primarily correcting axial colour within the system.

133
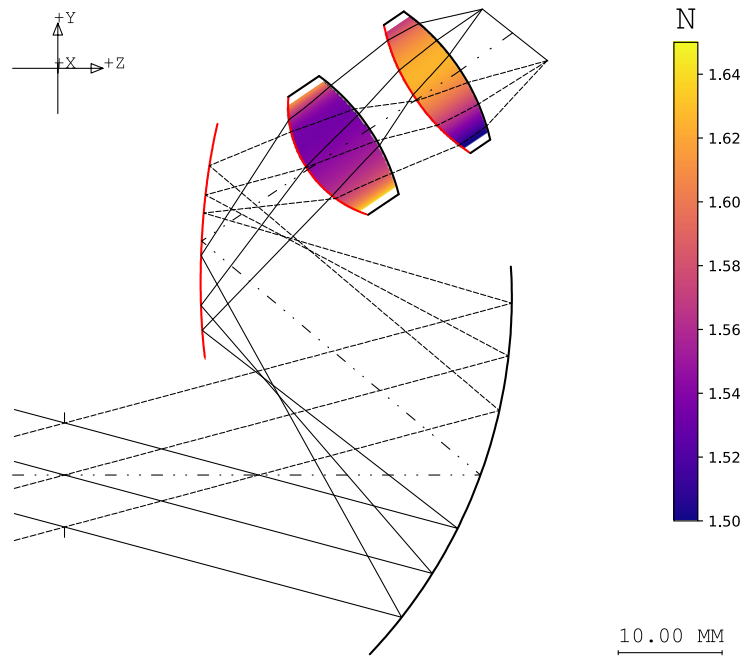
Figure 6.15: Raytrace of the two-element GRIN variant. Aspheric surfaces are illustrated in red. GRIN lenses are indicated by the shading of their refractive index distribution. (Patent Pending [1, AMBpat])
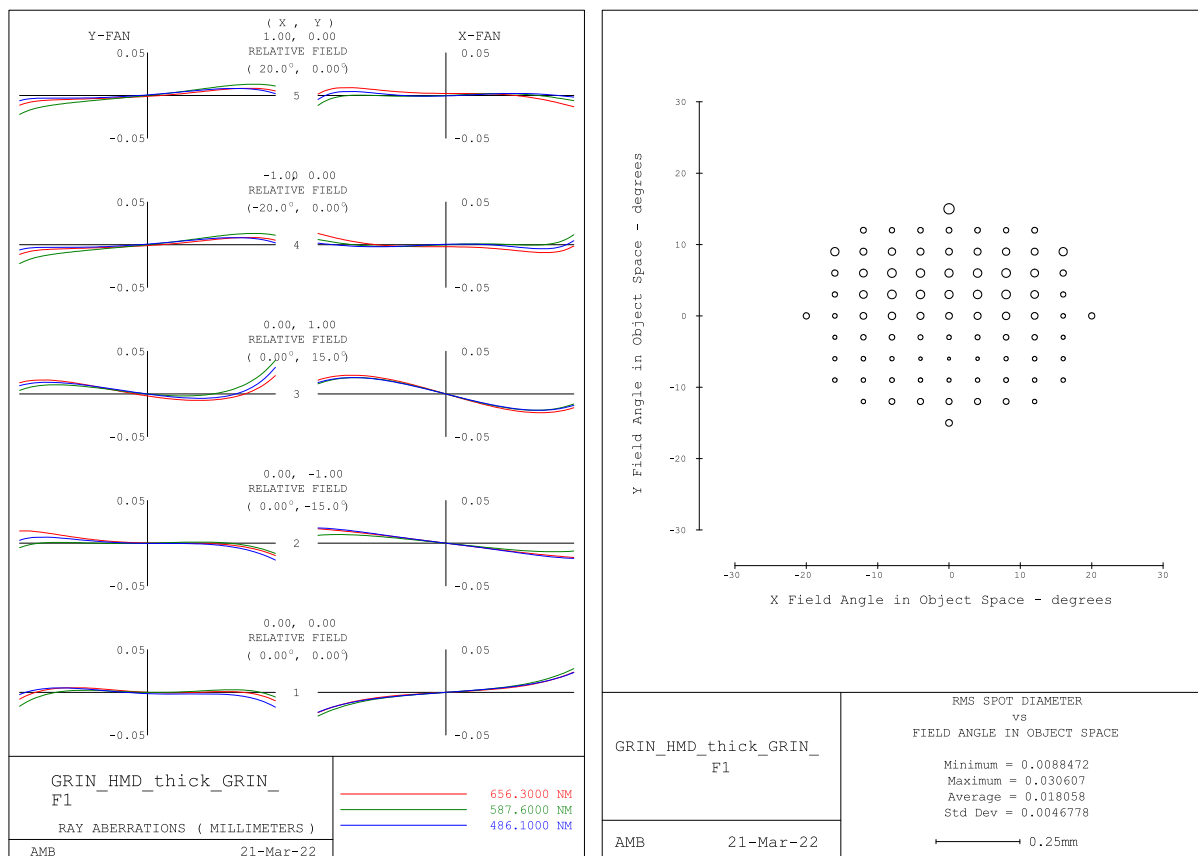
Figure 6.16: Performance data for the two-element GRIN lens variant. Left: Transverse ray errors over the X and Y field angles. Right: RMS spot size over full entrance pupil vs field.

134

Refractive Index Distribution - XY Section
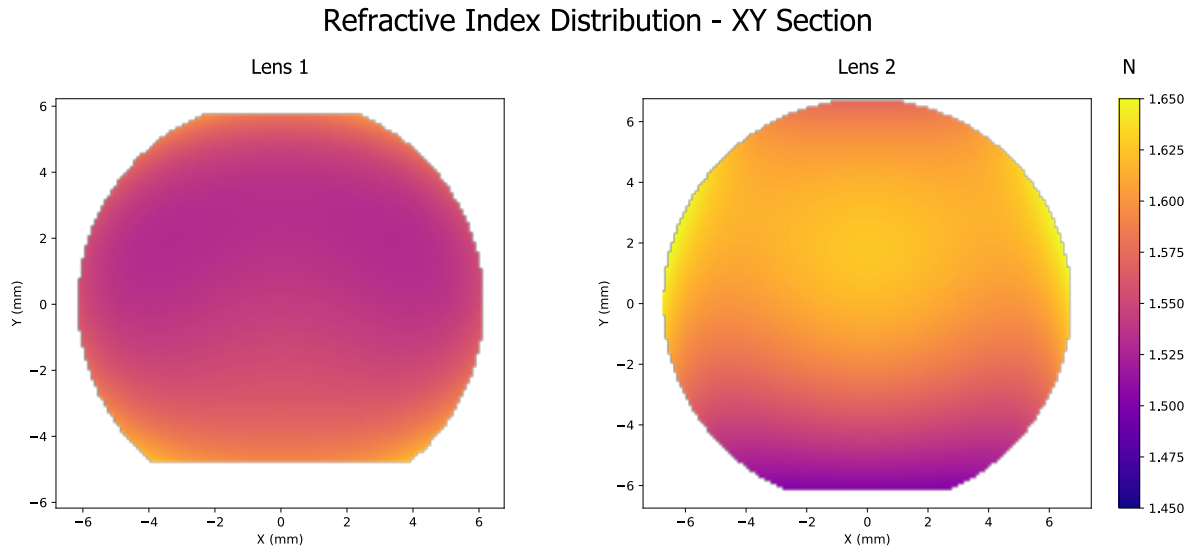
Figure 6.17: Refractive index cross-section for both lenses of the two-element GRIN solution. Coordinates are with respect to the local surface vertex.
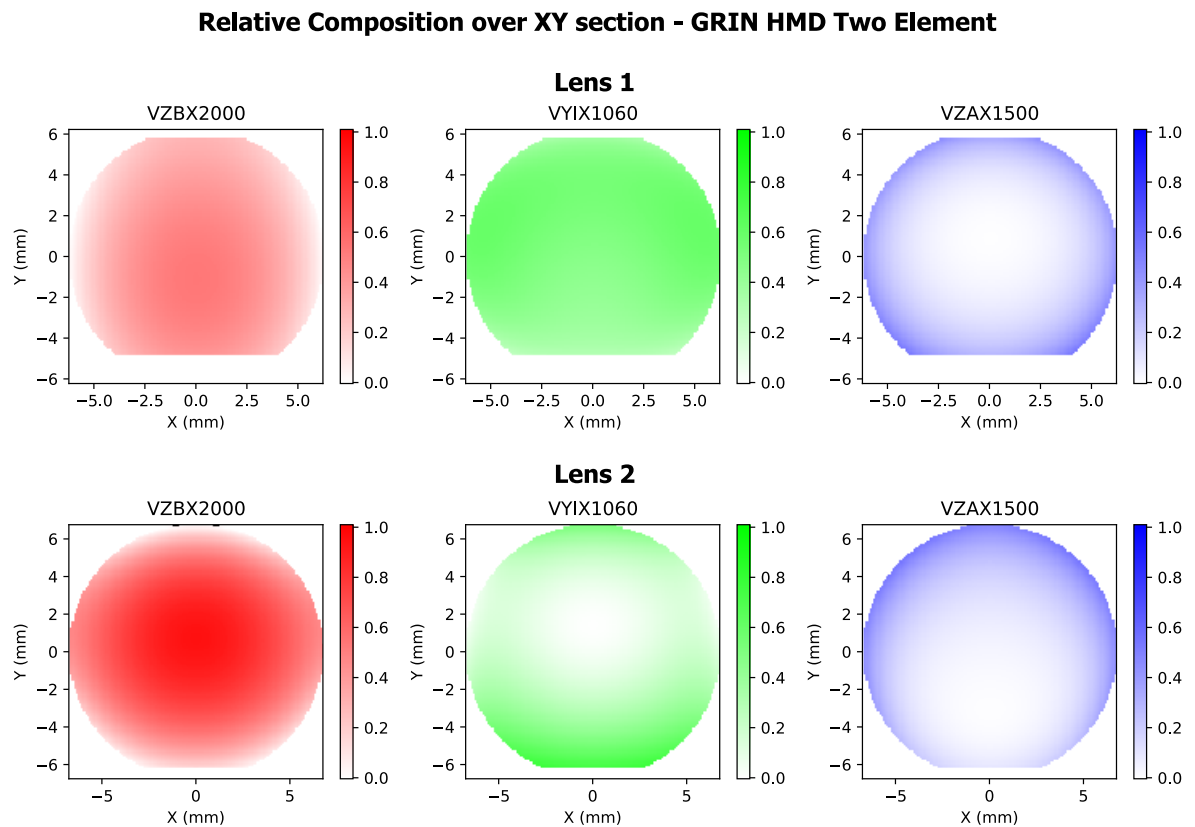
Figure 6.18: Normalised relative composition by material in x-y cross-section for both lenses of the two-element GRIN solution. Coordinates are with respect to the local surface vertex.

135

6.7.3. Three GRIN lens solution

The two-element GRIN solution demonstrates that performance in excess of the baseline toric variant is possible with a greatly reduced lens count, however the performance of this variant is lower than the six-element GRIN and six-element homogeneous freeform solutions. Inspection of the transverse ray errors in Figure 6.16 indicated that astigmatism was not entirely corrected over the full field of view. Further analysis of astigmatism over the field of view using a field map indicated a bimodal distribution of astigmatism (Figure 6.20 (A)) that would require additional non-rotationally-symmetric degrees of freedom to correct. To achieve this, a third freeform-GRIN lens was added to the system. The resulting optimised design is shown in Figure 6.19. Performance of the lens is shown in Figure 6.21. The RMS spot size over the field of view is significantly reduced due to improved astigmatism correction, as shown in Figure 6.20 (B). The bimodal distribution of astigmatism remains, but at a reduced amplitude that is on average over the field of view, approximately half that of the two-element GRIN design. Initially, the mass of this design was only slightly lighter than the homogeneous variants, at 3.5 grams when analysed with circular clear apertures like the two-element GRIN. This is due to the increased clear aperture of lens three that is caused by the altered power construction. When rectangular truncations are applied to the apertures, as was the case for the homogeneous variants, a reduced mass of 2.4 grams was obtained. This modification would increase the mechanical complexity of the lens housing, but the surfaces themselves still maintain a single optical axis.
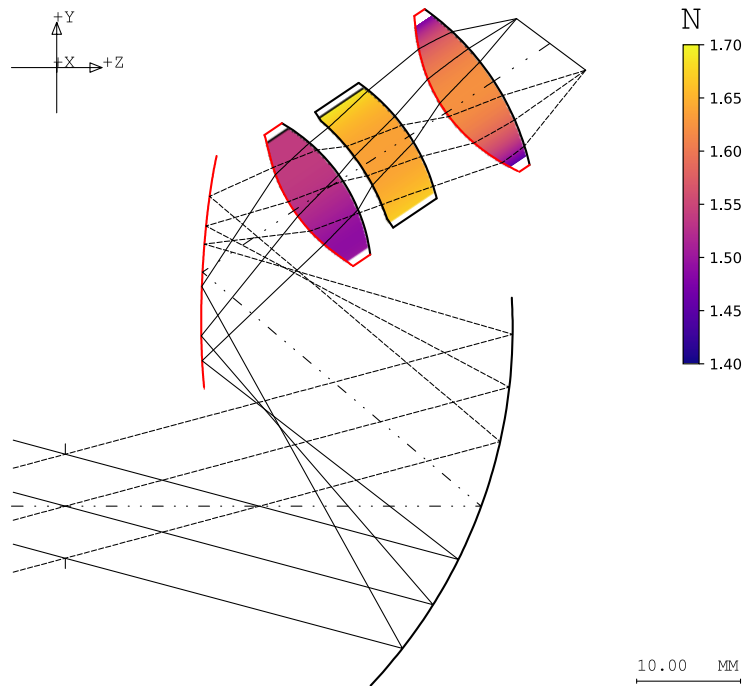
Figure 6.19: Raytrace of the three-element GRIN variant. Aspheric surfaces are illustrated in red. GRIN lenses are indicated by the shading of their refractive index distribution. Patent pending [1, AMBpat].
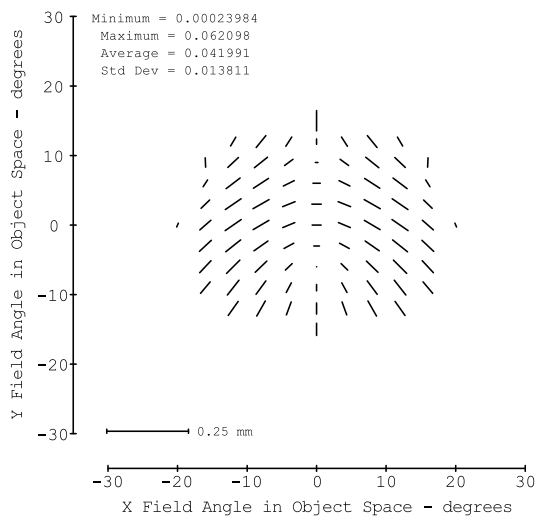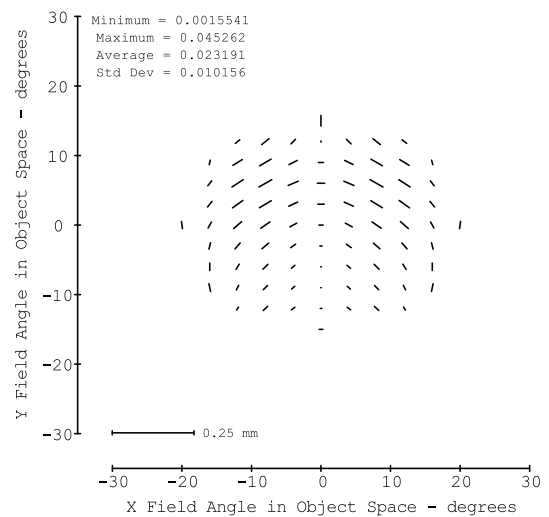
Figure 6.20: Distribution of astigmatism over the field of view of (a) the two-element freeform-GRIN solution, and (b) the three-element GRIN solution.

137
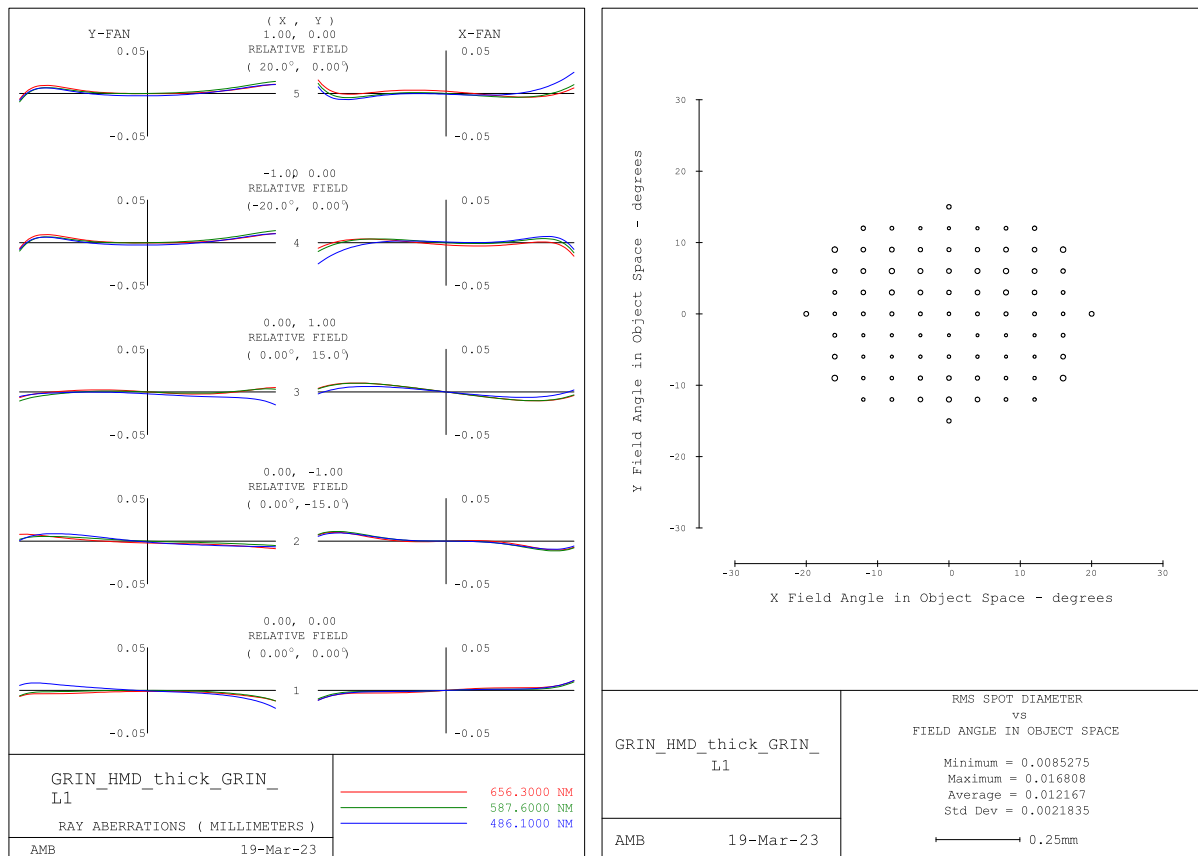
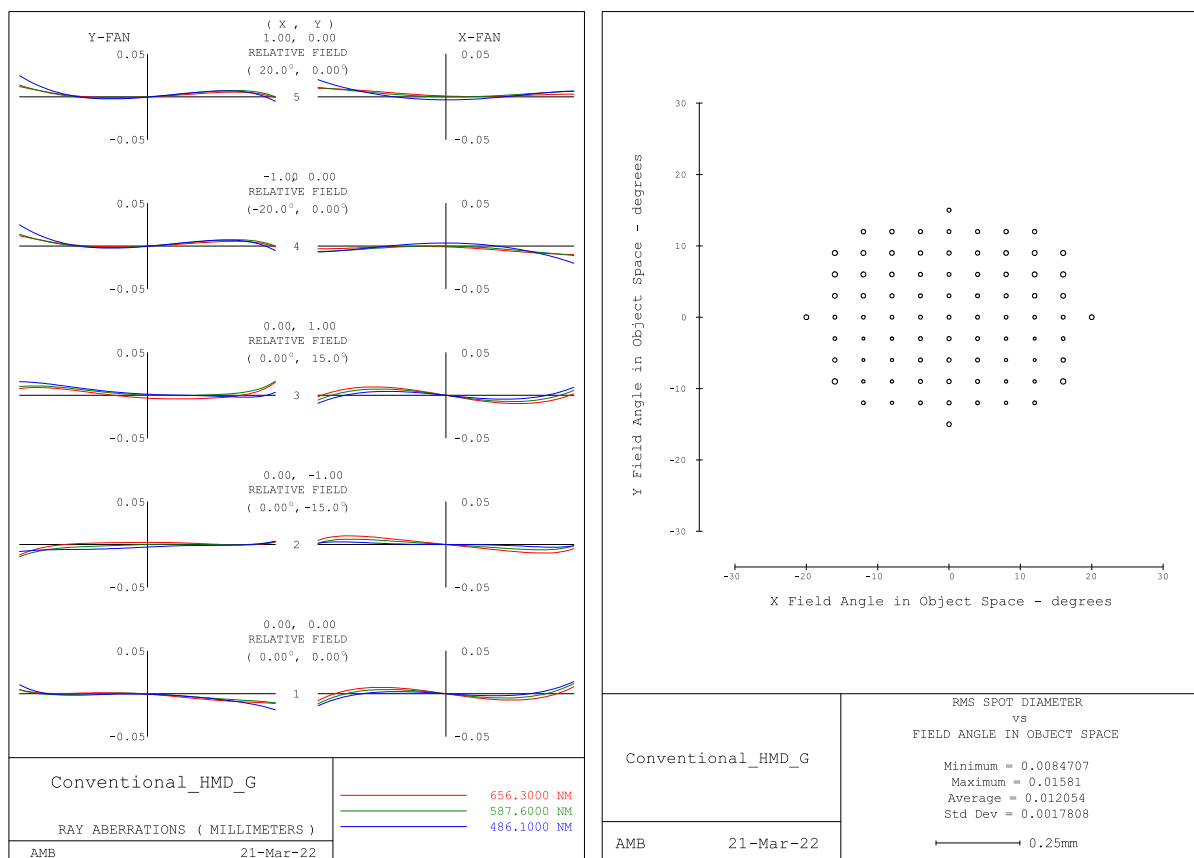Figure 6.21: Performance data for the three-element GRIN variant. Left: Transverse ray errors over the X and Y field angles. Right: RMS spot size over full entrance pupil vs field.

6.7.4. Single GRIN Lens Solution

The previous GRIN variants may be considered two-dimensional freeform GRINs, as the non-rotationally-symmetric index variation occurs perpendicular to the optical axis. A further design variant was generated that features a three-dimensional freeform-GRIN medium, with index variation in the x, y and z axes, with symmetry only in the y-z plane (only even polynomial terms in x). It was considered that if both rotationally-symmetric and non-rotationally-symmetric terms of the GRIN were allowed to vary along the optical axis, then an HMD design consisting of just one GRIN lens could be generated. The benefits of this approach are that further optical processing and alignment steps are removed from the system, albeit with the trade-off of potentially increased mass (compared to a two-element GRIN solution) and GRIN blank manufacture complexity. Additional manufacturing complexity is also generated due to the fact that the optical surfaces must be accurately positioned with respect to the GRIN in three dimensions rather than two (whilst accounting for lens thickness errors). Each surface of the single-element GRIN was aspheric. The lens variable coefficients ultimately spanned the entire available set listed in Table 6.1 over the same three materials as previous GRIN variants. Variable coefficients were activated gradually, starting with lower orders of aperture whilst allowing variation to the quadratic order in z to avoid descent into poor local minima.

The optimised single-element design is illustrated in Figure 6.22. Optical performance is illustrated in Figure 6.23. RMS spot size is intermediate to the two-element and six-element GRIN designs. The significant GRIN thickness of 22 mm allows excellent correction of non-rotationally-symmetric aberrations generated by the combiner, with a small amount of coma in the x-field and astigmatism in the y-field limiting performance. Some field curvature is also present over the field of view due to an absence of negative optical power in the system. Loosely, the design can be considered analogous to a Petzval lens, with the gradual distribution of optical power through the system minimising field curvature, but not correcting it.

The refractive index distribution is shown in Figure 6.24. The difference in symmetry between the x-z and y-z sections is readily apparent, with the y-z distribution approximately tilted with respect to the optical axis of the lens. Approximate mass of the solution is comparable to the six-element GRIN solution at 2.6 grams.
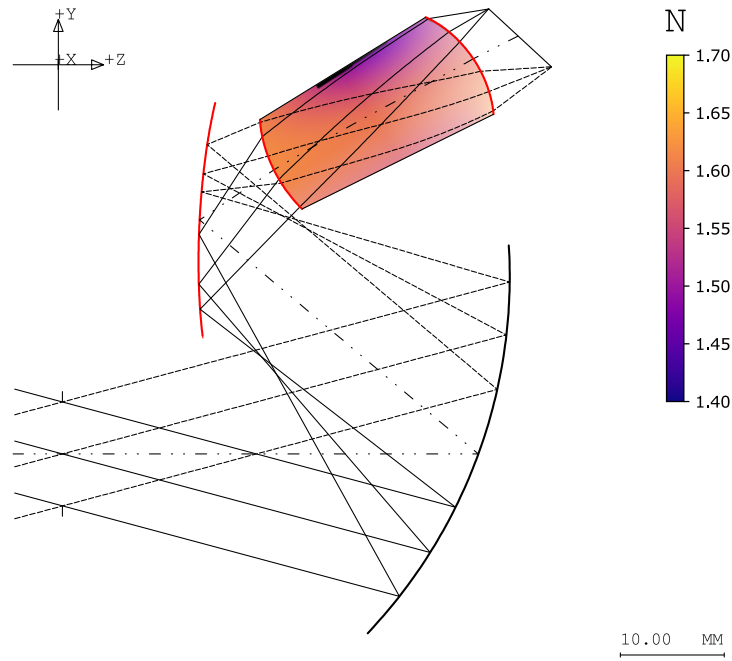
Figure 6.22: Raytrace of a single GRIN lens variant. Aspheric surfaces are illustrated in red. GRIN lenses are indicated by the shading of their refractive index distribution. (Patent Pending [1, AMBpat])
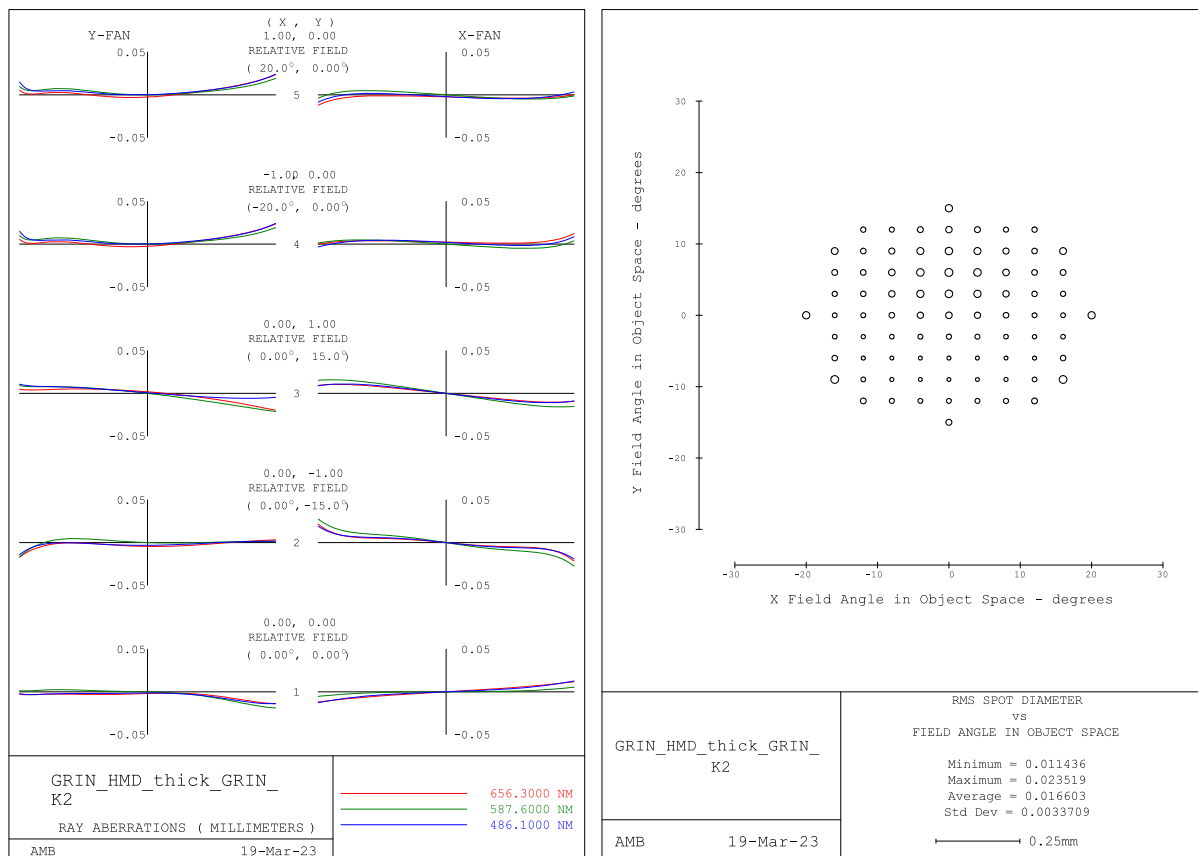
Figure 6.23: Performance data for the single GRIN lens variant. Left: Transverse ray errors over the x and y field angles. Right: RMS spot size over full entrance pupil vs field.
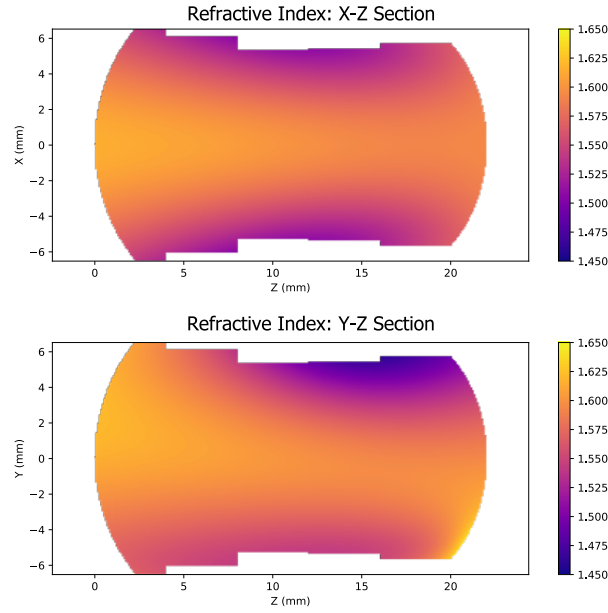
Figure 6.24: Refractive index cross-section for the x-z and y-z planes of the single GRIN lens solution. Coordinates are with respect to the local surface vertex.

Visualisation and Diagnostics

In order to diagnose and monitor the evolving lens solution for material space errors, as well as better observe the form of the index distribution, appropriate visualisation tools were developed. The highly arbitrary nature of the GRIN distribution renders 2D slices of the GRIN an incomplete means to obtain this information. Due to the truly freeform index distribution, there remains a risk that any compositional errors lie outside the analysis planes used. The solution to this is to present the entire three-dimensional index field in a manner that is interpretable by a human. A point cloud type visualisation approach was adopted using the "pptk" library in Python [99]. A large number of sample points were cast over the bulk of the lens design and the relative composition and refractive index evaluated at these points. The point cloud visualisation tools were then used to flag up any unphysical regions of negative relative composition.

An example of this approach is shown in Figure 6.25 for an earlier design scheme that contained a relative composition error due to an incorrectly coded optimisation constraint. A cloud of 16 million points was assigned over a box bounding the lens volume, where relative composition errors ($m_n < 0$) are indicated for m_A and m_B in red and blue respectively, whilst points with physically valid composition are coloured translucent white. These errors result in regions of refractive index that are outside of the allowable index range intended for optimisation. The trajectories of the ray bundles within the lens were used to define the boundary of the index point cloud. The design was temporarily "sliced" into a number of thinner lens segments by macro code. The positions of each ray at each surface were then recorded and the convex hull of these points generated for each lens segment. These convex hulls were then combined into a mesh, and a dense, random point cloud defined within. Any points within the mesh were evaluated for their refractive index and relative composition, whilst points external to the lens were deleted from the model.
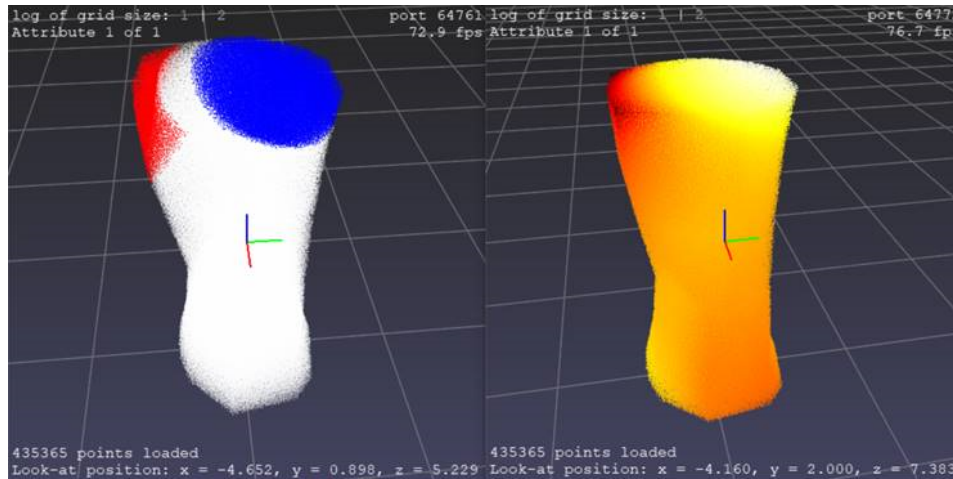
Figure 6.25: Left: relative composition point cloud indicating negative composition regions for m_A and m_B in red and blue respectively. Right: refractive index point cloud with lighter colours representing higher refractive index.

6.8. Distortion and Relative Illumination

An analysis of the image distortion of each design was performed by tracing rays from the centre of the eyebox pupil into a predefined angular grid that was representative of the truncated field of view requirement of Table 6.4. Distortion grids for each design are shown in Figure 6.26. All designs show similar levels, being primarily affected by "keystone" distortion induced by the tilted combiner and brow mirror. Some slight clipping in the lower half of the field of view was observed, which with further development of the design solution could be mitigated by reducing the x-azimuth focal length marginally. Maximum and minimum relative illumination of the designs with respect to the axial field is reported in Table 6.5. Some variation is noted over the solution set, but is at a level which can be digitally corrected over an emissive display without excessive loss of dynamic range.

	Relative Illumination (%)	
Solution	**Minimum**	**Maximum**
Homogeneous Toric	60.0	114.2
Homogeneous Freeform	61.1	110.7
Six-Element with GRIN	59.5	115.4
Single-Element GRIN	59.1	115.0
Two-Element GRIN	55.6	120.6
Three-Element GRIN	68.1	112.5

Table 6.5: Worst case relative illumination for each HMD design.
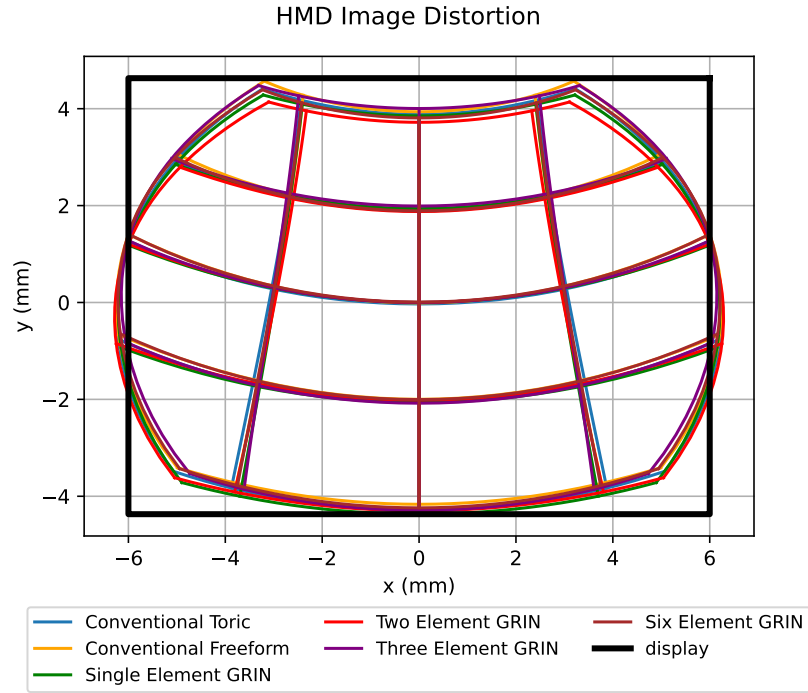
Figure 6.26: Image shape required on the display over the specification field of view for each HMD design.

6.9. Discussion

We have demonstrated the application of freeform-GRIN degrees of freedom to a HMD design with a tilted and powered combiner element. Freeform GRINs are shown to substantially reduce the aberrations caused by the systemic asymmetry generated by the tilt of the spherical combiner surface. It was shown by direct substitution of freeform GRINs for freeform surfaces within a six-element HMD system, that GRINs provide comparable performance to a homogeneous freeform-surface solution.

We have also shown that GRINs are capable of yielding comparable performance to more conventional HMD solutions whilst drastically decreasing the component count. GRIN-based optical designs are shown based on one, two, and three GRIN lenses. We have shown that a two-element freeform-GRIN solution has comparable performance to a homogeneous solution featuring six tilted and decentred components, with two aspheres and a toric surface. Addition of extra GRIN degrees of freedom through a three-element design further recovers performance to that of the six-element freeform-GRIN design. A single-element GRIN solution is also presented, utilising a fully freeform-GRIN distribution in three dimensions over a thick, aspheric lens geometry, which also yielded similar optical performance to the two-element GRIN and six-element toric designs.

Freeform-GRIN media enable a significant reduction in optical complexity by performing multiple aberration correction roles simultaneously. The GRIN medium provides rotationally-symmetric optical power, either as bulk focusing power or as highly dispersive optical power for chromatic aberration correction in conjunction with refractive optical surfaces. In superposition, the higher-order symmetric and non-rotationally-symmetric terms of the GRIN contribute to correction of the aberrations generated by the tilted combiner surface.

HMD solution Approximate Mass (g)
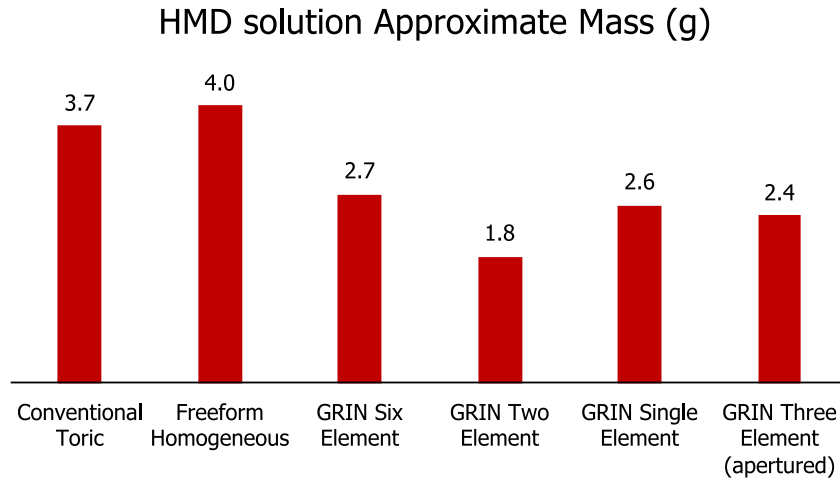
Figure 6.27: Comparison of approximate mass of HMD optical designs

Freeform-GRIN media also enable a significant potential reduction in the optical mass of an HMD. Figure 6.27 shows a comparison of the mass of each design solution. The degrees of freedom of the GRIN contained within a low-density medium are particularly effective in this regard. Conversion of two glass freeform elements to a lower density GRIN polymer enables a 30% mass reduction from a twin-freeform solution. Redesign of the solutions based on an all-GRIN approach enables even more significant mass savings. Comparing the six-element toric solution and two-element GRIN solution (which share similar performance), a 50% mass reduction is achieved. The single-element GRIN solution has slightly improved optical performance relative to these two solutions, while its mass is intermediate to them. It is also noteworthy that the mass estimates of the GRIN solutions are likely over-estimates as their density was assumed to be that of the densest material in the GRIN. An option to reduce the mass of the homogeneous solutions would be to replace some glass elements with polymers, however this results in a reduced N and V material space for the homogeneous design that reduces scope for correction of chromatic aberrations. Lower index materials are also less favourable for the correction of monochromatic aberrations. Diffractive surfaces would enable significant improvement in chromatic aberration correction, but with the aforementioned trade-off of spurious ghost images and veiling glare caused by adjacent diffraction orders.

This work, in conjunction with other examples from the literature is evidence that significant SWAP-C enhancement of tilted and off-axis lens systems is possible by using freeform-GRIN media as design degrees of freedom. Opportunities to further enhance the performance include consideration of a fourth material within the GRIN distribution, as well as further investigation into other mathematical representations for freeform-GRIN media, such as Zernike polynomials or similar orthonormal bases. Further exploration of the trade-space between thickness of the GRIN elements and the number of refractive surfaces is also worthy of investigation. Finally, the two and three-element GRIN designs in particular may benefit from the added degrees of freedom provided by a three dimensional GRIN distribution similar to that used in the single-element GRIN, with the caveat that such GRINs may add further manufacture and metrology complexity. This work justifies further development in the printing, optical processing, metrology and integration of freeform-GRIN lenses, which are also key challenges that must be addressed before mass deployment of this technology.

7

Optical Design of Athermal, Multispectral, Radial Gradient-Index Lenses

The contents of this chapter are derived and expanded from *"Optical design of athermal, multispectral, radial gradient-index lenses - Optical Engineering Vol. 57, No. 8, Jul 2018"* [4, AMBref].

7.1. Abstract

Many infrared systems operate in extreme environments (such as space or military) that require stable optical performance over an extended temperature range. A model is presented for the first-order optical design of athermal, radial-GRIN lens systems, which is based on a form of the thermo-optic glass coefficient adapted to inhomogeneous material combinations. It is found that radial GRIN components can significantly reduce the optical power balance of athermal, achromatic systems, thus reducing aberration contributions from individual lens elements and improving overall performance. This introduces the scope for a class of GRIN multispectral infrared imaging solutions. This enhanced first-order modelling technique is used to generate starting points for optimization of a short wave to long wave infrared (SWIR/LWIR) multispectral optical design. An example of SWIR/LWIR optical design for a weapon sight application is generated and shown to have significantly reduced mass and improved performance compared with a conventional non-GRIN solution. Furthermore, it is demonstrated that the milder optical power construction of the GRIN solution leads to reduced sensitivity to alignment tolerances.

7.2. Introduction

In recent years, in addition to the increased interest in visible-waveband GRINs, there has also been a resurgence of interest in GRIN optics for infrared applications. This is again substantially due to the development of novel manufacture methods [36, 40, 43]. Concurrently to

145

(A)   (B)   (C)
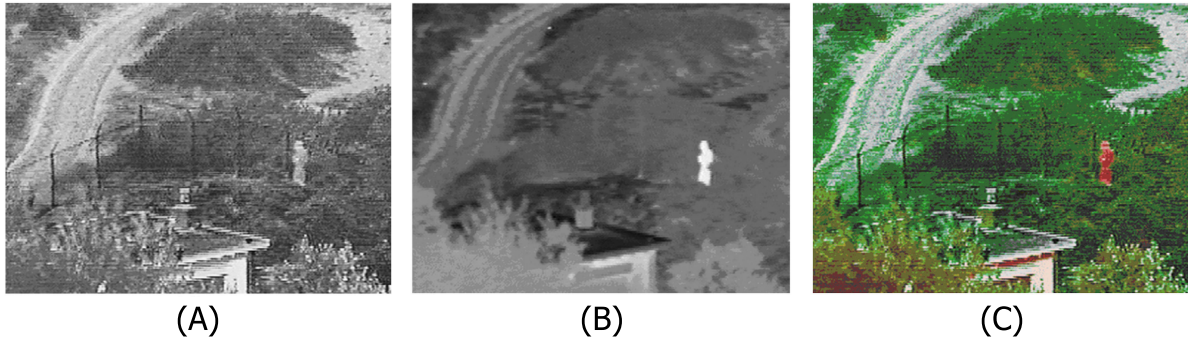
Figure 7.1: From Toet and Hogervorst [100]: (A) Visible and NIR imagery of a nighttime scene, (B) LWIR imagery of the same scene. (C) Fused multispectral image combining the visible-NIR and LWIR images.

the development of these manufacture methods, interest has grown in multispectral imaging as a means to convey more information to an observer from a scene of interest [4]. Conventionally, this is achieved by combining images from two separate sensors with separate optics and focal plane arrays. However this approach adds size and mass to the overall sensor package, which is a critical factor to many multispectral imaging applications such as defence and aerospace. Ideally, we would like a single-aperture optic to image radiation from multiple wavebands on to a single, broadband-sensitive (and selective) focal plane array.

Figure 7.1 outlines some of the benefits of multispectral imaging. Images (A) and (B) show the information conveyed by the visible and near-infrared (NIR) waveband, contrasted to the thermal long-wave infrared (LWIR). The visible waveband presents detail, often as a result of *reflected* light from objects of interest. Meanwhile, the thermal infrared channel substantially conveys *emitted* radiation, which is very useful in the detection of heat sources such as people and vehicles. Image (C) conveys the benefits of fusing both images. The combined image is colourised such that thermal infrared sources colour red within the scene. This enables enhanced detection of both the wire fence (which is difficult to see in the thermal waveband as it is in thermal equilibrium with its surroundings) and the standing person (who can be difficult to pick out of a cluttered scene, particularly if camouflaged). The combined information of both wavebands allows enhanced detection, as well as improved discrimination between friend, foe, or civilian in military environments.

The challenges of optical design and manufacture for multispectral wavebands are substantial; recent research has shown that imaging between the short-wave infrared (SWIR) and LWIR wavebands generally requires that the designer resort to unconventional materials or surfaces to achieve an achromatic solution. Conventional optical materials tend to lead to very heavy solutions with a large number of lens elements. Such designs may be heavier than two single waveband optics combined! In 2013, Thompson [101] demonstrated that colour correction over the SWIR-LWIR wavebands is possible via a number of routes: diamond-based lens elements, alkali-halide-based lens elements, and catadioptric or reflective systems. All these approaches have trade-offs, with diamond optics proving highly effective at colour correction in a reduced SWAP package, yet leaving significant fabrication challenges in generating and polishing such a hard material. Alkali halide lenses are effective at colour correction, yet are extremely delicate and soluble. As a result they again raise significant challenges in optical processing, as well as packaging and mounting of the lenses within a housing that can survive environmental shock loads and temperature variations. Catadioptric solutions suffer from the limitations alluded to in Chapter 1.5.3. In particular, the presence of a central obscuration reduces the optical performance due to suppression of the diffraction limit. This effect is il-

MTF vs Spatial Frequency of Obscured Pupils - 50mm F/1.0 λ=10.6μm
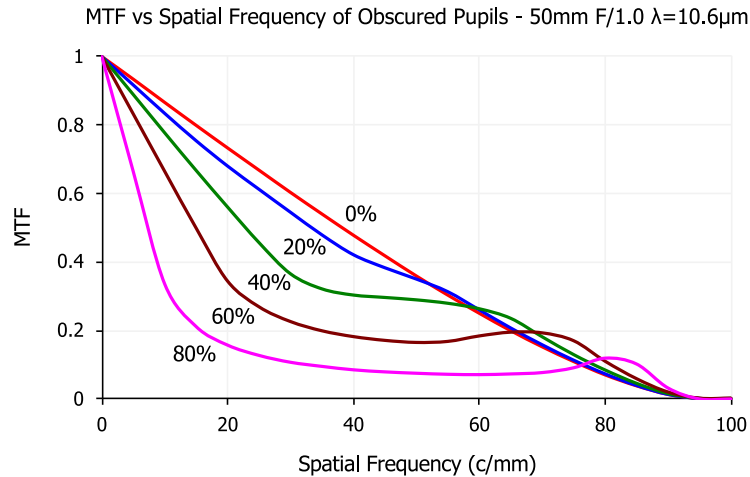
Figure 7.2: MTF vs spatial frequency for a diffraction limited F/1.0 (working) 50 mm system of effective wavelength 10.6 μm. Percentage obscuration of the pupil is indicated. The greater the obscured percentage of the pupil, the more MTF is suppressed at low frequencies.

lustrated in Figure 7.2 and is particularly severe in the LWIR waveband. In 2014, Rolland and Fuerschbach [90] demonstrated a freeform mirror-based solution with 8° x 6° field of view that removed the effect of the central obscuration. This was achieved by tilting the mirror surfaces such that no mirror aperture was obscured, then by applying freeform terms to the optical surfaces to correct the aberrations induced by surface tilt. The resulting design is inherently achromatic at all wavelengths and was diffraction limited at wavelengths above 5 μm. The principal trade-off of this approach is the system size relative to focal length, which is significantly larger than refractive systems. This effect is primarily due to the convex primary mirror that enables aberration correction over a wider field of view. Furthermore, depending on the system application, further features such as a lens hood may be required to reduce stray light effects which reflective systems are inherently vulnerable to.

In addition to chromatic aberration correction, it is highly desirable that optical modules exhibit athermalism via passive means [102, 103]. Broadly, optical systems (if not athermal) observe changes in optical performance over an extended temperature range due to the change in refractive index of optical materials with temperature and thermal expansion of the optical surfaces and housing. Passively athermal optical designs do not require active focus mechanisms to compensate for temperature changes at a uniform temperature soak, with thermal variation of the lens properties corrected in the optical design itself. This can improve system SWAP-C by elimination of mechanics (and potentially electronics) that compensate for thermal defocus. Passive athermalisation adds an additional challenge to the design of multispectral systems, as we require stable focus of the optical design over a wide range of wavelengths and temperatures simultaneously. In reflective systems this process is relatively simple. We simply require the system housing to have the same coefficient of thermal expansion (CTE) as the mirror surfaces. If this is the case, then uniform temperature changes simply result in a change of scale of the system. A number of materials exist that are amenable to such an approach. In particular aluminium can be used to generate mirror surfaces and housings, alternatively glass ceramic materials such as Schott Zerodur® may be combined with low-expansion alloys such as Invar. The approach required for refractive systems is more complex, as we must consider not only the thermal expansion of the housing and the optical materials, but also the thermal variation in refractive index or dN/dT. Correct selection of optical and housing materials and the power construction of the optical design itself allows

optical solutions that are passively optically athermal (with no user intervention required). We explore this approach in greater detail in Section 7.3.4. A related approach is passive mechanical athermalisation, whereby mechanical structures are engineered to produce an effective CTE for the optical housing that removes thermal defocus. Whilst effective in theory, this approach suffers from practical drawbacks including hysteresis (often due to a dependency on high CTE polymers), jamming, and increased cost due to mechanical complexity. Finally, optical systems may be *actively* athermalised, via a mechanism operated by the user or by the system mechatronics. Active athermalisation by the user is generally reserved for optical systems that already have focus mechanisms in place to account for changes in object distance, or quite simply in cases where it is not possible to achieve passive athermalisation alone due to other system constraints.

In this study we investigate how radial-GRIN lenses can be leveraged to simplify the design of athermal, multispectral objective lenses. We evaluate how GRIN elements influence the first-order imaging properties of such an optical system, in particular how these properties vary with respect to temperature and wavelength. We consider the SWAP-C impact of radial-GRIN elements for a 15° field of view multispectral objective lens, when compared to a conventional homogeneous optical solution. We do not consider the potential trade-offs of the manufacturing approach at this stage, rather we seek to determine if there is any theoretical benefit of a GRIN based approach. If such a benefit exists, there is justification for further investigation of potential manufacture routes.

7.3. A First-Order Model of a Multispectral GRIN Lens

7.3.1. Optical Power of Thin GRIN Lenses

We can estimate the optical power of a first-order system by modelling it as a number of thin lenses in contact. We define optical power in as the inverse of the focal length, f_{lens}.

$$K_{\text{lens}} = \frac{1}{f_{\text{lens}}} = K_1 + K_2 + \ldots + K_n \tag{7.1}$$

for a system of n lens elements. The power of a thin, homogeneous lens as a function of wavelength is defined as

$$K(\lambda) = (c_1 - c_2)(N(\lambda) - 1), \tag{7.2}$$
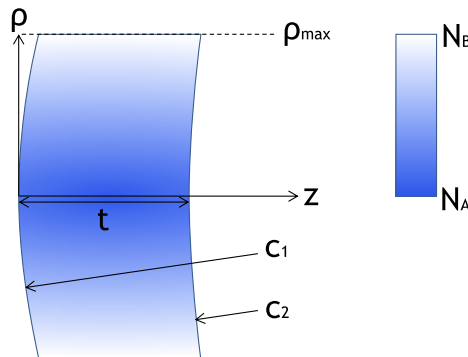
Figure 7.3: Geometry of a radial-GRIN lens

where c_1 and c_2 are the curvatures of the front and rear surfaces as illustrated in Figure 7.3, with the sign convention that a positive surface curvature generates a positive surface sagitta in the optical axis, z. We define $\mathcal{K}_S = c_1 - c_2$ as a power coefficient, as the level of lens "bending" does not affect the power of a thin lens. A radial-GRIN medium and its subsequent optical power contribution are defined in Equations 1.26 and 1.27. Thus, the total optical power of a curved, thin, radial-GRIN lens with thickness, t, is given by

$$K_{\text{lens}} = K_{\text{surf}} + K_{\text{GRIN}} = \mathcal{K}_S \left(\mathcal{N}_{00}(\lambda) - 1 \right) - 2\mathcal{N}_{20}t \tag{7.3}$$

The GRIN itself is composed of a quadratic variation in index between two base materials, A and B with refractive indices $N_A(\lambda)$ and $N_B(\lambda)$ respectively (as illustrated in Figure 7.3). The GRIN refractive index as a function of clear aperture radius, ρ, is given by

$$N(\rho, \lambda) = N_A(\lambda) + \mathcal{N}_{20}(\lambda)\rho^2, \text{ where } \quad \mathcal{N}_{20}(\lambda) = \frac{N_B(\lambda) - N_A(\lambda)}{\rho_{\text{max}}^2}. \tag{7.4}$$

This equation satisfies the conditions: $N(0, \lambda) = N_A(\lambda)$, $N(\rho_{\text{max}}, \lambda) = N_B(\lambda)$. We then define a power coefficient and wavelength scaling factor for our GRIN medium, $\mathcal{K}_G$ and κ respectively. κ is unity at a defined reference wavelength, λ_{ref}. The power of the GRIN is then given by

$$K_{\text{GRIN}} = \mathcal{K}_G \kappa(\lambda) = -2\mathcal{N}_{20}(\lambda_{\text{ref}})\kappa(\lambda)t, \tag{7.5}$$

where

$$\kappa(\lambda) = \frac{N_B(\lambda) - N_A(\lambda)}{N_B(\lambda_{\text{ref}}) - N_A(\lambda_{\text{ref}})} = \frac{\Delta N(\lambda)}{\Delta N(\lambda_{\text{ref}})}. \tag{7.6}$$

7.3.2. Colour Correction Over Multiple Wavebands with GRIN

We define axial primary chromatic aberration as the derivative of optical power with respect to wavelength. A system of thin lenses in contact is therefore achromatic at a given wavelength (λ_i) if this derivative is zero. This condition is shown for a system of M optical surfaces and P radial GRIN lenses with plano surfaces

$$\frac{dK_{\text{lens}}(\lambda_i)}{d\lambda} = \sum_{m=1}^{M} \mathcal{K}_m \frac{dN_m(\lambda_i)}{d\lambda} + \sum_{p=1}^{P} \mathcal{K}_p \frac{d\kappa_p(\lambda_i)}{d\lambda}, \tag{7.7}$$

where N_m is the refractive index of the mth homogeneous surface and κ_p is the wavelength scaling factor of the pth GRIN lens. It can be preferable to express Equation 7.7 in terms of the more familiar Abbé V value, as defined in Equations 1.15 and 1.29 for homogeneous and GRIN materials respectively. For a system with three sequential wavelengths $\lambda_{\text{long}} > \lambda_i > \lambda_{\text{short}}$, the Abbé value can be approximately related to the derivative of refractive index with respect to wavelength by

$$\frac{dN(\lambda_{\text{ref}})}{d\lambda} \approx \frac{N(\lambda_{\text{long}}) - N(\lambda_{\text{short}})}{\lambda_{\text{long}} - \lambda_{\text{short}}}, \quad V_i = \frac{N(\lambda_i) - 1}{N(\lambda_{\text{short}}) - N(\lambda_{\text{long}})}, \tag{7.8}$$

and by similar logic for GRIN materials by differentiating κ with respect to wavelength

$$\frac{d\kappa(\lambda)}{d\lambda} = \frac{d\Delta N(\lambda_i)/d\lambda}{\Delta N(\lambda_{\text{ref}})} \approx \frac{1}{\Delta N(\lambda_{\text{ref}})} \frac{\Delta N(\lambda_{\text{long}}) - \Delta N(\lambda_{\text{short}})}{\lambda_{\text{long}} - \lambda_{\text{short}}}. \tag{7.9}$$

149

This approach yields approximations for $dN(\lambda_i)/d\lambda$ and $d\kappa(\lambda)/d\lambda$

$$\frac{dN(\lambda_i)}{d\lambda} \approx \frac{N(\lambda_i) - 1}{-V_i(\lambda_{\text{long}} - \lambda_{\text{short}})}, \tag{7.10}$$

$$\frac{d\kappa(\lambda)}{d\lambda} \approx \frac{\kappa(\lambda_i)}{-V_{\text{GRIN}i}(\lambda_{\text{long}} - \lambda_{\text{short}})}. \tag{7.11}$$

Equations 7.10 and 7.11 are substituted into Equation 7.7 to yield

$$\frac{dK_{\text{lens}}(\lambda_i)}{d\lambda} \approx \frac{\Delta K_{\text{lens}}}{(\lambda_{\text{long}} - \lambda_{\text{short}})} \approx \sum_{m=1}^{M} \mathcal{K}_m \frac{(N_m(\lambda_i) - 1)}{-V_{mi}(\lambda_{\text{long}} - \lambda_{\text{short}})}$$

$$+ \sum_{p=1}^{P} \mathcal{K}_p \frac{\kappa_p(\lambda_i)}{-V_{\text{GRIN}pi}(\lambda_{\text{long}} - \lambda_{\text{short}})} = 0. \tag{7.12}$$

Pragmatically, we cancel the $(\lambda_{\text{long}} - \lambda_{\text{short}})$ term from Equation 7.12, as it is not required to ensure that $\Delta K_{\text{lens}} = 0$. For multispectral systems we can define multiple sub-bands $i, j, k, \ldots$, and assign our component materials separate Abbé V values for each sub-band.

7.3.3. Thermal Expansion of Inhomogeneous Materials
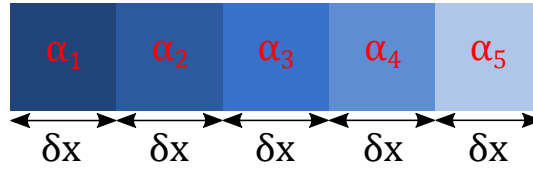
Figure 7.4: Inhomogeneous strip decomposed into homogeneous, infinitesimal elements

The linear thermal expansion of a homogeneous solid is given by the equation:

$$\Delta X(T) = \alpha \Delta T X, \tag{7.13}$$

where the temperature change $\Delta T = T - T_0$. X is a given dimension of the solid and α is the coefficient of thermal expansion or CTE. We can model the thermal expansion of an inhomogeneous strip in one dimension, by first considering the material as an array of infinitesimal homogeneous strips (see Figure 7.4). We can then derive an equation for a thermally perturbed coordinate. Integrating $d\alpha/dx$ as a function of the spatial coordinate x, we obtain

$$\Delta X = \int_0^{X_{T_0}} \frac{d\alpha(x)}{dx} \Delta T dx. \tag{7.14}$$

This now allows us to define a thermally perturbed GRIN distribution suitable for use in optical design software. An intrinsic difficulty in modelling inhomogeneous components is modelling the effect of mechanical stress induced by the spatial variation of the CTE. This important mechanical consideration may lead to thermal failures of GRIN components where the difference in CTE is too great [104, 105] . This is a complex problem, more suited to finite-element analysis, and therefore lies beyond the scope of the present work.

7.3.4. A Thermo-Optic Glass Coefficient for Radial-GRIN Lenses

The thermo-optic glass coefficient, γ, is a useful derived material property for the first-order design of athermal systems [102] . γ is the thermal derivative of the optical power of a given component divided by its optical power

$$\frac{dK_{\text{lens}}}{dT} = \gamma K_{\text{lens}}. \tag{7.15}$$

We can derive γ by differentiation of Equation 7.2 with respect to temperature, within which the lens radii of curvature and refractive index are functions of temperature. The thermal derivative of refractive index, dN/dT, must be determined experimentally for a given material. This is typically achieved using a refractive index measurement technique such as minimum beam deviation [106] within a controlled thermal chamber, although it can also be measured interferometrically [107]. The thermal derivative of surface curvature depends on the lens material CTE (which again must be determined experimentally). The lens material CTE then determines thermal variation in the radius of curvature, R, given by

$$R(T) = \frac{1}{c(T)}. \tag{7.16}$$

$$\Delta R = \alpha R \Delta T. \tag{7.17}$$

Using the chain rule, we then determine dc/dT

$$\frac{dc}{dT} = \frac{dc}{dR}\frac{dR}{dT} = -\frac{1}{R^2}\frac{dR}{dT} = -\alpha c. \tag{7.18}$$

Differentiating Equation 7.2 with respect to T, we obtain by using the product rule

$$\frac{dK}{dT} = \frac{dN}{dT}(c_1 - c_2) + (N - 1)\alpha\,(c_2 - c_1)\,, \tag{7.19}$$

$$\frac{dK}{dT} = \frac{dN}{dT}\frac{K}{N-1} - \alpha K, \tag{7.20}$$

where after collecting terms in K

$$\frac{dK}{dT} = K\left[\frac{dN}{dT}\frac{1}{N-1} - \alpha\right] = \gamma K, \tag{7.21}$$

hence

$$\gamma = \frac{dN}{dT}\frac{1}{N-1} - \alpha. \tag{7.22}$$

This assumes the material is in air, and that refractive index and dN/dT are relative to that of air [108]. The condition for an athermal optical system is that the thermal change in power is opposite to the expansion of the lens housing, α_H,

$$\frac{dK_{\text{lens}}}{dT} = -K_{\text{lens}}\alpha_H. \tag{7.23}$$

To find an expression for the thermo-optical glass coefficient for radial-GRIN lenses, we must follow a similar path to the homogeneous case and differentiate Equation 7.3 with respect to temperature. Using the product rule and substituting Equation 1.26 gives

$$\frac{dK_{\text{lens}}}{dT} = \frac{dK_{\text{GRIN}}}{dT} + \frac{dK_{\text{surf}}}{dT} = \frac{d}{dT}\left[-2t\frac{N_B - N_A}{\rho_{\max}^2}\right] + \frac{d}{dT}\left[(N_A - 1)\,(c_1 - c_2)\right]. \tag{7.24}$$

We address subsequently the temperature derivative of the GRIN and the surface contributions. Further expansion of the derivatives and substitution of Equation 7.4 gives

$$\frac{dK_{\text{GRIN}}}{dT} = \frac{(N_B - N_A)}{\rho_{\text{max}}^4}\left[-2\rho_{\text{max}}^2\frac{dt}{dT} + 2t\frac{d}{dT}(\rho_{\text{max}}^2)\right] + \frac{-2t}{\rho_{\text{max}}^2}\frac{d}{dT}(N_B - N_A). \tag{7.25}$$

We must now determine each of the derivatives in the right hand side of Equation 7.25. Of these, the N and dN/dT of the base materials must be provided for a given GRIN material combination.

To compute the derivatives of the lens curvatures and thickness, we assign coefficients of thermal expansion to our base materials. α_A and α_B define the CTE of materials A and B respectively. The CTE of the lens is therefore equal to α_A along the optical axis and α_B at ρ_{max}. We assume the lens CTE is constant along the optical axis and that there is no induced stress from the neighbouring material. The temperature derivative of the axial thickness is

$$\frac{dt}{dT} = t\alpha_A. \tag{7.26}$$

The derivative of ρ_{max}^2 is found by first using Equation 7.14 to express ρ_{max} as a function of T

$$\Delta\rho_{\text{max}}(T) = \int_0^{\rho_{\text{max}}}\left(\alpha_A\Delta T + \frac{(\alpha_B - \alpha_A)}{\rho_{\text{max}}^2}\rho^2\Delta T\right)d\rho. \tag{7.27}$$

Given that over a typical military operating temperature range for common optical materials, $\alpha\Delta T \approx 10^{-3}$, we can assume that any $(\alpha\Delta T)^2$ terms are negligible by comparison. This gives us the component derivative

$$\frac{d\rho_{\text{max}}^2(T)}{dT} = \rho_{\text{max}}^2\left(2\alpha_A + \frac{2(\alpha_B - \alpha_A)}{3}\right). \tag{7.28}$$

Substituting the component derivatives in Equations 7.26, 7.28, and 1.27 into Equation 7.25 gives us an equation for the thermal derivative of the GRIN medium power

$$\frac{dK_{\text{GRIN}}}{dT} = \left[\frac{\frac{dN_B}{dT} - \frac{dN_A}{dT}}{N_B - N_A} - \frac{(2\alpha_B + \alpha_A)}{3}\right]K_{\text{GRIN}}. \tag{7.29}$$

For a radial-GRIN lens, the optical surfaces themselves will be thermally perturbed by the GRIN medium. We can find what effect this has by differentiating the surface contribution to power with respect to temperature

$$\frac{dK_{\text{surf}}}{dT} = \frac{d}{dT}[(N_A - 1)(c_1 - c_2)] = \frac{dN_A}{dT}(c_1 - c_2) + (N_A - 1)(\frac{dc_1}{dT} - \frac{dc_2}{dT}). \tag{7.30}$$

To simplify our calculations, we assume that surfaces take the form of paraboloids (which are the first-order Taylor approximation to a sphere)

$$z = \frac{1}{2}c_n\rho^2, \quad n = 1, 2 \tag{7.31}$$

At the maximum aperture of the lens, the sag of surface n becomes

$$z_{\text{max}} = \frac{1}{2}c_n\rho_{\text{max}}^2. \tag{7.32}$$

We use the quotient rule to express $\frac{dc_n}{dT}$ in terms of z_{max} and ρ_{max} as

$$\frac{dc_n}{dT} = \frac{d}{dT}\left(\frac{z_{max}}{2\rho_{max}^2}\right) = \frac{\rho_{max}^2 \frac{d}{dT}(z_{max}(T)) - z_{max}\frac{d}{dT}(\rho_{max}^2(T))}{2\rho_{max}^4}. \tag{7.33}$$

We must now calculate $\frac{d}{dT}(z_{max})$. The GRIN medium itself induces curvature with temperature change, due to the difference in CTE between the optical axis and ρ_{max}. We make the assumption that this induced curvature manifests entirely in surface 1 for simplicity, although the thin lens assumption tells us that the relative distribution of induced curvature between surfaces 1 and 2 does not matter. Change in the surface sagitta of surface 1, $\Delta z_{max,1}$, is given by

$$\Delta z_{max,1} = \left[\alpha_B z_{max,1}(T_0) - (\alpha_B - \alpha_A)t\right]\Delta T. \tag{7.34}$$

Substitution of Equations 7.34 and 7.28 into 7.33 gives

$$\frac{dc_1}{dT} = \frac{2\left[z_{max}(T_0)\alpha_B + (\alpha_A - \alpha_B)\,t\right] - 2z_{max}(T_0)\left(\frac{4\alpha_A}{3} - \frac{\alpha_B}{3}\right)}{\rho_{max}^2(T_0)}. \tag{7.35}$$

Rearranging Equation 7.4 we obtain

$$\frac{2t}{\rho_{max}^2} = \frac{K_{GRIN}}{N_B(\lambda) - N_A(\lambda)}. \tag{7.36}$$

Using this and Equations 7.31 and 7.2 we obtain an expression for $\frac{dc_1}{dT}$ with terms that are factors of K_{GRIN} and K_{surf}

$$\frac{dc_1}{dT} = -\frac{K_{GRIN}(\alpha_A - \alpha_B)}{N_B(\lambda) - N_A(\lambda)} - \frac{K_{surf}}{N_A(\lambda) - 1}\left(\frac{4\alpha_A}{3} - \frac{\alpha_B}{3}\right). \tag{7.37}$$

Equation 7.37 becomes equivalent to the expansion of a homogeneous surface if $\alpha_A = \alpha_B$. There are two contributions to the thermal behaviour of the surface, namely the thermal expansion of the inhomogeneous surface, and an induced curvature term which depends on the thickness of the GRIN medium. We must now substitute our expressions for dc/dT into Equation 7.30. By substituting Equation 7.37 into Equation 1.28 we find:

$$\frac{dK_{surf}}{dT} = \frac{dN_A}{dT}\frac{K_{surf}}{N_A - 1} + \frac{K_{GRIN}(N_A - 1)(\alpha_B - \alpha_A)}{(N_B - N_A)} - K_{surf}(\frac{4}{3}\alpha_A - \frac{1}{3}\alpha_B). \tag{7.38}$$

Combining Equations 7.38 and 7.29 and rearranging with respect to medium and surface contributions, we arrive at a thermo-optic glass coefficient for radial-GRIN materials

$$\frac{dK}{dT} = K_{GRIN}\gamma_{20} + K_{surf}\gamma_{01}, \tag{7.39}$$

where the medium and surface thermo-optical coefficients are defined as γ_{20} and γ_{01} respectively and are given by

$$\gamma_{20} = \frac{\frac{dN_B}{dT} - \frac{dN_A}{dT}}{N_B - N_A} - \frac{(2\alpha_B + \alpha_A)}{3} + \frac{(N_A - 1)(\alpha_B - \alpha_A)}{(N_B - N_A)}, \tag{7.40}$$

and

$$\gamma_{01} = \frac{dN_A}{dT}\frac{1}{N_A - 1} - \frac{4}{3}\alpha_A + \frac{1}{3}\alpha_B. \tag{7.41}$$

In comparison to the homogeneous thermo-optic glass coefficient of Equation 7.15, we have additional complication due to the design choice of how optical power is distributed between the lens surfaces and the GRIN medium. This has led us to a final expression with two gamma terms. Whilst these thermo-optic coefficients are more complicated than the homogeneous equivalent, they nevertheless depend solely on the material properties of a given GRIN combination and are independent of lens geometry.

7.3.5. Design of an Athermal, Radial-GRIN Singlet

To test the validity of Equations 7.39-7.41, a radial-GRIN singlet composed of ZnS-ZnSe was designed. This was done to the first order by solving Equation 7.23 for zero thermal defocus, as well as by optimisation of a CodeV$^\circledR$ GRIN lens model for minimised RMS spot size on axis. An additional reference lens model consisting of a ZnS singlet was optimised in CodeV for comparison. The results of each approach were then compared. The system of equations that must be solved for a ZnS-ZnSe GRIN lens of focal power, K_{lens}, and zero thermal defocus is obtained by collecting Equations 7.3, 7.23 and 7.39 and is given by

$$K_{\text{lens}} = K_{\text{surf}} + K_{\text{GRIN}}$$

$$\frac{dK_{\text{lens}}}{dT} = \gamma_{01} K_{\text{surf}} + \gamma_{20} K_{\text{GRIN}} + \alpha_H K_{\text{lens}} = 0. \tag{7.42}$$

Solving Equation 7.42 for K_{surf} and K_{GRIN} gives

$$K_{\text{surf}} = \frac{-K_{\text{lens}} (\gamma_{20} + \alpha_H)}{(\gamma_{01} - \gamma_{20})}, \quad K_{\text{GRIN}} = \frac{K_{\text{lens}} (\gamma_{01} + \alpha_H)}{(\gamma_{01} - \gamma_{20})}. \tag{7.43}$$

We then use known literature values for N and dN/dT of ZnS and ZnSe to find γ_{01} and γ_{20} and subsequently solve Equation 7.43 for K_{surf} and K_{GRIN}. Material coefficients in the CodeV optical model are then determined using Equations 2.25 and 2.27, with judicious selection of a lens thickness such that the relative composition of ZnS and ZnSe remains positive at all points within the lens model. The lens was then optimised in CodeV through minimisation of the RMS spot size by varying the surface curvatures and GRIN material coefficients.

Raytraces of the CodeV models are shown in Figure 7.5. The values of K_{surf} and K_{GRIN} are shown in Table 7.1. These closely match the values obtained by optimisation of the CodeV GRIN model. To minimise the impact of third-order or higher aberrations, the front surface of the GRIN singlet was made aspheric and restricted to an F/8 aperture. Table 7.1 shows some residual thermal defocus remains in the CodeV model to balance the presence of thermally induced spherical aberration by the GRIN medium, as well as non-linearity in the $\frac{dN}{dT}$ values of the base materials. Such non-linearity in the thermo-optic coefficients may need to be considered for particularly broad temperature ranges, such as those in space applications.
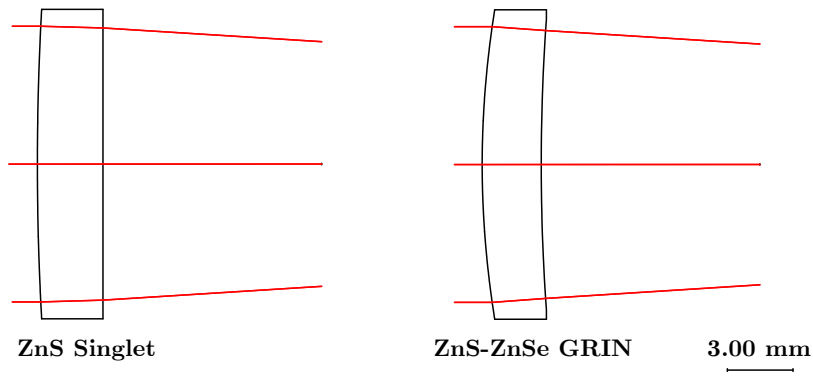
Figure 7.5: Homogeneous ZnS singlet and athermal ZnS-ZnSe radial-GRIN lens

Property	First-order solution	CodeV optimised design	Reference ZnS singlet
K_{lens} (mm^{-1})	0.01	0.01	0.01
F/#	NA	8	8
K_{surf} (mm^{-1})	0.01676	0.01618	0.01
K_{GRIN} (mm^{-1})	-0.00676	-0.006716	NA
Thermal defocus (mm) (-30°C to +70°C)	0	0.069	0.506

Table 7.1: Comparison of lens properties for a first-order GRIN singlet design, CodeV GRIN singlet design and reference ZnS singlet

7.3.6. The search for a Multispectral Starting Solution

We now use the first-order design tools derived in Sections 7.3.2 and 7.3.4 to find a starting solution for an athermal, multispectral objective lens. In a similar manner to Section 7.3.5, we generate a lens system requirement that defines a set of linear equations. These equations are then solved by a corresponding number of degrees of freedom provided by a set of thin lenses of different materials and optical powers. Our specification for a detailed optical design is defined in Table 7.3. Firstly, we assign three defining wavelengths for the system: $\lambda_i =1.4$ µm, $\lambda_j = \lambda_{ref} =4$ µm and $\lambda_k =10$ µm. To achieve SWIR-LWIR imaging onto a common focal plane, we would firstly like the focal power of the two sub-bands to be identical. We therefore constrain the focal power of the system at λ_i and λ_k to unity. We can evaluate performance at different focal lengths by simply scaling the system. Secondly, we would like the chromatic aberration of each sub-band to be controlled. We therefore solve for the focal power derivative with respect to wavelength, $dK/d\lambda$, at λ_i and λ_k. The refractive index derivative with respect to wavelength of each constituent material will be approximated by the Abbé V value for each sub-band, V_i and V_k, as per Equations 7.10 and 7.11. The combination of optical powers that yield zero chromatic aberration can then be found via Equation 1.14. Finally, we would like our system to be athermal. We achieve this by setting the thermal power derivative to be equal and opposite to the coefficient of thermal expansion of the housing, α_H, as per Equation 7.23. This set of requirements has a total of five parameters that must be solved for. This can be achieved using two GRIN lenses and one homogeneous lens, or five homogeneous lenses. This set of equations is represented as a matrix in equation 7.44 for a solution consisting of two GRIN lenses and one homogeneous lens element. Columns 1 and 2 of Equation 7.44 represent the first GRIN lens, columns 3 and 4 the second GRIN lens, and column 5 the homogeneous component. The first two rows of Equation 7.44 control the lens focal power in the SWIR and LWIR wavebands respectively. Rows three and four control the chromatic aberration at λ_i and λ_k respectively. Row five controls the thermal defocus of the lens system at λ_j.

$$\begin{pmatrix} N_1(\lambda_i) - 1 & \kappa_2(\lambda_i) & N_3(\lambda_i) - 1 & \kappa_4(\lambda_i) & N_5(\lambda_i) - 1 \\ N_1(\lambda_k) - 1 & \kappa_2(\lambda_k) & N_3(\lambda_k) - 1 & \kappa_4(\lambda_k) & N_5(\lambda_k) - 1 \\ \frac{N_1(\lambda_i)-1}{V_{1i}} & \frac{\kappa_2(\lambda_i)}{V_{GRIN2i}} & \frac{N_3(\lambda_i)-1}{V_{3i}} & \frac{\kappa_4(\lambda_i)}{V_{GRIN4i}} & \frac{N_5(\lambda_i)-1}{V_{5i}} \\ \frac{N_1(\lambda_k)-1}{V_{1k}} & \frac{\kappa_2(\lambda_k)}{V_{GRIN2k}} & \frac{N_3(\lambda_k)-1}{V_{3k}} & \frac{\kappa_4(\lambda_k)}{V_{GRIN4k}} & \frac{N_5(\lambda_k)-1}{V_{5k}} \\ [N_1(\lambda_j) - 1]\gamma_{011j} & \kappa_2(\lambda_j)\gamma_{202j} & [N_3(\lambda_j) - 1]\gamma_{013j} & \kappa_4(\lambda_j)\gamma_{204j} & [N_5(\lambda_j) - 1]\gamma_{5j} \end{pmatrix} \begin{pmatrix} \mathcal{K}_1 \\ \mathcal{K}_2 \\ \mathcal{K}_3 \\ \mathcal{K}_4 \\ \mathcal{K}_5 \end{pmatrix} = \begin{pmatrix} 1 \\ 1 \\ 0 \\ 0 \\ -\alpha_H \end{pmatrix} \quad (7.44)$$

Whilst a solution to Equation 7.44 can be found for any unique set of materials, this information alone is not sufficient to determine whether a given solution is a well-corrected design starting point. Residual chromatic aberrations exist at wavelengths other than $\lambda_{i,j,k}$, and thermal defocus can vary at $\lambda_{i,k}$. An additional figure of merit is derived from the peak-to-valley (P-V) of residual chromatic aberration and defocus due to temperature over the SWIR and LWIR sub-wavebands as illustrated in Figure 7.6. We also define the root-sum of squares (RSS) of individual element powers as

$$K_{RSS} = \sqrt{K_{S1}^2 + K_{GRIN1}^2 + K_{S2}^2 + K_{GRIN2}^2 + K_{lens3}^2}, \quad (7.45)$$

where K_{S1} and K_{GRIN1} are the surface and GRIN power contributions to GRIN lens 1 and K_{S2} and K_{GRIN2} are the surface and GRIN power contributions for lens 2. K_{lens3} is the power of the homogeneous lens 3. Real optical designs have *field* and *aperture*. A lens design with a steep balance of component optical powers induces greater optical aberrations as the
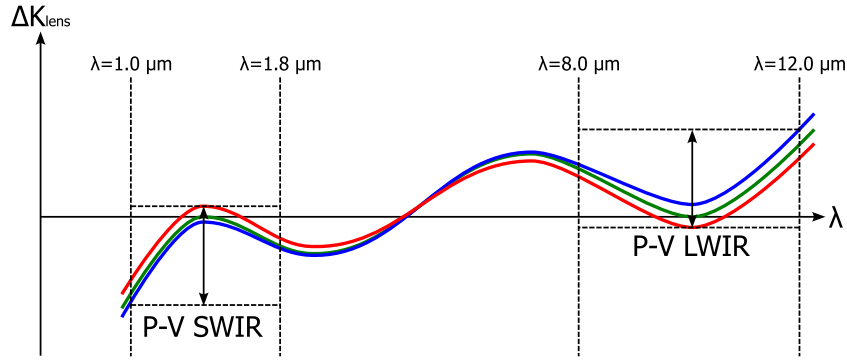
Figure 7.6: Definition of peak-to-valley for each sub-band of a multispectral thin lens solution.

aperture and field of view are increased. These aberrations then further induce higher-order aberrations which are very difficult to correct. Furthermore, optical systems with strongly powered lenses tend to be more sensitive to manufacturing tolerances than a solution with weaker components to the same overall specification. A good lens design heuristic is to minimise optical component power to simplify the task of correcting the system aberrations. A sample merit function derived from the weighted RSS of these quantities is defined as

$$FOM = \sqrt{K_{RSS}^2 + w_{SWIR}PV_{SWIR}^2 + w_{LWIR}PV_{LWIR}^2}, \tag{7.46}$$

where w_{SWIR} and w_{LWIR} are weighting factors applied to the peak to valley chromatic aberration over the design temperature range of -30°C to +70°C for each sub-band. w_{SWIR} and w_{LWIR} were assigned a value of 5000, as the value of P-V residual chromatic aberration and thermal defocus is much smaller than the RSS sum of lens powers. This merit function was used to optimise over the solution space of available materials. A brute-force optimisation was undertaken for the SWIR-LWIR solution space given the relatively small computational overhead required to search the solution space of approximately 95000 solutions for common IR materials.

Brute-force optimisation revealed the solution shown in Figure 7.7 and Table 7.2. Chromatic aberration is low over each sub-band and the thermal performance is stable. Some higher-order residual chromatic aberration exists at the short wavelength SWIR end of the system. We see some variation in the athermalisation over the extended waveband due to variation in material dN/dT with wavelength, with the athermalisation being under-corrected in the SWIR waveband but over-corrected in the LWIR. This *thermo-chromatic* aberration is the main source of residual P-V normalised power for the thin lens model. Additional components made from different materials may provide the degrees of freedom to correct this, but for this study we accept the residual level as acceptable for our design starting point.

It is particularly noteworthy that a design based on the same materials in their homogeneous form gives equivalent chromatic and thermal performance to the thin-lens GRIN solution, but the normalised RSS power is significantly higher at 9.44, compared to 1.51 for the GRIN solution. To the first order, a radial-GRIN lens is an equivalent degree of freedom to two conventional lenses of different materials, but the reduction in optical power balance caused by the GRIN also enables optical designs with greatly reduced lens element powers that make smaller aberration contributions, as well as a reduced lens count.

It is important to note that the first-order design approach only yields *starting points* from which a real solution can be optimised. It is not guaranteed that the solution with the best

157

GRIN lens 1	ZnSe-ZnS
GRIN lens 2	IRG24-IRG26
Lens 3	AMTIR1
$K_{lens1surf}$	-0.36
$K_{lens1GRIN}$	0.02
$K_{lens2surf}$	0.829
$K_{lens2GRIN}$	-0.55
K_{lens3}	1.07
K_{Total}	1.000
K_{RSS}	1.51
P-V K_{SWIR}	0.0023
P-V K_{LWIR}	0.0022

Table 7.2: First-order SWIR-LWIR solution data
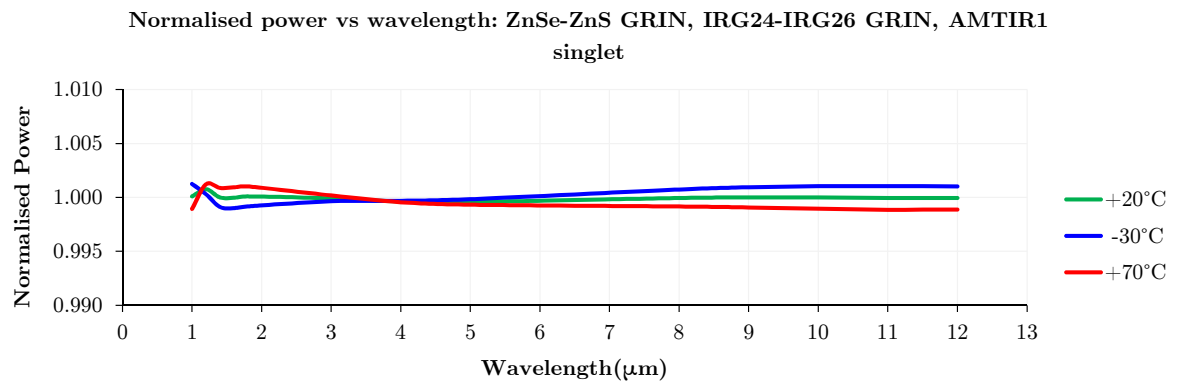
Figure 7.7: Multispectral first-order solution. Power versus wavelength.

158

first-order performance yields the best performance when optimised into a real optical design. Finite field of view, aperture and lens thickness/separation all have a substantial influence on optical designs and therefore a number of potential starting solutions should be evaluated during the design process.

7.4. SWIR-LWIR Objective Lens Optical Design

To test the first-order design method described in Section 7.3.6, a GRIN optical design was optimised against the specification shown in Table 7.3. This specification was for a weapon sight type requirement with a relatively narrow field of view and common SWIR-LWIR sensor array. Athermalisation was required to be passive, with no allowance for user focus mechanisms. A homogeneous SWIR-LWIR solution was also optimised to act as a baseline comparison. Optimisation used the default merit function in CodeV AUT, that minimises the RMS spot size. Optimisation variables consisted of lens surface curvatures, thicknesses, air gaps, and aspheric terms, and GRIN coefficients for the GRIN solution. The homogeneous solution was also found by using the CodeV "Glassexpert.seq" macro, which automatically substitutes glass types within a user-defined glass map then optimises the design until an optimal material set is found. Optimisation with glassexpert.seq was followed by manual substitution of aspheric surfaces to find an optimal overall solution. The GRIN solution was constructed from the first-order solution in Table 2.4, followed by local optimisation in CodeV and the addition of aspheres where necessary. More specifically, an aspheric surface was added to the front lens group of each design to aid in correcting aberrations of the pupil such as spherical aberration, while a dual aspheric component was introduced close to the image plane of each design to improve correction of astigmatism.

7.4.1. Homogeneous Solution

A solution consisting of AMTIR1, AMTIR2, ZnSe, cleartran, IRG24, KRS5 and GaAs was ultimately found (illustrated in Figure 7.8). KRS5 was necessary to improve athermalisation and axial colour correction. This is a highly undesirable material from a fabrication perspective due to its poor workability and very high toxicity. The dual aspheric GaAs element was necessary to correct aberrations of the field such as coma and astigmatism. Optical mass of this solution was 83.5g. MTF performance is shown in Figure 7.9. Despite the use of KRS5, athermalisation is relatively poor in the LWIR. There is significant thermo-chromatic aberration observed, with significant divergence in best focus between the SWIR and LWIR bands at extreme temperatures.

Focal length	50 mm
F/#	1.6
SWIR waveband	1-1.8 μm
LWIR waveband	8-12 μm
Semi field-of-view	7.5°
Operating temperature range	-30 °C to +70°C

Table 7.3: Multispectral objective lens specification

159
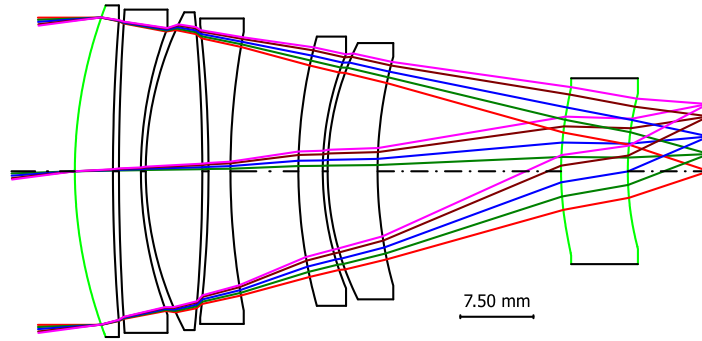
Figure 7.8: Conventional, homogeneous SWIR-LWIR optical design, aspheric surfaces are highlighted in green
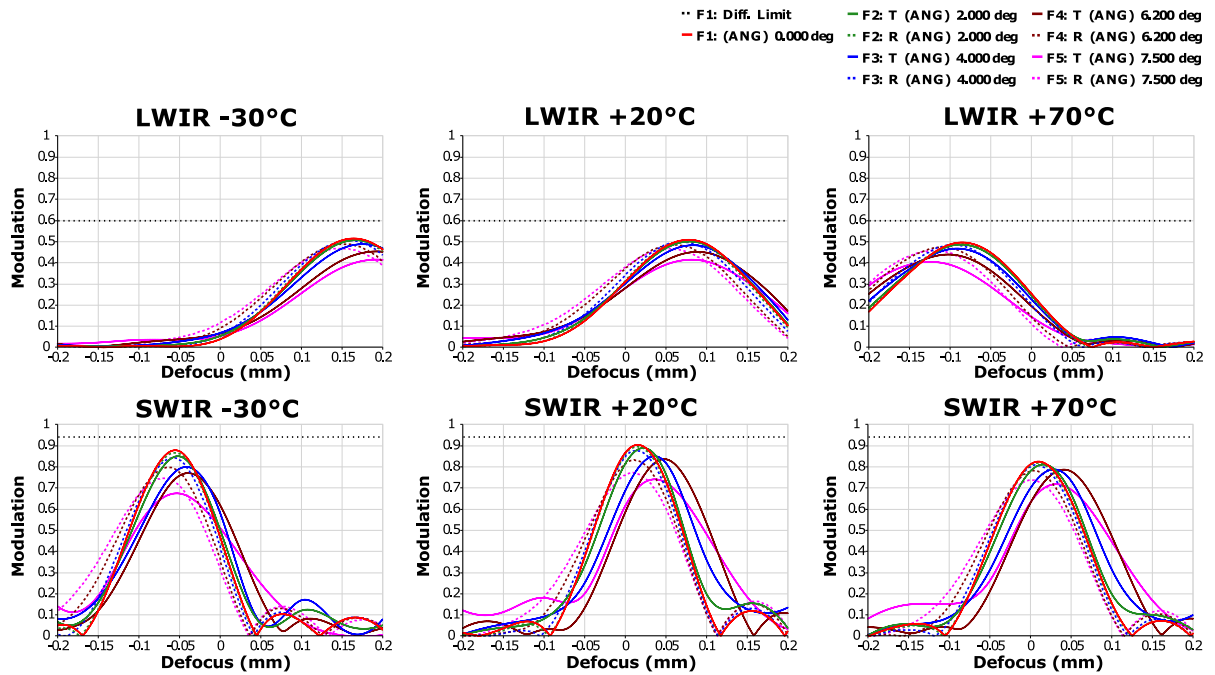
Figure 7.9: MTF vs defocus over temperature of a conventional SWIR-LWIR optical design. Coloured curves represent different field angles in the sagittal (dashed) and tangential (solid) sections.

7.4.2. GRIN Solution

The optimised GRIN optical design is shown in Figure 7.10 with the refractive index distribution overlaid upon the GRIN lens elements. One additional dual-aspheric gallium arsenide element placed near the image plane was required in order to give acceptable off-axis performance by correcting coma and astigmatism. Lens 1 forms a weakly positive GRIN distribution, whilst lens 3 forms a strongly negative GRIN. This is in broad agreement with the data in Table 7.2. MTF performance over the operating temperature range is shown in Figure 7.11. Athermalisation is greatly improved in the LWIR waveband. Some MTF loss in the SWIR waveband occurs at the extreme temperatures due to thermally induced chromatic aberration. Optical mass of this solution was 55 grams. Overall, size and mass of the GRIN solution is significantly reduced compared to the homogeneous design.
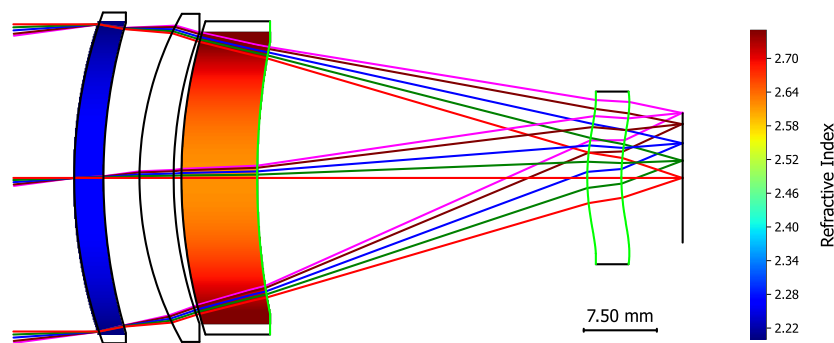
Figure 7.10: Multispectral GRIN lens optical design, aspheric surfaces are highlighted in green. GRIN lens elements have their refractive index distribution overlaid as a colour scale.

161
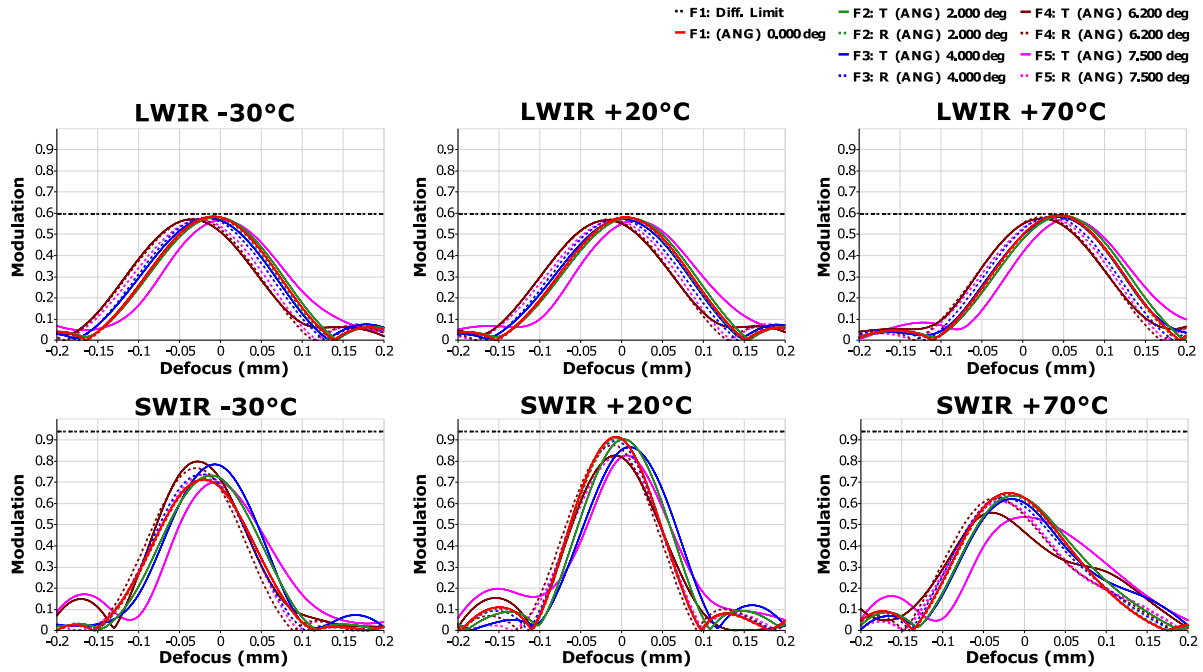
Figure 7.11: Through focus MTF performance over temperature of a radial-GRIN SWIR-LWIR optical design

7.4.3. Alignment Sensitivity

It was observed that the optical power construction of the GRIN design was significantly more relaxed than that of the conventional solution. The optical powers of each lens element for the GRIN and homogeneous solution are shown in Table 7.4. This contrast in optical power construction was also found to have ramifications for performance of the system with manufacturing tolerances. Frequently, the centration of lens elements within an optical system dominates the *as-built* performance. With this in mind, the two designs were analysed for the MTF sensitivity in the SWIR waveband of each lens element. Assessment of performance loss was undertaken using the CodeV TOR algorithm based on wavefront differentials, which gives a fast and accurate analysis of perturbations to lens designs provided the loss in MTF performance is small.

MTF loss in the SWIR waveband at 30 cycles/mm for each component in each design is plotted in Figure 7.12. These sensivity values were for a fixed, 30 μm decentre. It was observed that the homogeneous variant's lens elements were significantly more sensitive to

Lens Number	GRIN Element Power (mm^{-1})	Homogeneous Element Power (mm^{-1})
1	0.00511	0.02615
2	0.01137	-0.03738
3	0.00010	0.04972
4	0.00256	-0.02700
5		-0.01919
6		0.01931
7		0.00472

Table 7.4: Multispectral objective lens design focal powers
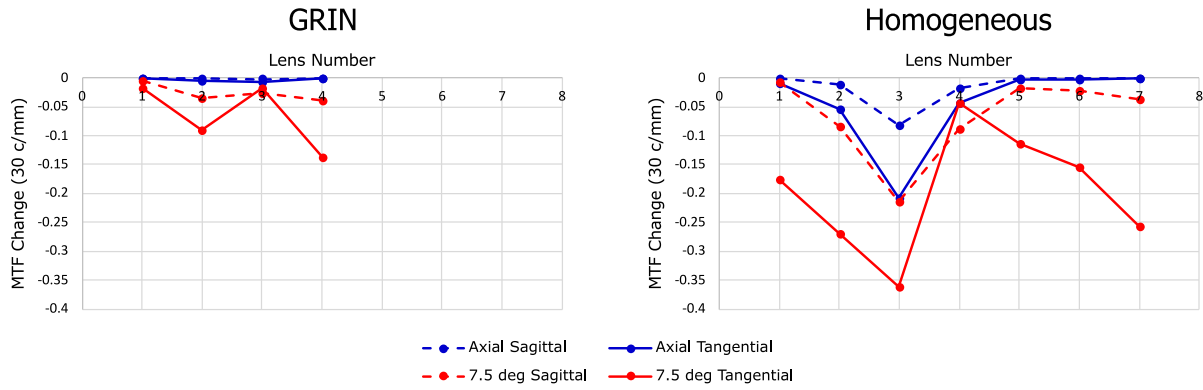
Figure 7.12: MTF loss for a 30 μm decentre of each lens element. Analysis at 30 c/mm for both axial and full field (7.5° semi-field). Left: GRIN solution. Right: Homogeneous solution.

decentre, and would require tighter tolerances to maintain an equivalent performance loss to the GRIN solution. Such a design would likely require optical alignment of one or more lenses in the system to compensate the performance loss, which would add significant cost.

At the time of analysis, a full performance comparison of the designs was not feasible due to a lack of information on tolerances of the GRIN media, which were hypothetically based on existing chalcogenide glasses. It is however noteworthy, for a given system wavefront error budget, that any future GRIN chalcogenide technology may give capacity for a larger error budget in the transmitted wavefront error of the GRIN components due to a reduced contribution to the system error budget from lens alignment errors.

7.5. Conclusion

A first-order design method for athermal and multispectral GRIN lenses was demonstrated. It was shown that a variant of the thermo-optic glass coefficient can be derived for a given pair of materials which form a radial-GRIN lens. Changes to the optical power are caused by changes in the base material refractive indices, thermal expansion of the lens thickness and curvatures, and finally an induced curvature term caused by the difference in CTE between the lens centre and outer aperture. It was found that the radial-GRIN thermo-optic coefficient, like its homogeneous counterpart, depends only on the lens consituent materials, with the added complication of relative power distribution between the GRIN lens surfaces and medium. There is significant utility in determining that the GRIN thermo-optical properties depend solely on the underlying materials, as it means that we do not need to trace rays to determine if a given material combination makes a useful GRIN. This is useful to the researcher/fabricator of GRIN materials, who can use this information to design useful GRIN material combinations based on the properties of the constituent glasses in their homogeneous form. Using predictive models of glass properties such as those discussed in Ryan-Howard & Moore [70], we may propose GRIN material combinations that have intrinsic athermal and achromatic properties.

The athermal, multispectral, first-order design method was used to find starting points for optimisation of a SWIR-LWIR multispectral objective lens. It was found for a given set of optical materials and system focal length, that GRIN solutions have greatly reduced optical component focal power. These reduced-power components generate reduced aberration contributions to the optical system, improving nominal optical performance as well as alleviated sensitivity to manufacturing tolerances. An optical design based on a starting solution found via this

method was optimised and analysed for optical performance over an extended temperature range. It was found that the use of radial-GRIN lenses can enable high quality imaging over a SWIR-LWIR waveband, whilst improving size and mass over a homogeneous solution. This raises the prospect of a new class of optical designs which have the potential to provide more scene information to the end user within a reduced size and mass package.

8

Conclusions

8.1. Summary of main results

Within this work we have presented a deep exploration of the optical design freedoms provided by generalised-gradient-index lenses. This work has broadly consisted of two themes, first exploring design tools for generalised GRINs, then their applications. As the mathematical representations and software design tools required to explore generalised-GRIN lenses were in a nascent state, it was necessary to develop them. Mathematical representations for GRIN lenses consisting of three or more materials were developed, based on the relative composition of the base materials therein. It was shown that such a representation allows calculation of the first-order properties of the GRIN, which can also be decomposed into contributions from the base materials. Expression of the material properties in this way is amenable to specification for optimisation and specification for manufacture, as demonstrated by the successful design of a three-material generalised-distribution GRIN magnifier with comparable performance to a homogeneous design with aspheric and diffractive surfaces.

A method for the construction of starting points for the optimisation of generalised-GRIN systems was also generated. Again, due to the nascent state of generalised-GRIN designs, there is a lack of existing starting solutions from which continuous optical system designs can be optimised. By analysis of the paraxial properties of homogeneous lens systems, followed by smoothing of their paraxial raypaths, it was demonstrated that it is possible to reconstruct homogeneous lens systems as a single GRIN medium that replicates the first-order properties of the parent solution with a high degree of fidelity.

Further consideration was given to the imaging properties of generalised GRIN lenses where the surface geometry is planar. It was shown that such "flat" optics ordinarily cannot correct for coma, due to their inability to satisfy the Abbé sine condition. For such lenses, a generalised GRIN distribution can correct for this, through variation of optical power over the lens thickness. It does however come at the expense of increased ΔN or lens thickness, while the combination of a radial GRIN with surface curvature can correct coma with a much smaller ΔN.

The second major theme of this work addressed applications of GRIN lenses. The degrees of freedom provided by spherically-distributed LGRIN lenses were assessed, demonstrating that

in a singlet they offer comparable optical correction to doublets and diffractive lenses. They achieve this whilst reducing optical mass by virtue of their low-density polymer construction and minimising the risk of stray light artefacts associated with diffractive optics.

A study of the potential performance benefits offered by 3D-printed GRIN lenses in tilted and off-axis lens designs was undertaken. It was shown that asymmetric *freeform-GRIN* distributions have the potential to significantly reduce the optical element count of a head-mounted display or similar off-axis system, allowing a single GRIN lens to simultaneously correct rotationally symmetric and asymmetric monochromatic aberrations as well as chromatic aberrations. Moving to nanoparticle-doped polymer GRINs from conventional glass materials also enabled a significant reduction in system mass.

Finally, the application of GRIN lenses to ultra-wide waveband multispectral imaging problems was investigated. Conventionally, such systems require many lens elements consisting of exotic materials. They also often require extreme distributions of optical power between lens elements, resulting in poor imaging performance, especially over a finite temperature range. It was found that GRIN lenses significantly ease the optical power construction of such systems, effectively by merging positive and negatively powered lens elements into a single, reduced-power lens. This enables a substantial reduction in lens count and improved optical performance over a finite temperature range, as demonstrated by the design of a GRIN SWIR-LWIR imaging system that compared favourably to its homogeneous equivalent.

8.2. Answers to Research Questions

8.2.1. Are there benefits to the SWAP-C of optical systems through the use of generalised GRIN lenses, and if so what are they?

Generalised-GRIN lenses allow several lens elements to be replaced by a single thick GRIN medium. The benefits with respect to optical element count are immediately clear in this regard. Fewer turning/polishing, coating and assembly operations are required to satisfy a given optical function. This replacement of lens elements also precipitates a substantial saving in mass where the GRIN lenses replace conventional glass lens elements with nanoparticle-doped polymers. This mass saving was particularly evident in the design of a HMD system. In some situations such as multispectral optics, GRIN lenses can be the difference between viability and non-viability of the imaging system, through improving performance, reducing mass, and replacing materials that are highly toxic and difficult to work with.

An important consideration we must apply to SWAP-C analysis of generalised GRIN lens designs is that of real-world base optical materials. It is trivial to show that a GRIN lens with an extremely large index variation gives a significant performance benefit, but such designs have little utility unless they can be made. In this work we have demonstrated methods to bind the optical design process of GRIN lenses to real materials, showing several examples where new and emerging GRIN manufacture processes exhibit sufficient variation in refractive index and chromatic dispersion to provide a significant performance benefit.

A trade-off occurs in generalised GRIN use, where we transfer manufacturing complexity from surface fabrication and alignment into the optical medium of lens elements. The GRIN distribution must be generated with sufficient precision and aligned with the lens surfaces during surface generation and polishing. We can therefore partially answer this research

question. Nominally, generalised GRINs show significant benefit, as demonstrated by the simplification of several lens designs to fewer, or sometimes even a single, lens element. In many cases this is demonstrated using material data representative of GRIN manufacture processes, such as the VIRGO printing process of NanoVox LLC. Replacement of homogeneous lens elements with generalised GRIN lenses near universally provides a performance benefit with respect to SWAP (omitting the "C" for cost). The additional complexity in processing may have ramifications for cost, but it is not feasible to quantify this in the present work.

8.2.2. Do Generalised GRIN Optics have a Future in SWAP-C-Critical Imaging Applications?

By the optical design approach undertaken in this work, we have shown that GRIN lenses frequently allow for an optical solution that is lighter, more compact, and with greater optical performance. Simply put, making use of the optical medium of a lens as well as its surfaces provides greater design degrees of freedom to an optical system and improves performance within a given size/mass/lens-count budget. The ample use of polymer materials in GRIN systems also enable significant mass reduction due to their lower density, as shown in the design of an HMD system using nanoparticle-doped polymers.

Conversely, the cost aspects of SWAP-C cannot be addressed meaningfully by this work due to a lack of certainty over the long-term cost potential of GRIN technologies. It is reasonably expected that the additional complexity in the preparation of GRIN material leads to an additional cost in the lens blank compared to a similar homogeneous material. For GRIN to provide a cost benefit, this cost should more than offset the additional expense of the extra lens elements (or more complex surfaces such as aspheres). At present, the cost-driving parameters of GRIN materials are not well known. GRIN manufacturing processes are in an early stage of commercial production (or still at low TRL levels requiring development before production can commence). There is little knowledge of what effect economies of scale will have. Design work can however set a target for cost reduction. From the designs in this work based on real-world GRIN materials, there is an approximate 3:1 reduction in lens count that can be generated via the use of GRINs, therefore, if the cost-delta of a GRIN lens is approximately that of two conventional lenses, we may estimate cost parity between approaches.

Factors beyond the nominal design also influence the feasibility and viability of GRIN lenses. To manufacture GRIN lenses, a reliable method of lens metrology must exist. A well-known maxim in optical engineering states that *if you can't measure it, you can't make it*. GRIN lenses generate additional challenges for metrology, as their media do not interact in the same way that optical surfaces do. For homogeneous lenses, surface form measurement can be performed in reflection, to isolate the effect of each optical surface. For GRIN, it is always necessary to measure in transmission which provides the confounding factor of interaction between the GRIN medium and the lens surfaces. Furthermore, in real optical systems, a GRIN lens will seldom easily provide a null test. A GRIN lens that forms part of a larger optical system will almost always have significant finite aberration that requires a more complex process to measure. This becomes an even more significant challenge for GRIN lenses with non-rotationally symmetric refractive index distributions.

GRIN metrology also may be split into two categories:

- **Acceptance**: where we wish to make a top-level assessment of the GRIN lens as to
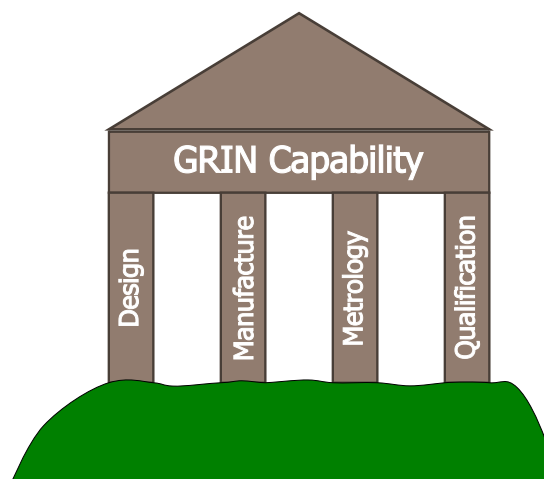
Figure 8.1: The four technical pillars that support a GRIN optics capability.

whether its performance is acceptable for use in a product, but with minimal information about what the error mechanisms are.

- **Diagnostic or Tomographic**: where we wish to make detailed measurements of the refractive index errors of a GRIN lens. In essence, where a GRIN lens fabrication has gone wrong and we want to know why. Understanding the error mechanisms allows us to drive a continuous improvement loop, by refining the process and re-measuring.

Developments in methodology for both of these metrology categories is a vital goal in the further development of GRIN lenses.

A further requirement for the application of GRIN lenses in real-world defence and aerospace applications is that of environmental qualification. In addition to being SWAP-C critical, such applications are also safety critical. Failure of avionic equipment vital to manoeuvre and navigation of aircraft would have very serious consequences and must occur at an extremely low probability. As a result, the long-term reliability of GRIN materials in challenging environments must also be demonstrated. For many applications, it is vital that GRIN systems do not show temporary or permanent degradation of performance over a finite temperature range.

Combined, we consider four technical "pillars" that support a real-world GRIN capability (Figure 8.1). As with conventional optics, it must be possible to design and analyse it, manufacture it, measure it, and ensure it works reliably in the target environment. This work has made significant progress towards the first "design" pillar. We have shown there is significant nominal benefit in a range of different contemporary GRIN processes, however further (ongoing) work is required to address the other pillars. Once the four pillars are addressed at a viable cost, one can readily conclude that GRIN has a future in SWAP-C-critical applications.

8.3. Future GRIN Optical Design Work

Whilst this work has demonstrated significant progress towards a production-ready GRIN design capability, substantial challenges remain and should be the subject of future work in this area.

The design of generalised GRIN over a finite temperature range remains a significant challenge. We require precise knowledge of the optical properties of GRIN lenses over an extended temperature range (around -50° C to +80° C) to understand their effects on the optical performance of an overall system. In this work we have made some preliminary steps towards solving this problem by some first-order analysis approximations. These approximations allow the optical designer to estimate whether a given GRIN material combination is suitable for use over a finite temperature range, but are generally limited to combinations with similar coefficients of thermal expansion and simple, radial-GRIN distributions. A confounding factor not addressed in this work is the effect of induced stress on GRIN parts due to the spatial variation of CTE and Young's modulus. This is a particular risk for polymer-based GRINs which have a large coefficient of thermal expansion and negative dN/dT. When applied to a GRIN of generalised distribution, thermal analysis requires a more general computation approach, such as finite element analysis, to determine the change in shape and refractive index of the lens. Induced stresses (particularly in polymers) also induce birefringence which may have a detrimental effect on imaging performance.

Optical design of GRINs would substantially benefit from further research into high-speed raytracing, which still acts as a bottleneck to the designer for the most complex systems. The rapid development of graphic processing units (GPUs) has the potential to increase ray tracing speed dramatically by parallelising it over many processing cores. Tracing speed increases well in excess of an order of magnitude have already been observed for homogeneous raytracing. A further area of development potentially lies in differential raytracing, which can offer great speed improvements by providing additional information in the raytrace about the derivatives of the ray with respect to system variables, negating the need for multiple raytraces to compute optimisation variable derivatives via finite differences [109]. The derivatives in differential raytracing can be accessed computationally for little overhead through a process known as automatic differentiation. This development is particularly useful for the most general GRIN systems as they can have a very large number of optimisable coefficients.

A further important contribution of the optical designer towards the design for manufacture of future GRIN systems is that of optical tolerance analysis. Tolerances provide limits on the deviation of key system parameters such as surface form and figure errors, centre thickness, wedge, and the positioning errors of lens elements. Optical materials also require limits to errors in their refractive index, dispersion, birefringence and homogeneity. At the time of writing, only basic limits to the wavefront error of GRIN lenses can be specified. This is due to the fact that the error mechanisms in GRIN materials are not well known. Ideally, tolerances are indicative of common failure modes in optical materials (such as the astigmatism and zonal "roll-off" produced by typical polishing processes). Once the error mechanisms in new GRIN manufacture processes are better known, the optical designer can develop models to establish their effect on optical performance and define limits. This work can provide further useful information in the continuous improvement of GRIN manufacture processes. When the most severe error mechanisms are known, this informs the priority to the fabricator of what aspects of the process to improve.

A

Transverse Ray Errors and their Interpretation

Transverse ray error plots (also known as rim-ray plots) are a powerful tool for the diagnosis of aberrations in optical systems. They map out the transverse (perpendicular to the optical axis) departure of rays at the image plane as a function of pupil. An example of this error mechanism is illustrated in Figure A.1. Variation of aberrations over the field is typically represented by several transverse ray error plots at defined field points. Plots are also typically generated in the sagittal and tangential sections for each field point for a rotationally symmetric optic. Transverse ray error is generally calculated with respect to the image plane position of the finite principal ray. Doing this essentially eliminates distortion from the plots (at a given reference wavelength). Distortion is often a much larger aberration than the scale of the RMS spot size (for example in fisheye lenses), and so is removed for readability of the transverse ray error plots, as it does not directly affect image quality.

A further consideration in transverse error plots concerns the definition of the normalised pupil coordinate which forms the abscissa of the plot. While it is possible to define this in either the entrance or exit pupil, it is more commonly defined as the height of a given ray in the plane of the aperture stop, normalised to the aperture stop semi-diameter. The reason for this is primarily to improve readability for lens systems with substantial pupil aberration (such as wide angle systems), where the scale of the abscissa would need to vary significantly over the field of view of the lens under analysis.

Performance metrics such as MTF or RMS spot size allow an assessment of the image quality
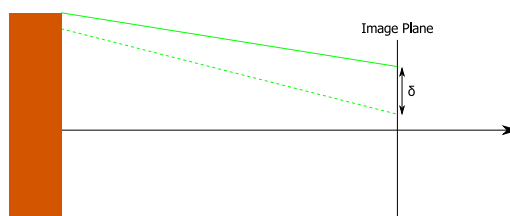
Figure A.1: Definition of transverse ray error in an azimuth defined by the plane of the page. The finite principal ray of a given field is shown as a dotted line, with a finite ray at a notional pupil coordinate shown as a solid line.

of an optical system, but provide less insight into what limits the optical correction. Transverse ray errors however allow insight into the design by the "signature" of certain aberration types and their combinations. A set of example transverse error plots are shown in Figure A.2 for the monochromatic Seidel aberrations and axial and lateral colour, to serve as an aid to the reader in interpretation of transverse ray error plots used in this thesis. The shape of these aberration curves indicates the types of aberration present in the lens. Understanding these forms of ray error is a key skill of the optical designer; the ability to diagnose combinations of aberrations as well as higher-order aberrations enables to designer to understand what limits system performance and how best to address it.
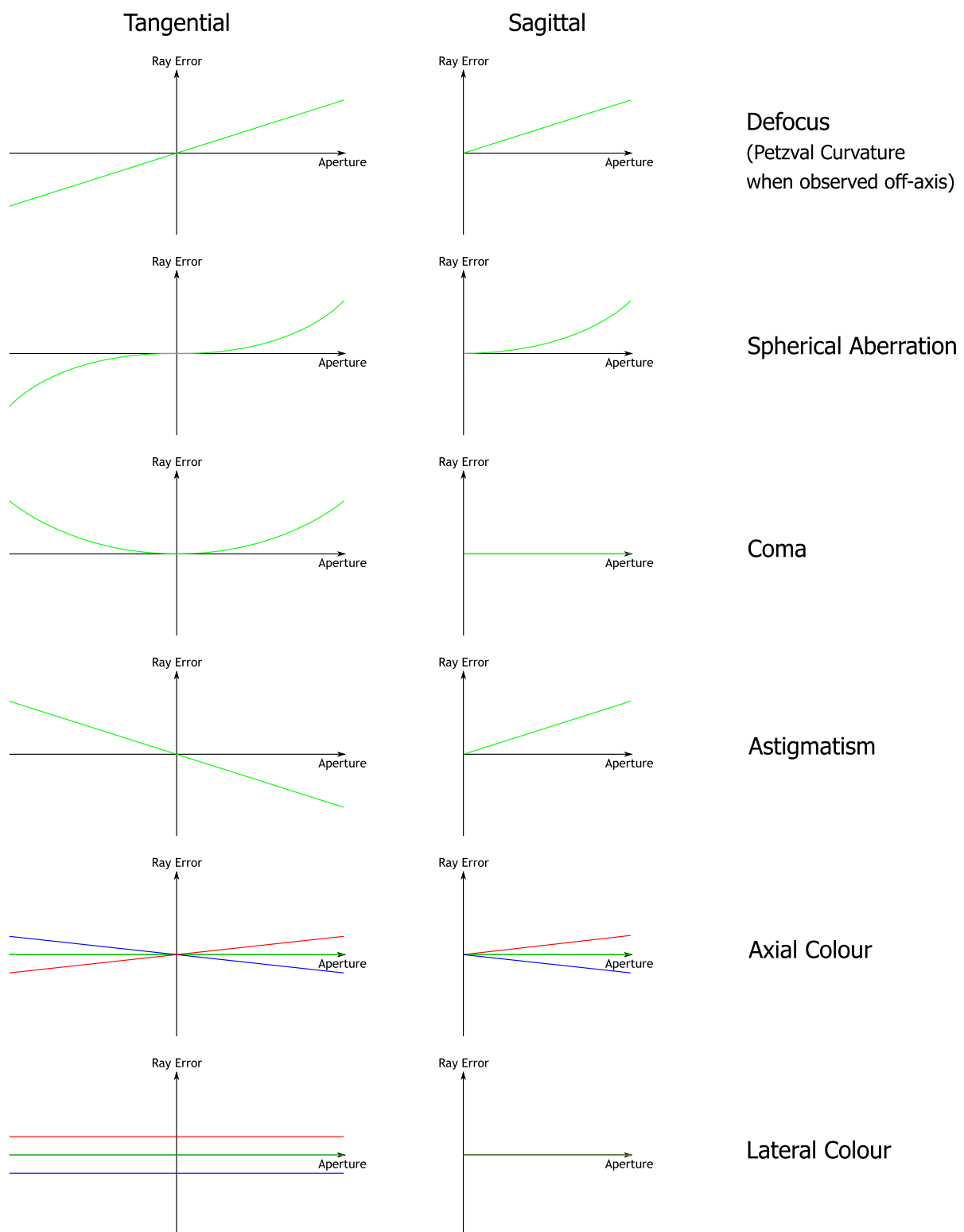
Figure A.2: Example of the functional form of common third order and chromatic aberrations when plotted as transverse ray errors.

B

Raytracing in Gradient-Index Media

In this appendix we derive the equations of ray propagation for GRIN media for both finite and paraxial rays. Raytracing is fundamental to the design of GRIN lenses, which rely on geometrical optics for their simulation in optical design software.

B.1. Finite Ray Propagation in an Inhomogeneous Medium

Herein we follow the derivation approach documented by Bociort [19][2.1.1] and Hopkins [52], where we determine the change in ray direction between two points, $\mathbf{r}$ and $\mathbf{r} + d\mathbf{r}$, defined with respect to an origin, O. $\mathbf{r}$ and $\mathbf{r} + d\mathbf{r}$ are embedded in a continuously differentiable, inhomogeneous, and isotropic medium, and located an infinitesimal distance, ds, apart. Figure B.1 illustrates the propagation of such a ray. By definition, the wavefront that the ray of Figure B.1 represents is perpendicular to the direction of propagation. We will derive a differential equation that describes the change in direction of the ray over ds, by determining the gradient of the wavefront at $\mathbf{r}$ and $\mathbf{r} + d\mathbf{r}$. Another vector, $\mathbf{a}$, has a unit length and represents the direction of propagation of the ray at $\mathbf{r}$. The change in phase of the ray between $\mathbf{r}$ and $\mathbf{r} + d\mathbf{r}$
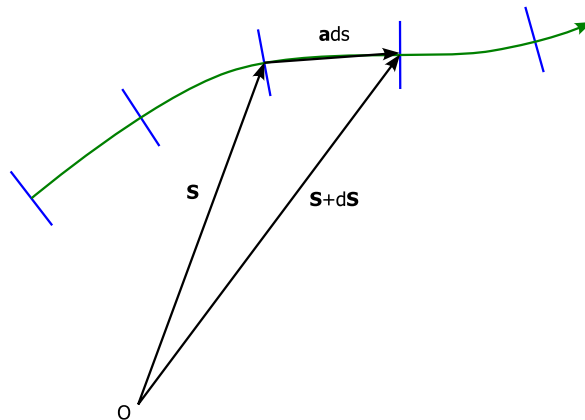
Figure B.1: Propagation of a ray (green) within an inhomogeneous medium, with perpendicular wavefronts indicated in blue. Ray positions vectors, $\mathbf{r}$ and $\mathbf{r} + d\mathbf{r}$, are indicated with respect to an origin, O.

173

is given by

$$d\Phi = \frac{2\pi}{\lambda}N(\mathbf{r})ds, \tag{B.1}$$

where λ is the wavelength of light in a vacuum, and $N(\mathbf{r})$ is the refractive index as function of $\mathbf{r}$. In the limit where ds is infinitesimally small, $d\mathbf{r}$ and $\mathbf{a}$ become parallel and so

$$d\mathbf{r} = \mathbf{a}ds, \tag{B.2}$$

where $\mathbf{r} = (x, y, z)$ and $\mathbf{a} \cdot \mathbf{a} = 1$, such that

$$ds^2 = dx^2 + dy^2 + dz^2. \tag{B.3}$$

We now express the left hand side of Equation B.1 in the same basis as $\mathbf{r}$

$$d\Phi = \frac{\partial \Phi}{\partial x}dx + \frac{\partial \Phi}{\partial y}dy + \frac{\partial \Phi}{\partial z}dz = \nabla\Phi d\mathbf{r}. \tag{B.4}$$

We combine Equations B.4, B.1 and B.2 to obtain

$$\nabla\Phi\mathbf{a} = \frac{2\pi}{\lambda}N(\mathbf{r}). \tag{B.5}$$

Again by definition of a ray as perpendicular to the propagating wavefront, we can state that $\mathbf{a}$ and $\nabla\Phi$ are parallel such that $\nabla\Phi \cdot \mathbf{a} = |\nabla\Phi|$ and $|\nabla\Phi|\mathbf{a} = \nabla\Phi$. We therefore multiply both sides of Equation B.5 by $\mathbf{a}$ to obtain

$$\nabla\Phi = \frac{2\pi}{\lambda}N(\mathbf{r})\mathbf{a}. \tag{B.6}$$

Differentiating Equation B.6 with respect to s gives

$$\frac{d}{ds}\nabla\Phi = \frac{2\pi}{\lambda}\frac{d}{ds}(N(\mathbf{r})\mathbf{a}) = \nabla\frac{d\Phi}{ds}. \tag{B.7}$$

From Equation B.1, the right hand side of Equation B.7 can be rewritten as

$$\nabla\frac{d\Phi}{ds} = \frac{2\pi}{\lambda}\nabla N(\mathbf{r}), \tag{B.8}$$

and so Equation B.7 can be rewritten as

$$\frac{d}{ds}(N(\mathbf{r})\mathbf{a}) = \nabla N(\mathbf{r}), \tag{B.9}$$

or by substituting Equation B.2 we obtain

$$\frac{d}{ds}\left(N(\mathbf{r})\frac{d\mathbf{r}}{ds}\right) = \nabla N(\mathbf{r}). \tag{B.10}$$

Whilst Equation B.10 is sufficient to solve the paths of rays in generalised GRIN media, it is not in a convenient form for numerical solution that is required for computational tracing of finite rays in optical design software. We therefore define another variable, t, such that

$$dt = \frac{ds}{N(\mathbf{r})}. \tag{B.11}$$

174

Multiplying both sides of Equation B.10 by $N(\mathbf{r})$ gives

$$N(\mathbf{r})\frac{d}{ds}\left(N(\mathbf{r})\frac{d\mathbf{r}}{ds}\right) = N(\mathbf{r})\nabla N(\mathbf{r}) = \frac{1}{2}\nabla N(\mathbf{r})^2. \tag{B.12}$$

Substituting Equation B.11 then gives

$$\frac{ds}{dt}\frac{d}{ds}\left(\frac{ds}{dt}\frac{d\mathbf{r}}{ds}\right) = \frac{1}{2}\nabla N^2(\mathbf{r}), \tag{B.13}$$

which simplifies to

$$\frac{d^2\mathbf{r}}{dt^2} = \frac{1}{2}\nabla N^2(\mathbf{r}). \tag{B.14}$$

This equation can now be solved using common numerical methods for second order differential equations such as the fourth-order Runge-Kutta method, with a small increment the quantity, t forming a stepping parameter for computation of the ray paths [63].

B.2. Paraxial Raytracing in General-Rotationally-Symmetric Gradient-Index Media

Paraxial optics enable great insight into the properties of an optical system for minimal computational effort. Computation is minimised by *linearising* raytracing of an optical system, simplifying the optical model to a set of 2x2 matrix products to model the behaviour of ray vectors between surfaces and media. This linearised approach gives us a full description of the first-order properties of an optical system, and by further calculation, the third-order aberrations. Paraxial raytracing becomes more complex for GRIN media however, as the paraxial ray propagation along a curved path through an inhomogeneous medium must be solved to yield its 2x2 ray-transfer matrix.

We therefore derive a simplified form of Equation B.14 applicable to the paraxial region only. We will follow the Lagrangian method outlined by Buchdahl [17]. Fermat's principle states that the optical path length, defined by the integral of refractive index, N, between two points, A and B, along a path of arc length, s, is a stationary point. Starting with an infinitesimal arc length, ds that we express in cartesian coordinates as per Equation B.3. We define a paraxial ray propagating in the y-z plane, using the z-axis as our optical axis and effect a change of variables to express ds in Cartesian coordinates

$$ds = \frac{ds}{dz}dz = dz\frac{\sqrt{dy^2 + dz^2}}{\sqrt{dz^2}} = dz\sqrt{\frac{dy^2}{dz^2} + 1}. \tag{B.15}$$

Fermat's principle can now be rewritten as a Lagrangian, using a dot notation to signify differentiation with respect to z

$$\delta\int N ds = \delta\int L(y, \dot{y}, z)\, dz = 0, \tag{B.16}$$

where

$$L = N(y, z)\sqrt{1 + \dot{y}^2}. \tag{B.17}$$

To obtain an equation of paraxial ray propagation within a GRIN medium, we solve the Euler-Lagrange equation [110, chapter 9.2.16], which for our coordinate system is given by

$$\frac{\partial L}{\partial y} - \frac{d}{dz}\left(\frac{\partial L}{\partial \dot{y}}\right) = 0. \tag{B.18}$$

To simplify the the square root term of Equation B.17, we expand as a Taylor series in $\dot{y}$

$$L = N(y,z)\left[1 + \frac{1}{2}\dot{y}^2 - \frac{1}{4}\dot{y}^4 + \ldots\right]. \tag{B.19}$$

We must now also define the refractive index distribution as a function of z, of the form described in Equation 1.23

$$N(\rho,z) = \mathcal{N}_0(z) + \mathcal{N}_2(z)\rho^2 + \mathcal{N}_4(z)\rho^4 + \ldots, \tag{B.20}$$

where $\rho = x^2 + y^2$. We now further expand Equation B.19 by multiplying the square root expansion with the refractive index distribution. As our ray propagates in the $y-z$ plane, we can substitute for $\rho^2 = y^2$. In applying the paraxial approximation, we assume that y and $\dot{y}$ are small numbers, and therefore higher-order terms can be neglected. We therefore collect any fourth order or higher terms in y from Equation B.21 in the term $\mathcal{O}_4$, and disregard them, giving

$$L = \mathcal{N}_0(z) + \left[\frac{1}{2}\mathcal{N}_0(z)\dot{y}^2 + \mathcal{N}_2(z)y^2\right] + \mathcal{O}_4. \tag{B.21}$$

Equation B.21 is now simple to differentiate with respect to y or z, which we substitute into the Euler-Lagrange equation to yield an equation of propagation for paraxial rays in a general rotationally symmetric GRIN medium

$$2\mathcal{N}_2(z)y - \frac{d}{dz}\left(\mathcal{N}_0(z)\dot{y}\right) = 0. \tag{B.22}$$

B.3. Analytical Solutions for Paraxial Rays in GRIN Media

The existence of analytical solutions to equation B.22 depends on the functional form of $\mathcal{N}_0(z)$ and $\mathcal{N}_2(z)$. Sands explored analytical paraxial solutions for axial and radial GRIN distributions [76]. It is beneficial to explore such solutions, as they can act as useful diagnostic tests for raytracing algorithms designed for more complex paraxial GRIN distributions, by providing a ground truth to which we may compare the numerical approach.

B.3.1. Radial GRIN

For a solely radial GRIN (the eponymous Wood lens), $\mathcal{N}_2(z)$ and $\mathcal{N}_0(z)$ are constants. Substitution into equation B.22 gives us the second order ordinary differential equation:

$$\ddot{y} = \frac{2\mathcal{N}_2}{N_0}y(z) \tag{B.23}$$

For the case of $\mathcal{N}_2 < 0$, a sinusoidal ansatz yields

$$
\begin{aligned}
y(z) &= A\cos(\alpha z) + B\sin(\beta z) \\
\dot{y}(z) &= -\alpha A\sin(\alpha z) + \beta B\cos(\beta z) \\
\ddot{y}(z) &= -\alpha^2 A\cos(\alpha z) - \beta^2 B\sin(\beta z).
\end{aligned}
\tag{B.24}
$$

Substitution of the ansatz into equation B.23 gives

$$\ddot{y} - \frac{2\mathcal{N}_2}{\mathcal{N}_0} y(z) = A\left(-\alpha^2 - \frac{2\mathcal{N}_2}{\mathcal{N}_0}\right)\cos(\alpha z) + B\left(-\beta^2 - \frac{2\mathcal{N}_2}{\mathcal{N}_0}\right)\sin(\beta z) = 0. \tag{B.25}$$

By substituting trial solutions at $z = 0$ and $\beta z = \pi$, we can obtain values for α and β. A becomes the parameter $y(0)$ and B can be found by substitution into $\dot{y}$. This gives us a paraxial ray equation for the Wood lens.

$$y(z) = y(0)\cos(\alpha z) + \frac{\dot{y}(0)}{\alpha}\sin(\alpha z), \qquad \text{where } \alpha = \sqrt{\frac{-2\mathcal{N}_2}{\mathcal{N}_0}} \tag{B.26}$$

B.3.2. Axial GRIN

For an axial GRIN distribution of the form described in Equation 1.25, $\mathcal{N}_2 = 0$ whilst $\mathcal{N}_0$ is a function of z. $\mathcal{N}_2 = 0$ simplifies Equation B.22 to obtain

$$\frac{d}{dz}\left(N_0(z)\dot{y}\right) = 0. \tag{B.27}$$

We assume the ray propagates through an axial GRIN medium from the z-axis origin to z. Integration of Equation B.27 with respect to z gives

$$\int_0^z \frac{d}{dz}\mathcal{N}_0(z)\dot{y}\,dz = \mathcal{N}_0(z)\dot{y}(z) - \mathcal{N}_0(0)\dot{y}(0) = 0. \tag{B.28}$$

We then rearrange this expression in terms of $\dot{y}$ and integrate with respect to z to obtain an expression for $y(z)$

$$\int_0^z \dot{y}(z)\,dz = y(z) - y(0) = \mathcal{N}_0(0)\dot{y}(0)\int_0^z \frac{1}{\mathcal{N}_0(z)}, \tag{B.29}$$

where the values $y(0)$ and $\dot{y}(0)$ describe the starting position and direction of the ray.

C

Introduction to Bézier curves

Bézier curves are a form of parametric curve widely used in graphics and product design. They were independently discovered by two mathematicians: Pierre Bézier, an engineer at the automaker Citroën, and Paul de Casteljau, an engineer at the same company who was unable to publish his interpretation of the approach until some years later. They are popular in engineering and software applications due to the complex curves they are able to produce and their numerical stability.

Two widely published approaches are used to define Bézier curves, these are Bernstein polynomials [82, Chapter 1.3.2] and De Casteljau's algorithm [82, Chapter 1.3.5].

C.1. The Bernstein Basis

The Bernstein polynomial basis is defined over the interval $0 \leq t \leq 1$, and will ultimately serve as a weighting function to define our Bézier curves. We define a Bernstein polynomial of order n as

$$B_{i,n}(t) = \frac{n!}{i!\,(n-i)!}\,(1-t)^{n-i}\,t^i, \qquad i = 0, \dots, n. \tag{C.1}$$

As an example, we sum the four Bernstein polynomials where $n = 3$

$$\sum_{i=0}^{3} B_{i,3}(t) = (1-t)^3 + 3\,(1-t)^2\,t + 3\,(1-t)\,t^2 + t^3. \tag{C.2}$$

Each of the four terms of our example Bernstein polynomial is plotted in Figure C.1 (noting that the summation index, i, starts with zero). It is noteworthy that the basis is symmetric about $t = 0.5$. Another noteworthy property of the basis is

$$\sum_{i=0}^{n} B_{i,n}(t) = 1. \tag{C.3}$$

This unity sum property makes the Bernstein basis in its pure form of little interest in defining curves, however its utility is transformed when we apply coefficients that represent control points of the curve to each term in the basis. This act of applying weighted control points
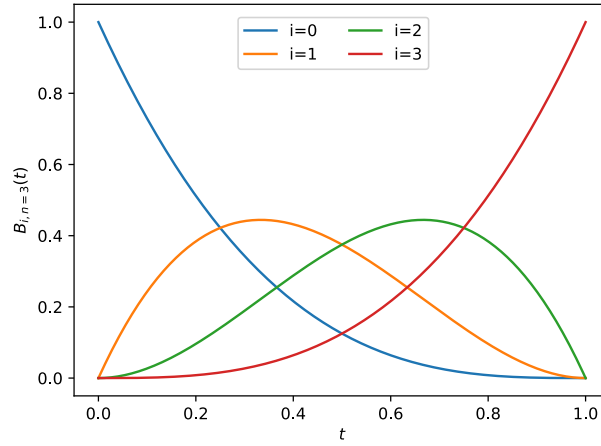
Figure C.1: Plot of the Bernstein basis where n=3.

transforms the Bernstein basis into a Bézier curve. In the paraxial reconstruction technique of Chapter 3, the control points are defined by sampled coordinates along the segmented paraxial ray paths of a homogeneous optic. Consider a Bézier curve example, of the same order as the Bernstein polynomial of Equation C.2, which requires a set of four control points, P,

$$\begin{aligned} P &= \{\mathbf{p}_1, \mathbf{p}_2, \mathbf{p}_3, \mathbf{p}_4\}, \quad \text{where} \\ \mathbf{p}_1 &= (0,0) \\ \mathbf{p}_2 &= (3/2, 7) \\ \mathbf{p}_3 &= (6, 3) \\ \mathbf{p}_4 &= (8, 7). \end{aligned} \tag{C.4}$$

For a given parameter, t, the value of the Bézier curve, $\mathbf{f}$, is given by

$$\mathbf{f}(t) = \mathbf{p}_1 \left(1 - t\right)^3 + 3\mathbf{p}_2 \left(1 - t\right)^2 t + 3\mathbf{p}_3 \left(1 - t\right) t^2 + \mathbf{p}_4 t^3. \tag{C.5}$$

The curve $\mathbf{f}(t)$ is plotted in Figure C.2. From inspection of Equation C.5, the values of $\mathbf{f}$ at $t = 0$ and $t = 1$ are $\mathbf{p}_1$ and $\mathbf{p}_4$ respectively. It must also be noted from Figures C.1 and C.2, that between the endpoints, no single point along the curve ever has a weighting of 1 (which would be required to intersect the control point). This means that Bézier curves *approximate* rather than interpolate the set of points over which they are defined [111].

179
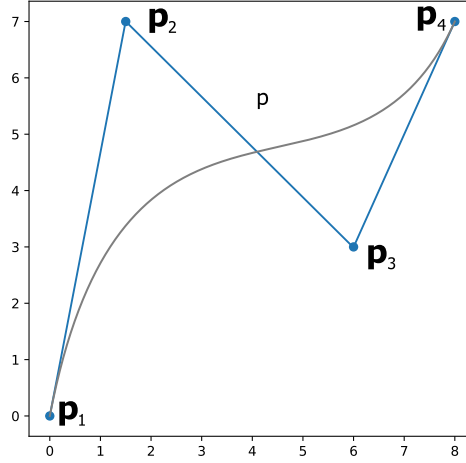
Figure C.2: Control points and resulting Bézier curve for example control points, $\mathbf{p}$.

C.2. De Casteljau's Algorithm

Another elegant (and equivalent) way to define a Bézier curve is via De Casteljau's algorithm. This algorithm consists of recursive linear interpolations along segments defined by the Bézier curve control points. Consider a Bézier curve, $\mathbf{f}(t)$ that is defined by a set of n control points

$$P = \{\mathbf{p}_1, \mathbf{p}_2, \mathbf{p}_3, ..., \mathbf{p}_n\}, \tag{C.6}$$

where the vectors $\mathbf{p}_1$ to $\mathbf{p}_n$ define said control points. As with the previous definition using the Bernstein basis, we parameterise the Bézier curve using a factor, $0 \geq t \leq 1$. De Casteljau's algorithm performs a linear interpolation between each successive pair of control points at each iteration, given by

$$\mathbf{p}_i' = \mathbf{p}_i + t(\mathbf{p}_{i+1} - \mathbf{p}_i) \tag{C.7}$$

for the ith and i+1th control points. When applied to the entire set, P, the result is a set of $n-1$ control points that form an intermediate curve, given by

$$P' = \{\mathbf{p}_1', \mathbf{p}_2', \mathbf{p}_3', ..., \mathbf{p}_{n-1}'\}. \tag{C.8}$$

De Casteljau's algorithm terminates when the interpolation process returns a single point. This point sits on the Bézier curve, $\mathbf{f}(t)$. This process of successive linear interpolation for a Bézier curve consisting of four control points, $\{\mathbf{p}_1, \mathbf{p}_2, \mathbf{p}_3, \mathbf{p}_4\}$, is illustrated in Figure C.3. A visual example of De Casteljau's algorithm is also shown in Figure C.4 for the same set of control points as defined in Equation C.4. Starting from the original control points that form the blue segmented line, successive linear interpolations yield the orange then green segmented lines, terminating with the red point that sits on the Bézier curve for the given t value.

$$\mathbf{f}(t)=\mathbf{p}_1''+t(\mathbf{p}_2''-\mathbf{p}_1'')$$

$$\mathbf{p}_1''=\mathbf{p}_1'+t(\mathbf{p}_2'-\mathbf{p}_1') \qquad \mathbf{p}_2''=\mathbf{p}_2'+t(\mathbf{p}_3'-\mathbf{p}_2')$$

$$\mathbf{p}_1'=\mathbf{p}_1+t(\mathbf{p}_2-\mathbf{p}_1) \qquad \mathbf{p}_2'=\mathbf{p}_2+t(\mathbf{p}_3-\mathbf{p}_2) \qquad \mathbf{p}_3'=\mathbf{p}_3+t(\mathbf{p}_4-\mathbf{p}_3)$$
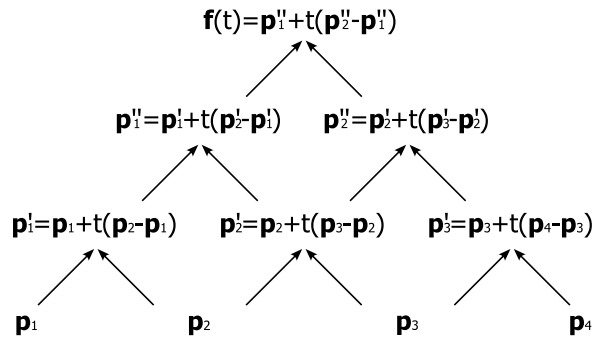
$$\mathbf{p}_1 \qquad \mathbf{p}_2 \qquad \mathbf{p}_3 \qquad \mathbf{p}_4$$

Figure C.3: Flowchart illustrating De Casteljau's algorithm for a Bézier curve defined from four control points, $\{\mathbf{p}_1, \mathbf{p}_2, \mathbf{p}_3, \mathbf{p}_4\}$. Each row of the pyramid indicates a successive iteration of the algorithm, culminating in a single point that sits on the Bézier curve.

t=0.25   t=0.5   t=0.75
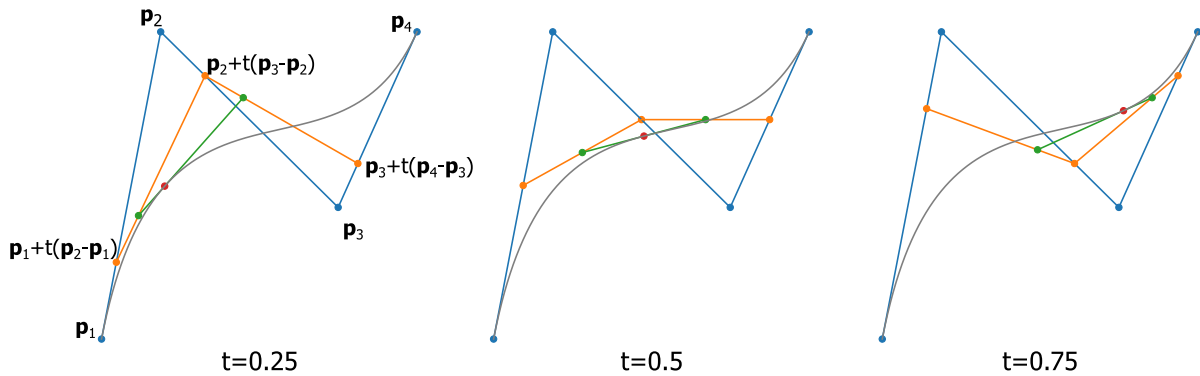
Figure C.4: Points on a Bézier curve defined via De Casteljau's algorithm for three values of t. The blue curve indicates the original set of control points defining the curve. The orange polygon has one less segment, and is formed by interpolating along each segment of the blue curve by a factor, t. The interpolated points are indicated on the leftmost example for the first iteration. The green line segment is formed when the same interpolation process is applied to the orange polygon. The process is again applied to the green segment to yield the red point, which can be interpolated no further and is a point on the Bézier curve.

181

C.3. Further Properties of Bezier Curves

C.3.1. Derivatives

The derivative of a Bézier curve (often referred to as its *hodograph*) is another Bézier curve of lower order [82, Chapter 1.3.4].

$$\dot{\mathbf{f}}(t) = \frac{d\mathbf{f}}{dt} = n \sum_{i=0}^{n-1} (\mathbf{p}_{i+1} - \mathbf{p}_i) \, B_{i,n-1}(t). \tag{C.9}$$

From inspection of Equation C.9, we observe that for $t = 0$ and $t = 1$ we obtain the following derivatives

$$\begin{aligned} \dot{\mathbf{f}}(0) &= n \, (\mathbf{p}_1 - \mathbf{p}_0) \\ \dot{\mathbf{f}}(1) &= n \, (\mathbf{p}_n - \mathbf{p}_{n-1}), \end{aligned} \tag{C.10}$$

we infer from these values that the derivatives at $t = 0$ and $t = 1$ are parallel to the end segments of the control points.

C.3.2. Diminished Variation

We define a more complex Bézier curve in Figure C.5. The largest area polygon that can be defined by the control points is known as the *convex hull*. A Bézier curve always sits within this region. Bézier curves produce minimal oscillation, even at very high orders, showing *diminished variation* with respect to the segmented line of control points.
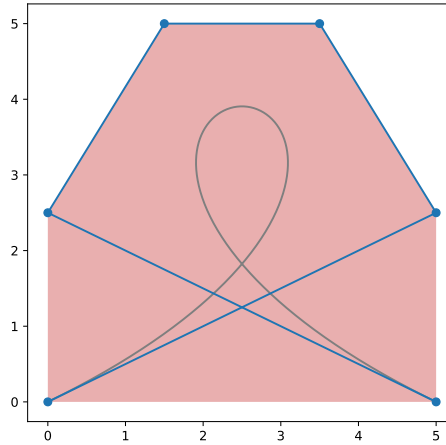
Figure C.5: Bézier curve where $P = \{(0,0), (5, 5/2), (7/2, 5), (3/2, 5), (0, 5/2), (5, 0)\}$. The convex hull of the control points is shaded in red.

D

Paraxial Reconstruction: Data Annexe

The following sections represent data for the lens designs of Chapter 3. GRIN coefficients and equations are broken out into separate tables as indicated. No indicated material implies an air medium.

D.1. Double-Gauss Example

D.1.1. Homogeneous Parent Design

F/#	2.0
Semi-Field (°)	14.0
Wavelengths (nm)	$\lambda_1 =486.1, \lambda_2 =587.6, \lambda_3 =656.3$
Spectral Weights	1.0 1.0 1.0

Label	Surface	Radius (mm)	Thickness (mm)	Clear Diameter (mm)	$N(\lambda_1)$	$N(\lambda_2)$	$N(\lambda_3)$	Glass
Object	0	INFINITY	INFINITY					
	1	56.20238	8.75	56.34	1.630455	1.622292	1.618769	NSSK2
	2	152.286	0.5	54.27				
	3	37.683	12.5	49.25	1.61486	1.607379	1.604134	NSK2
	4	INFINITY	3.8	45.79	1.614617	1.603417	1.598744	F5
	5	24.231	16.369	34.59				
Stop	6	INFINITY	13.748	31.40				
	7	-28.377	3.8	30.27	1.614617	1.603417	1.598744	F5
	8	INFINITY	11	34.50	1.627559	1.620408	1.617271	NSK16
	9	-37.925	0.5	37.85				
	10	177.412	7	40.70	1.627559	1.620408	1.617271	NSK16
	11	-79.411	61.488	41.55				
Image	12	INFINITY	-0.40	49.19				

183

D.1.2. Paraxial Reconstruction

F/#	2.0
Semi-Field (°)	14.0

Label	Surface	Radius (mm)	Thickness (mm)	Clear Diameter (mm)	Material
OBJECT	0	INFINITY	INFINITY		
	1	56.202	41.919	33.25	GRIN
STOP	2	INFINITY	36.048	18.7	GRIN
	3 -79.411	61.415	28.9		
IMAGE	INFINITY	0.00	35.7		

GRIN Coefficients

The GRIN distribution is of the form indicated in Equation 1.23, consisting of axially varying radial polynomial terms. The axial coefficients, $\mathcal{N}_0(z)$ and $\mathcal{N}_2(z)$ are determined by a ten knot cubic spline function, with knots at the Chebyshev-Lobatto nodes. For a spline consisting of Q nodes and interval, L, the location of the qth node is given by

$$z_q = \frac{L}{2}\left[1 - \cos\left(\frac{q}{Q-1}\pi\right)\right], \quad q = 0, 1, 2, \dots, Q - 1. \tag{D.1}$$

The GRIN distribution of the paraxially reconstructed Double Gauss has its vertex at surface 1, $L = 77.967$, $Q = 10$ with GRIN distribution

Knot	Location (mm)	$\mathcal{N}_0$	$\mathcal{N}_2$ (mm^{-2})
0	0	1.63046	-5.189×10^{-4}
1	2.351	1.62846	-4.289×10^{-4}
2	9.12045	1.54514	-1.171×10^{-5}
3	19.49185	1.25653	3.219×10^{-4}
4	32.21425	1.04711	2.387×10^{-4}
5	45.75315	1.03089	1.948×10^{-4}
6	58.47555	1.20233	2.695×10^{-4}
7	68.84695	1.52126	-9.547×10^{-5}
8	75.6164	1.64063	-9.417×10^{-4}
9	77.9674	1.62756	-1.269×10^{-3}

D.1.3. Optimised GRIN Design

Design is sliced into six segments with the GRIN distribution coordinate origin at the vertex of surface 1.

F/#	2.0
Semi-Field (°)	14.0

Label	Surface	Radius (mm)	Thickness (mm)	Clear Diameter (mm)	Material
OBJECT	0	INFINITY	INFINITY		
	1	1055.36	13.973	56.00	GRIN
	2	INFINITY	13.973	50.5	GRIN
	3	INFINITY	13.973	40.65	GRIN
STOP	4	12.016	36.15		GRIN
	5	INFINITY	12.016	36.95	GRIN
	6	INFINITY	12.016	39.15	GRIN
	7	-489.93	61.09	40.00	GRIN
IMAGE	8	INFINITY	61.551	51.9	

GRIN Coefficients

GRIN is of the form indicated in Equation 1.23, with each radial GRIN coefficient, $\mathcal{N}_n(z)$, determined by a set of Chebyshev-Lobatto-distributed spline nodes as per Equation D.1, with $Q = 10$, $L = 77.9674$, and knots given by

Knot	Location (mm)	$\mathcal{N}_0$	$\mathcal{N}_2$ (mm^{-2})	$\mathcal{N}_4$ (mm^{-4})	$\mathcal{N}_6$ (mm^{-6})
0	0	1.55528	2.69×10^{-4}	-5.23×10^{-7}	-2.22×10^{-10}
1	2.351	1.64011	-3.08×10^{-4}	-9.49×10^{-8}	-5.42×10^{-12}
2	9.12	1.69706	-4.47×10^{-4}	2.01×10^{-8}	-3.92×10^{-11}
3	19.492	1.50761	-2.88×10^{-4}	1.81×10^{-7}	3.21×10^{-11}
4	32.214	1.44373	1.95×10^{-4}	2.61×10^{-7}	1.12×10^{-10}
5	45.753	1.45701	7.05×10^{-4}	-9.42×10^{-7}	3.06×10^{-10}
6	58.476	1.52674	1.85×10^{-4}	-3.28×10^{-7}	-1.95×10^{-10}
7	68.847	1.59101	-6.88×10^{-4}	5.61×10^{-7}	3.58×10^{-10}
8	75.616	1.70572	-6.18×10^{-4}	5.73×10^{-7}	-7×10^{-10}
9	77.967	1.70412	9.1×10^{-4}	-3.07×10^{-6}	-3.26×10^{-9}

D.2. Lithographic Lens

D.2.1. Homogeneous Parent Design

Object Numerical Aperture	0.1923
Max Object Height	25.0 mm
Wavelength (nm)	589

Label	Surface	Radius (mm)	Thickness (mm)	Clear Diameter (mm)	Refractive Index
OBJECT	0	INFINITY	183.406	122.3	
	1	INFINITY	1000000	61.2	
STOP	2	INFINITY	-1000000	392003.1	
	3	INFINITY	16.9	122.3	1.672443
	4	-260.195	0.26	124.5	
	5	268.321	20.8	125.4	1.672443
	6	-379.188	0.26	124.2	
	7	95.8621	30.42	112.2	1.672443
	8	443.469	13	99.4	
	9	561.062	10.27	82.8	1.774162
	10	62.4221	29.9	68.3	
	11	-71.9383	15.6	63.3	1.672336
	12	-134.427	5.2	66.5	
	13	-82.986	15.21	66.3	1.633012
	14	-78.3661	0.26	70.4	
	15	4427.22	15.6	69.1	1.656007
	16	-336.107	6.5	67.8	
	17	INFINITY	6.5	66	
	18	336.107	15.6	67.8	1.656007
	19	-4427.22	0.26	69.2	
	20	78.3661	15.21	70.5	1.633012
	21	82.986	5.2	66.5	
	22	134.427	15.6	66.6	1.672336
	23	71.9383	29.9	63.5	
	24	-62.4221	10.27	68.6	1.774162
	25	-561.062	13	83.3	
	26	-443.469	30.42	100.1	1.672443
	27	-95.8621	0.26	112.9	
	28	379.188	20.8	125.2	1.672443
	29	-268.321	0.26	126.5	
	30	260.195	16.9	125.6	1.672443
IMAGE	31	INFINITY	186.063003	123.4	

D.2.2. Paraxial Reconstruction

Object Numerical Aperture	0.1923
Max Object Height	25.0
Wavelength	589 nm

Label	Surface	Radius (mm)	Thickness (mm)	Clear Diameter (mm)	Material
OBJECT	0	INFINITY	183.406	25.0000	
	1	INFINITY	180.180	71.91	GRIN
STOP	2	INFINITY	180.18	60.1	GRIN
	3	INFINITY	183.122	68.6	GRIN
IMAGE	4	INFINITY	0.00	25.0	

GRIN Coefficients

GRIN is of the form indicated in Equation 1.23, with the radial GRIN coefficients, $\mathcal{N}_0(z)$ and $\mathcal{N}_2(z)$, determined by a set of Chebyshev-Lobatto-distributed spline nodes as per Equation D.1. The origin of the GRIN distribution is at the vertex of surface 1, with $Q = 20$, $L = 360.36$, and knots given by

Knot	Location	$\mathcal{N}_0$	$\mathcal{N}_2$ (mm^{-2})
0	0	1.68742	-1.2962×10^{-4}
1	2.457	1.69357	-1.2438×10^{-4}
2	9.763	1.71481	-1.35×10^{-4}
3	21.716	1.74016	-1.5097×10^{-4}
4	37.993	1.64715	-8.7381×10^{-5}
5	58.147	1.36579	2.6852×10^{-5}
6	81.631	1.11979	7.4728×10^{-5}
7	107.803	1.07392	6.9113×10^{-5}
8	135.948	1.23279	2.6712×10^{-5}
9	165.301	1.45557	-4.3935×10^{-5}
10	195.059	1.45557	-4.3935×10^{-5}
11	224.412	1.23279	2.6712×10^{-5}
12	252.557	1.07392	6.9113×10^{-5}
13	278.729	1.11979	7.4728×10^{-5}
14	302.213	1.36579	2.6852×10^{-5}
15	322.367	1.64715	-8.7381×10^{-5}
16	338.644	1.74016	-1.5097×10^{-4}
17	350.597	1.71481	-1.35×10^{-4}
18	357.903	1.69357	-1.2438×10^{-4}
19	360.36	1.68742	-1.2962×10^{-4}.

D.2.3. Optimised Design

Design is sliced into 20 segments with the GRIN distribution coordinate origin at the vertex of surface 3.

Object Numerical Aperture	0.1923
Max Object Height	25.0
Wavelength (nm)	589

Label	Surface	Radius (mm)	Thickness (mm)	Clear Diameter (mm)	Material
OBJECT	0	INFINITY	183.4057	50	
	1	INFINITY	1000000	62.75	
STOP	2	INFINITY	-1000000	-	
	3	INFINITY	18.018	125.5	GRIN
	4	INFINITY	18.018	128	GRIN
	5	INFINITY	18.018	124.1	GRIN
	6	INFINITY	18.018	114.1	GRIN
	7	INFINITY	18.018	102.3	GRIN
	8	INFINITY	18.018	91.4	GRIN
	9	INFINITY	18.018	81.1	GRIN
	10	INFINITY	18.018	71.8	GRIN
	11	INFINITY	18.018	64.4	GRIN
	12	INFINITY	18.018	59.3	GRIN
	13	INFINITY	18.018	55.4	GRIN
	14	INFINITY	18.018	59.3	GRIN
	15	INFINITY	18.018	64.4	GRIN
	16	INFINITY	18.018	71.8	GRIN
	17	INFINITY	18.018	81.3	GRIN
	18	INFINITY	18.018	91.7	GRIN
	19	INFINITY	18.018	102.7	GRIN
	20	INFINITY	18.018	114.5	GRIN
	21	INFINITY	18.018	124.5	GRIN
	22	INFINITY	18.018	128.5	GRIN
	23	INFINITY	183.4064	126	
IMAGE	24	INFINITY	0	50	

GRIN Coefficients

GRIN is of the form indicated in Equation 1.23, with each radial GRIN coefficient, $\mathcal{N}_n(z)$, determined by a set of Chebyshev-Lobatto-distributed spline nodes as per Equation D.1, with $Q = 20$, $L = 360.36$, and knots given by

Knot	Location	$\mathcal{N}_0$	$\mathcal{N}_2$ (mm^{-2})	$\mathcal{N}_4$ (mm^{-4})
0	0	1.09237	7.3273×10^{-7}	-6.7007×10^{-10}
1	2.457	1.46417	9.3379×10^{-6}	-9.9016×10^{-9}
2	9.763	1.77599	-1.2937×10^{-4}	1.2934×10^{-10}
3	21.716	1.76277	-1.2055×10^{-4}	8.6712×10^{-10}
4	37.993	1.73877	-9.7305×10^{-5}	-8.1839×10^{-10}
5	58.147	1.20319	3.3677×10^{-5}	-5.6647×10^{-10}
6	81.631	1.05599	2.1733×10^{-5}	3.0968×10^{-9}
7	107.803	1.06237	-2.1853×10^{-5}	7.8586×10^{-9}
8	135.948	1.1258	2.2799×10^{-5}	9.5313×10^{-10}
9	165.301	1.57243	4.1362×10^{-5}	-1.053×10^{-8}
10	195.059	1.57243	4.1362×10^{-5}	-1.053×10^{-8}
11	224.412	1.1258	2.2799×10^{-5}	9.5313×10^{-10}
12	252.557	1.06237	-2.1853×10^{-5}	7.8586×10^{-9}
13	278.729	1.05599	2.1733×10^{-5}	3.0968×10^{-9}
14	302.213	1.20319	3.3677×10^{-5}	-5.6647×10^{-10}
15	322.367	1.73877	-9.7305×10^{-5}	-8.1839×10^{-10}
16	338.644	1.76277	-1.2055×10^{-4}	8.6712×10^{-10}
17	350.597	1.77599	-1.2937×10^{-4}	1.2934×10^{-10}
18	357.903	1.46417	9.3379×10^{-6}	-9.9016×10^{-9}
19	360.36	1.09237	7.3258×10^{-7}	-6.7007×10^{-10}

Knot	Location	$\mathcal{N}_6$ (mm^{-6})	$\mathcal{N}_8$ (mm^{-8})	$\mathcal{N}_{10}$ (mm^{-10})
0	0	-5.5818×10^{-13}	3.5209×10^{-16}	-4.9666×10^{-20}
1	2.457	-2.9312×10^{-13}	-6.0387×10^{-18}	-7.0593×10^{-22}
2	9.763	3.2011×10^{-13}	1.5717×10^{-17}	-2.7024×10^{-21}
3	21.716	2.8238×10^{-13}	-4.6336×10^{-18}	4.0261×10^{-22}
4	37.993	5.0479×10^{-14}	-6.8685×10^{-18}	2.8555×10^{-21}
5	58.147	-3.7371×10^{-13}	-1.3545×10^{-17}	-7.0485×10^{-23}
6	81.631	-6.7795×10^{-13}	-4.9631×10^{-17}	1.336×10^{-20}
7	107.803	1.2001×10^{-12}	1.8473×10^{-16}	-2.8746×10^{-20}
8	135.948	1.4901×10^{-12}	-3.7034×10^{-17}	3.9503×10^{-20}
9	165.301	-1.5456×10^{-12}	1.7891×10^{-16}	-1.0088×10^{-20}
10	195.059	-1.5456×10^{-12}	1.7891×10^{-16}	-1.0088×10^{-20}
11	224.412	1.4901×10^{-12}	-3.7034×10^{-17}	3.9503×10^{-20}
12	252.557	1.2001×10^{-12}	1.8473×10^{-16}	-2.8746×10^{-20}
13	278.729	-6.7795×10^{-13}	-4.9631×10^{-17}	1.336×10^{-20}
14	302.213	-3.7371×10^{-13}	-1.3545×10^{-17}	-7.0485×10^{-23}
15	322.367	5.0479×10^{-14}	-6.8685×10^{-18}	2.8555×10^{-21}
16	338.644	2.8238×10^{-13}	-4.6336×10^{-18}	4.0261×10^{-22}
17	350.597	3.2011×10^{-13}	1.5717×10^{-17}	-2.7024×10^{-21}
18	357.903	-2.9312×10^{-13}	-6.0387×10^{-18}	-7.0593×10^{-22}
19	360.36	-5.5818×10^{-13}	3.5209×10^{-16}	-4.9666×10^{-20}.

D.3. Cooke Triplet Example

D.3.1. Homogeneous Parent Design

F/#	5.0
Semi-Field (°)	20.0
Wavelengths (nm)	$\lambda_1 = 486.1$, $\lambda_2 = 546.1$, $\lambda_3 = 656.3$
Spectral Weights	1.0, 2.0, 1.0

Label	Surface	Radius (mm)	Thickness (mm)	Clear Diameter (mm)	$N(\lambda_1)$	$N(\lambda_2)$	$N(\lambda_3)$	Material
Object	0	INFINITY	INFINITY					
	1	16.878	3.25	16.3	1.6229	1.6276	1.6173	NSK16
	2	247.026	4.984	15.1				
Stop	3	-35.957	1.25	7.7	1.6241	1.6321	1.6151	NF2
	4	15.886	6.099	8.6				
	5	49.081	3.25	16.8	1.6229	1.6276	1.6173	NSK16
	6	-27.621	38.714	17.4				
Image	7	INFINITY	0	35.9				

D.3.2. Paraxial Reconstruction

Label	Surface	Radius (mm)	Thickness (mm)	Clear Diameter (mm)	Material
OBJECT	0	INFINITY	INFINITY		
	1	16.878	8.23	13.8	GRIN
STOP	2	INFINITY	10.6	8.6	GRIN
	3	-27.621	38.71	16.2	
IMAGE	4	INFINITY	0	46.4	

GRIN Coefficients

Refractive index of the GRIN distribution is determined by the relative composition of constituent materials, A, B, and C, as given by Equation 2.24. The compositional parameters: $m_A(\rho, z)$, $m_B(\rho, z)$, and $m_C(\rho, z)$, are polynomials in ρ with coefficients that are a function of the optical axis, z, given for the nth material by

$$m_n(\rho, z) = m_{n0}(z) + m_{n2}(z)\rho^2. \tag{D.2}$$

The ith axial coefficient of the nth material is given by a natural cubic spline interpolated function with seven evenly spaced knots spanning an interval, $L = 18.8334$. Knot values and locations are given by

Knot	Location	m_{A0}	m_{B0}	m_{C0}
0	0	4.092	−3.079	-1.357×10^{-2}
1	3.1389	1.187	-8.592×10^{-1}	6.725×10^{-1}
2	6.2778	2.38×10^{-1}	-1.555×10^{-1}	9.175×10^{-1}
3	9.4167	4.172×10^{-2}	-1.042×10^{-2}	9.687×10^{-1}
4	12.5556	3.253×10^{-1}	-2.251×10^{-1}	8.998×10^{-1}
5	15.6945	1.283	-9.323×10^{-1}	6.496×10^{-1}
6	18.8334	4.092	−3.079	-1.357×10^{-2}

Knot	Location	m_{A2}	m_{B2}	m_{C2}
0	0	2.924×10^{-3}	-2.289×10^{-3}	-6.346×10^{-4}
1	3.1389	6.909×10^{-3}	-5.46×10^{-3}	-1.449×10^{-3}
2	6.2778	1.914×10^{-2}	-1.518×10^{-2}	-3.963×10^{-3}
3	9.4167	2.325×10^{-2}	-1.843×10^{-2}	-4.818×10^{-3}
4	12.5556	1.3×10^{-2}	-1.038×10^{-2}	-2.617×10^{-3}
5	15.6945	-2.072×10^{-3}	1.391×10^{-3}	6.811×10^{-4}
6	18.8334	-1.471×10^{-2}	1.152×10^{-2}	3.194×10^{-3}

Refractive indices of the constituent materials, N_A, N_B, and N_C at the defining wavelengths of the system are given by

Wavelengths	656.3 nm	546.1 nm	486.1 nm
NA	1.61727	1.62286	1.62756
NB	1.61506	1.62408	1.63208
NC	1	1	1

D.3.3. Optimised Design

F/#	5.0
Semi-Field (°)	20.0
Wavelengths (nm)	$\lambda_1 = 486.1$, $\lambda_2 = 546.1$, $\lambda_3 = 656.3$
Spectral Weights	1.0, 2.0, 1.0

Label	Surface	Radius (mm)	Thickness (mm)	Clear Diameter (mm)	Material
OBJECT	0	INFINITY	INFINITY		
	1	INFINITY	6.962	15.1	
STOP	2	INFINITY	-6.962	10	
	3	16.886	2.622	14	GRIN
	4	INFINITY	1.122	13.1	GRIN
	5	INFINITY	1.122	12.1	GRIN
	6	INFINITY	1.122	10.9	GRIN
	7	INFINITY	1.122	9.6	GRIN
	8	INFINITY	1.122	8.4	GRIN
	9	INFINITY	1.267	8.2	GRIN
	10	INFINITY	1.267	9	GRIN
	11	INFINITY	1.267	9.8	GRIN
	12	INFINITY	1.267	10.8	GRIN
	13	INFINITY	1.267	11.9	GRIN
	14	INFINITY	4.267	12.8	GRIN
	15	-27.675	38.714	14.8	
IMAGE	16	INFINITY	0	36.9	

GRIN Coefficients

Refractive index of the GRIN distribution is determined by the relative composition of constituent materials, A, B, and C, as given by Equation 2.2. The compositional parameters:

190

$m_A(\rho, z)$, $m_B(\rho, z)$, and $m_C(\rho, z)$, are polynomials in ρ with coefficients that are a function of the optical axis, z, given for the nth material by

$$m_n(\rho, z) = m_{n0}(z) + m_{n2}(z)\rho^2 + + m_{n4}(z)\rho^4 + + m_{n6}(z)\rho^6. \tag{D.3}$$

The ith axial coefficient of the nth material is given by a natural cubic spline interpolated function with seven evenly spaced knots spanning an interval, $L = 18.8334$. Knot values and locations for each compositional material are given by

Knot	Location (mm)	M_{A0}	$M_{A2}(\text{mm}^{-2})$	$M_{A4}(\text{mm}^{-4})$	$M_{A6}(\text{mm}^{-6})$
0	0	9.377	-1.237×10^{-1}	-1.561×10^{-4}	-2.543×10^{-6}
1	3.1389	1.625	-3.32×10^{-2}	-1.82×10^{-5}	-1.795×10^{-7}
2	6.2778	2.134×10^{-2}	1.939×10^{-2}	-1.619×10^{-5}	8.335×10^{-8}
3	9.4167	6.39×10^{-3}	2.428×10^{-2}	2.643×10^{-5}	-4.846×10^{-7}
4	12.5556	9.535×10^{-2}	1.013×10^{-2}	-2.14×10^{-5}	-1.819×10^{-8}
5	15.6945	5.86×10^{-1}	-1.069×10^{-2}	1.308×10^{-5}	6.792×10^{-8}
6	18.8334	1.188	-2.337×10^{-2}	1.34×10^{-4}	-1.135×10^{-6}

Knot	Location (mm)	M_{B0}	$M_{B2}(\text{mm}^{-2})$	$M_{B4}(\text{mm}^{-4})$	$M_{B6}(\text{mm}^{-6})$
0	0	2.49×10^{-1}	8.433×10^{-2}	1.02×10^{-4}	-5.003×10^{-7}
1	3.1389	1.391×10^{-2}	2.179×10^{-2}	7.908×10^{-6}	1.589×10^{-10}
2	6.2778	3.617×10^{-1}	-1.216×10^{-2}	3.307×10^{-6}	1.97×10^{-7}
3	9.4167	3.169×10^{-1}	-1.359×10^{-2}	5.001×10^{-5}	-1.942×10^{-7}
4	12.5556	3.564×10^{-1}	-7.712×10^{-3}	-3.429×10^{-6}	1.532×10^{-7}
5	15.6945	3.854×10^{-2}	8.201×10^{-3}	1.302×10^{-5}	6.823×10^{-8}
6	18.8334	7.347×10^{-2}	9.87×10^{-3}	-4.796×10^{-5}	7.935×10^{-9}

Knot	Location (mm)	M_{C0}	$M_{C2}(\text{mm}^{-2})$	$M_{C4}(\text{mm}^{-4})$	$M_{C6}(\text{mm}^{-6})$
0	0	1.503×10^{-1}	-3.546×10^{-3}	1.638×10^{-5}	-9.217×10^{-8}
1	3.1389	2.106×10^{-1}	-8.204×10^{-4}	8.603×10^{-6}	6.461×10^{-8}
2	6.2778	1.255	-6.845×10^{-3}	-9.474×10^{-6}	-1.194×10^{-7}
3	9.4167	1.314	-1.599×10^{-2}	-2.627×10^{-5}	2.937×10^{-7}
4	12.5556	5.248×10^{-1}	-2.432×10^{-3}	3.359×10^{-5}	-1.73×10^{-7}
5	15.6945	2.2×10^{-2}	1.77×10^{-3}	7.857×10^{-6}	2.416×10^{-8}
6	18.8334	1.213×10^{-1}	4.083×10^{-4}	-4.033×10^{-5}	-7.755×10^{-8}.

Acknowledgements

To Florian, my supervisor, whose help and support has proven invaluable, and whose insights into this work have taught me many new ways of thinking.

To the Optics Research Group at TU Delft, who were so warm and welcoming when I spent time there. I trust the completion of this work is just the beginning of a much greater collaboration.

To all who took the time to review and feed back on this work (as well as the associated publications). The quality of this dissertation is vastly higher for all your efforts.

To the many leaders at St Asaph over the years who gave me this opportunity and supported me throughout. I hope this work repays your investment in me and contributes to a bright future for our business.

To Optical Design at St Asaph, whose shrewd eye for detail and sense of humour have never ceased to keep me on my toes.

To my family, loving and wise, who kept me focused in a world of distraction. In loving memory of Nana, Papa, and Grandad who always made me feel like I could achieve anything. In loving memory of Janet Hunt "Nanny Bee", whose love and joy will never be forgotten. To my beloved daughter Iris, as we embark on many an adventure together in post-PhD life.

To my friends, who always remind me that life should be fun even when work beckons. In loving memory of Michael Alexander Burke, a ray of light in every life he touched.

Finally to Kathryn, whose love has been my bedrock throughout all of this, whether stressful or joyful, you were always there.

To all of you, you'll never walk alone.

List of Publications

Refereed Articles

[AMBref1] A. M. Boyd and F. Bociort, *Paraxial reconstruction: conversion of homogeneous lens forms to continuous gradient-index media,* Appl. Opt. **63**, 7252 (2024).

[AMBref2] A. M. Boyd, M. Ponting, and H. Fein, *Layered polymer GRIN lenses and their benefits to optical designs,* Advanced Optical Technologies **4**, 429 (2015).

[AMBref3] A. M. Boyd, *Optical design of a freeform, gradient-index, head-mounted display,* Optical Engineering **62** (2023), 10.1117/1.OE.62.7.075102.

[AMBref4] A. M. Boyd, *Optical design of athermal, multispectral, radial gradient-index lenses,* Optical Engineering **57**, 1 (2018)

Conference Proceedings

[AMBproc1] A. M. Boyd, *Optical design of multi-material, general rotationally symmetric GRIN lenses,* in *Advanced Optics for Imaging Applications: UV through LWIR IV*, Vol. 10998, edited by J. N. Vizgaitis, P. L. Marasco, and J. S. Sanghera, International Society for Optics and Photonics (SPIE, 2019) pp. 54 – 69.

[AMBproc2] A. M. Boyd, *Optical design of athermal, multispectral, radial GRIN lenses,* in *Advanced Optics for Defense Applications: UV through LWIR II*, Vol. 10181, edited by J. N. Vizgaitis, B. F. Andresen, P. L. Marasco, J. S. Sanghera, and M. P. Snyder, International Society for Optics and Photonics (SPIE, 2017) p. 1018109.

[AMBproc3] *Paraxial reconstruction: a tool for conversion of homogeneous lenses to generalized gradient-index media*, Optica Design and Fabrication Congress 2023 (2024)

Patents

[AMBpat1] A. M. Boyd, *Gradient-index freeform head mounted display and head-up display,* patent application WO2022108725A1, (2021)

Conference Talks

[AMBtalk1] *Layered Polymer GRIN lenses and their benefits to optical designs*, European Optical Society Annual Meeting (2014).

[AMBtalk2] *Layered Polymer GRIN lenses and their benefits to optical designs*, UK Optical Design Meeting (2014).

[AMBtalk3] *Optical design of athermal, multispectral, radial GRIN lenses*, SPIE 10181, Advanced Optics for Defense Applications: UV through LWIR II, 1018109 (2017).

[AMBtalk4] *Optical Design of multi-material, general rotationally symmetric GRIN lenses*, SPIE 10998, Advanced Optics for Imaging Applications: UV through LWIR IV; 109980J (2019).

[AMBtalk5] *Gradient Index Optics for Defence and Aerospace Applications*, European Photonics Industry Consortium (EPIC) AGM 2019 (2019).

[AMBtalk6] *Optical Design of Generalised GRIN lenses*, CIOMP-DOC Optics and Optical Engineering International Conference 2022 (2022).

[AMBtalk7] *Challenges and Opportunities in Gradient-Index Optics*, DSPE Opto-Mechatronics Symposium 2023 (2023).

[AMBtalk8] *Paraxial reconstruction: a tool for conversion of homogeneous lenses to generalized gradient-index media*, Optica Design and Fabrication Congress 2023 (2023).

[AMBtalk9] *Exploring the Solution Space of Simple Generalised GRIN Lenses*, Freeform gradient-index optics and metasurfaces, NWO Physics 2024 (2024)

Bibliography

[1] H. Fein and M. Ponting, *SWaP advantage of replacing high performance glass achromatic doublet with a polymeric nanolayer GRIN achromatic singlet,* in *Advanced Optics for Defense Applications: UV through LWIR III*, Vol. 10627, edited by J. N. Vizgaitis, B. F. Andresen, P. L. Marasco, J. S. Sanghera, and M. P. Snyder, International Society for Optics and Photonics (SPIE, 2018) pp. 79 – 88.

[2] E. Bajart, *Abbe diagram, adapted from wikimedia commons.* .

[3] Marketsandmarkets.com, *Camera modules market by component (image sensors, lens modules, voice coil motors), focus type (fixed, auto), interface, pixel, process, application (consumer electronics, automotive, security and surveillance), and region - global forecast to 2025,* (2020).

[4] V. C. Coffey, *Multispectral imaging moves into the mainstream,* (2012).

[5] M. Southworth, *Using SWaP-C reductions to improve UAS/UGV mission capabilities,* Aerospace & Defense Technology Magazine (2016).

[6] G. Carles and A. R. Harvey, *Multi-aperture imaging for flat cameras,* Opt. Lett. **45**, 6182 (2020).

[7] J. Tanida, T. Kumagai, K. Yamada, S. Miyatake, K. Ishida, T. Morimoto, N. Kondou, D. Miyazaki, and Y. Ichioka, *Thin observation module by bound optics (TOMBO): concept and experimental verification,* Appl. Opt. **40**, 1806 (2001).

[8] G. Muyo, A. Singh, M. Andersson, D. Huckridge, A. Wood, and A. R. Harvey, *Infrared imaging with a wavefront-coded singlet lens,* Opt. Express **17**, 21118 (2009).

[9] A. I. Mahan, *Astronomical refraction - some history and theories,* Appl. Opt. **1**, 497 (1962).

[10] J. C. Maxwell, *Solutions of problems (prob. 3, vol. VII. p. 188),* The Cambridge and Dublin mathematical journal **9**, 9 (1854).

[11] R. K. Luneburg, *Mathematical Theory of Optics* (Brown University, 1944).

[12] R. W. Wood, *Physical Optics* (Macmillan, 1911).

[13] S. Exner, *Die Physiologie der facettirten Augen von Krebsen und Insecten: eine Studie* (Franz Deuticke, 1891).

[14] B. K. Pierscionek and J. W. Regini, *The gradient index lens of the eye: An opto-biological synchrony,* Progress in Retinal and Eye Research **31**, 332 (2012).

[15] I. Schwab, *The evolution of eyes: major steps. the Keeler lecture 2017: centenary of Keeler Ltd,* Eye **32**, 302 (2018).

[16] H. A. Buchdahl, *Optical Aberration Coefficients*, 1st ed. (Dover, New York, 1968).

[17] H. A. Buchdahl, *Section A: Algebraic methods for the determination of the geometrical higher order aberrations of optical systems*, Ph.D. thesis (1948).

[18] P. J. Sands, *Third-order aberrations of inhomogeneous lenses,* J. Opt. Soc. Am. **60**, 1436 (1970).

[19] F. Bociort, *Imaging properties of gradient-index lenses* (1994).

[20] D. T. Moore, *Design of singlets with continuously varying indices of refraction,* J. Opt. Soc. Am. **61**, 886 (1971).

[21] L. G. Atkinson, S. N. Houde-Walter, D. T. Moore, D. P. Ryan, and J. M. Stagaman, *Design of a gradient-index photographic objective,* Appl. Opt. **21**, 993 (1982).

[22] D. P. Hamblen, *Gradient refractive index optical lenses,* (U.S. Patent 3,486,808. Filed 1966).

[23] J. R. Hensler, *Method of producing a refractive index gradient in glass,* (U.S. Patent 3,873,408. Filed 1972).

[24] B. Messerschmidt, U. Possner, A. von Pfeil, and T. Possner, *Diffraction-limited gradient-index (GRIN) microlenses with high numerical apertures produced by silver ion exchange in glass: diffusion modeling and process optimization,* in *Inorganic Optical Materials*, Vol. 3424, edited by A. J. M. III, International Society for Optics and Photonics (SPIE, 1998) pp. 88 – 96.

[25] P. Sinai, *Correction of optical aberrations by neutron irradiation,* Appl. Opt. **10**, 99 (1971).

[26] M. A. Pickering, R. L. Taylor, and D. T. Moore, *Gradient infrared optical material prepared by a chemical vapor deposition process,* Appl. Opt. **25**, 3364 (1986).

[27] Gradient Lens Corporation, *Rochester, New York,* .

[28] K. Hamanaka, *Optical bus interconnection system using Selfoc lenses,* Opt. Lett. **16**, 1222 (1991).

[29] G. M. Williams Jr., *Additive manufacturing of freeform gradient index optics,* in *Optifab 2021*, Vol. 11889, edited by J. D. Nelson and B. L. Unger, International Society for Optics and Photonics (SPIE, 2021).

[30] R. Dylla-Spears, T. D. Yee, K. Sasan, D. T. Nguyen, N. A. Dudukovic, J. M. Ortega, M. A. Johnson, O. D. Herrera, F. J. Ryerson, and L. L. Wong, *3D printed gradient index glass optics,* Science Advances **6** (2020), 10.1126/sciadv.abc7429, https://advances.sciencemag.org/content/6/47/eabc7429.full.pdf .

[31] H.-R. Wang, M. J. Cima, and E. M. Sachs, *Alumina-doped silica gradient-index (GRIN) lenses by slurry-based three-dimensional printing (S-3DP),* (2002).

[32] B. McMorrow, R. Chartoff, P. Lucas, and W. Richardson, *Polymer matrix nanocomposites by inkjet printing,* in *16th Solid Freeform Fabrication Symposium, SFF 2005* (University of Texas at Austin (freeform), 2005) pp. 174–183.

[33] H. Trost, S. Ayers, T. Chen, W. Cox, M. Grove, and R. Hoenigman, *Using drop-on-demand technology for manufacturing GRIN lenses,* Proc. 2001 Ann. Mtg. ASPE , 533 (2001).

[34] M. Kang, T. Malendevych, G. Yin, I. B. Murray, M. C. Richardson, J. Hu, I. Mingareev, and K. A. Richardson, *Scalable laser-written Ge-As-Pb-Se chalcogenide glass-ceramic films and the realization of infrared gradient refractive index elements*, in *Advanced Optics for Imaging Applications: UV through LWIR IV*, Vol. 10998, edited by J. N. Vizgaitis, P. L. Marasco, and J. S. Sanghera, International Society for Optics and Photonics (SPIE, 2019) pp. 41 – 53.

[35] C. Ocier, C. Richards, D. Bacon-Brown, Q. Ding, R. Kumar, T. Garcia, J. Van de Groep, J.-H. Song, A. Cyphersmith, A. Rhode, A. Perry, A. Littlefield, J. Zhu, D. Xie, H. Gao, J. Messinger, M. Brongersma, K. Toussaint, L. Goddard, and P. Braun, *Direct laser writing of volumetric gradient index lenses and waveguides*, Light: Science & Applications **9**, 196 (2020).

[36] E. Lavanant, L. Calvez, F. Cheviré, M. Rozé, T. Hingant, R. Proux, Y. Guimond, and X.-H. Zhang, *Radial gradient refractive index (GRIN) infrared lens based on spatially resolved crystallization of chalcogenide glass*, Opt. Mater. Express **10**, 860 (2020).

[37] S. Ji, K. Yin, M. Mackey, A. Brister, M. Ponting, and E. Baer, *Polymeric nanolayered gradient refractive index lenses: technology review and introduction of spherical gradient refractive index ball lenses*, Optical Engineering **52**, 1 (2013).

[38] T. Yang, N. Takaki, J. Bentley, G. Schmidt, and D. T. Moore, *Efficient representation of freeform gradient-index profiles for non-rotationally symmetric optical design*, Opt. Express **28**, 14788 (2020).

[39] Y. Jin, H. Tai, A. Hiltner, E. Baer, and J. S. Shirk, *New class of bioinspired lenses with a gradient refractive index*, Journal of Applied Polymer Science **103**, 1834 (2007).

[40] M. Kang, L. Sisken, J. Cook, C. Blanco, M. C. Richardson, I. Mingareev, and K. Richardson, *Refractive index patterning of infrared glass ceramics through laser-induced vitrification*, Opt. Mater. Express **8**, 2722 (2018).

[41] M. Delaney, I. Zeimpekis, D. Lawson, D. W. Hewak, and O. L. Muskens, *A new family of ultralow loss reversible phase-change materials for photonic integrated circuits: Sb2S3 and Sb2Se3*, Advanced Functional Materials **30**, 2002447 (2020).

[42] P. Delullier, G. Druart, F. De La Barrière, L. Calvez, and M. Lancry, *Femtosecond laser direct writing of gradient index fresnel lens in GeS2-based chalcogenide glass for imaging applications*, Applied Sciences **12** (2022), 10.3390/app12094490.

[43] D. Gibson, S. Bayya, V. Nguyen, J. Sanghera, M. Kotov, and G. Drake, *GRIN optics for multispectral infrared imaging*, (2015).

[44] A. J. Yee, W. Song, N. Takaki, T. Yang, Y. Zhao, Y. Ni, S. Y. Bodell, J. P. Rolland, J. L. Bentley, and D. T. Moore, *Design of a freeform gradient-index prism for mixed reality head mounted display*, in *Digital Optics for Immersive Displays*, Vol. 10676, edited by B. C. Kress, W. Osten, and H. Stolle, International Society for Optics and Photonics (SPIE, 2018) p. 106760S.

[45] S. D. Campbell, J. Nagar, and D. H. Werner, *Multi-element, multi-frequency lens transformations enabled by optical wavefront matching*, Opt. Express **25**, 17258 (2017).

[46] D. H. Lippman, N. S. Kochan, T. Yang, G. R. Schmidt, J. L. Bentley, and D. T. Moore, *Freeform gradient-index media: a new frontier in freeform optics*, Opt. Express **29**, 36997 (2021).

[47] S. D. Campbell, J. Nagar, and D. H. Werner, *Extending the performance of quasiconformal lens transformations using geometrical optics principles,* in *2017 IEEE International Symposium on Antennas and Propagation USNC/URSI National Radio Science Meeting* (2017) pp. 1667–1668.

[48] J. Li and J. B. Pendry, *Hiding under the carpet: a new strategy for cloaking,* (2008), 10.1103/PhysRevLett.101.203901, arXiv:0806.4396 .

[49] M. Bass, C. DeCusatis, J. Enoch, V. Lakshminarayanan, G. Li, C. Macdonald, V. Mahajan, and E. Van Stryland, *Handbook of Optics, Third Edition Volume I: Geometrical and Physical Optics, Polarized Light, Components and Instruments(Set)*, 3rd ed. (McGraw-Hill, Inc., New York, NY, USA, 2010).

[50] W. T. Welford, *Aberrations of optical systems* (Adam Hilger, Bristol, England, 1986).

[51] H. H. Hopkins, *The Nature of the Paraxial Approximation I. Systems of Uniform Refractive Index,* Journal of Modern Optics **38**, 427 (1991).

[52] H. H. Hopkins, *The nature of the paraxial approximation ii. systems containing media of radial and of axial non-uniform refractive index: Invariants,* Journal of Modern Optics **38**, 447 (1991).

[53] W. J. Smith, *Modern Optical Engineering 4th Ed* (McGraw Hill, New York, 2008).

[54] T. Stone and N. George, *Hybrid diffractive-refractive lenses and achromats,* Appl. Opt. **27**, 2960 (1988).

[55] C. R. Bigwood, *New infrared optical systems using diffractive optics,* (2002).

[56] J. J. Moré, *The levenberg-marquardt algorithm: Implementation and theory,* in *Numerical Analysis*, edited by G. A. Watson (Springer Berlin Heidelberg, Berlin, Heidelberg, 1978) pp. 105–116.

[57] G. Côté, J.-F. Lalonde, and S. Thibault, *On the use of deep learning for lens design,* in *OSA Optical Design and Fabrication 2021 (Flat Optics, Freeform, IODC, OFT)* (Optica Publishing Group, 2021) p. 120781A.

[58] O. Faehnle, E. Langenbach, and I. Livshits, *Balancing optical system design and optical fabrication chain design,* in *Eighth European Seminar on Precision Optics Manufacturing*, Vol. 11853, edited by A. Haberl, G. Fütterer, O. W. Fähnle, and R. Rascher, International Society for Optics and Photonics (SPIE, 2021) p. 118530A.

[59] H. H. Hopkins, *The numerical evaluation of the frequency response of optical systems,* Proceedings of the Physical Society. Section B **70**, 1002 (1957).

[60] E. W. Marchand, *Gradient Index Optics* (Academic Press, New York, 1978).

[61] M. Born and E. Wolf, *Principles of Optics: Electromagnetic Theory of Propagation, Interference and Diffraction of Light (7th Edition)*, 7th ed. (Cambridge University Press, 1999).

[62] B. D. Stone, *Practical considerations for GRIN raytracing with commercial software,* in *Optical Modeling and Performance Predictions XI*, Vol. 11484, edited by M. A. Kahan, International Society for Optics and Photonics (SPIE, 2020) pp. 1 − 7.

[63] A. Sharma, D. V. Kumar, and A. K. Ghatak, *Tracing rays through graded-index media: a new method,* Appl. Opt. **21**, 984 (1982).

[64] A. Sharma and A. K. Ghatak, *Ray tracing in gradient-index lenses: computation of ray–surface intersection,* Appl. Opt. **25**, 3409 (1986).

[65] B. D. Stone and G. W. Forbes, *Optimal interpolants for runge–kutta ray tracing in inhomogeneous media,* J. Opt. Soc. Am. A **7**, 248 (1990).

[66] D. Shafer, *A perfect lens design hiding in plain sight for 167 years,* in *OSA Optical Design and Fabrication 2021 (Flat Optics, Freeform, IODC, OFT)* (Optica Publishing Group, 2021) p. 120780P.

[67] A. J. Visconti, K. Fang, J. A. Corsetti, P. McCarthy, G. R. Schmidt, and D. T. Moore, *Design and fabrication of a polymer gradient-index optical element for a high-performance eyepiece,* Optical Engineering **52**, 112107 (2013).

[68] D. H. Lippman and G. R. Schmidt, *Prescribed irradiance distributions with freeform gradient-index optics,* Opt. Express **28**, 29132 (2020).

[69] P. J. Sands, *Inhomogeneous lenses, V. chromatic paraxial aberrations of lenses with axial or cylindrical index distributions,* J. Opt. Soc. Am. **61**, 1495 (1971).

[70] D. P. Ryan-Howard and D. T. Moore, *Model for the chromatic properties of gradient-index glass,* Appl. Opt. **24**, 4356 (1985).

[71] J. Bentley, *Integration of the design and manufacture of gradient-index optical systems,* Ph.D. thesis, University of Rochester (1995).

[72] J. N. Mait, G. Beadie, R. A. Flynn, and P. Milojkovic, *Dispersion design in gradient index elements using ternary blends,* Opt. Express **24**, 29295 (2016).

[73] G. Beadie, J. Mait, R. A. Flynn, and P. Milojkovic, *Ternary versus binary material systems for gradient index optics,* (2017).

[74] A. X. Desai, G. R. Schmidt, and D. T. Moore, *Achromatization of multi-material gradient-index singlets.* Optics express **30 22**, 40306 (2022).

[75] K.-E. Peiponen and T. Asakura, *Dispersion theory for two-phase layered-geometry nanocomposites,* Optical Review **6**, 410 (1999).

[76] P. J. Sands, *Inhomogeneous lenses, III. paraxial optics,* J. Opt. Soc. Am. **61**, 879 (1971).

[77] F. Bociort and J. Kross, *Seidel aberration coefficients for radial gradient-index lenses,* Journal of The Optical Society of America A-optics Image Science and Vision - J OPT SOC AM A-OPT IMAGE SCI **11** (1994), 10.1364/JOSAA.11.002647.

[78] F. Bociort, *Aberration correction with thin radial gradient-index lenses,* (1996).

[79] S. Nemoto and T. Makimoto, *Refractive-index distribution for a prescribed ray path,* J. Opt. Soc. Am. **69**, 450 (1979).

[80] N. S. Kochan, G. R. Schmidt, and D. T. Moore, *Replacing optical surfaces with gradient index functions which preserve ray trajectory,* Opt. Lett. **47**, 1311 (2022).

[81] J. E. Gómez-Correa, A. L. Padilla-Ortiz, J. P. Trevino, A. Jaimes-Nájera, N. Lozano-Crisóstomo, A. Cornejo-Rodriguez, and S. Chávez-Cerda, *Symmetric gradient-index media reconstruction,* Opt. Express **31**, 29196 (2023).

[82] N. Patrikalakis and T. Maekawa, *Shape Interrogation for Computer Aided Design and Manufacturing* (2002).

[83] D. Hermes, *Helper for Bézier curves, triangles, and higher order objects,* The Journal of Open Source Software **2**, 267 (2017).

[84] P. Virtanen, R. Gommers, T. E. Oliphant, M. Haberland, T. Reddy, D. Cournapeau, E. Burovski, P. Peterson, W. Weckesser, J. Bright, S. J. van der Walt, M. Brett, J. Wilson, K. J. Millman, N. Mayorov, A. R. J. Nelson, E. Jones, R. Kern, E. Larson, C. J. Carey, İ. Polat, Y. Feng, E. W. Moore, J. VanderPlas, D. Laxalde, J. Perktold, R. Cimrman, I. Henriksen, E. A. Quintero, C. R. Harris, A. M. Archibald, A. H. Ribeiro, F. Pedregosa, P. van Mulbregt, and SciPy 1.0 Contributors, *SciPy 1.0: Fundamental algorithms for scientific computing in Python,* Nature Methods **17**, 261 (2020).

[85] *The high resolution projection copying magnification lens, jp,47-035017,b(1972),* (1972).

[86] J. J. M. Braat, *Abbe sine condition and related imaging conditions in geometrical optics,* in *Fifth International Topical Meeting on Education and Training in Optics*, Vol. 3190, edited by C. H. F. Velzel, International Society for Optics and Photonics (SPIE, 1997) pp. 59 – 64.

[87] W. C. Sweatt, *Describing holographic optical elements as lenses,* J. Opt. Soc. Am. **67**, 803 (1977).

[88] M. Ponting, A. Hiltner, and E. Baer, *Polymer nanostructures by forced assembly: process, structure, and properties,* in *Macromolecular symposia*, Vol. 294 (Wiley Online Library, 2010) pp. 19–32.

[89] A. J. Visconti, J. A. Corsetti, K. Fang, P. McCarthy, G. R. Schmidt, and D. T. Moore, *Eyepiece designs with radial and spherical polymer gradient-index optical elements,* Optical Engineering **52**, 1 (2013).

[90] J. P. Rolland, K. Fuerschbach, G. E. Davis, and K. P. Thompson, *Pamplemousse: The optical design, fabrication, and assembly of a three-mirror freeform imaging telescope,* Proc. SPIE **9293**, 92930L (2014).

[91] M. Talha, C. Jun, Y. Wang, T. Zhang, D. Cheng, and Z. Sun, *Design, tolerancing and stray light analyses of a freeform hmd optical system,* Optik **121**, 750 (2010).

[92] J. Wang, Y. Liang, and M. Xu, *Design of a see-through head-mounted display with a freeform surface,* Journal of the Optical Society of Korea **19**, 614 (2015).

[93] A. Cameron, *The application of holographic optical waveguide technology to the Q-Sight family of helmet-mounted displays,* in *Head- and Helmet-Mounted Displays XIV: Design and Applications*, Vol. 7326, edited by P. L. Marasco, P. R. Havig, S. A. Jennings, and T. H. Harding, International Society for Optics and Photonics (SPIE, 2009) pp. 150 – 160.

[94] A. Desai, G. Schmidt, and D. Moore, *Multi-material freeform gradient-index spectrometers,* Optics Express **30**, 42912 (2022).

[95] F. Bociort, *Chromatic paraxial aberration coefficients for radial gradient-index lenses,* J. Opt. Soc. Am. A **13**, 1277 (1996).

[96] U. L. Anika Broemel and H. Gross, *Freeform surface descriptions. part I: Mathematical representations,* Advanced Optical Technologies **6**, 327 (2017).

[97] D. Malacara, *Optical shop testing*, (Wiley, 2007) Chap. 18, pp. 832–851, https://onlinelibrary.wiley.com/doi/pdf/10.1002/9780470135976.ch18 .

[98] C. Bigwood and D. Lingwood, *Head-up display analysis developments at Thales Optics Ltd.* in *Novel Optical Systems Design and Optimization VII*, Vol. 5524, edited by J. M. Sasian, R. J. Koshel, P. K. Manhart, and R. C. Juergens, International Society for Optics and Photonics (SPIE, 2004) pp. 240 – 249.

[99] HERE Europe B.V., *Point processing toolkit, a Python package for visualizing and processing 2-d/3-d point clouds,* .

[100] A. Toet and M. A. Hogervorst, *Progress in color night vision,* Optical Engineering **51**, 1 (2012).

[101] N. A. Thompson, *Optical design of common aperture, common focal plane, multispectral optics for military applications,* Optical Engineering **52**, 061308 (2013).

[102] T. H. Jamieson, *Thermal effects in optical systems,* Optical Engineering **20**, 202156 (1981).

[103] D. S. Grey, *Athermalization of optical systems,* J. Opt. Soc. Am. **38**, 542 (1948).

[104] P. O. McLaughlin and D. T. Moore, *Models for the thermal expansion coefficient and temperature coefficient of the refractive index in gradient-index glass,* Appl. Opt. **24**, 4342 (1985).

[105] S. D. Fantone, *Design , engineering, and manufacturing aspects of gradient index optical components*, Ph.D. thesis (1979).

[106] A. Symmons and M. Lifshotz, *Field Guide to Infrared Optical Materials* (SPIE Press, 2021) p. 4.

[107] J. A. Corsetti, W. E. Green, J. D. Ellis, G. R. Schmidt, and D. T. Moore, *Simultaneous interferometric measurement of linear coefficient of thermal expansion and temperature-dependent refractive index coefficient of optical materials,* Appl. Opt. **55**, 8145 (2016).

[108] *TIE 19: Temperature coefficient of the refractive index,* (2016).

[109] M. Balasubramanian, S. Campbell, and D. Werner, *Sequential differential ray tracing formulation for homogeneous and gradient-index lenses using automatic differentiation,* Optical Engineering **62** (2023), 10.1117/1.OE.62.2.021009.

[110] M. L. Boas, *Mathematical methods in the physical sciences; 3rd ed.*, 3rd ed. (Wiley, Hoboken, NJ, 2006).

[111] W. Matusik, *Mit opencourseware, 6.837 computer graphics, bézier curves and splines,* (2012)